



Photovoltaic Performance Enhancement in Monocrystalline
Silicon Solar Cells

A thesis submitted for the degree of Doctor of Philosophy

by

Fanchao Meng

Department of Mechanical, Aerospace and Civil Engineering

College of Engineering, Design and Physical Sciences

Brunel University London

April 2019

Abstract

The approaching depletion of fossil fuels and the increasingly serious global climate change have driven people to search for clean and renewable alternative energy sources. Photovoltaic (PV) cells, which allow the transformation of sunlight directly into electric energy, are expected to play an important role in addressing the above-mentioned challenges. Despite of this huge potentiality, these devices are suffering from the low efficiency and high generation cost of electricity. To meet the ever-growing demand for energy in a sustainable manner, the production of cost-effective device has become the urgent affairs for the development of solar industry.

In this work, applications of effective titanium dioxide (TiO_2)-based aerogels nanomaterials and rare earth cations-activated photoluminescent down-conversion phosphor materials to the domain of energy conversion, particularly for the photovoltaic performance enhancement of single-junction monocrystalline silicon (mono-Si) solar cells are investigated. Improved conversion efficiency in solar cell was demonstrated by developing novel and low-cost anti-reflection coatings (ARCs) on the cell's textured surface through screen printing technique.

TiO_2 has been widely used in silicon PV devices as ARCs owing to its outstanding optical properties. This study looks at investigating the influence of high surface area anatase TiO_2 based nanoaerogels for the light harvesting enhancement in solar cells, specifically at the ultraviolet (UV)-blue wavelengths of solar spectrum. Mesoporous TiO_2 and magnesium oxide (MgO)-doped TiO_2 aerogels were prepared using a precipitation method in conjunction with a modified sol-gel process. The anti-reflection coating (ARC) was formed by screen printing an optimised mixture solution comprising TiO_2 -based aerogels nanomaterials and a co-polymer resin of ethylene vinyl acetate (EVA) on the textured surface solar cell. The obtained results revealed an optimum relative enhancement of 6.0% in conversion efficiency for MgO-doped TiO_2 coating and 3.4% for the undoped- TiO_2 under a simulated one-sun illumination. Given that the silicon solar cells exhibit weak response to the short wavelength of incident light, an alternative ingenious approach to suppress the spectral mismatch and increase the device efficiency has been executed based on the method of spectrum modification by employing down-converting photoluminescent phosphor materials. Silicon PV cells were coated with a luminescent layer composed of EVA and high-quantum yield terbium-activated gadolinium oxysulfide ($\text{Gd}_2\text{O}_2\text{S:Tb}^{3+}$) phosphor using rotary screen printing. The modified cells showed an optimum enhancement of 3.6% in conversion efficiency relative to those for a bare cell. The obtained results also demonstrated that the down-conversion (DC) effect induced by the doping agent (Tb^{3+}) is solely responsible for the PV cells performance enhancement.

Acknowledgements

First and foremost, I would like to express my deep and sincere gratitude to my parents for their continuous support, inspiration, and unparalleled love throughout my PhD studies and my life. Thank you for providing me such an opportunity and experience to chase my dream. This work would not have been possible without your great spiritual encouragement.

I would like to convey my extremely appreciation and respect to Dr. Zahir Dehouche and Dr George Fern for their invaluable help, support, and patience through the course of my thesis. It is my great honor to work with this supervisory team. I learned how to be more creative and energetic, which are particularly essential to scientific research. This work would not have been completed without their endless advice and guidance.

Additionally, I would really like to thank Dr Terry Ireland for his technical support and substantial help in the work of phosphor fabrication and photoluminescence measurements during my PhD study in the department of Chemical and Materials Engineering, Brunel University London. His comments and feedbacks were very beneficial in improving the quality of this thesis work.

My sincere thanks have to also go to the members from the Experimental Techniques Centre (ETC) at Brunel University. Thank you for providing me with useful training, assistance, during the execution of the experiments. I would like to thank Dr Ashley Howkins for the help with TEM analysis, Dr Lorna Anguilano for XRD training and assistance, and Dr Nico Nelson for his full support on SEM measurements. Furthermore, I wish to acknowledge Dr Anna Howson from Quantachrome UK Ltd for the Brunaur-Emmett-Teller tests and Dr Shashi Paul from DeMontfort University, UK for proceeding the ellipsometry measurements.

Finally, I would like to express my deepest gratitude to all of my colleagues and friends for their remarkable patience and support during my whole experience of the PhD study at Brunel University.

Declaration of Originality

I hereby declare that this thesis is entirely the output of my own work. I have faithfully and accurately cited all of my sources, including books, journals, and internet resources. To the best of my knowledge, it contains no work published elsewhere in the form of books or articles or written by someone else for the award of other academic degrees, except where due acknowledgement is made at the respective place in the text. This thesis was carried out by me for the degree of Doctor of Philosophy at Brunel University London, Uxbridge, UK.

Signed:

Fanchao Meng

Date:

April 2019

Photovoltaic Performance Enhancement in Monocrystalline Silicon Solar Cells

PhD Thesis

College of Engineering, Design and Physical Sciences

Brunel University London, Uxbridge, UB8 3PH, UK

List of abbreviations

AM	Air Mass
ASTM	American Society for Testing Materials
ARC	Anti-Reflection Coating
ARCs	Anti-Reflection Coatings
BET	Brunaur-Emmett-Teller
BIPV	Building Integrated Photovoltaics
CIE	International Commission on Illumination
CL	Cathodoluminescence
c-Si	Crystalline Silicon
DC	Down-Conversion
DLARC	Double Layer Anti-reflection Coating
DSC	Differential Scanning Calorimetry
EDS	Energy Dispersive X-ray spectroscopy
EQE	External Quantum Efficiency
ETC	Experimental Techniques Centre
EVA	Ethylene Vinyl Acetate
FE-SEM	Field Emission-Scanning Electron Microscope
FE-TEM	Field Emission-Transmission Electron Microscope
FWHM	Full Width at Half Maximum
GHG	Greenhouse Gas
HAADF	High Angle Annular Dark Field
JCPDS	Joint Committee on Powder Diffraction Standards
mono-Si	Mono-Crystalline Silicon
NIST	National Institute of Standards and Technology
NREL	National Renewable Energy laboratory
IR	Infrared
NPs	Nanoparticles
PCE	Power Conversion Efficiency
PECVD	Plasma-Enhanced Chemical Vapour Deposition
PL	Photoluminescence
PLE	Photoluminescence Excitation
PMMA	Poly Methyl Methacrylate
PV	Photovoltaic
QY	Quantum Yield
RI	Refractive Index
R2R	Roll-to-Roll
SR	Spectral Response
SRM	Standard Reference Material
STC	Standard Test Condition
UC	Up-Conversion
UV	Ultraviolet
XRPD	X-Ray Powder Diffraction

List of Nomenclature

E_{ph}	Photon Energy	eV
E_c	Conduction band	eV
E_g	Bandgap energy	eV
E_v	Valence band	eV
FF	Fill factor	–
G	Solar irradiance	W/m ²
I	Current	A
I_{sc}	Short-circuit current	A
I_{mp}	Current at maximum power point	A
I_{in}	Incident irradiance	W/m ²
J_{sc}	Short-circuit current density	A/cm ²
V	Voltage	V
V_{oc}	Open-circuit voltage	V
V_{mp}	Voltage at maximum power point	V
P_{max}	Maximum power	W
R_s	Series resistance	Ω
R_{sh}	Shunt resistance	Ω
α	Absorption coefficient	–
θ	Angle	°
η	Efficiency	(%)
τ	Crystallite size	Å
λ	Wavelength	nm
d_{hkl}	Interplanar spacing	Å

List of Publications

Publications arising from this thesis

Some parts of work presented in this thesis have given rise to the following publications and conference proceedings.

Publications and conference proceedings

Meng, F. C., Dehouche, Z., Ireland, T.G, Fern, G.R. (2019). “Improved photovoltaic performance of monocrystalline silicon solar cell through luminescent down-converting $\text{Gd}_2\text{O}_2\text{S:Tb}^{3+}$ phosphor”. *Progress in Photovoltaics: Research and Applications*. **27**(7): pp. 640-651.

Meng, F. C., Dehouche, Z., Nutasarin, A., Fern, G. R. (2018). “Effective MgO-doped TiO_2 nanoaerogel coating for crystalline silicon solar cells improvement”. *International Journal of Energy Research*. **42**(12): pp. 3915-3927.

Meng, F. C., Nutasarin, A., Dehouche, Z., and Fern, G. R. (2016). “Nanostructured MgO-doped TiO_2 Aerogels for Enhanced Monocrystalline Silicon Solar cells”. *Proceedings of the 32nd European PV Solar Energy Conference and Exhibition (EU PVSEC)*, pp. 583-588.

Oral Presentations

Meng, F. C., Dehouche, Z., Ireland T. G., Fern, G. R., “Energy Performance Enhancement of c-Si Solar Cells with Down-Converting Photoluminescence Phosphors”. In 4th Annual Research Institutes Conference, Brunel University London, Uxbridge, UK, June 27th, 2018.

Meng, F. C., Dehouche, Z., Nutasarin, A., Fern, G. R., “Improved monocrystalline Silicon solar cell by integrating MgO-doped TiO_2 nanoaerogels via a screen printing process”. In 8th SOLARIS Conference, Brunel University London, Uxbridge, UK, July 27-28, 2017.

Poster Presentations

Meng, F. C., Dehouche, Z., Ireland T. G., Fern, G. R., “Photoluminescence of green-emitting $\text{Gd}_2\text{O}_2\text{S}:\text{Tb}^{3+}$ phosphor for enhanced monocrystalline silicon solar cells”. In 2nd International Conference in Advanced Energy Materials (AEM), University of Surrey, Guildford, England, September 11-13, 2017.

Meng, F. C., Nutasarin, A., Dehouche, Z., and Fern, G. R., “Nanostructured MgO-doped TiO_2 Aerogels for Enhanced Monocrystalline Silicon Solar cells”. The 32nd European PV Solar Energy Conference and Exhibition (EU PVSEC), Munich, Germany, June 20-24, 2016.

Meng, F. C., Dehouche, Z., Nutasarin, A., Fern, G. R., “MgO doped TiO_2 nanomaterials for enhanced monocrystalline solar cell”. The 9th Annual Research Student Conference, Brunel University London, Uxbridge, May 25-26, 2016.

Publications and proceedings not included in this thesis

Fern, G. R., Silver, J., Tarverdi, K., Ireland T. G., **Meng, F. C.**, Dehouche, Z. (2017). “Development of Nano-Phosphors Films for Polymer Protection and Plant Growth”. Proceedings of the 24th International Display Workshops (IDW), Sendai, Japan, December 6-8, 2017, pp 187-190.

Table of Contents

Abstract	I
Acknowledgements	II
Declaration of Originality	III
List of abbreviations	IV
List of Nomenclature	V
List of Publications	VI
List of Figures	XII
List of Tables	XVIII
Chapter 1 Introduction	1
1.1 Motivation.....	4
1.2 The thesis objectives	6
1.3 Thesis Outline	7
Chapter 2 Literature review of Photovoltaic fundamentals and technologies	8
2.1 Solar radiation.....	8
2.2 Solar cells technology review	14
2.3 Operational principles of photovoltaic solar cells.....	17
2.3.1 Photovoltaic effect	17
2.3.2 Carrier transport in p-n junction solar cell	19
2.3.3 Recombination of charge carriers	22
2.4 I-V characteristics of photovoltaic cells.....	23
2.5 Quantum efficiency and spectral response.....	28
2.6 Energy losses in p-n junction silicon solar cells	31
2.6.1 Intrinsic losses of ideal solar cells.....	31
2.6.2 Extrinsic losses of non-ideal cells	32
2.6.2.1 Fresnel reflection losses	32
2.6.2.2 Solar cell collection losses	34
2.6.2.3 Recombination losses	34
2.6.2.4 Ohmic losses	35
2.6.2.5 Summary	36
2.7 Solar cell efficiency limits	37
2.8 Efficiency enhancement for solar PV cells	39
2.8.1 Spectrum modification.....	39
2.8.1.1 Rare earth ions.....	42
2.8.1.2 Quantum dots and Organic dyes.....	47

2.8.2 Optical path length enhancement	48
2.8.3 Anti-Reflection	51
2.8.3.1 Silicon oxide ARC and related work	53
2.8.3.2 High surface area of TiO ₂ ARC	55
2.8.4 Other factors.....	56
2.9 Summary	57
Chapter 3 Characterisation of Crystalline Silicon Solar Cells	58
3.1 Solar Cells.....	58
3.2 Solar Cells Preparation	60
3.2.1 Solar Cells Cutting	60
3.2.2 Solar Cells Soldering	61
3.3 Electrical Characterisation	63
3.4 Materials Fabrication Machines.....	73
3.4.1 High Pressure Compact Laboratory (HPCL) Reactor.....	73
3.4.2 Chamber Box Furnaces.....	74
3.5 Instruments for optical characterisation.....	75
3.5.1 Ultra Violet (UV/Vis) spectrophotometer.....	76
3.5.2 Ellipsometry Measurements.....	78
3.6 Materials characterisation instruments.....	80
3.6.1 Scanning Electron Microscope	80
3.6.2 Transmission Electron Microscope.....	83
3.6.3 X-Ray Powder Diffraction	84
3.6.4 Photoluminescence spectroscopy.....	86
3.6.5 Nitrogen (N ₂) gas physisorption.....	87
3.7 Differential Scanning Calorimetry.....	88
3.8 Summary	90
Chapter 4 Titanium Oxide-Based Nanoaerogels for Crystalline Silicon Solar Cells	92
4.1 Introduction.....	92
4.2 TiO ₂ and its applications	93
4.3 Experimental Methods	100
4.3.1 Materials used for the fabrication of TiO ₂ -based aerogels.....	100

4.3.2 Synthesis of TiO ₂ based aerogels	100
4.3.3 Formation of the deposited layer	103
4.3.3.1 Binding Materials	103
4.3.3.2 Polymer Solvent	105
4.3.3.3 EVA Layer Preparation.....	106
4.3.3.4 Composite Layer Preparation.....	108
4.3.3.5 Layer Application	109
4.3.4 Equipments used in experiment	111
4.4 Results and Discussion	112
4.4.1 Synthesised TiO ₂ -based nanoaerogels	112
4.4.1.1 Crystalline phases and Morphology analysis	112
4.4.1.2 Structural properties	117
4.4.2 Solely EVA Layer.....	119
4.4.3 EVA/TiO ₂ and EVA/MgO-TiO ₂ composite layer.....	123
4.4.3.1 Electrical characteristics of coated solar cell.....	123
4.4.3.2 Microstructure of coated solar cell	128
4.4.3.3 Optical characteristics of coated solar cell	130
4.4.3.4 External quantum efficiency of coated solar cell	136
4.5 Silicon Oxide for Crystalline Silicon Solar Cells	137
4.5.1 Introduction.....	137
4.5.2 Experiment method.....	138
4.5.3 Result and discussion	140
4.6 Summary.....	143
Chapter 5 Phosphor for Crystalline Silicon Solar Cells.....	144
5.1 Introduction.....	144
5.2 Spectrum Modification for Silicon Solar Cells.....	144
5.2.1 Performance Enhancement through Luminescent Materials	150
5.2.2 Encapsulation of Luminescent Materials	151
5.3 Experimental Methods	152
5.3.1 Preparation of Gd ₂ O ₂ S:Tb ³⁺ phosphor particles.....	152
5.3.2 Formation of the luminescent layer.....	155
5.3.2.1 EVA and EVA/Phosphor layer preparation.....	156
5.3.2.2 Layer application	157
5.3.3 Instruments used for experiment.....	159
5.4 Results and Discussion	160

5.4.1 Phosphor characterisation	160
5.4.1.1 X-Ray Powder Diffraction (XRPD)	160
5.4.1.2 Photoluminescence properties of Gd ₂ O ₂ S:Tb ³⁺ phosphor	161
5.4.1.3 Crystal structures and morphological analysis	164
5.4.2 EVA Layer	167
5.4.3 EVA/Gd ₂ O ₂ S:Tb ³⁺ and EVA/Gd ₂ O ₂ S layer	170
5.4.3.1 Electrical characteristics	170
5.4.3.2 Optical Properties	172
5.4.3.3 External quantum efficiency characterisation	177
5.4.3.4 Microstructure of the EVA/phosphor-coated cell	179
5.5 Energy Performance Enhancement of Crystalline Silicon Solar cells Using Broadband Luminescent Down-converting Phosphor.....	181
5.5.1 Introduction.....	181
5.5.2 Experiment method.....	181
5.5.3 Results and Discussion.....	182
5.5.4 Conclusion	186
5.6 Summary	187
Chapter 6 Summary and Future Work	188
6.1 Summary and Conclusion	188
6.2 Outlook and Future Direction	191
References	193
Appendix A Supplementary Information	207
A.1 Supplementary information: Comparison of solely EVA-coated solar cells by using two different screen-printing techniques.....	207
A.2 Supplementary information: Electrical characteristics of EVA/Gd ₂ O ₂ S:Tb ³⁺ coated cells under natural sunlight	208
A.3 Supplementary information: Discussion of experimental attempts with regard to Ethyl Cellulose for PV cell encapsulation	209
Appendix B Poster Presentations	210

List of Figures

Figure 1.1. CO ₂ emissions from global energy consumption (includes fossil fuel and industrial processes) for the time of 2000-2017 [2].	1
Figure 1.2. Solar Photovoltaic (PV) installed capacity by region from 2007 to 2017 [7].	3
Figure 2.1. Geometric diagram showing the sun-earth relationships. Figure is adapted from [24].	9
Figure 2.2. The path length in units of Air Mass which varies with the zenith angle. Figure is adapted from [26].	10
Figure 2.3. Spectral comparison between extraterrestrial (AM 0) solar spectrum (olive) and the standard AM 1.5 global spectrum (orange). Inset plot shows the geometrical position in terms of a 37 degree tilted surface under the AM 1.5 illumination [27].	11
Figure 2.4. Spectral intensity distribution of black body radiation as a function of wavelength at temperature of 3000 K, 4000 K, 5000 K, 5800 K, and 6000 K respectively. Figure is reproduced with permission from PVEDucation.org [29].	12
Figure 2.5. Average hourly radiation per day for each month of the year in Wh/m ² , for Gatwick, London [31].	13
Figure 2.6. Classification of PV solar cell. Figure is reproduced with permission from [34].	14
Figure 2.7. Solar cell efficiency revolution from 1975 to 2023 [39].	16
Figure 2.8. Energy band gap diagrams for a typical semiconductor showing the excitation from a donor state where an electron is generated in the conduction band. Figure is adapted from [45].	18
Figure 2.9. P-N junction semiconductor diode for a silicon solar cell (Left) and the forward-biased schematic diagram (right) showing its working principle. Figure is adapted from [45], [46].	20
Figure 2.10. Equivalent circuit of single-diode model of an ideal solar cell.	21
Figure 2.11. Energy level diagram of partial chemical elements in the gap of silicon, letter "A" and "D" represent the "acceptor" and "donor" impurity respectively [44].	22
Figure 2.12. Typical I-V & P-V curves of a single-junction solar cell.	24
Figure 2.13. I-V & P-V curves showing the definition of fill factor.	25
Figure 2.14. Irradiance and temperature effects on the I-V characteristics of PV cells.	26
Figure 2.15. Equivalent circuit of single-diode model of a practical solar cell.	27
Figure 2.16. Effects of variations in (a) series resistance (R_s) and (b) shunt resistance (R_{sh}) on the I-V characteristic of a solar cell.	28
Figure 2.17. External, Internal quantum efficiency and reflectance responses curves for industrial SiN _x -passivated Si-wafer based crystalline solar cell [55].	30
Figure 2.18. Fundamental energy losses in a single-junction silicon solar cell. The inset shows the band structure with the splitting of the quasi-Fermi energy levels [59].	32
Figure 2.19. The optical reflection losses in a single-junction crystalline silicon solar cell with flat surface (left), and the modified solar cell with improved light trapping capability by combining surface texturing and anti-reflection coating (right).	33
Figure 2.20. The effects of high series resistance (olive), low shunt resistance (red), and combined effects (orange dashed line) on the electrical characteristics of single-diode ideal solar cell.	35
Figure 2.21. Energy losses in a single-junction solar cell: {1} lattice thermalisation loss; {2} transmission loss; {3} recombination loss; {4} junction loss, and {5} contact loss. Figure is adapted with permission from [61].	36

Figure 2.22. Schematic energy diagrams showing the working mechanisms in DC, DS, and UC respectively. A high-energy incident photon is absorbed by the DC layer and is then emitted into two lower-energy photons (left). A high-energy photon is absorbed in the DS layer with the emission of one lower-energy photon and thermalisation losses (dashed line in middle). Two lower-energy photons are absorbed in the UP layer followed by the emission of one high-energy photon (right).	40
Figure 2.23. Energy level diagrams of RE ³⁺ ions incorporated in LaCl ₃ crystals [70].....	43
Figure 2.24. Sketch showing the optical path length enhancement in a silicon solar cell obtained by decorating metallic nanoparticles at the cell's surface. Light is directed at an angle away from the normal (red versus blue). A transparent dielectric spacer layer is placed between the metal particles and the silicon surface.	49
Figure 2.25. Sketch showing the comparison of surface reflection between a flat (left) and a textured silicon substrate with pyramidal like shape (right). In case of textured surface, light is multiply reflected, improving the chances of being internally refracted.	50
Figure 2.26. Sketch showing the destructive interference occurred in a quarter-wavelength anti-reflection coating on a flat silicon solar cell. The two reflected waves with same frequency and amplitude cancel each other which enable more coupling of light.....	51
Figure 3.1. Motech monocrystalline silicon solar cells: XS156-200R (top) and T6S-3A (bottom)...	59
Figure 3.2. TMX90 Laser cutter (Top left), solar cell layout on the working area of wooden plate (Top right), setting up process in computer (Bottom left), and the comparison of solar cell before and after cutting (Bottom right).	61
Figure 3.3. Photographs showing the manual soldering process with corresponding soldering components.	62
Figure 3.4. Sketch showing the experimental set-up of I-V electrical characteristics measurement.	63
Figure 3.5. The irradiance spectrum of a Trisol TSS 156 Xe flash solar simulator. For comparison, the AM 1.5G spectrum is also plotted.	64
Figure 3.6. Calibration of the solar simulator. Inset images show the clear version of the pyranometer (left) and reference solar cell (right) which was encased in a metal enclosure with a protective optical filter glass window.....	65
Figure 3.7. Photograph showing the experimental set-up of I-V measurements where the tested cell is masked by an artificially designed plate (left), and a sketch showing the clear version of the mask (right).	66
Figure 3.8. Flow diagram of the data acquisition system for temperature measurement.	67
Figure 3.9. Calibration of thermocouples and data logging device.....	68
Figure 3.10. Calibration curve for the thermocouple.	69
Figure 3.11. J-V characteristics of (a) XS156B3-200R and (b) T6S-3A mono-Si solar cells before and after laser cutting.	70
Figure 3.12. Bentham PVE 300 monochromator-based solar cell response system.	72
Figure 3.13. Experimental set-up of the EQE measurement.	72
Figure 3.14. Digital graph of the high-pressure compact stirred reactor.	74
Figure 3.15. Photograph showing the experimental set-up for materials fabrication where the furnace (at left) and reactor system (at right) are placed inside the laboratory fume hood.	75
Figure 3.16. Photograph of PerkinElmer Lambda 650S UV/Vis Spectrometer system.	76
Figure 3.17. Optical layout of the dual-beam UV/Vis spectrophotometer. The optical path is highlighted in green lines [113].....	77

Figure 3.18. The Rudolph Auto EL III for ellipsometry measurements.....	78
Figure 3.19. The configuration of the as-used null ellipsometer (top), and a schematic diagram showing its operating principle (bottom). The figure is reproduced from [115]......	79
Figure 3.20. The p-type silicon wafer used for the ellipsometry measurement.	80
Figure 3.21. ZEISS SUPRA 35VP field emission scanning electron microscope.	81
Figure 3.22. Photograph of the Polarab sputter coater.	83
Figure 3.23. JEOL JEM-2000F scanning transmission electron microscope.....	84
Figure 3.24. Bruker D8 Advance X-ray powder diffractometer. Inset photographs show the standard XRD sample holder with and without powder sample.....	85
Figure 3.25. Bentham M300 monochromator detector system.	86
Figure 3.26. NOVAtouch surface area and pore size analyser [118].....	87
Figure 3.27. Differential scanning calorimetry system. Inset image shows the standard aluminum sample pans and covers used for enclosing the EVA sample.	89
Figure 4.1. Sketch showing the titanium dioxide ($[\text{TiO}_6]^{8-}$) octahedral geometry and its connection methods.	95
Figure 4.2. Crystal structures of TiO_2 anatase (tetragonal, $I4_1/amd$) and rutile (tetragonal, $P4_2/mmm$) polymorphs. Figure is adapted from [127]......	95
Figure 4.3. Geometrical structures of the unit cells in respect to: (a) anatase and (b) rutile TiO_2 . The blue and red spheres are Ti and O atoms, with corresponding coordination number of 6 and 3 respectively [129]......	95
Figure 4.4. XRD patterns of TiO_2 powders calcined at 300-800 °C [122]......	97
Figure 4.5. Schematic representation of the different stages of the sol-gel process.....	99
Figure 4.6. Solution mixing process (left) and vessel (right) of the high-pressure compact stirred reactor.....	101
Figure 4.7. TiO_2 (top) and MgO-doped TiO_2 (bottom) aerogel nanomaterials before and after annealing at 400 °C for 10 hours.	102
Figure 4.8. Chemical structures of ethylene and vinyl acetate comonomers, and poly ethylene vinyl acetate [160]......	104
Figure 4.9. EVA sheet (left) and the preparation of EVA/p-xylene solution (right) where the beaker is placed on top of the hotplate magnetic stirrer.	107
Figure 4.10. Ultrasonic bath used for dispersing TiO_2 -based nanoaerogels in p-xylene solvent.	109
Figure 4.11. Blade screen printing process of mono-Si solar cell.	109
Figure 4.12. Coated solar cells after curing at 190 °C for 5 mins.	111
Figure 4.13. Flow diagram showing the fabrication process of TiO_2 based nanoaerogels and their integration onto the surface of mono-Si solar cell.....	111
Figure 4.14. X-ray powder diffractometer patterns of (a) TiO_2 and (b) MgO-doped TiO_2 nanoparticles annealed at 400 °C for 10 hours.	114
Figure 4.15. Field emission scanning electron microscope micrographs of (a), (b) TiO_2 and (c), (d) MgO-doped TiO_2 nanoaerogels annealed at 400 °C.....	115
Figure 4.16. Energy-dispersive X-ray spectroscopy (EDS) of (a) TiO_2 and (b) MgO-doped TiO_2 nanoaerogels. Inset SEM micrographs refer to the corresponding selected area, and the scale bar for each case is 10 μm	116
Figure 4.17. (a) to (c), Field emission transmission electron microscope microrgraphs of TiO_2 . (d), MgO-doped TiO_2 nanoaerogel annealed at 400 °C.	117
Figure 4.18. N_2 -sorption isotherms of (a) representative TiO_2 aerogel and (b) MgO-doped TiO_2	

aerogel; c and d, the corresponding pore size distribution plots are shown.	118
Figure 4.19. The differential scanning calorimetry heating curves of raw ethylene vinyl acetate material.....	119
Figure 4.20. Transmission spectra of solely EVA layers with different weight ratio (wt%) deposited on the glass substrate.....	120
Figure 4.21. Reflection and absorption spectra of uncoated cell and cell coated with various weight ratios of EVA.....	121
Figure 4.22. Photovoltaic J-V curves of mono-Si solar cell before and after coating with 15 wt% EVA examined at 1000 W/m ² and 25 °C, with illuminated surface area of 8.553 cm ²	122
Figure 4.23. Viscosity as a function of temperature for different concentrations of EVA/p-xylene solutions.	123
Figure 4.24. Photovoltaic J-V curves of mono-Si solar cells before and after coating with solely EVA, EVA/TiO ₂ , and EVA/MgO-doped TiO ₂	124
Figure 4.25. Enhancement in power conversion efficiency of mono-Si solar cells coated with EVA/TiO ₂ and EVA/MgO-doped TiO ₂	126
Figure 4.26. Fundamental temperature coefficient of open circuit voltage as a function of cell temperature. The inset fitting equations were derived for each case of tested solar cell.....	127
Figure 4.27. J-V characteristics of the uncoated cell and cells coated with solely EVA, EVA/TiO ₂ , and EVA/MgO-doped TiO ₂ under UV illumination with light intensity of 45.9 W/m ²	127
Figure 4.28. Cross section SEM images of the coated mono-Si solar cells with (a) EVA/TiO ₂ and (b) EVA/MgO-doped TiO ₂	129
Figure 4.29. Energy-dispersive X-ray spectroscopy of mono-Si solar cells coated with (a) EVA/TiO ₂ and (b) EVA/MgO-doped TiO ₂	129
Figure 4.30. Comparison of optical reflectance and absorption spectra for uncoated and coated cells with the following configurations: (a), (b) EVA/TiO ₂ -coatd and (c), (d) EVA/MgO-doped TiO ₂ -coated cells compared to those of bare cells.	130
Figure 4.31. Optical (a) reflectance and (b) absorbance of uncoated and cells coated with solely EVA (15-wt%), EVA/TiO ₂ (0.3-mg/ml) and EVA/MgO-doped TiO ₂ (0.3-mg/ml).	131
Figure 4.32. Ultra-visible absorption spectra of quartz substrate and the deposited nanocomposite films of EVA/TiO ₂ and EVA/MgO-doped TiO ₂	132
Figure 4.33. Transmission spectra for glass substrate and the deposited composite films with the following configuration: glass with solely EVA, glass with EVA/TiO ₂ , and glass with EVA/MgO-doped TiO ₂	134
Figure 4.34. Transmission spectra for glass substrate and the deposited composite films with the following configuration: (a) EVA/TiO ₂ and (b) EVA/MgO-TiO ₂ at different particle densities.	134
Figure 4.35. Optical energy bandgap of EVA/TiO ₂ and EVA/MgO-TiO ₂ composite films obtained by extrapolating the linear portion of the versus hv value.	135
Figure 4.36. External quantum efficiency (EQE) curves and (b) enhancement factor of EQE for cell coated with Solely EVA, EVA/TiO ₂ , and EVA/MgO-TiO ₂ , compared that of bare cell.....	137
Figure 4.37. Photograph of PECVD coating system.	138
Figure 4.38. J-V curves of the coated cells at the maximum performance enhancement acquired using AM 1.5 illumination. Inset shows a photograph of coated cells with different surface colour compared to the uncoated cell.....	140
Figure 4.39. Optical reflectance (a) and absorption (b) spectra of coated cells with single and double	

layers of SiO ₂ coating compared to those for a bare cell.	141
Figure 4.40. Transmission spectra for quartz substrate and double anti-reflection layers for solar cells with optimum enhancement obtained.....	142
Figure 5.1. (a) Spectral response (SR) and (b) external quantum efficiency (EQE) as a function of wavelength for Motech T6S-3A mono-Si solar cell.....	145
Figure 5.2. Sketch showing the working principle of the luminescent down-converting material. Figure is adapted from [161].	146
Figure 5.3. Schematic crystal structure of Ln ₂ O ₂ S (Ln = Gd, Y).....	149
Figure 5.4. Reaction solution was heated at 85 °C with continuous stirring.	153
Figure 5.5. The resulting precipitates filtered by a Buchner funnel. Inset image shows the soft precursor powders dried at 100 °C for 24 hours.	154
Figure 5.6. Schematic diagram of sulfuration method of as prepared Gd(OH)CO ₃ :Tb ³⁺ precursor powder. Inset photographs show the front and top view of the alumina crucible with the mixed powder filled in.	155
Figure 5.7. Preparation of EVA/p-xylene/Gd ₂ O ₂ S:Tb ³⁺ solution where the glass beaker is placed on top of the hotplate magnetic stirrer.....	157
Figure 5.8. Rotary screen printing process in current work (left), and a photograph of the K Lox Hand Proofer (right).	157
Figure 5.9. A photograph of solar cell coated with EVA/Gd ₂ O ₂ S:Tb ³⁺ composite layer irradiated by UV light.....	158
Figure 5.10. Flow diagram showing the fabrication process of Gd ₂ O ₂ S:Tb ³⁺ and the integration of composite material (EVA/Gd ₂ O ₂ S:Tb ³⁺) on textured surface of mono-Si solar cell.	159
Figure 5.11. XRPD patterns of Gd ₂ O ₂ S:Tb ³⁺ and undoped-Gd ₂ O ₂ S samples annealed at 900 °C for 1h in air atmosphere, compared to that of uncalcined precursor powder.	160
Figure 5.12. Excitation (λ _{em} = 543 nm) and emission (λ _{ex} = 292 nm) spectra of Gd ₂ O ₂ S:Tb ³⁺ particles calcined at 900 °C for 1 h. The inset shows the schematic energy level diagram of a free Tb ³⁺ cation with proposed excitation and emission process, and a photograph of as-prepared phosphor sample showing bright green emission under irradiation with a 365 nm quartz tube lamp.	162
Figure 5.13. CIE chromatic diagram showing the x and y coordinates of Gd ₂ O ₂ S:Tb ³⁺ sample excited by 254 nm UV light.....	163
Figure 5.14. FE-SEM images of (a) representative Gd ₂ O ₂ S:Tb ³⁺ and (b) undoped-Gd ₂ O ₂ S particles fired at 900 °C.....	164
Figure 5.15. Histogram of (a) Gd ₂ O ₂ S:Tb ³⁺ and (b) undoped Gd ₂ O ₂ S submicron phosphor samples showing Lorentzian curve fit in red.	165
Figure 5.16. EDS spectra of (a) Gd ₂ O ₂ S:Tb ³⁺ phosphor and (b) undoped-Gd ₂ O ₂ S host materials..	166
Figure 5.17. STEM micrographs of (a) single crystals of Gd ₂ O ₂ S:Tb ³⁺ ; (b) total visible light (CL) image using the VULCAN detector; (c) overlay of images of (a) and (b).	167
Figure 5.18. Transmission spectra of solely EVA layers with different weight ratio (wt%) deposited on the quartz substrates.	168
Figure 5.19. Reflection spectra of uncoated cell and solar cells coated with different ratios of EVA.	169
Figure 5.20. Photovoltaic J-V curves of mono-Si solar cell before and after coating with 15 wt% EVA examined at 1000 W/m ² and 25 °C, with illuminated surface area of 8.553 cm ² . Inset shows a photograph of mono-Si solar cell with and without an EVA layer.	170

Figure 5.21. J-V curves of mono-Si solar cells with the following configurations: a bare cell, a cell coated with solely EVA (15-wt%) binder, a cell coated with EVA/undoped-Gd ₂ O ₂ S (2.0-mg/ml), and a cell coated with EVA/Gd ₂ O ₂ S:Tb ³⁺ (2.0-mg/ml). Inset shows a digital photograph of solar cell coated with EVA/Gd ₂ O ₂ S:Tb ³⁺ (2.0-mg/ml) composite layer irradiated by UV light.	171
Figure 5.22. Enhancement in PCE of mono-Si solar cells coated with different concentrations of Gd ₂ O ₂ S:Tb ³⁺ and Gd ₂ O ₂ S (blank) materials.	172
Figure 5.23. Comparison of reflectance and absorption spectra for uncoated and coated cells with EVA/Gd ₂ O ₂ S:Tb ³⁺ at different phosphor concentrations.	173
Figure 5.24. Comparison of reflectance and absorption spectra for uncoated and coated cells with solely EVA, EVA/Gd ₂ O ₂ S:Tb ³⁺ (2.0-mg/ml), and EVA/undoped-Gd ₂ O ₂ S (2.0-mg/ml).	174
Figure 5.25. Pie charts showing the recorded beam positions of coated films on top of silicon wafer; (a) EVA/Gd ₂ O ₂ S:Tb ³⁺ (2.0-mg/ml), (b) EVA/undoped-Gd ₂ O ₂ S (2.0-mg/ml), (c) solely EVA (15-wt%).	176
Figure 5.26. (a) EQE curves at maximum enhancement for solar cells integrated with Gd ₂ O ₂ S submicron phosphors; (b) enhancement factor of EQE for solar cells coated with solely EVA, EVA/Gd ₂ O ₂ S:Tb ³⁺ , and EVA/undoped-Gd ₂ O ₂ S, compared to that of bare cell.	177
Figure 5.27. FE-SEM cross-section image of the mono-Si solar cell after coating with EVA/Gd ₂ O ₂ S:Tb ³⁺	179
Figure 5.28. EDS spectrum and top-view SEM image of solar cell coated with EVA/Gd ₂ O ₂ S:Tb ³⁺ at a concentration of 2.0-mg/ml; the scale bar is 3 μm.	180
Figure 5.29. (a) XRPD pattern of SrAl ₂ O ₄ :Eu ²⁺ annealed at 1350 °C for 3h. (b) PLE and PL spectra of SrAl ₂ O ₄ :Eu ²⁺ at room temperature. Inset shows the digital photograph of as-prepared phosphor under 365 nm illumination.	183
Figure 5.30. (a), (b) FE-SEM micrographs of SrAl ₂ O ₄ :Eu ²⁺ annealed at 1350 °C. (c) EDS spectra of EVA/SrAl ₂ O ₄ :Eu ²⁺ composite film deposited on mono-Si solar cell. Inset SEM micrograph shows the top-view of coated cell.	184
Figure 5.31. (a) J-V curves of mono-Si solar cells before and after coating with EVA, EVA/SrAl ₂ O ₄ :Eu ²⁺ (3.0-mg/ml). Inset image shows the coated cell with EVA/ SrAl ₂ O ₄ :Eu ²⁺ composite layer under UV illumination. (b) Enhancement in PCE of coated cells at different.	185
Figure 5.32. Reflectance spectra of all evaluated solar cells.	186
Figure A-1. Reflectance spectra (a) and J-V curves (b) of 15wt% solely EVA coated cells using two different screen-printing techniques.	207
Figure A-2. (a) Distribution of solar irradiance per time of a particular day in July (the solar time for each recorded local clock time is labeled underneath, and the solar hour angle “ω” with regard to the corresponding solar time is highlighted). Inset image and table show separately the experimental set-up and the timely irradiance intensity as well as the geographic information. (b) J-V curves of solar cells before and after coating with solely EVA and EVA/Gd ₂ O ₂ S:Tb ³⁺ (2.0-mg/ml) under natural sunlight illumination (1000 W/m ²). (c) J-V curves of optimised solar cells at different irradiance levels. (d) Comparison of PCE between uncoated and coated cell with EVA/Phosphor as a function of irradiance variations. Inset table demonstrates an example of the phosphor application on a commercial Motech mono-Si PV module where the daily electric generations for XS60CB310 module with and without phosphor coating (2.0-mg/ml) are compared. The mass of Gd ₂ O ₂ S:Tb ³⁺ phosphor for covering the effective area for a module is estimated to be at 506.7 mg.	208

List of Tables

Table 2.1. Confirmed conversion efficiency of solar cells and commercial PV modules measured under the global AM1.5 spectrum (1000 W/m ²) at 25 °C [20].	16
Table 2.2. Variation of ideality factors in terms of the recombination type [47].	22
Table 2.3. Electronic structures of RE ³⁺ ions (except for Sc ³⁺ and Y ³⁺) [72].	44
Table 2.4. Common quantum dots used as down-shifting layers.	47
Table 2.5. Commercial organic dyes used as down-shifting layers.	48
Table 3.1. Electrical parameters of the under-study mono-Si solar cells, provided from Motech manufacture.	60
Table 3.2. Physical properties of leaded solder alloys (Sn-Pb-Ag) [104].	62
Table 3.3. Comparison of spectral irradiance distribution in percentage (%) between the OAI simulator and the global reference IEC 60904-9 [105].	64
Table 3.4. Dimension data of the circular hole.	66
Table 3.5. Calibration data for type K thermocouple used in this work.	69
Table 3.6. J-V characteristics of XS1563-200R mono-Si solar cells before and after laser cutting.	71
Table 3.7. J-V characteristics of T6S-3A mono-Si solar cells before and after laser cutting.	71
Table 3.8. Equipments and instruments for experimental tests.	91
Table 4.1. Properties comparison between anatase and rutile TiO ₂ [128].	96
Table 4.2. Elvax 150 EVA properties [159].	104
Table 4.3. Physical properties of the solvents.	106
Table 4.4. Variation of Scherrer constant K for crystallites of different shapes [174].	113
Table 4.5. The tetragonal lattice parameters of TiO ₂ and MgO-doped TiO ₂ nanoparticles from XRPD data.	113
Table 4.6. Elemental composition of TiO ₂ and MgO-TiO ₂ powder samples from the EDS spectra.	116
Table 4.7. Structural properties of TiO ₂ -based nanoaerogles.	119
Table 4.8. PCE change in mono-Si solar cell coated with different wt% ratios of EVA.	122
Table 4.9. J-V characteristics of mono-Si solar cells before and after coating with solely EVA, EVA/TiO ₂ and EVA/MgO doped-TiO ₂ .	125
Table 4.10. Electrical characteristics of the uncoated and coated solar cells under UV illumination with light intensity of 45.9 W/m ² .	128
Table 4.11. Summary of the coating parameters and conditions for mono-Si solar cells with single and double antireflection layers of silicon oxide [228].	139
Table 4.12. Electrical characteristics of all evaluated solar cells in this work under AM1.5 illumination condition.	140
Table 5.1. The crystallite size and hexagonal lattice parameters of Gd ₂ O ₂ S:Tb ³⁺ phosphor and Gd ₂ O ₂ S host particles from XRPD data.	161
Table 5.2. PL quantum yield and energy absorption efficiency of the Gd ₂ O ₂ S:Tb ³⁺ phosphor sample.	163
Table 5.3. Elemental composition of Gd ₂ O ₂ S:Tb ³⁺ and undoped-Gd ₂ O ₂ S powder samples from the EDS spectra.	166
Table 5.4. PCE change in mono-Si solar cell coated with different wt% ratios of EVA.	169
Table 5.5. J-V characteristics of all evaluated solar cells.	172
Table 5.6. Index of refraction (n) and film thickness (d) at 638.2 nm.	176

Table 5.7. J-V characteristics of all evaluated solar cells.....	185
Table A-1. Comparison of electrical characteristics of solely EVA coated cells using different screen-printing techniques.....	207
Table A-2. J-V characteristics of mono-Si solar cells coated with EVA and EVA/Gd ₂ O ₃ :Tb ³⁺ (2.0-mg/ml) under natural sunlight illumination (light intensity =1000 W/m ²).....	208

Chapter 1 Introduction

Energy is the developmental basis of national economy in modern society, and is essential for sustaining the human life. Over the last five decades, the rapid increase of energy demands driven by the ever-increasing global population and strong economic growth, which has made exploitation of fossil fuels to increase exponentially. Currently, almost 85% of world energy demand is still fulfilled by fossil fuels, such as coal, oil, and natural gas [1]. Despite of being served as the major energy sources, their impacts on environment, especially the greenhouse gas (GHG) emissions released from the combustion of fossil fuels continue to threaten the ecosystem, which are blamed for the global warming and climate change. It was reported that the global carbon dioxide (CO₂) emissions resulting from fossil fuels have hit a “historic high” of 32.5 gigatonnes (Gt) in 2017, as shown in Figure 1.1. This represents an increase of 460 million tonnes (Mt) from 2016 [2].

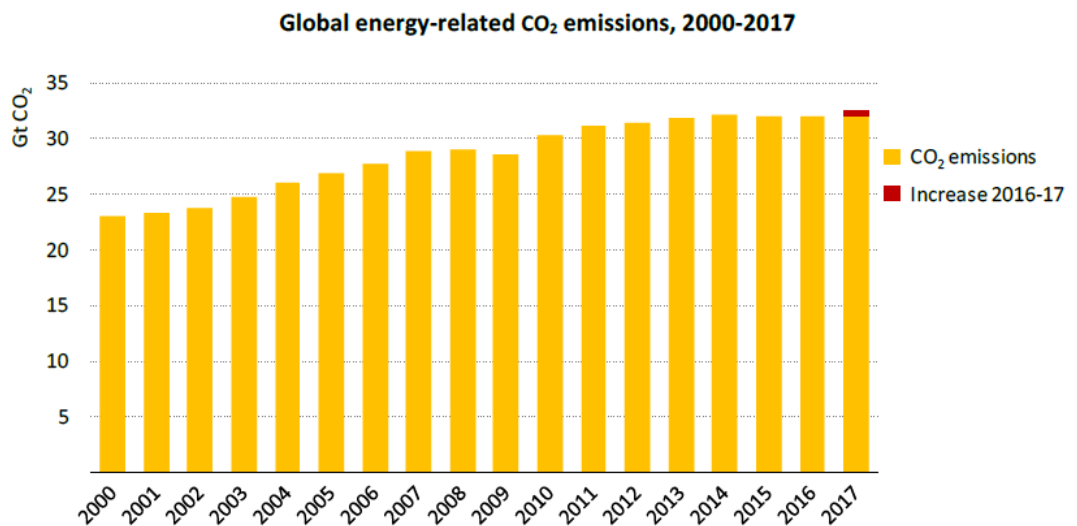


Figure 1.1. CO₂ emissions from global energy consumption (includes fossil fuel and industrial processes) for the time of 2000-2017 [2].

The increase in emissions was driven by the higher energy consumption arising from a robust growth of global economic, the lower fossil-fuel prices as well as the lack of sufficient energy efficiency efforts that led to increased energy demand for cooling and heating. However, CO₂ emissions stagnated since 2014 and even declined in 2015

and 2016, in spite of continuous expanding of global economy, which was mainly due to the low-carbon technology deployment and remarkable energy efficiency enhancements, giving rise to a decline in coal demand by 2.3% in 2015 and 2.1% in 2016 respectively. This is led by lower demand in the power sector in key markets such as China and the United States. For instance, a significant decline came from the China, where the emissions dropped by 0.6% in 2015, which was primarily the result of a slowdown in economic growth and most importantly, a continued switching from coal toward gas and renewable energy sources [2].

On the other hand, as the limited and non-renewable source of energy, fossil fuels cannot offer us adequate supply in a long term. Latest statistics show that the global oil consumption in 2017 was 4621 million tones, corresponding to 34.2% of total world energy and will reach its peak before 2020 [3]. Hence, it becomes an urgent issue to look for employment of renewable sources as substitutes to provide clean and reliable energy. Wind, solar, geothermal, biofuel and hydropower are recognised as feasible alternative sustainable approaches for power generation and energy saving without any harm to environment and ecosystem [4]. Considering the potential gravity of the climate crisis, the World Group III of the Intergovernmental Panel on Climate Change (IPCC) issued a call in 2007 to reduce the global GHG emissions by 50% to 85% in 2050, as compared with 2000. This target would restrict the growth of atmospheric CO₂ level to 445 parts per million (ppm) [5]. In addition, the European Union made a commitment in 2014 to achieve at least 27% shares being generated from renewable energy sources and a reduction of 40% in EU's GHG emissions by 2030, compared to 1990 [6].

As the cleanest and most abundant energy source on this planet, solar energy is expected to become a significant component in a sustainable energy system. At present, solar power is still the third most important renewable energy source in terms of global power generating capacity, trailing only hydropower and wind energy.

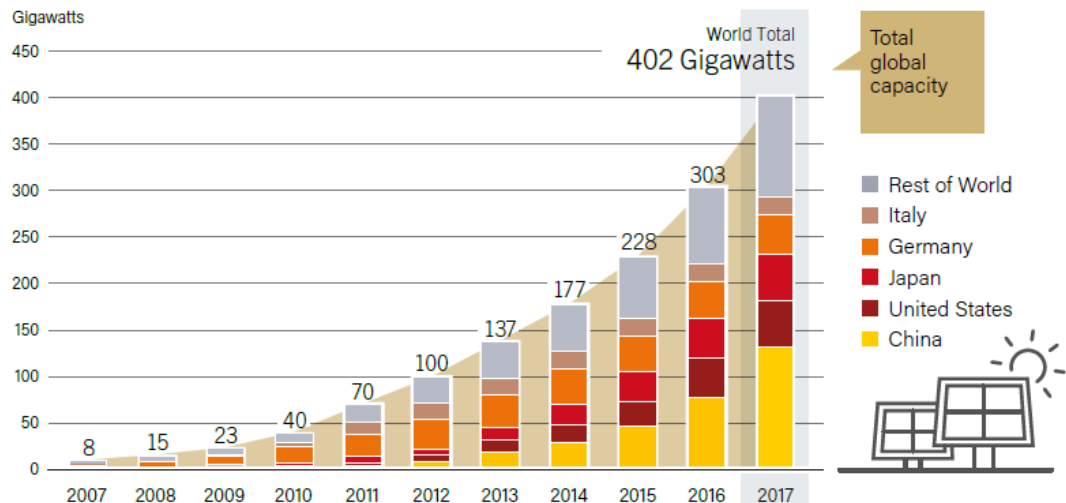


Figure 1.2. Solar Photovoltaic (PV) installed capacity by region from 2007 to 2017 [7].

The readily availability and the greatest potential of solar energy source has made rapid changes and development in the application of solar photovoltaic (PV) systems for power generation over the last decade. Figure 1.2 shows the share of global cumulative PV installations from 2007 to 2017. The market growth of solar photovoltaic worldwide installed capacity witnessed a record high of 402 GW in 2017, raising total capacity by nearly 33% over 2016, which was primarily driven by the new installations in China [7]. If this trend continues, it is predicted that the cumulative global photovoltaic installed capacity will potentially reach 3000 GW in 2050, which is roughly equivalent to 11% of total global electricity supply. By that time, the solar energy may eclipse fossil fuels and become the world's most widely used source of electricity generation [8]. Solar photovoltaic (PV) technology has been recognised as the optimal and most effective method to harness the solar energy since it allows the direct transformation of sunlight into electrical energy with small or even without any moving parts, which could help to relieve the energy shortages and environmental issues. Furthermore, photovoltaic have the advantages of providing non-overlap complementarities with other renewable energy systems: (i) flexibility in terms of implementation, i.e., solar panels can be installed on rooftops of building or used as a stand-alone system in power station; (ii) environmental friendly energy services, since they produce nearly zero emission of GHG and noise which are considered to be an ideal solution in addressing energy supply especially in urban areas; (iii) solar panels require relatively low operating and

maintenance costs in comparison with other renewable energy systems and they are currently witnessing an acceleration in falling of market price, which makes them unique in the world of energy and leads to their rapid expansion [9,10]. Solar photovoltaics has come a long way since its first application in space satellite and now it already becomes a mature, reliable, and low-cost renewable energy technology in different regions of the world. Thanks to the advancements technology and industry development, the solar PV has already achieved the grid parity in many countries, and its robust growth will continue to meet the global renewable targets [11].

1.1 Motivation

Along with the rapid development in photovoltaic market, crystalline silicon based solar cells are still the most commonly used photoelectric converting devices, which constitute about 85% to 90% global market share of worldwide production of PV modules, and are predicted to remain a dominant PV technology until 2020 [1]. However, the relatively high generation cost and limited conversion efficiency are the main barriers to the development of these systems at large scale [12]. For a single-junction silicon solar cell, the conversion efficiency is primarily constrained by the spectral mismatch losses, non-radiative recombination, and Fresnel reflection losses. Among which the former represents the highest loss in silicon solar cells, accounting for nearly 50% of incident power from the solar spectrum. This is because of the non-absorbable or sub-bandgap photons with energy below the bandgap ($h\nu < E_g$), which is also referred as transmission losses, and strong thermalisation caused by above-bandgap photons ($h\nu > E_g$) [13]. Since the electrons beyond the required amount to cross the band gap cannot be recovered, this energy is thus converted into heat and lost due to the relaxation of electron and hole to the conduction and valence band edges respectively. As a result, around 47% of energy conversion is lost as the lattice thermalisation resulting from the high energy photons within the spectrum of short wavelength [14].

To reduce these losses and minimise the recombination, the promotion of light

absorption through the solar cell is required. A number of approaches have been developed, such as, anti-reflection coating (ARC) [15], surface texturing [16], spectrum modification [17], and incorporation of nanostructured light trapping materials [18].

ARC is one of the most common methods that applying thin film of anti-reflection materials to the front surface of the solar cell in order to suppress the reflection losses at the interface between air and silicon wafer. Silicon nitride (SiN_x), silicon oxide (SiO_2) and titanium dioxide (TiO_2) are frequently used as the anti-reflection layers for commercial silicon solar cells due to their appropriate index values and excellent passivation properties that could effectively inhibit carrier recombination at the cell surface [5, 12, 221]. Surface texturing aims at introducing random or regular features on solar cell surface through chemical etching process, which could trap light and contributes to an elongation in optical path length even without the addition of any light-harvesting materials [16]. Spectrum modification through down-converting or luminescence down-shifting (LDS) process can help harvest full solar energy by expanding the operating spectral range toward the ultraviolet (UV) range. The most commonly used photoluminescent materials include rare earth element-doped lanthanide oxysulfides (e.g., $\text{Gd}_2\text{O}_2\text{S:Tb}^{3+}$, $\text{Gd}_2\text{O}_2\text{S:Eu}^{3+}$) and alkaline-earth aluminate or silicate phosphors, such as green $\text{SrAl}_2\text{O}_4:\text{Eu}^{2+}$, $\text{BaAl}_2\text{O}_4:\text{Eu}^{2+}$ and $\text{Ba}_2\text{SiO}_4:\text{Eu}^{2+}$ [17, 229, 230]. Additionally, metal silver (Ag) and gold (Au) nanoparticles exhibit large scattering cross section to improve the light absorption owing to their unique localised surface plasmon resonances while they are limited by the expensive resources [18, 89].

Recently, researchers have obtained a new record high conversion efficiency of 25.7% for crystalline solar cell by using n-type silicon wafers with passivated electron contact [19]. Improving the cells' efficiency is also for the sake of further reducing the cost of electricity, thereby, securing our energy supplies. Although silicon is not an ideal semiconductor material to achieve the optimum value for solar-to-electricity energy conversion, its abundance on earth, stability, non-toxicity, and high carrier mobility make it practically useful and commercially reliable to be used in the photovoltaic cells. In addition, crystalline silicon technology has by far the highest commercial efficiency

in comparison with all other types of solar cells [12, 20].

The gradual increase in global energy consumption and the approaching depletion of fossil fuels are the motive force of this work through the systematic investigation and study on the photovoltaic performance enhancement of silicon solar cells. This thesis focuses on improving the light absorption of commercial single-junction monocrystalline silicon solar cells within both UV and visible region of solar spectrum through the application of high surface area TiO₂-based aerogel nanomaterials and rare-earth-doped ultraviolet (UV) spectral down-converting phosphor materials. Successful fabrication and integration of those light-harvesting materials on the textured surface of solar cell have been demonstrated, in an attempt to compensate for the relatively low spectral response of silicon solar cell at the UV-blue wavelengths while improving the conversion efficiency.

1.2 The thesis objectives

In order to obtain a remarkable enhancement in conversion efficiency of mono-Si solar cells, a variety of oxide materials are employed and investigated which include nanostructured titanium dioxide (TiO₂) and magnesium oxide doped-titanium dioxide (MgO-TiO₂) UV-photocatalytic materials, silicon oxide (SiO₂) ARC, terbium-doped gadolinium oxysulfide (Gd₂O₂S:Tb³⁺) and europium-doped strontium aluminates (SrAl₂O₄:Eu²⁺) down-converting phosphors. The main aims and objectives of this work are: (1) to explore and demonstrate cost-effective safe processing methods for the energy performance enhancement of mono-Si solar cell; (2) to compare quantitatively the effects of these light harvesting materials to the cells performance enhancement; (3) to characterise and compare the optical, electrical, and external quantum efficiency analyses in terms of the enhanced conversion efficiency in modified solar cells; (4) to clarify the reasons behind the improved light absorption and scattering in photovoltaic cells when anti-reflection coatings or down-converting layers are integrated on cells' top surface.

1.3 Thesis Outline

In this section, the content of each chapter of this thesis is highlighted. There are a total of six chapters in which the relevant details are explained and discussed comprehensively. The supporting information for each related chapter was also included in the appendix. The organisation and layout of the thesis are briefly presented as follows:

Chapter 1 provides an overview of the world energy situations and discusses about its long term effects, particularly on eco-environment, economic growth, and social development. Moreover, it showed the potential of PV technology as a sustainable alternative for energy production and in addressing the environmental issues.

Chapter 2 describes the fundamental theory of the photovoltaics principle, the parameters that were used to characterise the performance of the PV cell, and the factors affecting its conversion efficiency. It also introduces the current design concepts and the most innovative techniques for improving the energy performance of crystalline silicon solar cells, as well as the identified opportunities for solar PV application.

In **Chapter 3**, the specific experimental apparatus and instruments used in this study were introduced in detail. It also describes the functions of particular equipment and the experimental methods in carrying out the laboratory tests.

Chapter 4 gives a detailed description of experimental works on developing novel anti-reflection coatings (ARCs) on top surface of mono-Si solar cell using high surface area of TiO₂-based aerogel nanomaterials and thin films of silicon oxide in which the results on enhanced solar cells are also presented.

Chapter 5 focuses on the work carried out on improving the photovoltaic performance of mono-Si solar cells through the spectral modification by employing down-converting rare-earth lanthanide oxysulfide and alkaline aluminates phosphors. The J-V characteristics, optical reflectance, and external quantum efficiency response of modified mono-Si solar cells are demonstrated.

In **Chapter 6**, a summary of the main findings from the experimental tests, the recommendations for future research directions and studies regarding the identified gaps in this work are given.

Chapter 2 Literature review of Photovoltaic fundamentals and technologies

This chapter gives a brief overview of semiconductors physics. It describes basically the working principles of solar cells. Some core concepts such as charge collection and recombination, semiconductor p-n junction, energy bandgap, I-V characteristics, as well as the mechanisms in which energy conversion losses may occur in solar cells are given with a detailed description and explanation. In addition, the development of solar photovoltaic systems and novel suitable methods for energy performance enhancement of crystalline silicon solar cell are introduced.

2.1 Solar radiation

Solar photovoltaic conversion is the process which a fraction of sunlight spectrum is absorbed and converted directly into electricity based on the photovoltaic effect. The sunlight is a radial patterning of the electromagnetic radiation, which is made up of tiny energy capsules called photons. These photons carry a packet of energy that depends upon their source spectral properties. Generally, a single photon can be characterised by its wavelength (λ) or an equivalent energy, denoted by (E_λ). The relationship between these parameters is described by the Planck's equation of the energy carried by a photon with a specific wavelength of λ [21]:

$$E_\lambda = \frac{hc}{\lambda} \quad (2.1)$$

where h represents the Planck's constant (6.626×10^{-34} J·s), c is the speed of light in vacuum (2.998×10^8 m/s).

This inverse relationship indicates that light within short wavelength of solar spectrum exhibits high photon energy whereas light consisting of lower energy photons are usually located in the longer wavelength regions. By expressing the photon energy in terms of electron volt, the above equation can be re-written as:

$$E \text{ (eV)} = (6.626 \times 10^{-34} \text{ J}\cdot\text{s}) \times (2.998 \times 10^8 \text{ m/s}) \times (1\text{eV}/1.602 \times 10^{-19} \text{ J})/\lambda$$

$$= \frac{1239.8}{\lambda(\text{nm})} \quad (2.2)$$

The sun can be discussed comprehensively in terms of its characteristics while there are two most important parameters of which will fundamentally affect the photovoltaic performance of solar cells: the solar irradiance, with the standard unit of W/m^2 , which represents the amount of incident energy per unit area on a surface, symbolised by “G”. Another factor is the spectral characteristics of the light, including the electromagnetic spectrum, light speed, and the polarization of light [22]. Figure 2.1 shows the geometric diagram of the sun-earth relationships.

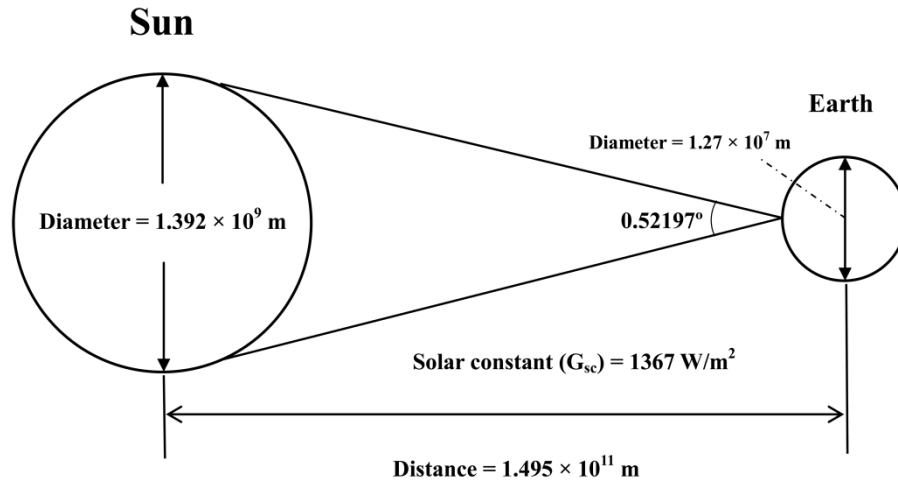


Figure 2.1. Geometric diagram showing the sun-earth relationships. Figure is adapted from [24].

Solar irradiance outside the earth’s atmosphere is referred as solar constant (G_{sc}), with a value of $1367 \text{ W}/\text{m}^2$, which represents the radiant power from the sun per unit time received on per unit area perpendicular to the sun’s rays at a mean earth-sun distance of 149.5 million kilometers [23, 24]. This irradiance would be reduced by at least 30% after being transmitted through the earth’s atmosphere since partial of solar spectrum, particularly short wavelengths were either scattered or absorbed by the upper atmospheric molecules, dust particles, aerosols, and other air molecules including water vapour, carbon dioxide, oxygen, and ozone. In addition, the earth’s albedo could reflect a partial solar radiation back into the outer space. Solar radiation coming from the sunlight without having been scattered is called direct radiation or beam radiation while

scattered solar flux that reach the surface of earth is referred as diffuse radiation. These two components make-up of the total radiation on a horizontal surface [24].

However, since the above mentioned attenuation is highly inconstant, which usually varies with the time and geographical location, the light path length through the atmosphere is therefore identified as the most important parameter to determine the total amount of sunlight that incident on the earth's surface. This length is the shortest when the sun is at the zenith and the ratio of actual light path length to this path length vertically upwards is defined as the optical air mass (AM). It is given by the equation [25]:

$$\text{Air Mass (coefficient)} = \frac{L}{L_0} \approx \frac{1}{\cos\theta_z} \quad (2.3)$$

where L represents the effective path length of solar radiation through the atmosphere, L_0 is the vertical thickness of the atmosphere (also referred to as zenith path length). θ_z is the zenith, which is the angle between the line passing through the sun and the perpendicular to the horizontal plane. Figure 2.2 shows the definitions for optical AM and the daily motion of the sun where the solar altitude angle θ_a and zenith angle are illustrated.

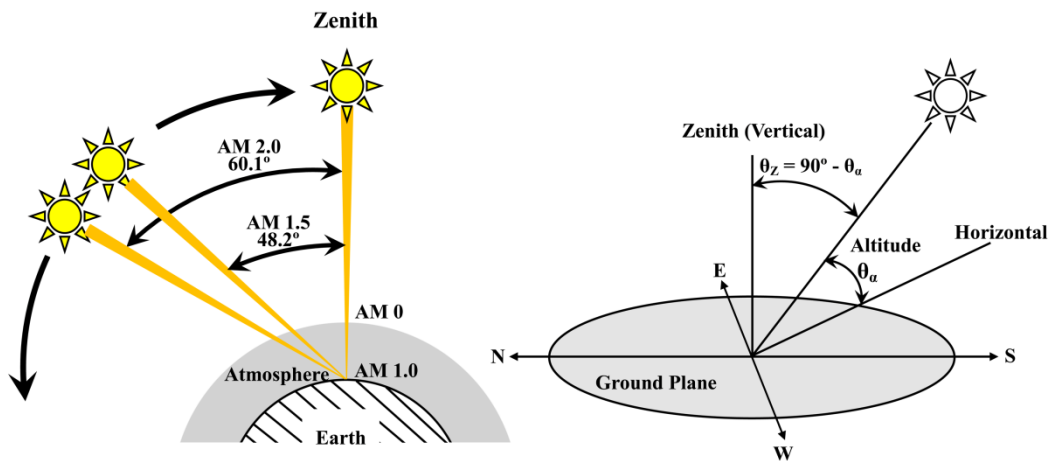


Figure 2.2. The path length in units of Air Mass which varies with the zenith angle. Figure is adapted from [26].

For a zenith angle θ_z of 0° , which means when the sun is directly overhead, the air mass coefficient is 1. AM 1 atmosphere could achieve around 70% of solar radiation after both direct and diffused fluxes. Figure 2.3 shows the spectral distribution of

sunlight in case of AM 0 and AM 1.5. For the purpose of characterising the energy performance of various types of PV devices, the standard spectrum at AM 1.5 ($\theta_z = 48.19^\circ$) was used, which is normally defined in two standards: AM1.5G and AM 1.5D. The AM 1.5 global spectrum (AM 1.5G) is usually designed for flat PV modules that face a hemisphere, with a normalised irradiance of 1000 W/m^2 (100 mW/cm^2), while for solar concentrating system with lower capability of acceptance of solar radiation, the AM 1.5 direct spectrum (AM 1.5D) is used as the standard spectrum and therefore it has a relatively lower total irradiance of 900 W/m^2 . In addition, both two standards specify that the receiving surface (solar panel illuminated surface) is regarded by default as an inclined plane at 37° tilt toward to the equator, facing the sun at an elevation angle of 41.81° above the horizon, as can be seen in the inset plot of Figure 2.3). The AM 0 spectrum is also referred to as extraterrestrial solar spectrum, which represents the solar irradiance outside the earth's atmosphere (the altitude is higher than the sea level). AM 0 radiation flux is in numerical equal to the solar constant (1367 W/m^2) while it varies with the periodic changes in earth-sun distance, and with the sunspot activities [24].

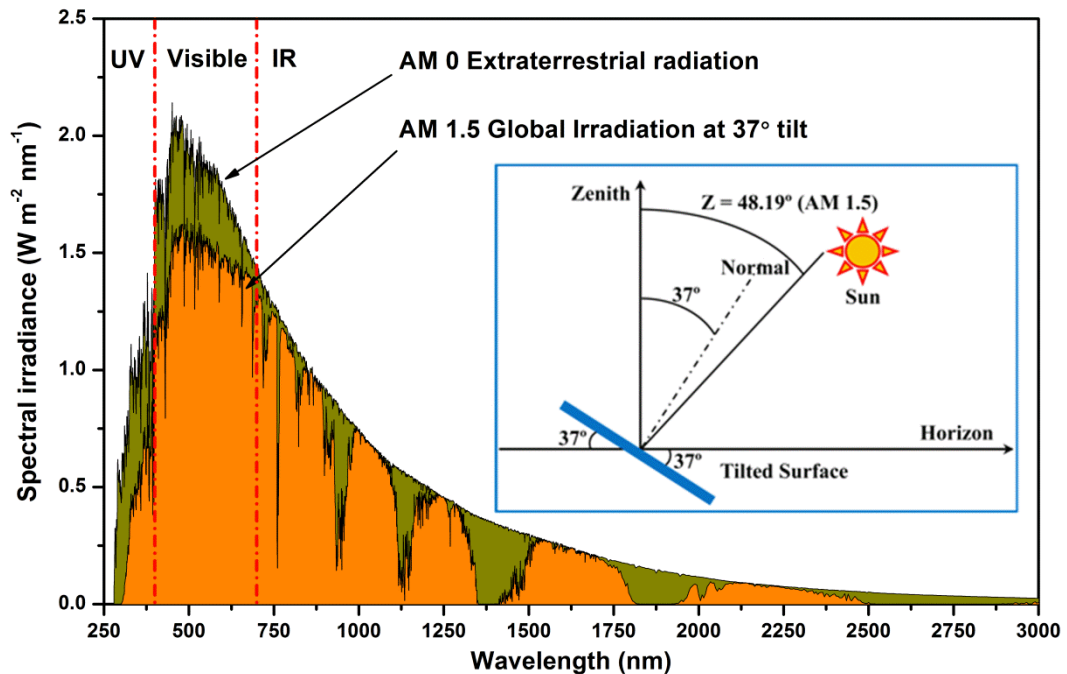


Figure 2.3. Spectral comparison between extraterrestrial (AM 0) solar spectrum (olive) and the standard AM 1.5 global spectrum (orange). Inset plot shows the geometrical position in terms of a 37 degree tilted surface under the AM 1.5 illumination [27].

Since the sunlight can be considered as a blackbody emitter at a surface temperature around 6000 K, the spectral irradiance at a certain temperature “T” and wavelength “λ” is modeled and given by the Planck’s law [28]:

$$F(\lambda, T) = \frac{2\pi hc^3}{\lambda^5 (e^{\frac{hc}{\lambda kT}} - 1)} \quad (2.4)$$

where F is the spectral irradiance in $\text{Wm}^{-2}\mu\text{m}^{-1}$, h and c are the Planck constant and the light speed respectively, which have been demonstrated previously. The standard spectrum of AM 0 is approximately to a 5800 K black body radiation and is mostly used for space solar cell applications. Figure 2.4 shows the Planck’s black body distribution over a wide range of wavelengths in solar spectrum at various temperatures between 3000 and 6000 K.

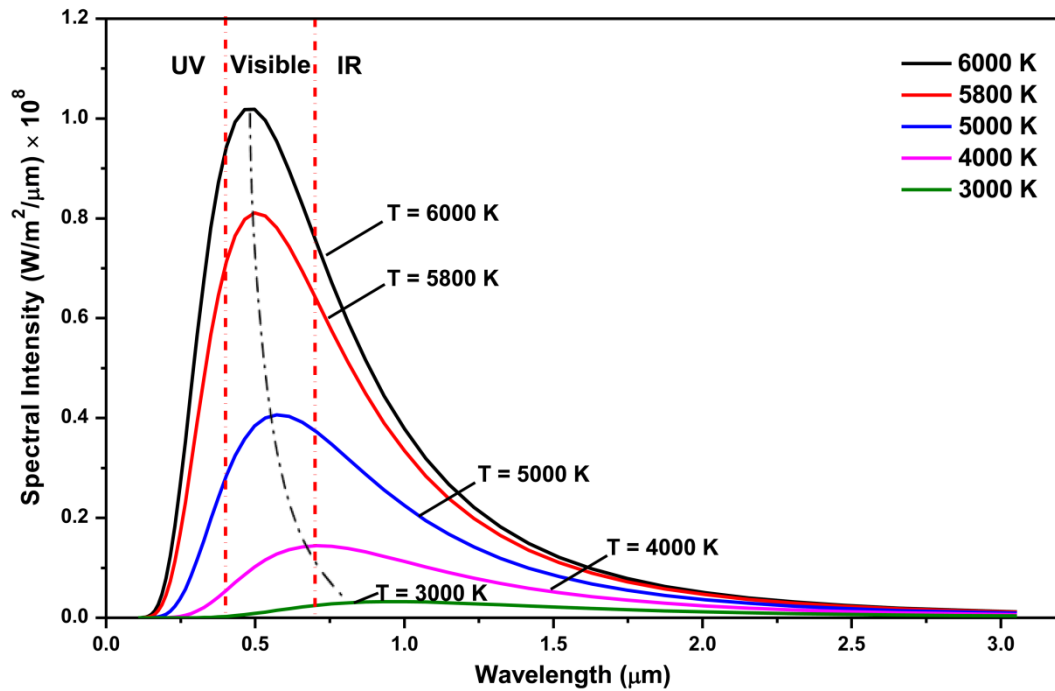


Figure 2.4. Spectral intensity distribution of black body radiation as a function of wavelength at temperature of 3000 K, 4000 K, 5000 K, 5800 K, and 6000 K respectively. Figure is reproduced with permission from PVEDucation.org [29].

As indicated by the curves that the wavelength corresponding to the peak intensity of the blackbody (λ_{max}) decreases with the increasing of temperature. This relationship is known as Wien’s displacement law [28] and is shown in the equation 2.5:

$$\lambda_{\text{peak}} T = 2.898 \times 10^{-3} \text{ m} \cdot \text{K} \quad (2.5)$$

where λ_{peak} is the wavelength in “meter” at which the peak spectral irradiance is emitted and T is the Kelvin temperature of the blackbody (K). Wien’s law is used for the estimation of the temperatures of radiant objects which are much higher than that of their surroundings. The spectral energy distribution of sunlight is important for the investigation and performance analysis on solar cells since they respond differently to the variation of photon energy (or wavelength) [25].

Solar radiation data is essential when calculating the electricity generation from photovoltaic systems. With the knowledge of the climate condition and the corresponding geographical information, the estimation of the incident radiation on both horizontal and tilted planes can be obtained by means of solar irradiation models based on the empirical relationships [30]. Examples are shown in Figure 2.5 where the average hourly radiation per day of sunshine for each month within a year for the location of Gatwick, London is illustrated (Weather data are provided from the US department of Energy’s Building Technologies Office through the EnergyPlus website [32]).

	Jan	Feb	Mar	Apr	May	Jun	Jul	Aug	Sep	Oct	Nov	Dec	hour	Avg year	
0:01- 1:00	0	0	0	0	0	0	0	0	0	0	0	0	0	1	0
1:01- 2:00	0	0	0	0	0	0	0	0	0	0	0	0	0	2	0
2:01- 3:00	0	0	0	0	0	0	0	0	0	0	0	0	0	3	0
3:01- 4:00	0	0	0	0	0	0	0	0	0	0	0	0	0	4	0
4:01- 5:00	0	0	0	0	8	13	9	1	0	0	0	0	0	5	3
5:01- 6:00	0	0	0	13	60	64	56	20	2	0	0	0	0	6	18
6:01- 7:00	0	0	9	72	155	153	148	99	38	7	0	0	0	7	57
7:01- 8:00	0	6	60	167	276	253	249	198	128	57	9	0	0	8	117
8:01- 9:00	17	53	135	279	381	352	366	317	221	137	57	13	0	9	194
9:01-10:00	65	121	225	349	460	462	440	405	312	212	119	54	0	10	269
10:01-11:00	108	164	263	411	516	539	523	479	383	272	167	89	0	11	326
11:01-12:00	140	195	289	453	564	594	580	518	412	290	173	116	0	12	360
12:01-13:00	142	204	331	464	565	560	596	518	400	269	180	124	0	13	363
13:01-14:00	128	187	296	467	537	510	567	549	365	218	148	94	0	14	339
14:01-15:00	78	151	229	381	480	471	503	469	318	165	87	48	0	15	282
15:01-16:00	31	87	167	296	379	378	400	373	234	93	28	11	0	16	206
16:01-17:00	2	25	89	189	286	282	290	251	125	26	1	0	0	17	131
17:01-18:00	0	1	22	84	176	180	192	120	34	1	0	0	0	18	68
18:01-19:00	0	0	1	14	62	80	84	31	2	0	0	0	0	19	23
19:01-20:00	0	0	0	0	7	17	15	2	0	0	0	0	0	20	3
20:01-21:00	0	0	0	0	0	0	0	0	0	0	0	0	0	21	0
21:01-22:00	0	0	0	0	0	0	0	0	0	0	0	0	0	22	0
22:01-23:00	0	0	0	0	0	0	0	0	0	0	0	0	0	23	0
23:01-24:00	0	0	0	0	0	0	0	0	0	0	0	0	0	24	0

Figure 2.5. Average hourly radiation per day for each month of the year in Wh/m², for Gatwick, London [31].

2.2 Solar cells technology review

Photovoltaics or solar cells are known as the devices which can convert solar energy directly into electricity. Ever since Edmond Becquerel observed for the first time of the photovoltaic effect in 1839 [33], the continuous innovation in solar PV technologies has been the goal in the scientific research domain for the sustainable energy development and for the progress of human society. Researchers have termed the advance of photovoltaic systems into three technological generations which is schematically shown in Figure 2.6.

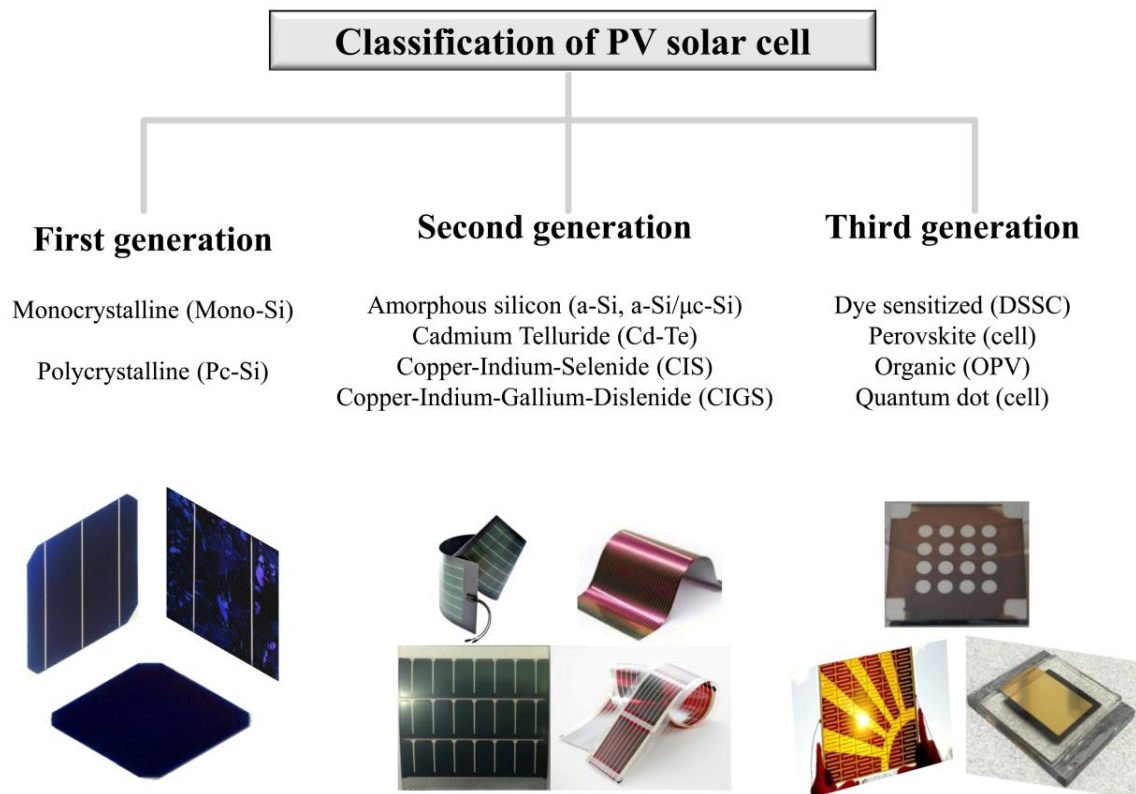


Figure 2.6. Classification of PV solar cell. Figure is reproduced with permission from [34].

“First generation” technology is referred to as the traditional or wafer-based solar cells which are made by semiconductors such as monocrystalline and poly-grain silicon. This technology benefited from its abundant and non-toxic raw materials, as well as the moderate conversion efficiency. Despite of being dominating almost 90% of the market share, it was challenged by the low performance-cost ratio or the trade-off relationships

between the material's purity and thickness since Si-based solar cell could not satisfy the requirements of thin in thickness and high in purity at a low-cost base [37,38].

From thence, the photovoltaic industry switched to the “second generation” based on thin film technology at which solar cells are made from thin layers (1~4 micrometers in thickness) comprising other semiconductor materials, include amorphous silicon (a-Si), Cadmium Telluride (CdTe), Copper-Indium-Selenide (CIS), and Copper-Indium-Gallium-Diselenide (CIGS). Compared to silicon wafer-based cells, thin film PV technology requires smaller quantity of semiconductors and thus light in weight, which provides access to obtain ultra-thinner thickness with lower production cost and can be more easily integrated into large-scale photovoltaic power station or small stand-alone power system. However, the application of second generation solar cells in PV market are greatly constrained by the influence of low efficiency (up to 12% for a-Si cell and less efficient per single unit area), insufficient stability, high-toxicity (cadmium), and scarcity of raw materials (indium) [35].

Due to these drawbacks and limitations, a new technology has been introduced. “Third-generation” technology aspires at achieving the lowest fabrication cost and further higher conversion efficiency by minimising the spectrum losses. In this case, a number of novel approaches such as multi-junction solar cells, intermediate band cells, hot carrier cells, multiple carrier excitation, and optical up/down conversion of the photons etc that are mostly on the basis of thin film cells, have been devised, in the pursuit of making the utmost use of the solar spectrum. Nevertheless, most of these concepts with theoretical high conversion efficiency in this generation are still in the research stage [36].

. Table 2.1 summarises the most recent recorded electrical characteristics of single-junction solar cells and commercial PV modules where their prospective growth in recorded efficiency from 1977 to 2018 is presented in Figure 2.7 [39].

Table 2.1. Confirmed conversion efficiency of solar cells and commercial PV modules measured under the global AM1.5 spectrum (1000 W/m²) at 25 °C [20].

Generation	Classification	Efficiency (%)	
		Cell	Module
1 st	Monocrystalline Silicon	26.7	24.4
	Polycrystalline Silicon	22.3	19.9
2 nd	CIGS (cell)	21.7	19.2
	CdTe (cell)	21.0	18.6
	Amorphous Silicon	11.9	12.3
	Dye (cell)	11.9	N/A
	Perovskite (cell)	20.9	N/A
3 rd	Organic (cell)	11.2	8.7
	III Multi-junctions:		
	InGaP/GaAs/InGaAs	37.9	31.2

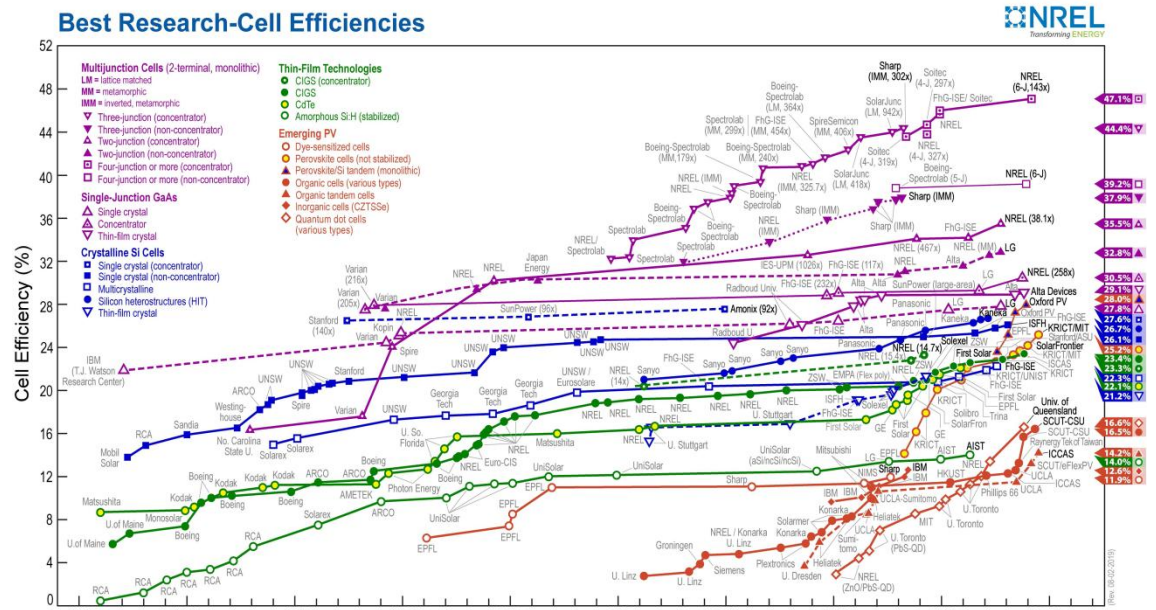


Figure 2.7. Solar cell efficiency revolution from 1975 to 2023 [39].

It has been 64 years since the Bell laboratories created the first crystalline silicon (c-Si) photovoltaic cell. The c-Si cell has witnessed a significant increase in conversion efficiency from its earliest ~6% [40], to now, almost reaching a 27% for laboratory scale, and even 24% efficiency is commercially available at module level [41]. Impressive progress made in photovoltaic (PV) technology contributes directly to the cost reduction of power generation. Due to the continued capacity expansions, the c-Si PV modules cost from 2011 to 2018 dropped drastically from \$1.6 to \$0.34 per peak

watt, with a reduction rate around 79% [42]. Since the costs in regard to the cell processing consumes less than 20% of the total module cost, improving the conversion efficiency of solar cell is actually to further reduce the levelised cost of electricity [43].

2.3 Operational principles of photovoltaic solar cells

2.3.1 Photovoltaic effect

Photovoltaic solar cells are the semiconductor devices that can convert sunlight directly into electricity while the actual creation of the electrical current occurs at an atomic level. Solar cells employ semiconducting materials such as silicon, to form a p-n junction. These semiconductors are usually doped with admixtures of other elements at a controlled amount as a way to improve their conductivity properties. The basic operating principles of solar cells depend on the photovoltaic effect, which requires the creation of both current and voltage to generate electric power. In this process, incident light, in the form of photons, strikes the active area of a solar cell where the absorption of light energises electrons that then move from the valence band to the conduction band (as shown in Figure 2.8) and each of an electron leaves behind an empty space, called hole in the valence band, which is similar to an electron with positive charge. At the force of internal electric field (E-field), the electrons and holes flow to the N-type and P-type semiconductor respectively, which is known as the separation of photo-generated charge carriers (electron-hole pairs). It is in this mobility process where the electrons and holes enable the current to flow through external circuit under existence of potential gradient in the solar cell [44].

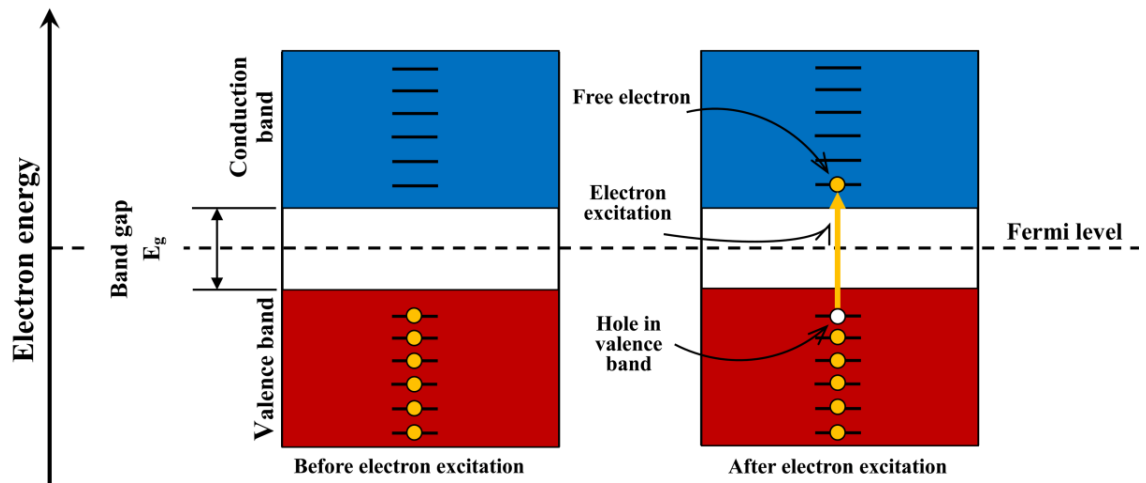


Figure 2.8. Energy band gap diagrams for a typical semiconductor showing the excitation from a donor state where an electron is generated in the conduction band. Figure is adapted from [45].

The band structure in semiconductors before excitation is typically an entirely filled valence band with electrons and empty conduction band, separated from the valence by a narrow energy band gap. In general, the electrons can be excited thermally by lattice vibrations or by absorbing the adequate energy provided by a photon of light. The energy required is equal to the difference between the two states, namely band gap energy ($E_g = E_c - E_v$). When the light is absorbed by semiconductor, photons of solar radiation possessing energy higher than the band gap energy (i.e. $h\nu > E_g$) dislodge some of the electrons. As soon as the electron is transferred to the conduction band, and then it is free to move and to act as an electricity carrier.

The absorption behavior for semiconductor is characterised by the absorption edge, for silicon, its band edge lies within infrared light at wavelength of 1100 nm, at which, the photon energy is 1.12 eV. Therefore, if the energy of a photon of light is equal to or greater than this, the electron in the outer shell will become excited and therefore able to freely move around within the material. Conversely, photon with energy below this value will not dislodge electrons while the energy will dissipate through the cell causing unwanted heat. Also, any extra energy from a photon that is left over after exciting an electron will create heat in the cell [44].

2.3.2 Carrier transport in p-n junction solar cell

In order to further understand the operating principle of photovoltaic solar cells, a fundamental knowledge regarding the collection mechanism of photo-generated carriers in p-n junction is pivotal. Solar cells are fabricated from semiconductor materials such as Silicon (Si), Cadmium Sulphide (CdS) and Gallium Arsenide (GaAs) while some of semiconductors possess excessively low conductivity, thus are not utilised to facilitate photons absorption. With the aim of altering the conductivity of the host material in PV cell, a process called doping is a vital and essential step, at which, semiconductors are doped with a certain amount of impurity atoms having either one more or less valence electron. For instance, replacing a silicon atom by a “donor” impurity (i.e. phosphorous) will add five valence electrons in the crystal while only four of them contribute to the bonding interactions in valence band and the extra electron is therefore loosely bound, being ionised and ready for the transition from valence band to the conduction band once the absorbed energy is sufficient. As a consequence, this excess electron becomes negatively charged and increases the negative conductivity of the semiconductor, which is known as the n-type semiconductor. The elements from the fifth group such as phosphorous, arsenic, antimony of the periodic table are commonly used as the donor dopants. On the contrary, when silicon semiconductor is doped by an “acceptor” impurity (i.e. Boron), a hole is created in the bond due to the missing of electron, thereby, resulting in an increase in the positive conductivity, and is referred to as a p-type semiconductor. Such “acceptor” or trivalent dopants include boron, aluminum, gallium, and indium, which are from the third group of the periodic table [45].

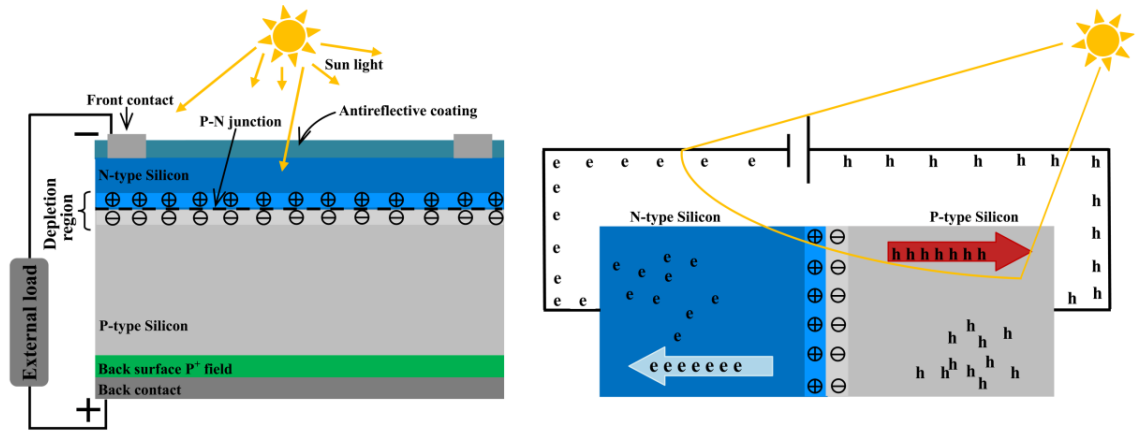


Figure 2.9. P-N junction semiconductor diode for a silicon solar cell (Left) and the forward-biased schematic diagram (right) showing its working principle. Figure is adapted from [45], [46].

Figure 2.9 shows the schematic diagram of p-n junction diode under forward bias for a typical silicon solar cell. The basic electronic component of the vast majority of semiconductor devices is a semiconductor body which two different doping areas adjoin each other, in which a p-n junction is formed at the interface (see dashed line in Figure 2.9). At the p-n junction, some freely moving of electrons (n-region) and holes (p-region) wander across the junction to the p-region and n-region respectively meanwhile leaving behind static positive and negative charges. This action potentially builds up a “barrier”, which repels further diffusion of charge carriers until a forward bias was applied on the junction. The region near the p-n junction is thus called depletion region or space charge region where there is inexistence of mobile charge carriers. When semiconductor is exposed to the sunlight, it will dislodge electrons, generating charge carriers (electron-hole pairs). As can be seen in Figure 2.9 (right), the electric field (E-field) inside the depletion zone makes the electron move to the n-type area and the hole to the p-type area while the current starts flowing into the external load that connected to the semiconductor. The resulting separation of charge carriers is how the voltage is developed. The current-voltage (I-V) characteristic of an ideal and darkened p-n junction solar cell is described by the Shockley ideal diode equation [47]:

$$I = I_0 \left\{ \exp\left(\frac{qV}{nkT}\right) - 1 \right\} \quad (2.6)$$

where I is the current through diode at applied voltage V ; I_0 represents the diode reverse (dark) saturation current, which is determined by the quality of p-n junction, the purity

of semiconductor material, as well as the doping density; q is called the absolute value of electron charge or the elementary positive charge in Coulombs (1.602×10^{-19} C); k is the Boltzmann's constant (1.381×10^{-23} J/K), and T is the absolute temperature of the p-n junction in Kelvin. When solar cell is illuminated, the electric circuit can be regarded as a current source driven by the sunlight which is connected in parallel with a real diode, as shown below in Figure 2.10. Under a fixed temperature and solar irradiance, the net current produced by the PV cell is given as follow [47]:

$$I = I_L - I_D = I_L - I_0 \left\{ \exp\left(\frac{qV}{nkT}\right) - 1 \right\} \quad (2.7)$$

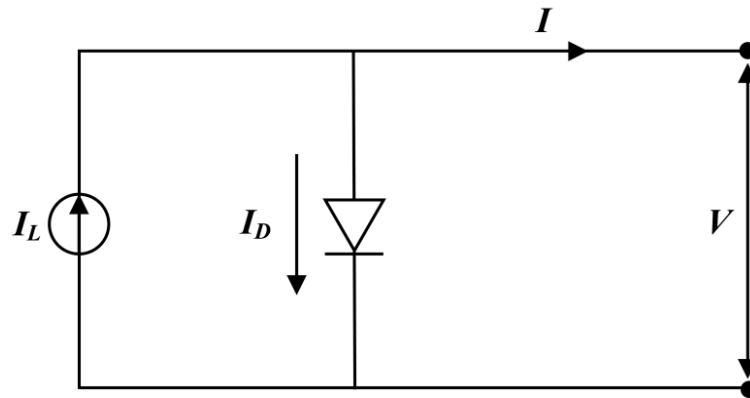


Figure 2.10. Equivalent circuit of single-diode model of an ideal solar cell.

One notable parameter here is the ideality factor “ n ” of a diode which describes how closely the diode follows the ideal diode model. Since above equation assumes that all the recombination occurs through either band to band or via traps in the bulk areas rather than in the junction of the device. In such case, the default value of “ n ” is 1. However, in reality, recombination can occur in other ways or in different areas of the semiconductor device, which may result in deviation of ideality factors from the “ideal”. Ideality factor thereby offers an alternative way of describing these particular conditions. For single-junction solar cells, uncertainties and variations of “ n ” in terms of a variety of recombination types are described in detail, as shown in below Table 2.2.

Table 2.2. Variation of ideality factors in terms of the recombination type [47].

<i>Recombination Type</i>	<i>Ideality factor</i>	<i>Description</i>
Shokley-Read-Hall, band to band (through defects or traps)	1	Recombination dominated by minority carrier
Auger	2/3	Two majority and one minority carriers required for recombination
Shokley-Read-Hall, Depletion region (p-n junction)	2	Recombination limited by both majority and minority carrier types

2.3.3 Recombination of charge carriers

Since light absorption is a thermodynamic process, the generated charge carriers can recombine again causing themselves to disappear if the thermal equilibrium is disrupted, which is known as the recombination. In semiconductors, radiative recombination and non-radiative recombination through defect states are the two most important recombination mechanisms. Radiative recombination can be described as the transition of excited electrons from the conduction band to recombine and annihilate with equal numbers of holes in the valence band meanwhile releasing photons with energy equal to the corresponding band gap. The effect of radiative recombination for indirect semiconductor (i.e. Silicon) is insignificant. Figure 2.11 shows the energy levels of partial of chemical elements in the energy gap of silicon.

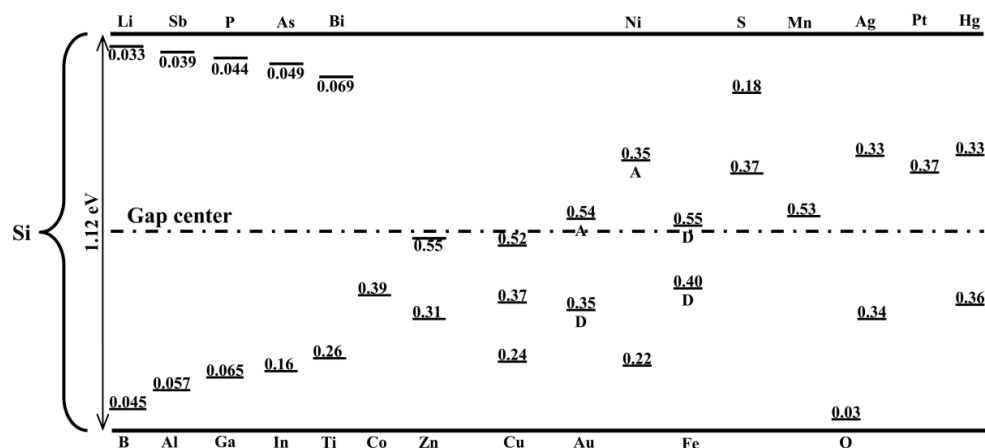


Figure 2.11. Energy level diagram of partial chemical elements in the gap of silicon, letter "A" and "D" represent the "acceptor" and "donor" impurity respectively [44].

Due to the presence of impurities and lattice defects in silicon, the excited electrons may not directly move back to the valence band but through the defects, which depends on their energy levels. Defect lies deeply in the forbidden band are referred to as deep defects which act as traps, determining the recombination of charge carriers. It can be seen from Figure 2.11 that some chemical elements make energy level located near the centre of forbidden gap, which are called recombination centres since they tend to impel freely mobile electrons to recombine with holes across the gap. This process is generally non-radiative and the recombination frequency increases with the decreasing of distance between where a defect level situated and the gap centre [44].

Hence, the solar cells with excellent performance should have longer diffusion length than their thickness to obtain a longer carrier lifetime. Furthermore, considering the trade-off between the carrier separation and surface recombination as well as adequate use of the solar spectrum, the wafer thickness for most of the conventional bulk crystalline silicon cells (mono- and poly-), is between 200 to 300 μm . The electrical contact is made by either metallic busbars or grid patterns to maximise the collection of photo-generated charge carriers. In addition, anti-reflection coatings such as silicon nitride (SiN_x), silicon oxide (SiO_2), and titanium dioxide (TiO_2) are commonly used and deposited on the front surface of solar cell, as an approach to inhibit the recombination of charge carriers at the cell's surface [12, 48].

2.4 I-V characteristics of photovoltaic cells

P-N junction solar cells are the smallest units of PV system for effective electricity generation and their electrical characteristics are the most important criteria for performance evaluation as well as in design of the photovoltaic system. In previous section, the operating mechanisms of solar cells are briefly introduced while the two most important parameters used to characterise the PV cells photovoltaic conversion performance for a given irradiance, operating temperature, and spectrum are the short-circuit current (I_{sc}) and the open-circuit voltage (V_{oc}).

The short-circuit current is the current through the solar cell at zero voltage, which

represents the maximum current delivered by the solar cell at any irradiance level and is ideally equal to the light-generated current (I_L). On the other side, the open-circuit voltage, V_{oc} , is the maximum voltage at zero current when the load resistance is infinitely large. The open circuit voltage can be determined from the equation [49]:

$$V_{oc} = \frac{nkT}{q} \ln \left[\frac{I_{sc}}{I_0} + 1 \right] \quad (2.8)$$

Below in Figure 2.12, it shows the typical current-voltage (I-V) and the power-voltage (P-V) curve of a silicon solar cell where the I_{sc} and V_{oc} are indicated respectively.

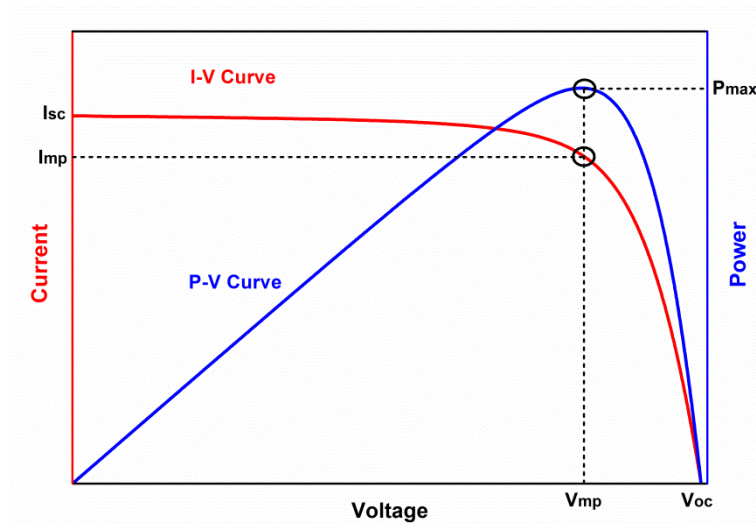


Figure 2.12. Typical I-V & P-V curves of a single-junction solar cell.

The performance of the solar cell can be evaluated by considering various parameters such as the maximum power (P_{max}), the energy conversion efficiency (η), and the fill factor (FF). It can be seen that the maximum power point (MPP) is located at the peak point of P-V curve or alternatively the “knee” of I-V curve, which gives its maximum power value. It is the product of the maximum cell current (I_{max}) and voltage (V_{max}).

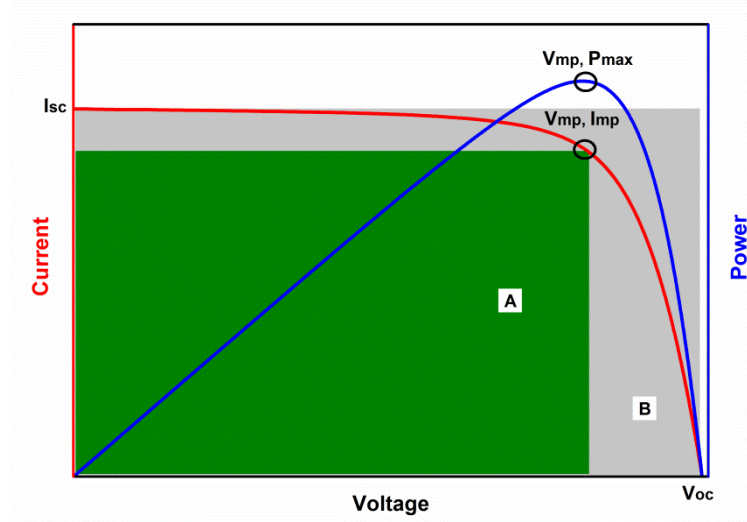


Figure 2.13. I-V & P-V curves showing the definition of fill factor.

The fill factor (FF) can be described as the ratio of the maximum power from the solar cell to the product of V_{oc} and I_{sc} , which is defined by [49]:

$$FF = \frac{P_{max}}{I_{sc} \times V_{OC}} = \frac{I_{max} \times V_{oc}}{I_{sc} \times V_{oc}} \quad (2.9)$$

Graphically, FF represents the squareness ratio of A/B as shown in Figure 2.13. Fill factor is a measure of quality of the solar PV device and any impairment that reduces the fill factor will result in a decrease in power output. For wafer-based crystalline silicon solar cells, the fill factor should reach a typical value range of 0.7-0.8 [44].

The conversion efficiency (η) is defined as the ratio of the maximum power output to the power input to the cell at a given irradiance and temperature, which is expressed by [49]:

$$\eta = \frac{P_{max}}{A \times G} = \frac{FF \times I_{sc} \times V_{oc}}{A \times G} \quad (2.10)$$

where G is the total irradiance (W/m^2), A is the effectively illuminated area (m^2). The conversion efficiency of a solar cell depends on various factors such as the irradiance level, temperature condition, and the spectrum of incident light. Figure 2.14 shows the effects of the solar irradiance and temperature on the electrical characteristics of solar cell.

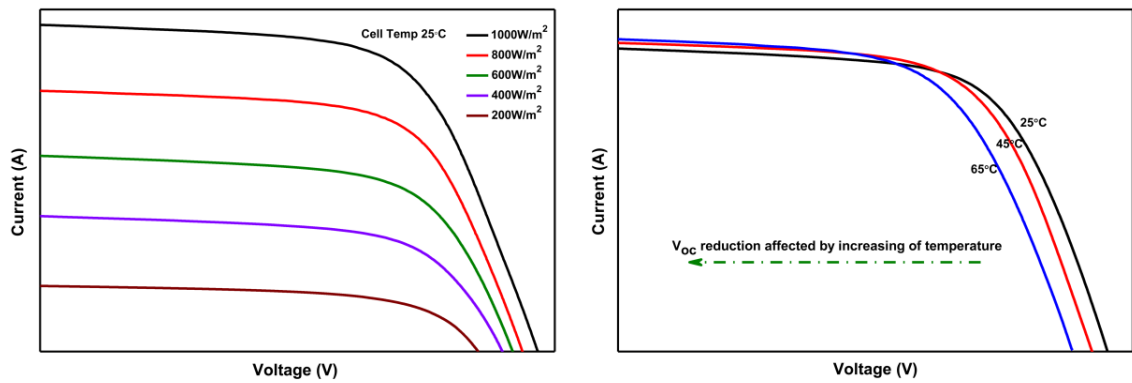


Figure 2.14. Irradiance and temperature effects on the I-V characteristics of PV cells.

As shown in Figure 2.14, with the increase of irradiance, both the V_{oc} and I_{sc} increase at different levels. The variation in irradiance affect significantly in I_{sc} whereas little in V_{oc} . On the other hand, the increase in temperature leads to a decrease in band gap, thus giving a higher intrinsic carrier concentration which in turn, exponentially increase the reverse saturation current (I_0). As a result, this variation gives rise to slight increase in the I_{sc} while major reductions in the V_{oc} [50].

In addition, for the photovoltaic module, the conversion efficiency also depends on the encapsulation materials and the incident angle of sunlight where it strikes on the module's surface. Since the irradiance varies greatly with the time, as well as the weather and geographical conditions, the efficiency along with other electrical parameters of solar cell are therefore characterised under standard test conditions (STC). The standard test condition specifies an irradiance of 1000 W/m^2 and a cell temperature of $25 \text{ }^\circ\text{C}$ with an AM 1.5G spectrum, which could ensure a relatively independent evaluation and comparison of electrical performance of various types solar devices [51].

In previous section, the equivalent circuit of solar cells has been demonstrated, however, in the practical operation, the I-V characteristics of solar cells are different from the ideal model (see Figure 2.10) Figure 2.15 below shows the single diode circuit of a practical solar cell.

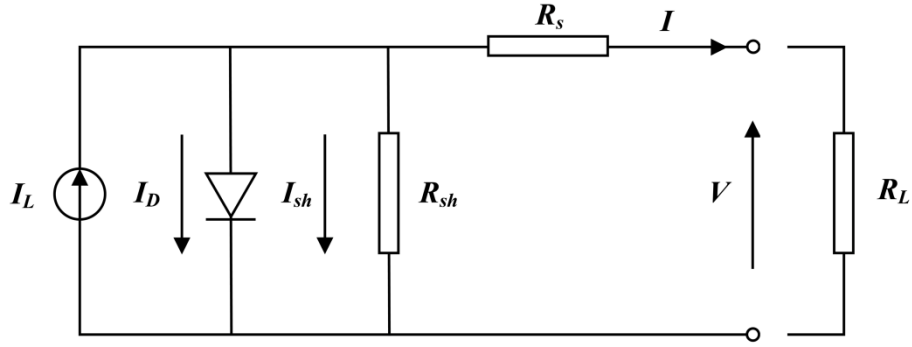


Figure 2.15. Equivalent circuit of single-diode model of a practical solar cell.

In the practical circuit model, series resistance, R_s , and shunt resistance, R_{sh} , are introduced. As a result, the diode equation of solar cell is then modified into the following form:

$$I = I_L - I_D - I_{sh} = I_L - I_0 \left\{ \exp \frac{q(V + IR_s)}{nkT} - 1 \right\} - \frac{(V + IR_s)}{R_{sh}} \quad (2.11)$$

Series resistance is the sum of the total internal resistances that appear in series with the capacitance of the solar cell, which represent the majority of resistive losses at the metal contacts while minor at the emitter and the base of solar cell. Unlike series resistance, the presence of shunt resistance is mostly like arisen from the inherent defects during the manufacturing process, which represents the leakage of current across the solar cell p-n junction. The effects of variations in parasitic resistances on the solar cell I-V curve are shown below in Figure 2.16.

As can be seen from the curves, series and parasitic shunt resistances play different roles in affecting the fill factor and thus the conversion efficiency. Series resistance scarcely affects the open circuit voltage (V_{oc}) since there is no light-generated current “ I_L ” flow through it while the voltage drop near the V_{oc} region becomes increasingly obvious with increase of series resistance, shifting the I-V curve toward the current and becoming a linear line at the late stage {see Figure 2.16(a)}. At this point, the short-circuit current is also reduced, in this case, the R_s becomes a concern mainly at high irradiance levels, determining the performance of solar cells [52].

On the contrary, the influence brought by a shunt resistance is significant particular

at lower irradiance level. Due to the shadow effect, it creates a parallel high conductivity path in the solar cell, leading partial amounts of current away from the load circuit which in turn leads to a decrease of the load current and thus power losses, which can be expressed by the following equation:

$$P'_{MP} = P_{MP} \left(1 - \frac{V_{OC}}{I_{SC}} \frac{1}{R_{SH}} \right) \quad (2.12)$$

It can be seen from Figure 2.16(b), with the decrease of shunt resistance, the voltage starts to dominate the I-V curve, dragging it down toward the x-axis, leading to a drastic reduction in the open circuit voltage. In addition, reducing the shunt cell resistance may generate excess heat and hotspots in the solar photovoltaic module, resulting in performance degradation of the encapsulating materials. Therefore, for the purpose of solar array design, the shunt resistance is suggested to be as high as possible with little leakage currents flowing throughout the device [53].

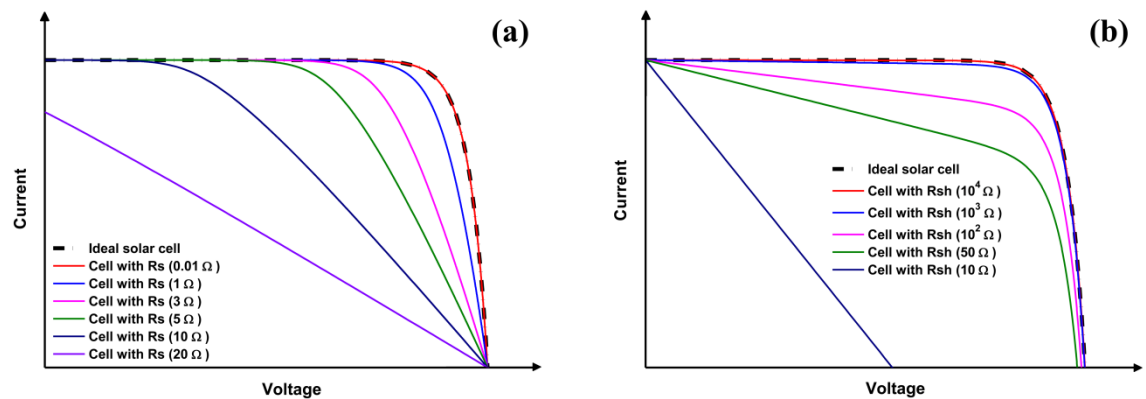


Figure 2.16. Effects of variations in (a) series resistance (R_s) and (b) shunt resistance (R_{sh}) on the I-V characteristic of a solar cell.

2.5 Quantum efficiency and spectral response

Quantum efficiency (QE) is an important parameter that is implemented to describe the semiconductors' photoelectric conversion capability, which is closely related to the photo-generated current, and thus the conversion efficiency. In a broad sense, the quantum efficiency of a solar cell represents the percentage of incident photons that convert and then produce the charge carriers in a certain wavelength range of light. To a large extent, it is also a measure of the spectral response (SR) of a photovoltaic cell

which estimates the spectral distribution of short-circuit current. Therefore, the quantum efficiency for photons with energy below the band gap is zero.

The quantum efficiency can be classified as two different types, namely external quantum efficiency (EQE) and internal quantum efficiency (IQE). The former is defined as the ratio of the number of charge carriers contributing to the short-circuit current to the number of incident photons with photon energy of E_{ph} . The EQE can be expressed in terms of the spectral response, which is formulated [54]:

$$EQE(\lambda) = \frac{hc}{q\lambda} \times SR \quad (2.13)$$

Mathematically, dividing the short-circuit current density (J_{sc}) by the incident irradiance (I_{in}) gives the SR as:

$$SR(\lambda) = \frac{J_{sc}(\lambda)}{I_{in}(\lambda)} \quad (2.14)$$

Therefore, the EQE can be derived as:

$$EQE(\lambda) = \frac{E_{ph}(\lambda) \times I_{sc}(\lambda)}{q \times I_{in}(\lambda)} = \frac{J_{sc}(\lambda)}{q \phi(\lambda)} \quad (2.15)$$

where $\phi(\lambda)$ represents the photon flux (photons/m³). EQE is directly obtained from the spectral response measurement and it provides the information of how a solar cell can potentially respond and convert the incident photons to electrons.

In addition, it also reflects the optical loss mechanisms for certain types of solar cells. Figure 2.17 shows the EQE response for a typical crystalline silicon solar cell.

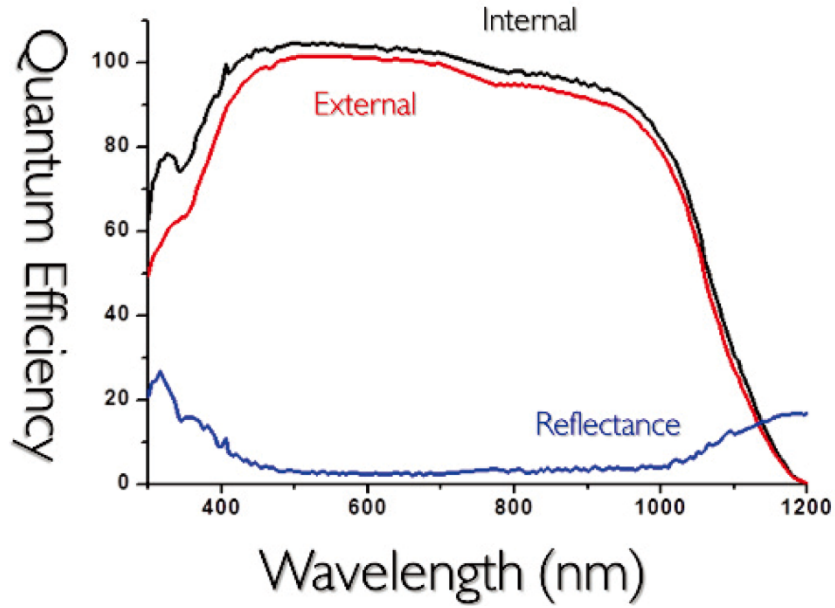


Figure 2.17. External, Internal quantum efficiency and reflectance responses curves for industrial SiN_x-passivated Si-wafer based crystalline solar cell [55].

Due to the surface reflection loss and recombination, only a small portion of light is converted into electron-hole pairs at short wavelength of solar spectrum while at the long wavelength ($\lambda \geq 1100$ nm), most photons directly transmit through the solar cell before being absorbed. This is due to the insufficient diffusion length of absorbing layer when compared to the penetration depth, making itself becomes transparent [55]. It can be seen that in a broad wavelength band, the EQE is close to 0.9, indicating that most of the incident photons are converted into electron-hole pairs.

Unlike the EQE, IQE represents the fraction of photons absorbed by the photoreactive surface of solar cell that create electrons in the device. The IQE can be expressed by [56]:

$$IQE = \frac{1}{1-R(\lambda)} \times \frac{J_{sc}(\lambda)}{q \phi(\lambda)} = \frac{EQE(\lambda)}{1-R(\lambda)} \quad (2.16)$$

where R is the reflectance in the active layer. It neglects the effects brought by the parasitic absorption and the rear surface transmittance, and thus IQE is usually higher than EQE while below unity (100%).

2.6 Energy losses in p-n junction silicon solar cells

Photoelectric conversion process in p-n junction solar cells includes the generation of electron-hole pairs through absorption of incident photons and the separation of charge carriers in terms of their intrinsic properties. However, this instantaneous process is always accompanied by various types of energy losses which affect significantly their electrical performance. Hence, to address it with appropriate approaches, the knowledge of the mechanisms in which energy losses may occur in solar photovoltaic cell is pivotal.

2.6.1 Intrinsic losses of ideal solar cells

Spectral mismatch losses

Silicon (Si) has been widely employed as the semiconductor materials to produce solar photovoltaic devices. However, the typical single p-n junction solar cells are only able to convert photons within a limited portion of solar spectrum, with ultraviolet (UV) and most infrared (IR) region of light untapped. Since silicon has a band gap of ~ 1.12 eV, corresponding to an absorption cut-off wavelength of around 1100 nm, any light with wavelength longer than it or below the band gap ($E_{ph} < E_g$) is insufficient to excite electrons and thus transmit directly through the silicon, which is referred to as the sub-band gap or the transmission loss.

On the other hand, photons with energy greater than the band gap of silicon ($E_{ph} > E_g$) can be absorbed while the excess energy beyond the required amount to cross the band gap is converted into heat and be lost due to the relaxation of hot carriers into the band edge, which is known as the lattice thermalisation. Figure 2.18 shows the fundamental losses in a single-junction silicon solar cell under realistic AM1.5G solar spectrum. Above two energy losses can be attributed to the intrinsic characteristics of silicon that result in the spectral mismatch between incident light and absorption functionality of the semiconductor materials. These losses account for above 50% loss in single junction crystalline silicon solar cells [57].

Another loss is arisen from the relative energy reduction of open-circuit voltage (qV_{oc}) compared to the band gap (see inset plot in Figure 2.18) and it would become more apparent for real solar cells situation due to the increasing recombination current, which will be discussed in detail in the latter section [58].

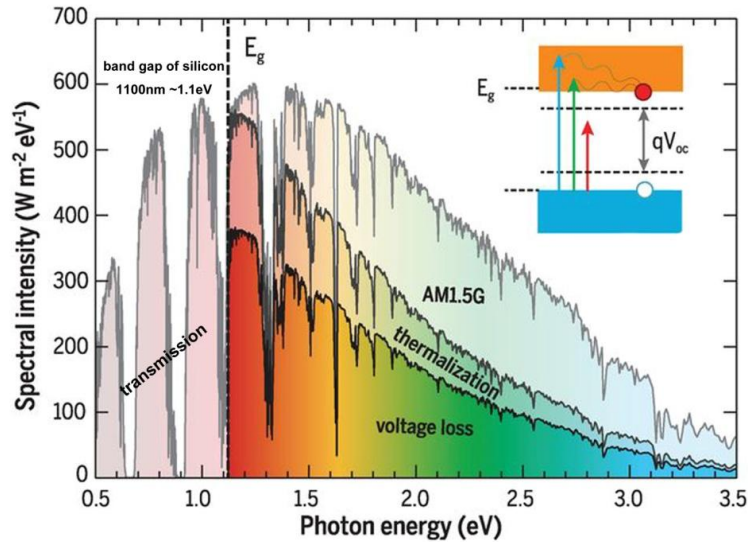


Figure 2.18. Fundamental energy losses in a single-junction silicon solar cell. The inset shows the band structure with the splitting of the quasi-Fermi energy levels [59].

2.6.2 Extrinsic losses of non-ideal cells

It is worthy to note that the above energy losses mechanisms are based on the ideal model in which all extrinsic losses that caused by external factors such as optical reflection, non-radiative recombination, ohmic and other additional limiting impacts are neglected, which are discussed in detail as follow:

2.6.2.1 Fresnel reflection losses

In the real solar cell operating model, the electrical performance is also determined by the optical properties deriving from the optical reflective index, denoted by n . Due to the high contrast of refractive indices between the surrounding air ($n \approx 1$) and silicon ($n \approx 3.4$), a portion of the light is reflected back when it hits the interface between the two media, which may in turn result in over 30% loss of incident energy. The effective reflectance at normal incidence is given by [60]:

$$R(\lambda) = \left| \frac{n_{\text{air}}(\lambda) - n_{\text{Si}}(\lambda)}{n_{\text{air}}(\lambda) + n_{\text{Si}}(\lambda)} \right|^2 \quad (2.17)$$

where n_{air} and n_{Si} are the refractive indices of air and silicon respectively, λ represents the wavelength of incoming light. Hence, the greater difference in refractive between two different materials gives the higher value in reflectance. An effective approach to minimise the reflectance losses of such a surface is by adding an intermediate layer with index of refraction between them. Typically, coating an anti-reflective layer on the front surface of solar cell could reduce the contrast on the new-formed interface, and thus reduce the overall reflectance. Moreover, to further reduce the reflectance losses, texturing the surface through the chemical etching has been widely used commercially since this could elongate the optical path length in the solar cell. The basic reflection losses with appropriate modified methods as discussed are illustrated in below Figure 2.19:

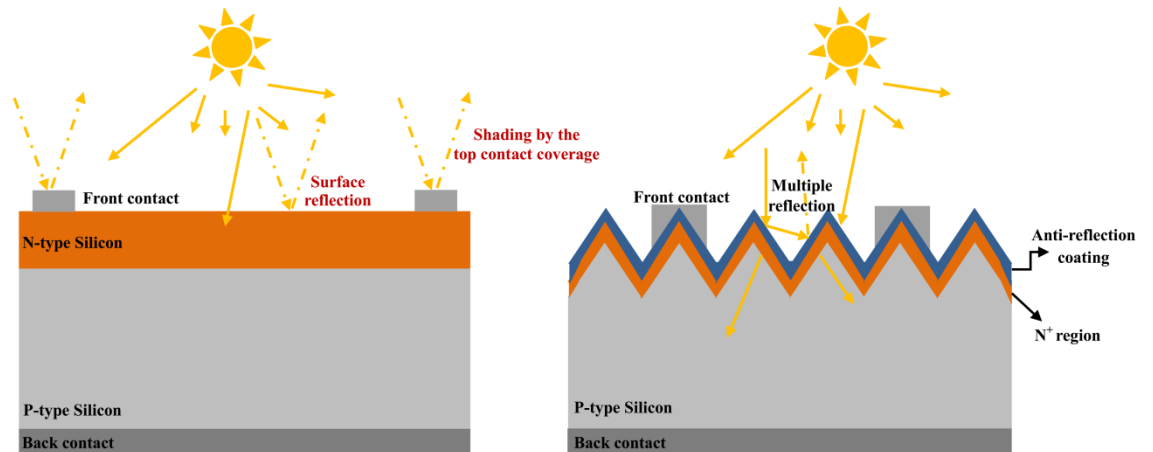


Figure 2.19. The optical reflection losses in a single-junction crystalline silicon solar cell with flat surface (left), and the modified solar cell with improved light trapping capability by combining surface texturing and anti-reflection coating (right).

For most of crystalline solar cells, the thin metal strips or grids are commonly placed on the front side to provide electrical contacts. However, these electrodes may block the incident light and thus reduce the photo-active surface area of the cell. The fraction of the active area of a solar cell is determined by the coverage factor:

$$C_f = \frac{A_f}{A_{\text{tot}}} \quad (2.18)$$

where A_f is the area that is uncovered by the electrode, A_{tot} represents the total area of

the cell. It is clear that the higher the coverage factor of a solar cell, the less shading loss it could avoid. Therefore, it is of great importance when designing the electrode since both a high coverage factor and a sufficient cross-section need to be considered.

2.6.2.2 Solar cell collection losses

The collection of charge carriers in a solar cell is strongly influenced by the charge transport, which is driven by the diffusion. For instance, when electron-hole pairs are generated in the p-type region of the solar cell, the minority electron carriers with relatively short lifetime have to diffuse to the edge of depletion zone to avoid being recombined by the high concentration of positive charges. In this case, the distance that these charge carriers are able to diffuse before being annihilated by recombination plays an important role in determining the collection capability of a p-n junction solar cell since only charge carriers generated within a certain diffusion length from the edge of space charge region will contribute to the production of current and the remaining electron-hole pairs will be lost to heat through non-radiative relaxation [44, 49]. Therefore, as discussed in the previous section, to ensure a long lifetime of minority charge carriers thus high efficiency, the solar cells are expected to achieve a sufficient length of effective thickness (diffusion lengths plus depletion zone) that may even larger than the cell thickness.

2.6.2.3 Recombination losses

Recombination of excess charge carriers inevitably results in additional energy losses which have been briefly introduced earlier. In a non-ideal p-n junction silicon solar cell, the effect brought by the non-radiative recombination is more significantly due to the impurities and crystal lattice defects in silicon where it can occur irregularly in the bulk material, at the surface of p-n junction, or even at the interface. Under a high recombination condition, the forward bias diffusion current increased rapidly which in turn reduces the open-circuit voltage (V_{oc}) and fill factor (FF). Minimisation of recombination losses can be achieved by increasing the doping level in the wafer or by

passivating the cell's surface [12].

2.6.2.4 Ohmic losses

The ohmic losses in non-ideal solar cells can be classified as series (R_s) and parallel shunt resistance (R_{sh}) losses. There are three causes which could lead to the variation of series resistance: firstly, the movement of currents through the emitter, which depends on the total number of connected components in the circuit; secondly, the contact resistance between the p-n junction and electrodes, including also the bulk resistance of the junction; and finally, the resistance at the electrodes (e.g., the metal contacts at top or rear surface of the cell) [49].

Series resistance affect mainly the fill factor as can be seen in Figure 2.20 (olive curve) where it impels more current through the diode and thus moving the curve down toward the y-axis. In addition, these losses become more apparent particularly at high currents through the load, which can be explained by the Ohm's law:

$$W = I \times (R_s)^2 \quad (2.19)$$

where W is the rate of the energy loss at a given resistance R_s . Hence, to ensure a good performance of solar cell, the R_s should be as low as possible.

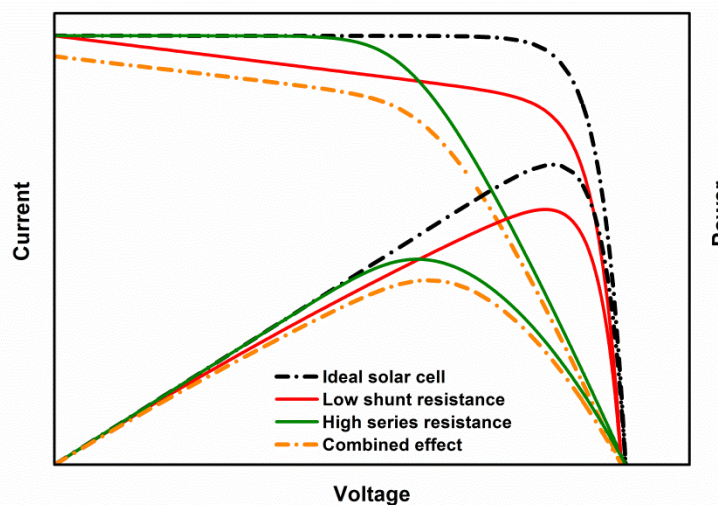


Figure 2.20. The effects of high series resistance (olive), low shunt resistance (red), and combined effects (orange dashed line) on the electrical characteristics of single-diode ideal solar cell.

However, the influences of shunt resistance to the solar cell performance stem from the crystal defects, pinholes, and impurity precipitates in the bulk junction during the manufacturing process. It reflects the effect of leakage current of a photovoltaic cell. Shunt resistance affects mainly on the open-circuit voltage (V_{oc}) and thus the power output as shown in Figure 2.20 (red curve), this effect is severe when irradiance levels is reduced. A higher shunt resistance means a less current that leaving away from the intentional load. Therefore, it is suggested to be as large as possible, especially for the PV array [49].

2.6.2.5 Summary

To summarise the components that represent all potential energy losses in a p-n junction solar cell with energy band gap of E_g , a schematic diagram is plotted in below Figure 2.21. These losses are either due to the intrinsic properties of the semiconductor materials or because of the technical limitations during the manufacturing process, which should be minimised to enhance the devices efficiencies.

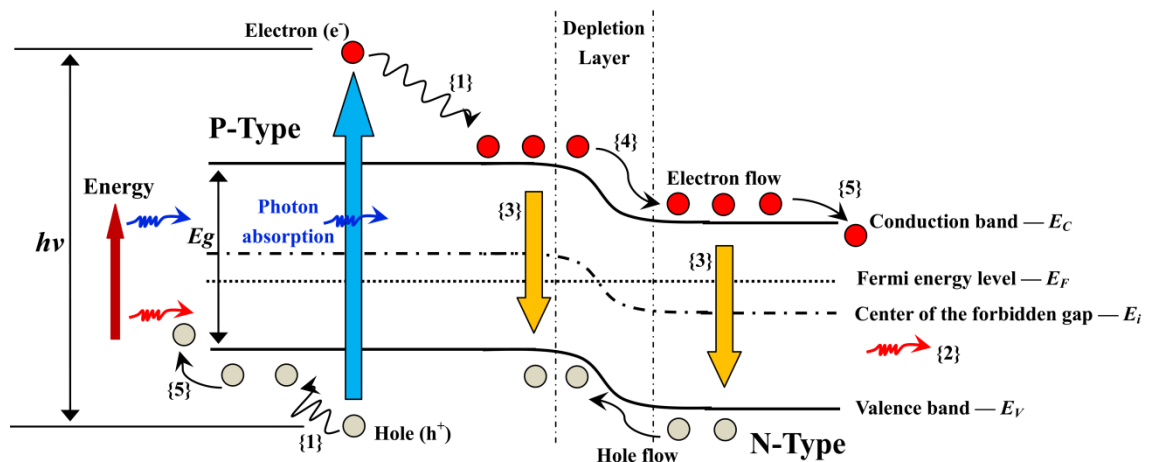


Figure 2.21. Energy losses in a single-junction solar cell: {1} lattice thermalisation loss; {2} transmission loss; {3} recombination loss; {4} junction loss, and {5} contact loss. Figure is adapted with permission from [61].

To improve the light trapping capability and reduce the energy losses of solar cells, a number of approaches have been proposed, such as antireflective coating (ARC), surface texturing, and incorporation of nanostructured light harvesting materials.

Furthermore, the spectral up/down conversion photoluminescence materials in terms of spectrum modification have been widely applied in various types of solar devices, which will be further discussed in latter section. In addition, several multiple schemes including band gap collaboration, hot carrier collection, and multiple carrier excitation that are based on the thin films cells are interested while are not the scope of this work.

2.7 Solar cell efficiency limits

In order to find out how efficient a typical solar cell can be, William Shockley and Hans Joachim Queisser calculated and proposed an upper limit for the efficiency of an ideal single-junction solar cell based on the detailed balance limit, which is referred to as the Shockley-Queisser (SQ) limit. The detailed balance principle in this calculation makes some fundamental assumptions as listed below:

- The solar cells were illuminated under non-concentrated sunlight and only one electron-pair is excited per incoming photon. Excess energy that greater than the band gap is converted into heat.
- Photons with energy above the band gap of the semiconductor materials are absorbed with absorption capability of 100%, which means all optical losses are ignored.
- In addition to the dopants, there are no other impurities and crystal defects existed in the solar cell, and hence no recombination centres that reduce the minority carrier lifetime, only radiative recombination losses process is taken place.
- Photons absorbed by the solar cell should have a number that equal to the sum of the number of recombined charge carriers and the number of electron-hole pairs generated by the cell.

Under these assumptions, the derivation of SQ limit proposed that the maximum theoretical efficiency for a single-junction silicon solar cell (cell temperature at 300 K)

with band gap of 1.12 eV can reach 29.4%, and 33.1% at 1.34 eV, under the AM 1.5G solar radiation spectrum. This efficiency can elevate to 44% by using a 6000 K blackbody radiation (cell temperature at 0 K) [62]. Apparently, this is an idealised model which may not applicable for indirect bandgap semiconductors in which the non-radiative recombination is the dominating recombination mechanism. However, in the real case, all of the components that are neglected in above assumptions are need to be taken into account. To visually express the conversion efficiency of a real solar cell with corresponding components that represent particular losses during the energy conversion process, we firstly adapt the external quantum efficiency, as can be approximated by:

$$EQE(\lambda) = (1-R) IQE_{op}(\lambda) \eta_g(\lambda) IQE_{el}(\lambda) \quad (2.20)$$

where IQE_{op} is the internal optical quantum efficiency, which represents the possibility of photons being absorbed in the absorber layer of the solar cell; IQE_{el} is the electrical quantum efficiency which describes the probability that photo-generated carriers are collected; η_g represents the number of electron-pairs generated per absorbed photon.

Using equation (2.10) and (2.15), and then the conversion efficiency η can be expressed by [63]:

$$\eta = \underbrace{\frac{\int_0^{\lambda_g} (\lambda) \phi^0 \frac{hc}{\lambda} d\lambda}{\int_0^{\infty} (\lambda) \phi^0 \frac{hc}{\lambda} d\lambda}}_{(1)} \underbrace{\frac{E_g \int_0^{\lambda_g} (\lambda) \phi^0 d\lambda}{\int_0^{\lambda_g} (\lambda) \phi^0 \frac{hc}{\lambda} d\lambda}}_{(2)} \underbrace{\frac{A_f}{A_{tot}}}_{(3)} \underbrace{(1-R)}_{(4)} \underbrace{\eta_g}_{(5)} \underbrace{IQE_{op}}_{(6)} \underbrace{IQE_{el}}_{(7)} \underbrace{\left(\frac{qV_{oc}}{E_g}\right)}_{(8)} FF \quad (2.21)$$

where $\phi^0(\lambda)$ denotes the photon flux density, which is defined as the number of photon per unit area per time and unit wavelength. From the integrated equation, the potential factors that affect the conversion efficiency of a solar cell can be classified as:

- (1). Loss by sub bandgap photons.
- (2). Loss by photons with excess of energy.
- (3). Loss by coverage of metal contacts (electrodes).

- (4). Loss due to the optical reflectance.
- (5). Loss by incomplete light absorption in the absorber layer.
- (6). Loss due to recombination.
- (7). Loss due to the voltage drop.
- (8). Loss due to the fill factor.

2.8 Efficiency enhancement for solar PV cells

The losses of energy conversion in solar cells have become an obstacle in narrowing the gap between the current efficiencies and the detailed balance limit which need to be overcome to make PV technologies cost-competitive compared with other types of energy sources. In this work, the core target is to improve the photovoltaic performance of commercial single-junction monocrystalline silicon solar cells through the simple and cost-effective processing methods. The main idea is to deposit light-harvesting particles on the front surface of solar cell, taking advantage of their outstanding light scattering capabilities to enhance the overall light trapping in silicon panel, thus compensating for the insufficient exploitation of solar spectrum. This idea is built on the basis of three fundamental schemes: spectrum modification, optical path length enhancement, and anti-reflection.

2.8.1 Spectrum modification

Solar radiation represents the largest flow of energy from the sunlight. After reaching the earth's surface, around 49% of the energy is in the solar spectrum of near-infrared region ($\lambda > 700$ nm), 45% is in the visible range (400 nm $< \lambda < 700$ nm), and the rest of 6% is ultraviolet radiation (< 400 nm) [64]. Generally, the crystalline silicon (c-Si) solar cells are only able to absorb photons within a limited portion of solar spectrum, with ultraviolet (UV)-blue and most infrared (IR) region of light unexploited. One of the most prominent solutions to address the fundamental spectral mismatch losses is by tuning the incident photon energy to a certain level that close to the

semiconductor band gap through spectral conversion, which can be split into three major processes: down-conversion (DC), down-shifting (DS), and up-conversion (UC).

Figure 2.22 shows the schematic energy diagrams of photon absorption in a typical case of down-conversion, down-shifting, and up-conversion respectively. In a down-conversion (DC) process, a high-energy incident photon within short wavelengths is absorbed and re-emitted as two or more lower-energy photons at longer wavelengths where the silicon solar cells exhibit a robust spectral response. The emission of photons is actually associated with the radiative recombination of an electron from the excited state to the ground state. As a result, a greater number of electron-pairs are generated for the collection of charge-carriers and thus the increase in short-circuit current. Down-conversion is expected to contribute to a quantum yield over 100%, and it is therefore referred to as quantum cutting [65].

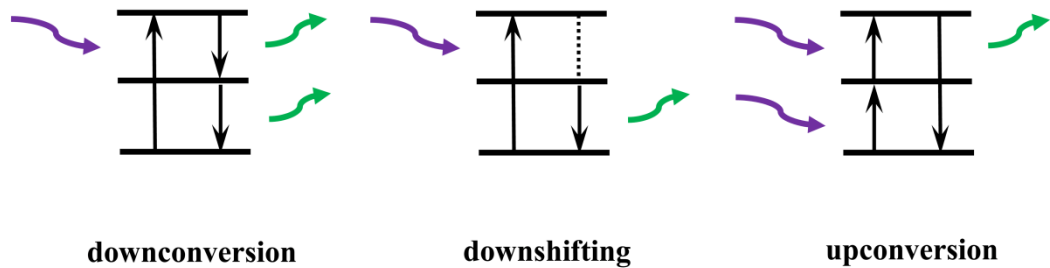


Figure 2.22. Schematic energy diagrams showing the working mechanisms in DC, DS, and UC respectively. A high-energy incident photon is absorbed by the DC layer and is then emitted into two lower-energy photons (left). A high-energy photon is absorbed in the DS layer with the emission of one lower-energy photon and thermalisation losses (dashed line in middle). Two lower-energy photons are absorbed in the UP layer followed by the emission of one high-energy photon (right).

As with similar functionality of down-conversion, the down-shifting exhibits the function of emitting only one photon and thence the quantum yield of this conversion process is less than 100%. In spite of lower number of emitted photons when comparing with the DC process, there is still an overall increase in the electron-hole pair generation as the photons are much easier to be absorbed by the silicon cell in the visible region than in the UV-blue region of spectrum.

DC and DS layer are generally situated at the front surface of solar cell in order to convert more UV-blue photons into visible region for better absorption. In addition, the

intensity of emitted photons in both cases scales linearly with the input light intensity since only one incident photon is involved per conversion process.

In case of up-conversion, two or more low energy photons that cannot be absorbed by the solar cells are converted into one high-energy photon. It effectively reduces the transmission losses by shifting sub-band gap photons in the infrared (IR) part of spectrum to the near-IR or visible region [17]. Up-conversion layers are usually located on the back surface of solar cell with a reflector placed behind, in order to protect the luminescence from escaping out of the rear. In this case, it would not interfere with the absorption of high-energy incident photons at the front surface of solar cell, and thus a real harvest of photocurrent.

Modifying the spectrum via up/down-conversion or -shifting could effectively reduce the fundamental spectral losses in single-junction silicon solar cells thereby improving the conversion efficiency [61].

The selection of materials used in the photoluminescent layer is crucial in determining the level of benefits from its application. For the purpose of maximising the conversion efficiency of solar cells, there are some general characteristics that those luminescent species are desired to possess [66]: (1) luminescent quantum efficiency close to 100% for DS layers, 200% or even higher for DC layers; (2) a relatively broad excitation band in the absorption spectrum is required in order to offset the wavelength region where the solar cells exhibit a poor spectral response; (3) a relatively narrow band in the emission spectrum where the peak emission wavelength is well consistent with the maximum EQE value of the cell; (4) non-overlapping between the excitation and emission spectra to minimise the energy losses caused by the re-absorption of emitted photons; (5) a low refractive index is essential to reduce the reflection losses at front surface of the cell; (6) a relatively low fabrication cost.

A variety of materials can be served as DC, DS, and UC layers for different types of solar cells which can be generally grouped into three categories: rare-earth ions, quantum dots (QDs), and organic dyes.

2.8.1.1 Rare earth ions

Rare earth elements consist of the lanthanide elements from La (atomic number 57) to Lu (atomic number 71) where the 4f electrons are shield from the surroundings by the $5s^2$ and $5p^6$ electrons and therefore the ions have the electronic configuration $[\text{Xe}] 4f^n 5s^2 5p^6$. The incompletely filled inner shell also gives them unique optic and magnetic properties that can be used as efficient luminescent materials in a wide range of applications such as optical fibers and amplifiers, lasers, fluorescent tubes, LEDs, television and computer displays [67-69].

Since they are mostly stable in the trivalent form and thus the energy levels of 4f electrons of the trivalent rare earth ions (RE^{3+}) have been extensively investigated by Dieke [70] and extended by other researchers [71], which is known as Dieke energy diagram (see Figure 2.23). This energy level diagrams specify that the energy states were experimentally determined by considering the optical spectra of individual metal ions doped into the LaCl_3 crystals. The semicircles below the bars indicates the light-emitting levels while the order of magnitude of crystal field splitting is represented by the width of the energy state bars. Note that the diagram almost applies to ions in all host lattices due to the little interaction between the 4f electrons and the environmental electric field.

The electronic structures of RE^{3+} ions are derived from gradually filling 4f orbitals from $\text{La}^{3+}(4f^0)$ to $\text{Lu}^{3+}(4f^{14})$, which are demonstrated in Table 2.3. Since the 4f electrons are well shield from the surroundings, the RE^{3+} ions at excited states have long life time and their absorption and emission transitions yield sharp line in the photoluminescence spectra.

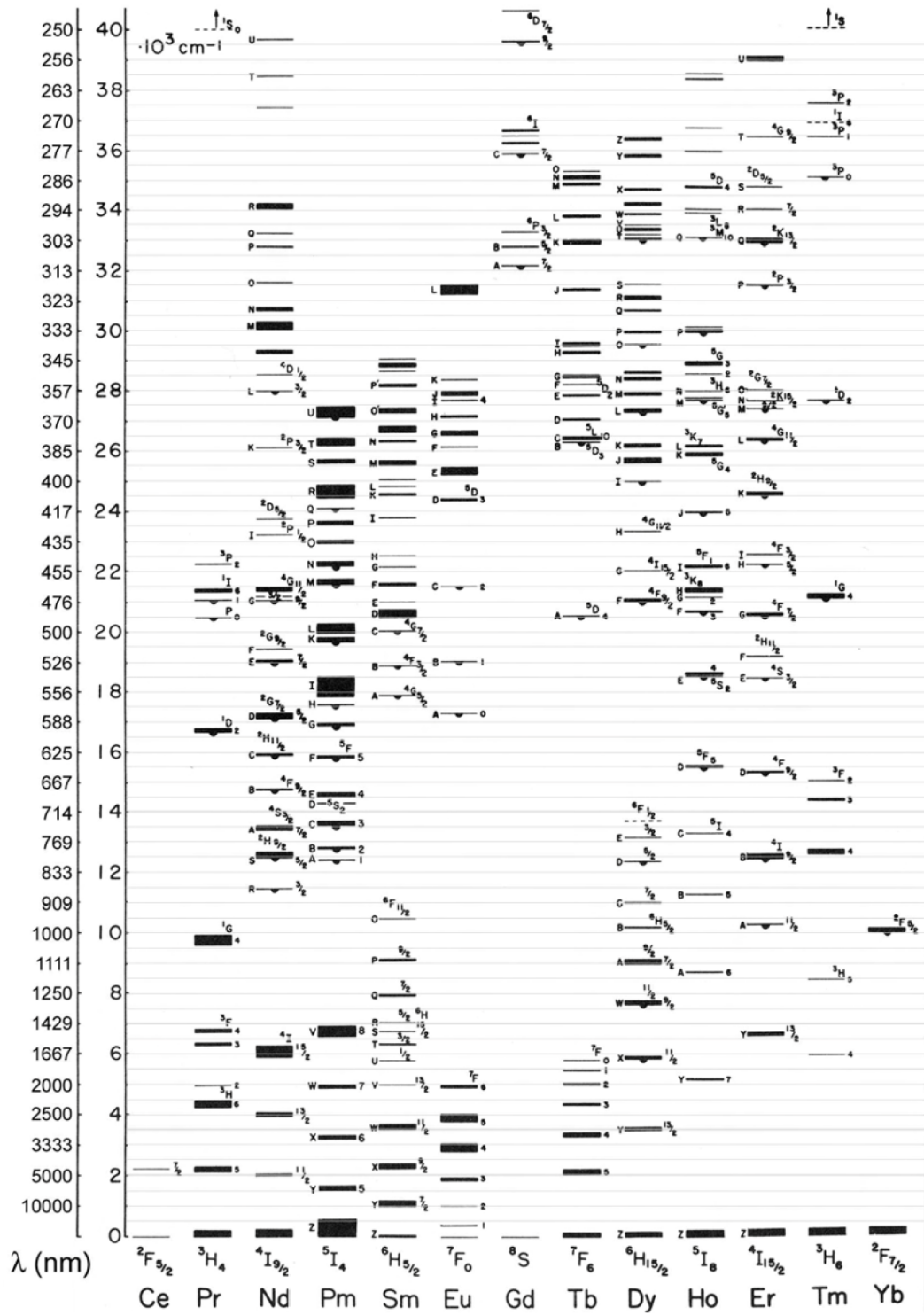


Figure 2.23. Energy level diagrams of RE³⁺ ions incorporated in LaCl₃ crystals [70].

Table 2.3. Electronic structures of RE³⁺ ions (except for Sc³⁺ and Y³⁺) [72].

<i>Atomic number</i>	<i>Element symbol</i>	<i>Configuration RE³⁺</i>	<i>Ground state of RE³⁺</i>
57	La	[Xe]	¹ S ₀
58	Ce	[Xe] 4f ¹	² F _{5/2}
59	Pr	[Xe] 4f ²	³ H ₄
60	Nd	[Xe] 4f ³	⁴ I _{9/2}
61	Pm	[Xe] 4f ⁴	⁵ I ₄
62	Sm	[Xe] 4f ⁵	⁶ H _{5/2}
63	Eu	[Xe] 4f ⁶	⁷ F ₀
64	Gd	[Xe] 4f ⁷	⁸ S _{7/2}
65	Tb	[Xe] 4f ⁸	⁷ F ₆
66	Dy	[Xe] 4f ⁹	⁶ H _{15/2}
67	Ho	[Xe] 4f ¹⁰	⁵ I ₈
68	Er	[Xe] 4f ¹¹	⁴ I _{15/2}
69	Tm	[Xe] 4f ¹²	³ H ₆
70	Yb	[Xe] 4f ¹³	² F _{7/2}
71	Lu	[Xe] 4f ¹⁴	¹ S ₀

DC, DS and UC have been observed from a variety of RE³⁺ hosts, such as oxide, oxysulfides, silicates, and fluorides. Among the rare earth elements, europium (Eu) is a good selection for serving as DS layers since it exhibits multiple absorption lines in the UV region and intense emission lines in the red-to-green spectral range. Eu³⁺ ions are excellent red activator and they possess sharp intra 4f shell electronic transitions while divalent europium (Eu²⁺) ions are able to offer efficient broad band green-emission under ultraviolet excitation. Generally, the excitation band extends from 200 to 400 nm with absorption peak centred at 310 nm while the emission band located in the range of 580 to 650 nm with emission peak at 612 nm, which is ascribed to the ⁵D₀ → ⁴F₂ transition and it is usually independent to the host materials [75].

In recent years, Eu-doped strontium aluminates phosphors have seen an explosion of interest since they provide outstanding features such as high initial luminescent intensity and quantum efficiency, bright emission especially in the visible region, as well as good stability compared to sulfide phosphorescent phosphors, which allows them to be applied in a variety of fields e.g. luminous paints in highway, airport, buildings and ceramic products [229, 230]. According to the literature, the SrAl₂O₄:Eu²⁺ phosphor exhibited a broad green-emission band centred at 520 nm under 344 nm

excitation, which is assigned to the transition of $4f^65d^1$ (${}^6P_{7/2}$) excited state to the ground state $4f^7$ (${}^8S_{7/2}$) configuration of the Eu^{2+} ions. Moreover, the excitation spectra could cover the spectral range of 200 to 425 nm which reveals that it can efficiently absorb the energy of the natural light [231]. Additionally, it shows relatively lower value of refractive index ($n = 1.66$) [232] compared to SiN_x ($n = 1.9$) [180] that may potentially convert more UV photons into longer wavelength region where solar cell has better response. This also suggests that such a candidate can be used as an efficient spectral down-converter in silicon solar cell, in an attempt to improve the light absorption, thus increasing the cell conversion efficiency.

Luminescence spectra consisting of many lines due to ${}^5D_j \rightarrow {}^7F_j$ are observed for terbium (Tb^{3+}). Among the emission lines from the 5D_4 state, the ${}^5D_4 \rightarrow {}^7F_5$ emission line at approximately 545 nm is the strongest in nearly all host crystals when the Tb^{3+} concentration is a few mol% or higher since this transition has the largest possibility for both electric-dipole and magnetic-dipole induced transitions [76]. Oxysulfide phosphors have high luminescence efficiency not only when activated with Tb^{3+} (blue-white to green) but also with Eu^{3+} (red), Pr^{3+} (green) and other rare earths. This family of phosphors plays an important role compared to that of zinc sulfide group in electron- and X-ray-excited applications [76].

One of the most glaring examples is terbium-doped gadolinium oxysulfide ($\text{Gd}_2\text{O}_2\text{S}:\text{Tb}^{3+}$). $\text{Gd}_2\text{O}_2\text{S}:\text{Tb}^{3+}$ scintillator gives 1.8 times greater light output than CaWO_4 (the latter was the commonly used tungstate phosphor) [213] and substantially better light output than the classic $\text{ZnS}(\text{Ag})/\text{LiF}$ material by its higher neutron capture cross-section and intrinsic conversion efficiency [208, 209]. In addition, the emission of Tb^{3+} in lanthanide oxysulfide hosts ($\text{Ln}_2\text{O}_2\text{S}$) shows much stronger intensity than in borate hosts such as ScBO_3 , InBO_3 and LuBO_3 due to the approximately equivalent ionic radii between Gd^{3+} (average ionic radius = 1.125 nm) and Tb^{3+} (average ionic radius = 1.135 nm). Furthermore, although YVO_4 is also a good host material for various Ln^{3+} ions, however, Tb^{3+} does not luminescence in this host [76]. $\text{Gd}_2\text{O}_2\text{S}:\text{Tb}^{3+}$ has a broad excitation band in the wavelength region of 220 to 300 nm and a prominent

green emission line at 545 nm, which is reported as the most commonly used phosphor in commercial x-ray intensifying screens for medical diagnosis. It is also widely used for display applications in cathode-ray (CRT) tube and TV screens owing to its highly bright and efficient green emissions under cathode ray and UV excitations [207]. The high density (7.34 g/cm^3) and UV absorption efficiency, low phonon energy (520 cm^{-1}), wide band gap (4.6-4.8 eV) and adequate refractive index value (2.1-2.3) enable it to effectively trap x-ray photons [205, 206, 210]. This also indicates that $\text{Gd}_2\text{O}_2\text{S:Tb}^{3+}$ might be suitable to serve as a green phosphor for UV-blue lights that is capable of resolving the spectral mismatch and Fresnel reflection of silicon solar cells.

The rest of RE^{3+} ions such as Er^{3+} , Tm^{3+} , and Ho^{3+} that conform the standard on energy state structures for UC activators are the most frequently used UC phosphors [77] whereas they are beyond the current research scope and thus not comprehensively discussed in this thesis. From the recent research works, rare earth ions doped phosphor, such as $\text{Gd}_2\text{O}_2\text{S:Eu}^{3+}$ [195], $\text{Gd}_2\text{O}_2\text{S:Er}^{3+},\text{Tb}^{3+}$ [216], $\text{YVO}_4:\text{Bi}^{3+},\text{Eu}^{3+}$ [193], $\text{KGaGd}(\text{PO}_4)_2:\text{Eu}^{2+}$ [188], $\text{Ba}_2\text{SiO}_4:\text{Eu}^{2+}$ [194] and $\text{NaYF}_4:\text{Yb}^{3+},\text{Er}^{3+}$ [197] have witnessed their contributions in improving the energy performance of different types of photovoltaic devices. The main advantages of the matrices doped with rare-earth elements are as follows [78]: (1) high internal luminescent quantum yield close to 70~100%, which includes the transitions in the infrared region; (2) Stokes shift (distance between the prominent excitation and emission peaks) of the luminescence is large; (3) luminescent band is narrow; (4) photostability of rare-earth elements is high.

Due to their rich and unique energy level structure, rare-earth ions are considered as promising candidates to realise efficient down conversion. In addition, they provide the capability of photon management when these “activators” are doped in the host material. Furthermore, their high photoluminescence quantum yield allows for an efficient spectral conversion, thus ensuring an enhanced EQE in solar cell.

2.8.1.2 Quantum dots and Organic dyes

Quantum dots (QDs) are nanocrystals (particle size: 1~20 nm) in semiconductors which consists of 100~1000 atoms and they were firstly used in luminescent concentrators to replace the organic dye molecules. The exact shape and size of QD play an important role in determining many of its electrical and optical properties [79, 80]. Reduction of the size of QDs leads to an enlarged fraction of the total number of atoms on the surface and thus a high specific surface area. Hence, QDs usually possess a significant difference in physical and chemical properties compared to the bulk materials. In addition, the high specific surface area may cause poor luminescence properties since the surface-related non-radiative relaxation dominates in the strong confinement regime [72].

The main advantages of QDs over organic dyes are as follows [78]: (1) Tunable absorption edge by changing their particle size; (2) They exhibit a broad absorption profile which covers the UV region; (3) They are inherently more stable than organic dyes can be kept constant throughout the decades; (4) High quantum yield with more than 80% at room temperature. Common QDs that used in DC and DS purposes are CdSe, CdS, Si-nC, ZnS and PbS where their excitation and emission bands are summarised in Table 2.4.

Table 2.4. Common quantum dots used as down-shifting layers.

<i>QD</i>	<i>Excitation λ_{max} (nm)</i>	<i>Emission λ_{max} (nm)</i>
Si-nC [81]	300 - 500	700 - 900
CdSe/ZnS [82]	220 - 620	470 - 620
CdS [83]	300 - 480	430 - 600

However, the overlap of its absorption and emission band can result in significant photon re-absorption losses and thus decrease of the quantum yield, even if this can be minimised by spreading the particle size. Furthermore, some QD elements such as lead and cadmium in CdS and PbS are toxic and therefore has to be considered. In addition, most importantly, QDs are substantially more expensive in comparison with organic dyes [78].

The application of organic dyes as luminescent layers to improve the UV response of single-junction solar cells was firstly proposed by adding fluorescent organic dyes to GaAs and amorphous silicon (a-Si) solar cells. An absolute efficiency gain of 2% was observed for the GaAs while minor enhancement in the case of a-Si. This can be further improved by minimising the reflections losses in near infrared regions [84]. Nowadays, organic dyes possess relatively high absorption coefficients, close to unity quantum yield (90~100%), and are easy to process in polymeric matrices (such as, e.g., PMMA) [85]. Organic dyes incorporated into polymeric host are efficient DS layers when integrated to various types of solar cells such as mono/poly-Si, a-Si, GaAS, CdTe, CIGS, and DSSC. Table 2.5 shows the luminescent properties of some common commercial organic dyes that are frequently used as down-shifting layers.

Table 2.5. Commercial organic dyes used as down-shifting layers.

<i>Organic Dye</i>	<i>Excitation λ_{max} (nm)</i>	<i>Emission λ_{max} (nm)</i>	<i>Quantum yield (QY)</i>
Lumogen®F V570 [86]	378	413	>85%
Lumogen®F O240 [86]	524	539	>90%
Lumogen®F R305 [86]	578	613	>90%
Sumipex 652 [87]	470	520	>91%

However, the main drawbacks of dyes are their limited life time. An investigation of commercial Violet 570 dye has proved that the luminescent intensity of PMMA-doped dye sample reduced by 50% from its initial value after exposure for two years [88]. Apparently, this would not cover the initial power of silicon solar cells (in the warranty period of 25 years). Therefore, to efficiently convert solar energy into electricity, high chemical stability to UV irradiation and long degradation period are both need to taken into consideration.

2.8.2 Optical path length enhancement

The diffusion length in a solar cell, as described earlier in section 2.6, is important for the collection of minority charge carriers. Low diffusion length would result in insufficient absorption of light, especially at the long wavelength of solar spectrum. However, only making the solar cells to be thicker is not enough in addressing the

collection losses. An alternative way is to geometrically increase the length of path where light travels inside the semiconductors.

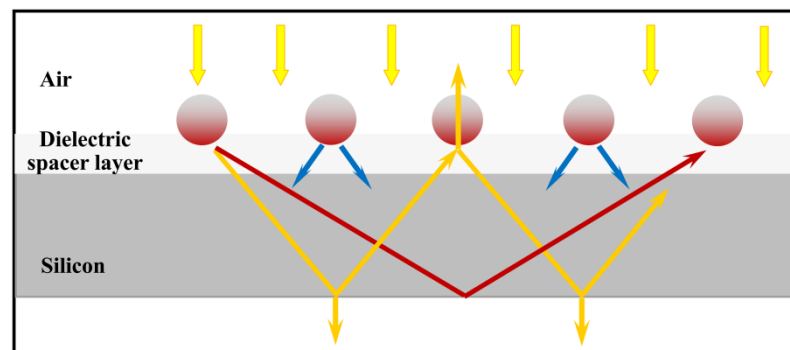


Figure 2.24. Sketch showing the optical path length enhancement in a silicon solar cell obtained by decorating metallic nanoparticles at the cell's surface. Light is directed at an angle away from the normal (red versus butter). A transparent dielectric spacer layer is placed between the metal particles and the silicon surface.

As shown in Figure 2.24, if the incident light could be scattered through the silicon at a higher angle (red) than normal (butter), the internal reflectance at bounding interfaces would increase, meanwhile, the transmission coefficient of the absorber layer would significantly reduce, thus effectively trapping the light. This could be achieved by incorporating metal nanoparticles into the solar cells, taking advantage of their unique localised surface plasmon resonance (LSPR) characteristics. When light hits a metal particle which the size is much smaller than that wavelength, the free electrons on its conduction band will move away from their atomic nucleus, which in turn creates an opposing electromagnetic field for the oscillating electrons. Such oscillations are maximised when the frequency of light matches the inherent oscillating frequency of the nanoparticles. It is in this process that metallic nanoparticles (NPs) could effectively couple and trap freely propagating waves by folding the light into high angles, and therefore, contributing to the light harvesting. The light scattering effects depend largely on the selected plasmonic metal NPs, their shapes, and sizes, as well as their host dielectric environment [89].

For obtaining high efficiency crystalline silicon cells, it is essential that a thin layer of dielectric film be inserted on the silicon surface to suppress the recombination of photogenerated carriers and improve the devices electric properties [90]. Moreover, the

thin dielectric spacer layer between the p-type silicon and metal particles not only contributes to the minimisation of parasitic plasmonic absorption of infrared light in the metal layer, but also helps to elongate the internal optical path length in the device [91]. Such effective interface passivation is usually achieved by dielectric materials like silicon nitride, silicon oxide and aluminum oxide owing to their moderate index values and dielectric properties [12].

In addition to LSPR, surface texturing has been regarded as a commonly used solution in reducing the reflection losses for different optoelectronic devices. Texturing on the front surface of solar cells enables multiple reflections to occur at the silicon surface, and therefore it can increase the probability of light absorption. On the other hand, it provides the benefit of elongating the optical path of light due to the variation in the angle of incidence where light strikes the cell, as can be seen in Figure 2.25.

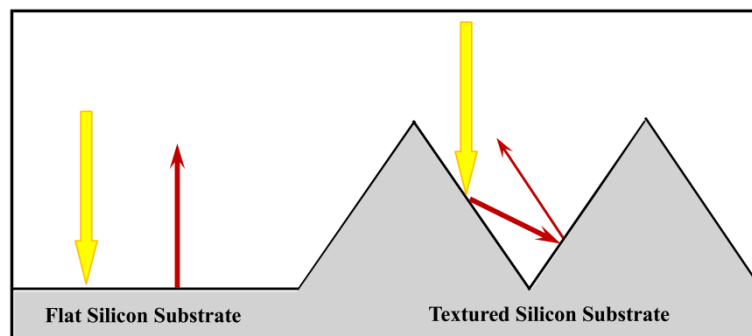


Figure 2.25. Sketch showing the comparison of surface reflection between a flat (left) and a textured silicon substrate with pyramidal like shape (right). In case of textured surface, light is multiply reflected, improving the chances of being internally refracted.

Additionally, it could also compensate for the collection losses caused by the low diffusion length since the refracted photons which inside the silicon will propagate at a certain angle, resulting in being absorbed closer to the junction, and thus effective collection of minority charge carriers [92].

For most of single and polycrystalline silicon solar cells, the textured surface can be created in a number of techniques such as mechanical grooving [93], laser sculpturing [94], wet chemical and plasma etching [95]. Among them, wet chemical etching is by far the most frequently used method which requires etching along the faces of the

silicon crystal planes, creating random pyramids with a slope angle of 55 °[96].

2.8.3 Anti-Reflection

The contrast of refractive indices between two different media would result in partial reflection of light at the interface. For a bare flat silicon surface with refractive index of 3.4, around 40% of incident light from the solar spectrum is reflected back to the air, and be lost. Typically, applying a thin film of dielectric material that exhibit high transparency, low absorption coefficient, and an intermediate index value on the front surface of silicon solar cell could effectively suppress the Fresnel reflection loss. Such coating is referred to as the anti-reflection coating (ARC), which has been used comprehensively in the domain of high-accuracy optical components, solar cells, scanner and camera lenses, in attempts to improve the optical transmittance. ARC in combination with surface texturing (see Figure 2.20) are expected to achieve an overall reduction factor of 10 [16].

Figure 2.26 shows the reflection mechanism of a single-layer of transparent ARC on a typical silicon solar cell. Whenever the thickness of the thin layer “ d_1 ” is equal to a quarter of the incoming light “ λ ”, the reflection waves from the top (R_1) and bottom (R_2) sides of the coating will destructively interfere and offset each other as they are “out-of-phase”. As a result, light is completely refracted into the silicon which contributes to a zero reflected energy.

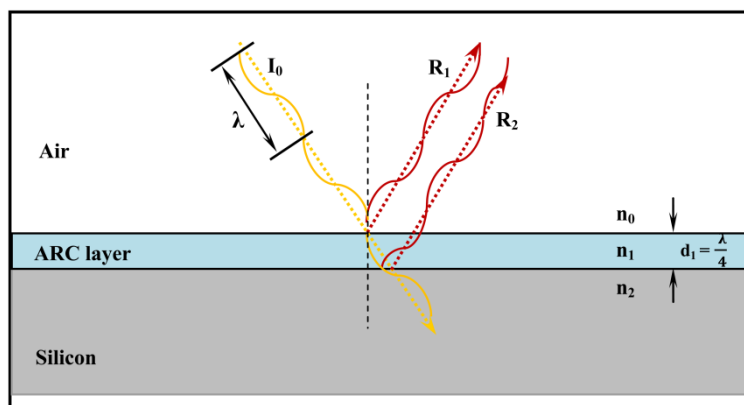


Figure 2.26. Sketch showing the destructive interference occurred in a quarter-wavelength anti-reflection coating on a flat silicon solar cell. The two reflected waves with same frequency and amplitude cancel each other which enable more coupling of light.

The main idea of anti-reflection coatings (ARCs) for photovoltaic application is to reduce the reflection while improving coupling of light, in this case, the optimal thickness is pivotal in maintaining the anti-reflection effects along a certain region of the spectrum as well as yielding destructive interference in light reflected from the different refractive index layers. For a quarter-wave ARC with a refractive index n_1 , and incident light with wavelength λ , the thickness which corresponding the minimum reflection is given by [97]:

$$d_1 = \frac{\lambda}{4n_1} \quad (2.22)$$

Since the light shows peak power of solar spectrum at wavelength close to 600 nm (see Figure 2.3), the optimum thickness of ARC with index of 1.9~2.1 is desired to be in the range of 70~80 nm, which gives the reference for solar cell design. Furthermore, to obtain the minimum reflection in a typical single-layer ARC, the refractive index (RI) of antireflective material should be equal to the square root of refractive indices of the materials bounding the coating, which can be expressed by: $n_1 = \sqrt{n_0 n_2}$. In our case, n_0 and n_2 represent the indices of air and silicon respectively. However, the performance of a single-layer coating is constrained by the reflection of normal incident of single wavelength. Greater reduction is commonly achievable when two coating layers are introduced as it enhances the destructive interference and thereupon a further reduced reflectance can be obtained through the extra reflectance minima [98]. For scenarios like this, the refractive indices for the top and bottom antireflective materials should conform to both of the following formula [97]:

$$n_{\text{top}}^3 = n_0^2 n_{\text{si}}; n_{\text{bot}}^3 = n_0 n_{\text{si}}^2 \quad (2.23)$$

where n_{si} and n_0 represent the refractive indices of silicon ($n_{\text{si}} \approx 3.4$) and the ambient media respectively. In case of double layer anti-reflection coating (DLARC) in the air ($n_0 \approx 1$), the most suitable refractive indices for top and bottom layers are $n_{\text{top}} = 1.58$ and $n_{\text{bot}} = 2.49$. Hence, based on this principle, it is an accepted approximation that SiO_2 and TiO_2 (anatase) are the most desirable anti-reflective materials owing to their

close-matching refractive indices ($n_{\text{TiO}_2} \approx 2.3$ and $n_{\text{SiO}_2} \approx 1.5$) and these two typical anti-reflective light harvesting candidates will be described in more details in this section.

General techniques for vacuum deposition of silicon dioxide ARCs include thermal evaporation, liquid phase deposition, reactive sputtering, and plasma-enhanced chemical vapour deposition (PECVD), which are expected to produce homogeneous films with uniform thickness as well as to provide the possibility of deposition at low temperature (300~400 °C) that could largely reduce the degradation of solar cells metal contacts and contamination caused by impurities [99].

2.8.3.1 Silicon oxide ARC and related work

Silicon nitride (SiN_x) is frequently used as a standard ARC layer that deposited on commercial silicon solar cells by low-temperature PECVD method. This is attributed to its conjunction effects of both optical and electronic properties that contribute to maximising the photo-generated current within the silicon substrate and reducing carrier recombination at the surface of the silicon solar cell, as a result of enhancement in conversion efficiency [222]. However, it has the drawback of narrow wavelength range for visible light absorption with its spectral operating capability limited to only UV region, and thus mediocre energy performance in silicon solar cell. To address this weakness, a double ARC is applied to the solar cell by using silicon oxide [223].

The integration of silicon oxide/silicon nitride onto the solar cell surface is a more promising scheme for substantial efficiency gains due to the advantages of surface passivation, broader light absorption range and lower surface reflectance in comparison with that of a single layer ARC. Moreover, it is reported that silicon oxide thin film possesses the potentiality to be served as a dual-functional ARC and down-conversion layer on the solar cells due to its intrinsic optical property of absorbing ultraviolet radiation and re-emitting the energy as red light (635~700 nm) where the silicon solar cells exhibit robust spectral response [224].

The implement of fabricating low-cost effective crystalline silicon solar cells requires new technological schemes such as the use of safer process and maintaining low processing temperature (300~400 °C) since these could ensure the diffusion of dopant in the semiconductor is minimised to create “shallow junction”. In addition, high-temperature processing (reaching up 1000 °C) consumed much resource (silicon substrate) and can easily induce product defects such as crystallographic damages, degradation of metal contacts and contamination due to the impurities diffusion whereas all of these defects can be largely avoided by using a low-temperature deposition method. Various deposition techniques can be used for silicon oxide deposition which includes Chemical Vapour Deposition (CVD), Liquid Phase Deposition (LPD), reactive sputtering and spin-on glass, etc. Among them, CVD is a superior approach due to its unique versatility, possibility of deposition at low temperature (< 275 °C) [225].

Silane has a long history of use as the raw materials for preparation of silicon thin films by using PECVD systems [226]. However, considering its toxicity and pyrophoric nature that can generate an explosion hazard particularly in mass manufacturing processes which require considerable amount of silane gases for storage, it is currently replaced by another alternative organosilicon, like liquid/vapour-phase TMS [228].

Research done by Cojocar et al. indicated that the tetramethylsilane is a suitable candidate for the source of silicon in replacing the silane gas in the photovoltaic cell manufacturing processes due to its high stability, non-pyrophoric and volatile at room temperature. In addition, it has the advantage of reducing fabrication cost as there is no requirement for introducing extra heating instruments to obtain vapour flows due to its high vapour pressure (11.66 psi at 20 °C) [227].

Kim et al. reported a successful fabrication of double layer of SiN_x/SiO₂ ARC for reducing the Fresnel reflection from the surface of mono-crystalline silicon solar cell through PECVD method. Experimental results showed that the optimal design by depositing a double layer ARC on the solar cell surface contributed to a maximum absolute enhancement of 0.31% in conversion efficiency as compared to the efficiency gains (0.12%) that obtained from a single ARC with SiN_x [222].

2.8.3.2 High surface area of TiO₂ ARC

Titanium dioxide (TiO₂) is one of the transition-metal oxides, which has been extensively studied in the last two decades owing to its unique optical and dielectric properties. TiO₂ (especially anatase phase) exhibits good reactivity under ultraviolet (UV) light, optical refractive index (1.8~2.9), low fabrication cost, excellent chemical resistance to the majority of the chemicals used in PV industry, which make it an attractive option for being employed as a cost-effective ARC to suppress the Fresnel reflection and more importantly, the poor response of silicon solar cell in the UV-blue spectral range [98,121].

Generally, the photocatalytic performance of TiO₂ depends strongly on its phase structure, specific surface areas, grain size, and pore structure [128]. Comparing with other two polymorphs (rutile and brookite) of TiO₂, anatase TiO₂ has more surface defects that can be served as shallow traps, which allows efficient inhibition of carriers' recombination, thus gives superior photoreactivity and longer lifetime of photoexcited electrons and holes. In addition, anatase exhibits higher surface adsorption capability to hydroxyl groups due to its larger specific areas [125].

Nanostructured TiO₂ with high surface-to-volume ratio and porous structures opens up new possibility for light diffusion on the solar cell interface, which promotes rapidly the separation of charge carriers (photogenerated electron-hole pairs) at the surface of TiO₂ NPs [128]. Furthermore, the porous structure and high surface area comparing to bulk materials allow multiple reflections of incident light and provide a good scattering effect, which enhances the optical path as well as light harvesting capability of TiO₂ across a broad wavelength range [144-147].

However, TiO₂ has a wide bandgap of TiO₂ (3.2 eV for anatase and 3.0 eV for rutile) and is able to only absorb UV region (<380 nm) of solar light. For obtaining improved photocatalytic activity, it is necessary to extend the photoresponse of TiO₂ from the UV to the visible range. In this case, a number of studies have been conducted, such as

doping blank TiO₂ with transition metallic such as iron (Fe), manganese (Mn), chromium (Cr), and magnesium (Mg) [133-135, 138, 140,141] and nonmetallic elements (e.g., N, S) [135, 142, 143] into the TiO₂ lattice, which could effectively improve the photocatalytic activity of TiO₂ in both UV and visible regions.

2.8.4 Other factors

In addition to obtaining the RI matching for an anti-reflection layer, there are some fundamental criteria which have to be satisfied during the fabrication process [100]

1. Homogeneous layer of coating is required so that it could sustain the antireflective functionality over a broad spectrum of incident light.
2. Omni-directional antireflection feature is provided by the coated layer, in order to optimise the photon absorption throughout the day.
3. In regard to practical applications, the coatings are desirable to be mechanically robust and are able to withstand the environmental condition in which they were exposed.

Above design concepts could help to improve the photovoltaic performance of crystalline silicon solar cells by addressing the limitations of current technology, which are the main scope of the conducted research. In addition, some factors that may contribute to increasing the collection probability of charge carriers and thus high efficiency are listed below [12]:

- Selective-emitter (i.e. n⁺-layer for front contact while n-layer for active surface region; p⁺-layer for rear contact and p-layer for active surface).
- Surface passivation (i.e. SiO₂ coating on both front and rear surface of solar cell).
- Thin metal finger or grid on the front side.
- Metal back contact (i.e. back metallisation with small contact area to the base material).

2.9 Summary

In this chapter, detailed background in regard to the p-n junction photovoltaic solar cell operation and the parameters that affecting its conversion efficiency have been reviewed. Spectral mismatch and non-radiative recombination losses are still two of the major obstacles that crystalline silicon solar cells face today, which need a perspective of the current development concepts for enhancing their energy performance. Antireflection coating and spectral down-conversion through appropriate use of light harvesting materials are expected to provide effective solution of promoting the light absorption of silicon solar cells at both short and long wavelength bands in a low-cost manner. Under this background, a variety of potential oxide materials such as high surface area of TiO₂-based nanoaerogels, SiO₂ thin films, as well as the rare earth ion-doped gadolinium and alkaline aluminates phosphors will be comprehensively studied in this thesis, in order to identify their suitability for promotion of light absorption that contributes to photocurrent and efficiency enhancement of commercial silicon solar photovoltaic devices.

The next chapter will introduce the equipments for solar cells characterisation where the function of particular devices, the experimental procedures as well as the approaching in conducting these experiments will be described in detail.

Chapter 3 Characterisation of Crystalline Silicon Solar Cells

The experimental processes executed in the laboratory for the fulfillment of this study were carried out at Brunel University London. This chapter describes in detail the methodology followed and moreover all the requisite equipments and instruments used to characterise the solar cells. The functions of corresponding apparatus in carrying out the experiments are also introduced.

3.1 Solar Cells

Photovoltaic solar cells used for the experimental procedure of this project are model XS156B3-200R and T6S-3A mono-crystalline silicon cells supplied by Motech Industries, Taiwan. The solar cells are made by cutting p-type (boron-doped) mono-crystalline silicon into wafers leaves with pseudo-square shape of 156 mm × 156 mm ± 0.5 mm in size, and 200 ± 20 μm (± 30 μm for T6S-3A cell) in thickness. Then cleaning and texturing was separately done on the p-type silicon wafers through chemical etching using alkaline-based solutions in order to remove the unwanted particles and to reduce the surface reflection. The etching process forms anisotropically pyramid structures on the cell's surface, which could scatter light inside the wafer and elongate the optical path length, thus improve light trapping. To create the p-n junction, the n-type layer was then formed on the p-type wafer using phosphorus diffusion technique where the phosphorus atoms are penetrated into the silicon wafer, making the top of the cell a negative electrode and the rear surface a positive electrode. Such an “n-on-p or n⁺-n-p-p⁺” type of solar cell is currently being widely used because the n-type silicon gives superior surface quality. A critical step prior to the diffusion is the edge isolation where the edge and backside of the silicon wafer are masked by a diffuse barrier paste so as to isolate the unwanted diffusion.

The specifications and features, as well as the electrical parameters of the under-study monocrystalline silicon solar cells are shown below in Figure 3.1 and

summarised in Table 3.1 respectively. At the front surface of solar cell, the metal contact is formed by a 3-stripe silver bus bar and each bar has a dimension of 1.4 mm in width (1.5 mm for T6S-3A cell), while the back surface is entirely covered by aluminum where 3 discontinuous silver soldering pads were attached, each of which has a width of 2.5 mm (1.9 mm for T6S-3A cell). In addition, dark silicon nitride (SiN_x) anti-reflection coatings (ARCs) were deposited on the front-textured surface by low pressure plasma-enhanced chemical vapour deposition (PECVD) method with an average thickness of ~ 80 nm. Such design is determined from the derivation of “a quarter-wave ARC equation” (Equation 2.22) as introduced in the previous chapter where for obtaining the destructive interference and thus minimum reflection on the silicon cell surface at peak solar power wavelength (λ) around 600 nm, the desired ARC thickness (d) with average refractive index (n) of 1.9 can be expressed by: $d = \lambda/4n \approx 80$ nm.

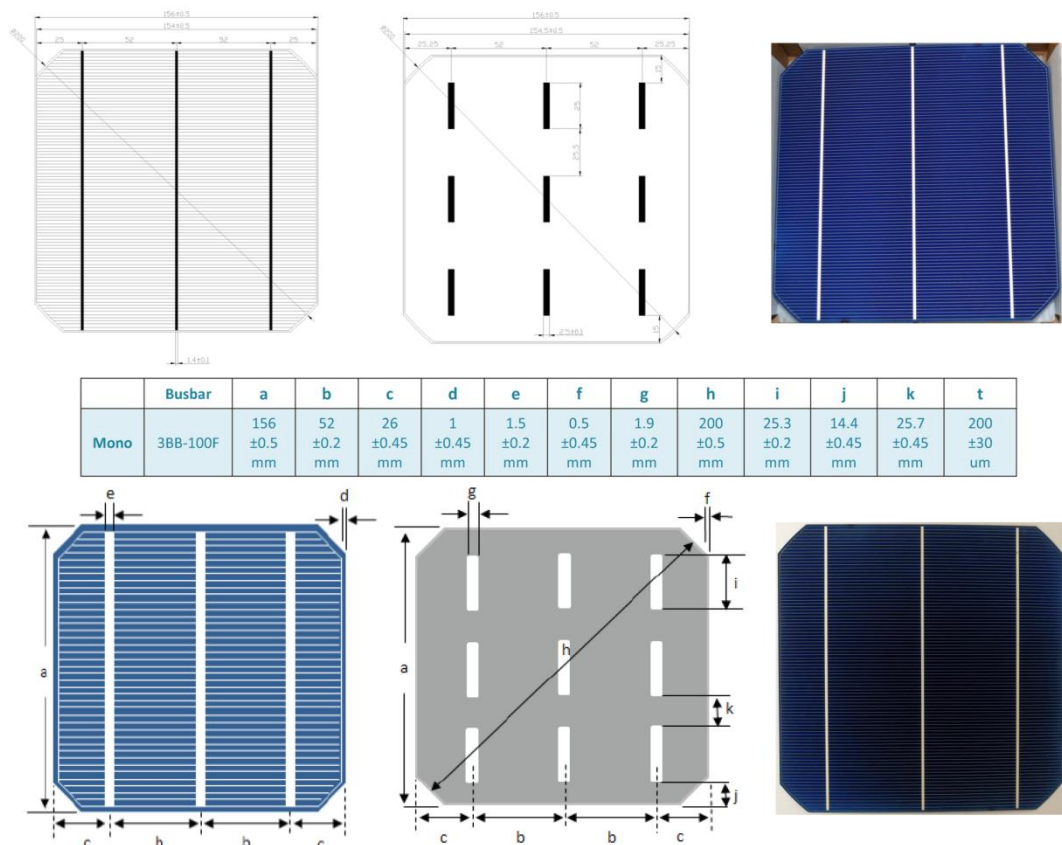


Figure 3.1. Motech monocrystalline silicon solar cells: XS156-200R (top) and T6S-3A (bottom).

Table 3.1. Electrical parameters of the under-study mono-Si solar cells, provided from Motech manufacture.

<i>Product code</i>	<i>PCE (η)</i> (%)	<i>Pmax</i> (W)	<i>Isc</i> (A)	<i>Voc</i> (mV)	<i>FF</i> (%)	<i>Voltage</i> <i>coefficient</i>	<i>Power</i> <i>coefficient</i>
XS156B3-200R	19.2	4.59	8.99	641	79.65	-0.33%/ °C	-0.41%/ °C
T6S-3A	19.8	4.73	9.30	646	78.73	-0.32%/ °C	-0.43%/ °C

3.2 Solar Cells Preparation

3.2.1 Solar Cells Cutting

For experimental purposes, the solar cells were split into three equal parts (15.6 cm \times 5.2 cm) using a direct current (DC)-power CO₂ laser cutting-engraving machine (TMX90, CTR, UK). Solar cells that were cut into smaller sizes could provide convenience for certain types of experiments, e.g., in case of cells coating and annealing, a limited size of sample is required to be placed inside the chamber. Secondly, additional cells could serve as backups since they are fragile, and thus are easily cracked during handling and operating process of experiments. Thirdly, the additional cells can be used to calculate the standard error for each case of initial experiment so as to increase the data accuracy.

The DC laser cutter (as shown in Figure 3.2) is equipped with a sealed electronic water cooling unit fitted with a circulating fan which cools the air around the water cooler to help control the cooling temperature. During the cutting process, the solar cells were placed on the working area of a wooden plate which situated on the knife-edge bar bed of the laser cutter (see top right in Figure 3.2). The wooden plate has been previously engraved with a pattern based upon the dimension of solar cell, in convenience for tracing the working area, thus ensuring an accurate cutting. Under a 100 W laser power, the beam was directed to the cutting head by a mirror where a lens focuses it to a single red spot with a diameter of 0.1 mm. The spot was finally focused onto the surface of solar cell with a power density of 125 W/mm². Subsequently, the fume of the laser is shut and the laser beam starts moving along the cutting path that

designed by its build-in version-5.3 Easy cut software (see bottom left in Figure 3.2). The beam speed is set to 10 mm/s during the whole cutting process.

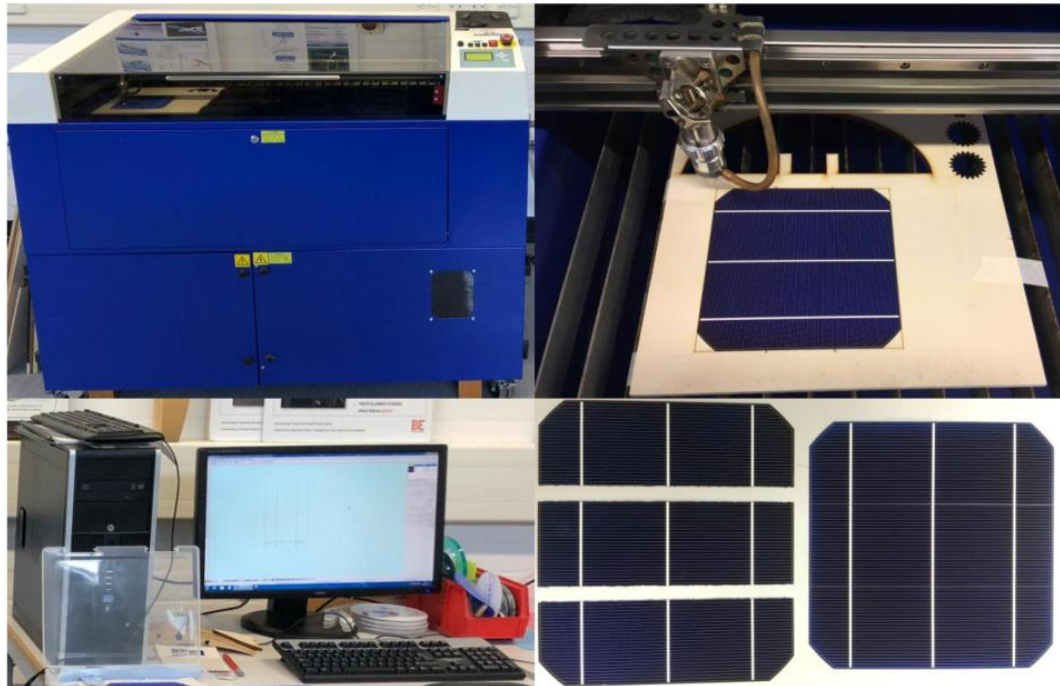


Figure 3.2. TMX90 Laser cutter (Top left), solar cell layout on the working area of wooden plate (Top right), setting up process in computer (Bottom left), and the comparison of solar cell before and after cutting (Bottom right).

3.2.2 Solar Cells Soldering

Solar cell soldering is a critical step to ensure an accurate characterisation of the cell's electrical performance. The soldering process is carried out by using an AT60D digital soldering station (TENMA, UK) fitted with a plug-in soldering iron and a control panel (see top left in Figure 3.3) which provides adjustable heating temperature range of 150 to 450 °C. The tabbing wire (Ulbrich Solar Technology, Inc, USA) has a dimension of 1.4 ± 0.08 mm in width, and 0.1 ± 0.008 mm in thickness, with all sides coated by leaded solder alloys in which its chemical composition and physical properties are summarised in Table 3.2.



Figure 3.3. Photographs showing the manual soldering process with corresponding soldering components.

Table 3.2. Physical properties of leaded solder alloys (Sn-Pb-Ag) [104].

<i>Alloy Composition</i>	<i>Tin (Sn)</i>	<i>Lead (Pb)</i>	<i>Silver(Ag)</i>
percent by Mass (%)	62	36	2
Density (g/cm ³)		8.88	
Colour		Silvery grey	
Melting Point (°C)		183 °C (solder alloy)	
Electricity Resistivity (μΩ·cm)		10-15	
Yield strength (MPa)		< 90	
Tensile strength (MPa)		< 270	
Elongation (%)		> 25%	

The following procedure was performed during the soldering process:

- The tabbing wires were cut into 5 cm for each soldering.
- Applying flux on the silver bus bar and silver pad at the front and rear surface of the solar cell respectively by using a resin flux pen in order to provide better soldering effect.
- The soldering iron was heated up to 250 °C so as to melt partially the tabbing wire onto the solar cell while elevated soldering temperature could induce mechanical and thermal stresses in the solder joints, which in turn result in cell breakage [103].

- Holding the wire down and pulling the soldering iron along the tabbing wire with adequate force. Repeating this process for the back surface soldering and then two tabbing wires were soldered onto the surface of solar cell, one at the front and the other at the rear, which represent negative and positive polarities, respectively.

3.3 Electrical Characterisation

Photovoltaics current-voltage (I-V) characteristics measurements were performed by illuminating an effective surface area of the monocrystalline solar cells using a Trisol TSS156 Class AAA xenon flash solar simulator (OAI, USA).

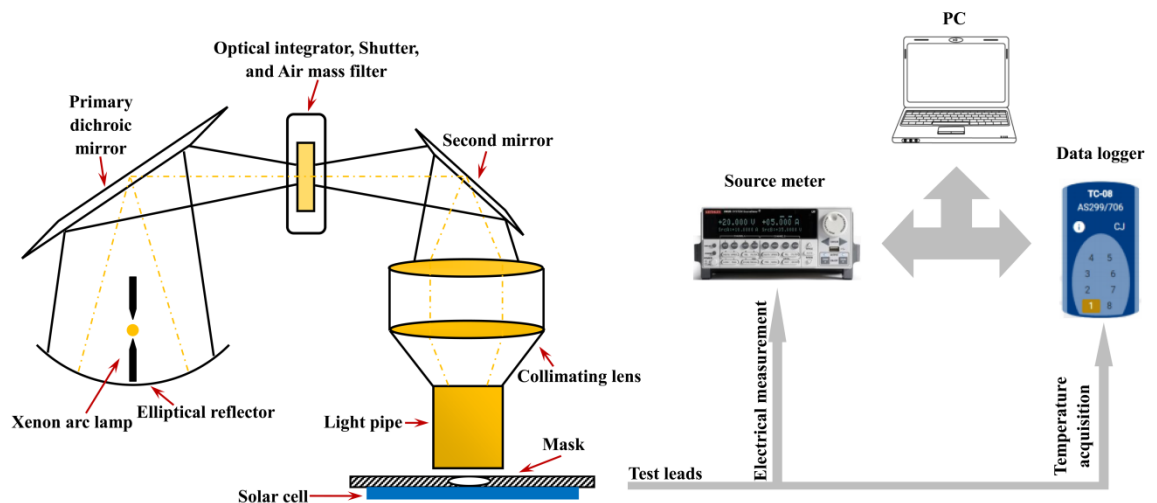


Figure 3.4. Sketch showing the experimental set-up of I-V electrical characteristics measurement.

As it is shown in Figure 3.4, the experimental set-up is to simulate the standard test conditions (1000 W/m^2 , $25 \text{ }^\circ\text{C}$) where the solar cells are connected to an electrical source meter and a temperature monitor that operated by a terminal computer. The solar simulator is capable of providing a constant simulation from the sunlight and the characterisation can be done much more quickly since it is independent to the environmental conditions.

The illumination source of the simulator was a 1000 W arc xenon lamp which offers high intensities and an unfiltered spectrum (400 to 1100 nm) similar to the sunlight. The spectrum produced from the solar simulator and the standard AM 1.5G

solar spectrum are shown below in Figure 3.5. In addition, a comparison of spectral irradiance distribution between the OAI simulator and the International Electrotechnical Commission (IEC) 60904-9 standards is given in Table 3.3.

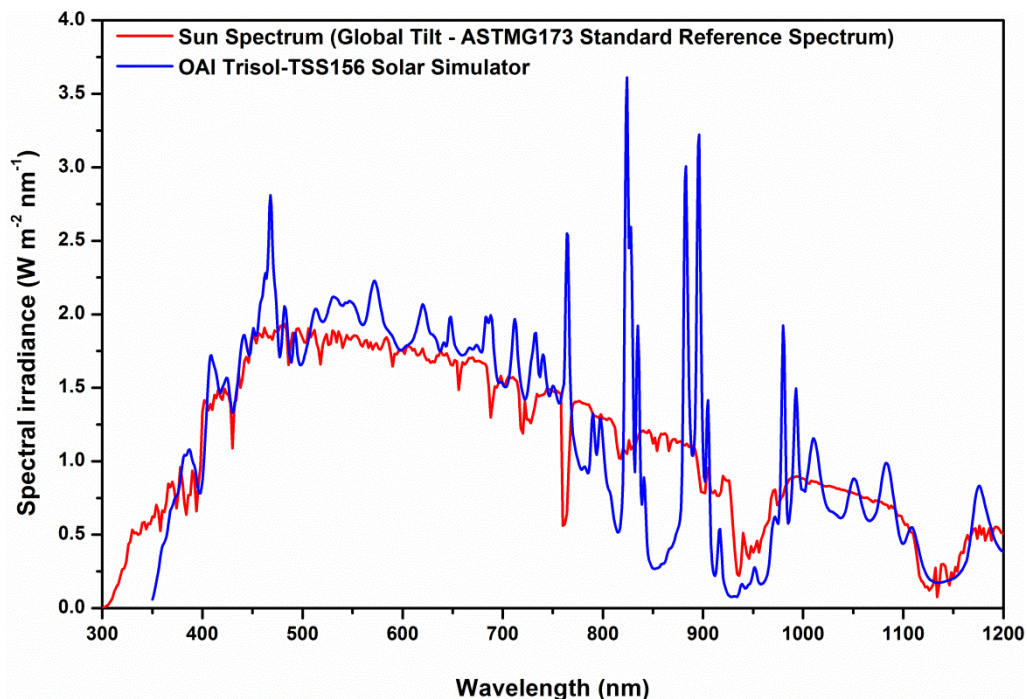


Figure 3.5. The irradiance spectrum of a Trisol TSS 156 Xe flash solar simulator. For comparison, the AM 1.5G spectrum is also plotted.

Table 3.3. Comparison of spectral irradiance distribution in percentage (%) between the OAI simulator and the global reference IEC 60904-9 [105].

Wavelength range (nm)	Percentage of total irradiance in the wavelength of 400-1000 nm (%)	IEC60904-9 (%) [89]
400 - 500	18.5	18.4
500 - 600	20.1	19.9
600 - 700	18.3	18.4
700 - 800	14.8	14.9
800 - 900	12.2	12.5
900 - 1100	16.1	15.9

Prior to the measurement, the solar simulator was calibrated by a flash power meter incorporated with a National Renewable Energy Laboratory (NREL) calibrated KG-filtered Si solar reference cell (20 mm × 20 mm), in order to simulate the one-sun illumination at light intensity of 1000 W/m². The illumination intensity was also confirmed by a standard pyranometer (CMP3, Kipp & Zonen, Netherlands) with

operating spectral range of 300 to 2800 nm. A photograph of the reference solar cell and pyranometer used for the calibration is shown in Figure 3.6.



Figure 3.6. Calibration of the solar simulator. Inset images show the clear version of the pyranometer (left) and reference solar cell (right) which was encased in a metal enclosure with a protective optical filter glass window.

The measurement of photocurrent follows the method which employs the source measure units (SMUs) to provide a precise sourcing of current and simultaneously recording the resulting current, and vice versa. In these particular experiments, the solar cells are connected to a Keithley source-meter, model 2601B, USA, with embedded TSP Express software. By sweeping the voltage across the solar cell's electrodes (typically in the range from -1 to 1 V), the current density-voltage (J - V) characteristics of the devices can be obtained for further analysis.

To ensure a minimum variation of irradiance over the illuminated area, and to facilitate such a situation when coating materials is applied on partial surface of the solar cells, a mask template was employed. During the electrical measurement, the uncoated and coated part of each solar cell was covered by an artificially designed plate that made of acrylic materials, with a circular hole (hole diameter = 33.00 ± 0.053 mm) to determine an illuminated surface area of about $\sim 8.553 \pm 0.027$ cm².

Experimental set-up of electrical testing is shown below in Figure 3.7 (left) where the solar cell is masked, with only an effective area exposed to light. The diameter of

the hole is obtained by measuring the distance of straight light with various orientations which pass through the radius centre of the circle (see right in Figure 3.7), using an electronic digital caliper (RS Pro, UK), and the measured dimension data are summarised in Table 3.4.

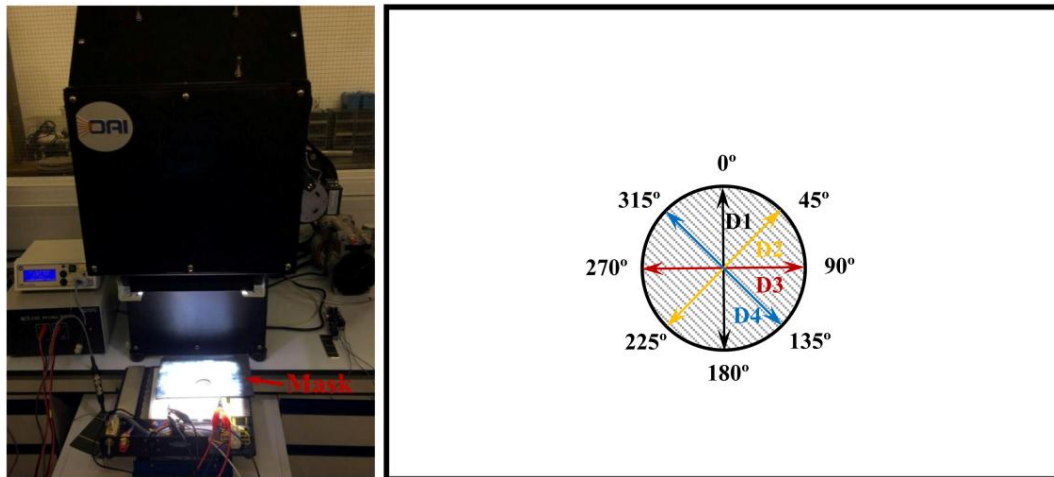


Figure 3.7. Photograph showing the experimental set-up of I-V measurements where the tested cell is masked by an artificially designed plate (left), and a sketch showing the clear version of the mask (right).

Table 3.4. Dimension data of the circular hole.

<i>Parameter</i>	<i>D1</i>	<i>D2</i>	<i>D3</i>	<i>D4</i>	<i>Average</i>	<i>Standard Deviation</i>	<i>Uncertainty</i>
Diameter (mm)	33.07	32.97	32.95	33.01	33.00	0.053	0.16%
Surface area (cm ²)	8.589	8.537	8.527	8.558	8.553	0.027	0.32%

Temperature measurements were carried out on the illuminated solar cells where a thermocouple is in contact with the back surface of the cell. The data was recorded and analysed by a thermocouple data logger with a USB port that connected to a computer. The operating principle of the thermocouple follows the thermoelectric effect, in which the temperature difference is occurred at the hot and cold junctions of two different types of metal wires that are joined together. As a result, a voltage is created at the junction ends, which is used to represent the temperature [106].

In this particular experiment, the type K thermocouple (SE001, Pico technology,

UK) is used, which is composed of the chromel/alumel alloys, with a tip diameter of 1.5 mm and temperature measuring range of -60 to 350 °C. The tolerance over this range is ± 1.5 °C, within that of the American Society for Testing Materials (ASTM) standards in which the limits of error for type K thermocouples is ± 2.2 °C [107]. The USB TC-08 data logger (Pico technology, UK) has 8 independent units of input channels which are compatible for different types of thermocouples. An integrated data acquisition system for temperature measurement in this study is illustrated below in Figure 3.8.

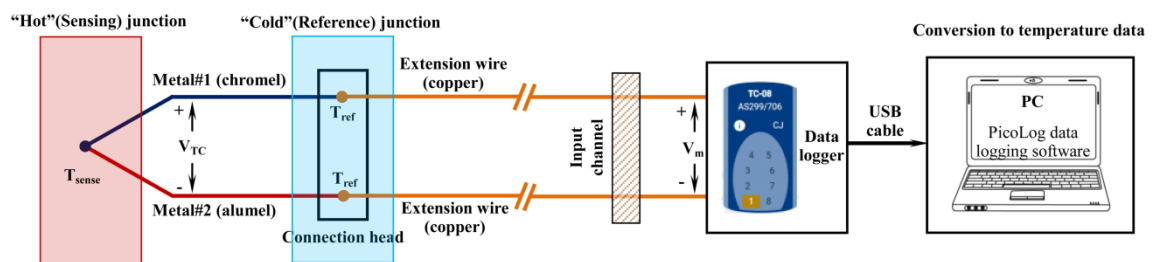


Figure 3.8. Flow diagram of the data acquisition system for temperature measurement.

To reduce the measuring error which caused by the errors from thermocouples and extension wires, as well as the data logging device, and thus to obtain accurate reading from above temperature acquisition system, the data logger was previously connected to an OMEGA model CL3512A temperature thermometer/calibrator (OMEGA Engineering, USA), as shown in Figure 3.9 where it provides precise simulations of voltage signals for different types of thermocouples (K/J/T/E) in terms of the standard ASTM specifications. Furthermore, the calibrator is cold-junction compensated for the varying ambient temperatures at junctions and the operating range is 0 °C to 50 °C, with an accuracy of $\pm 0.1\%$ [108].

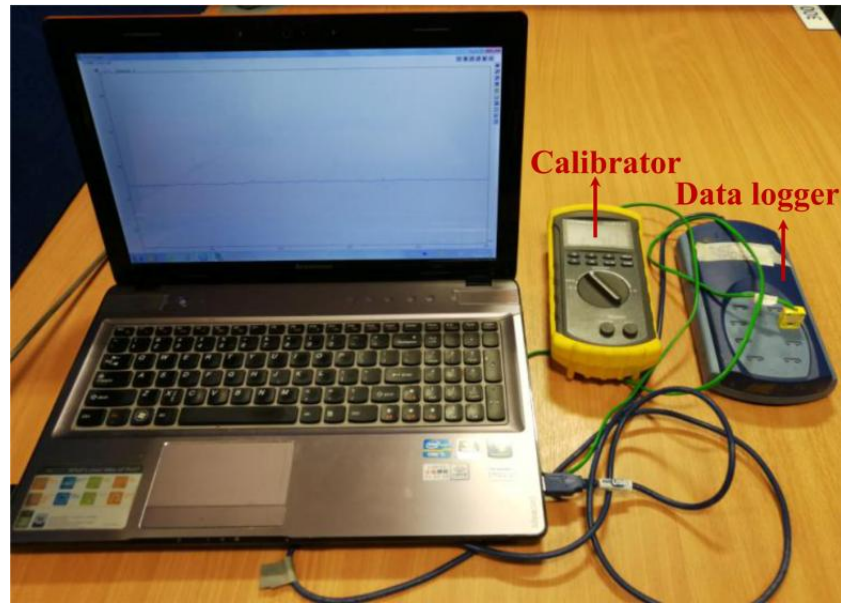


Figure 3.9. Calibration of thermocouples and data logging device.

Calibration of thermocouple was done by creating a 9-point calibration curve across the temperature range of 10 °C to 50 °C. This process includes cooling water down to 10 °C in a water bath. Next, one junction of the thermocouple is placed into the bath and then the voltage can be recorded once the reading on the calibrator is stable. The voltage is recorded again when water is heated to 15 °C. By repeating this process with five degree increments for each set of recordings until the temperature is reached to 50 °C, the voltage for the thermocouple at room temperature can be determined, and then the calibration curve can be obtained by using a curve-fitting method based on the recorded voltage values.

Figure 3.10 shows the calibration curves for the thermocouples in which each point is obtained by calculating the mean value from 5 readings of each set of recordings. In addition, the reciprocal slope of the curve which represents the voltage increase per degree of temperature increase is shown in inset. The detailed calibration data is summarised in Table 3.5.

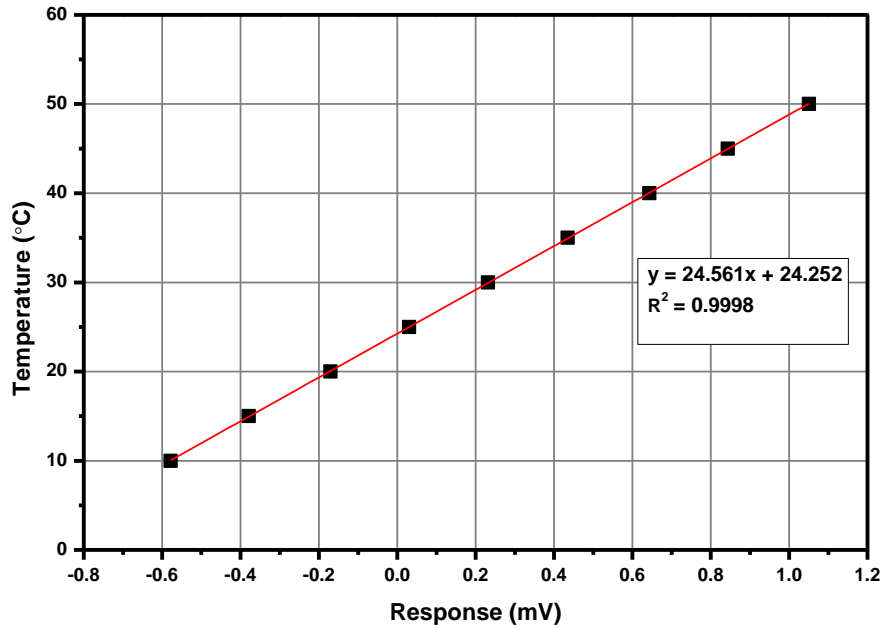


Figure 3.10. Calibration curve for the thermocouple.

Table 3.5. Calibration data for type K thermocouple used in this work.

<i>Ref</i> (°C)	<i>Res1</i> (mV)	<i>Res2</i> (mV)	<i>Res3</i> (mV)	<i>Res4</i> (mV)	<i>Res5</i> (mV)	<i>Average</i>	<i>Standard Deviation</i> (mV)	<i>Standard Deviation</i> (°C)	<i>Uncertainty</i>
10	-0.577	-0.579	-0.576	-0.580	-0.579	-0.578	0.00164	0.040	0.40%
15	-0.376	-0.380	-0.379	-0.381	-0.378	-0.379	0.00192	0.047	0.31%
20	-0.169	-0.170	-0.170	-0.171	-0.173	-0.171	0.00152	0.037	0.19%
25	0.030	0.028	0.031	0.032	0.030	0.030	0.00148	0.036	0.15%
30	0.230	0.233	0.231	0.234	0.230	0.232	0.00182	0.045	0.15%
35	0.436	0.434	0.433	0.435	0.436	0.435	0.00130	0.032	0.09%
40	0.643	0.645	0.644	0.642	0.643	0.643	0.00114	0.028	0.07%
45	0.843	0.846	0.841	0.842	0.845	0.843	0.00207	0.051	0.11%
50	1.048	1.050	1.051	1.049	1.055	1.051	0.00270	0.066	0.13%

The “Ref” represents the reference temperature recorded from the calibrator in degree Celsius (°C), the “Res” is the input voltage response from the pico-data logger in mV.

Since the solar cells were cut into three equal sizes prior to the layer coating process, it is possible that there might be little performance degradation. For this reason, all the devices were previously measured and compared on the same surface of both entire and laser cut cell, and the tested results show insignificant variation in electrical characteristics.

Figure 3.11 compares the J-V curves of as-used mono-Si solar cells before and after laser cutting, the corresponding electrical characteristics that were obtained are

summarised in Table 3.6 and 3.7 respectively. It can be seen that all the cut cells exhibited negligible changes in both J_{sc} and V_{oc} . Other parameters such as P_{max} , FF , and power conversion efficiency (PCE) also show marginal fluctuations compared to those of cells before cutting. Therefore, the cutting does not affect the energy performance of tested cells.

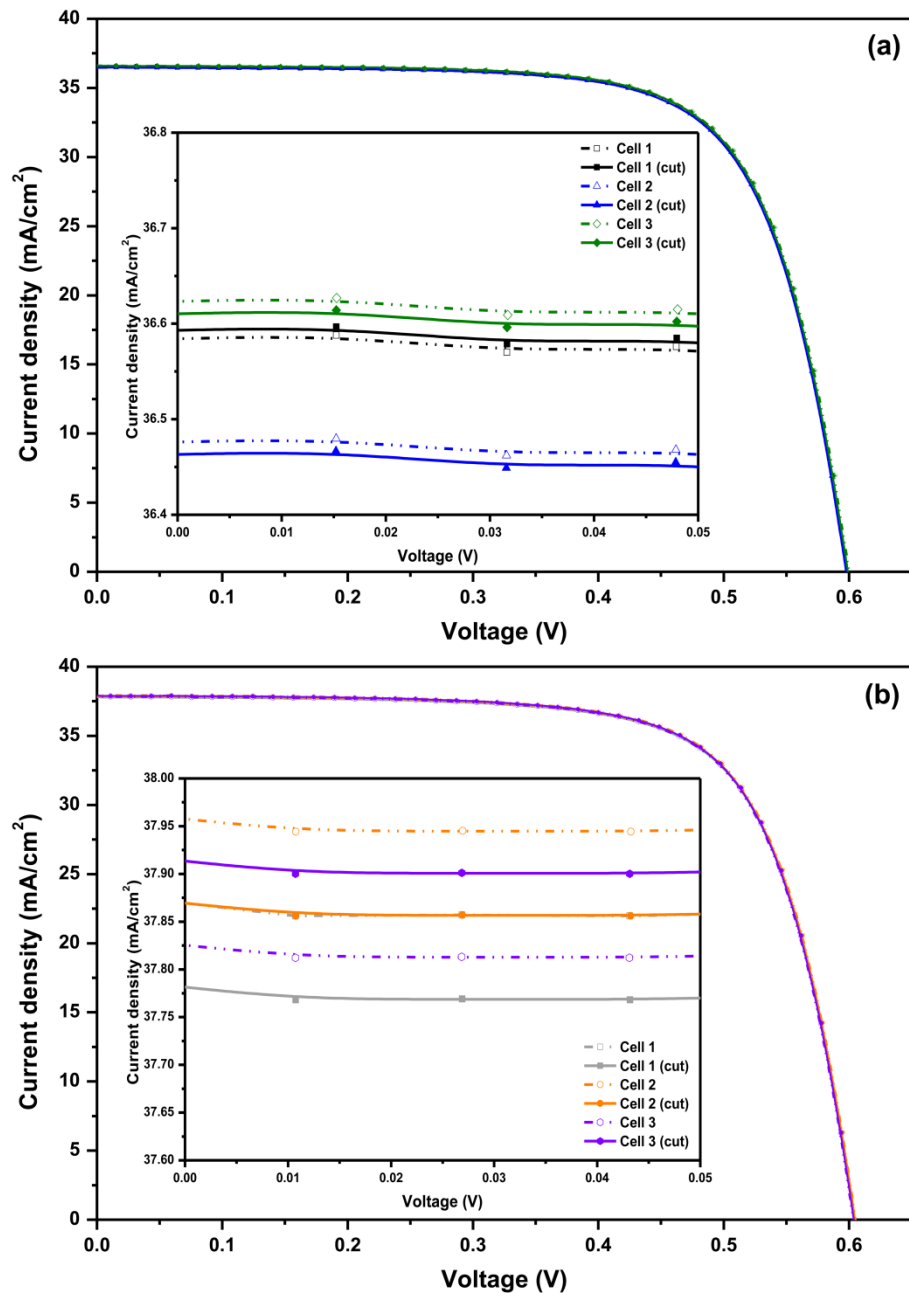


Figure 3.11. J-V characteristics of (a) XS156B3-200R and (b) T6S-3A mono-Si solar cells before and after laser cutting.

Table 3.6. J-V characteristics of XS1563-200R mono-Si solar cells before and after laser cutting.

<i>Cell Type:</i> XS156B3-200R	J_{sc} (mA/cm ²)	V_{oc} (mV)	P_{max} (W)	FF (%)	PCE (%)
Cell NO.1	36.59	599.1	0.1348	71.91	15.76
Cell NO.1 (cut)	36.59	599.1	0.1349	71.93	15.77
Cell NO.2	36.50	597.6	0.1342	71.90	15.70
Cell NO.2 (cut)	36.47	598.0	0.1341	71.90	15.68
Cell NO.3	36.63	600.3	0.1352	71.92	15.81
Cell NO.3 (cut)	36.61	599.0	0.1349	71.85	15.78

Table 3.7. J-V characteristics of T6S-3A mono-Si solar cells before and after laser cutting.

<i>Cell Type:</i> T6S-3A	J_{sc} (mA/cm ²)	V_{oc} (mV)	P_{max} (W)	FF (%)	PCE (%)
Cell NO.1	37.85	604.6	0.1405	71.81	16.43
Cell NO.1 (cut)	37.78	604.7	0.1403	71.80	16.41
Cell NO.2	37.94	605.4	0.1412	71.88	16.52
Cell NO.2 (cut)	37.87	604.9	0.1408	71.90	16.47
Cell NO.3	37.82	603.5	0.1402	71.81	16.40
Cell NO.3 (cut)	37.91	603.8	0.1407	71.89	16.46

In addition to the photovoltaic I-V measurement, the photon-electron generation performance of mono-Si solar cells before and after coating was also evaluated through the characterisation of external quantum efficiency (EQE) response.

EQE measurements were carried out by using a monochromator-based solar cell response system (Bentham PVE 300, UK) incorporated with BenWin+ control software, as shown in Figure 3.12. The light source of the monochromatic probe consists of a 75 W xenon lamp and a 100 W quartz halogen lamp, which covers a broad spectral range of 300 to 1100 nm.

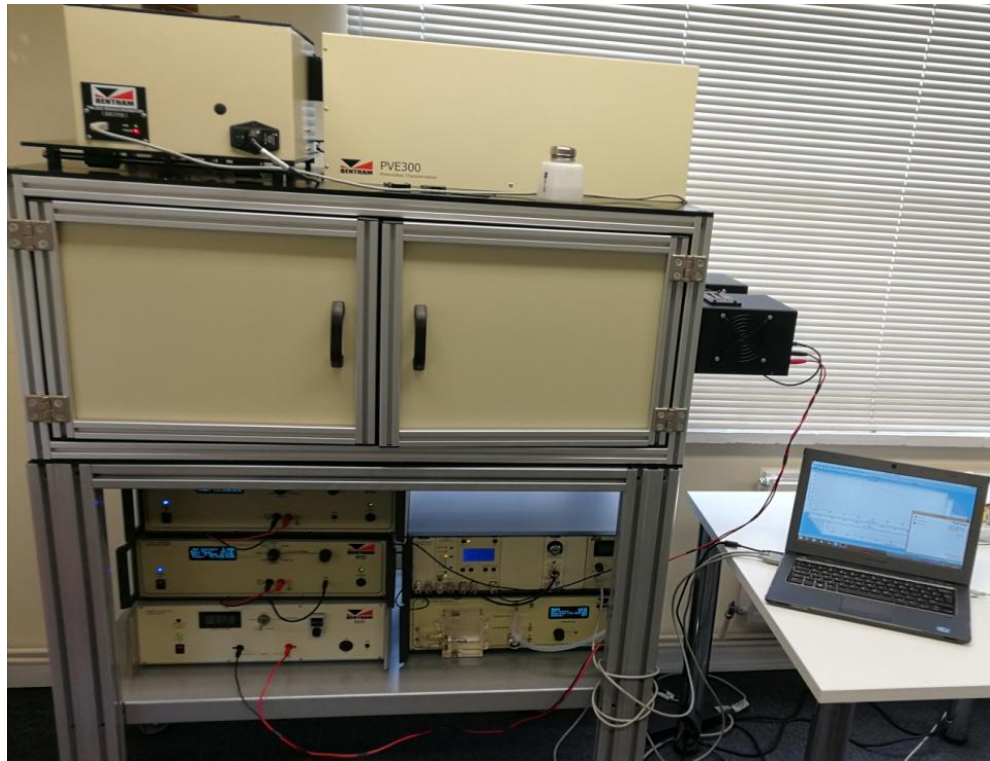


Figure 3.12. Bentham PVE 300 monochromator-based solar cell response system.

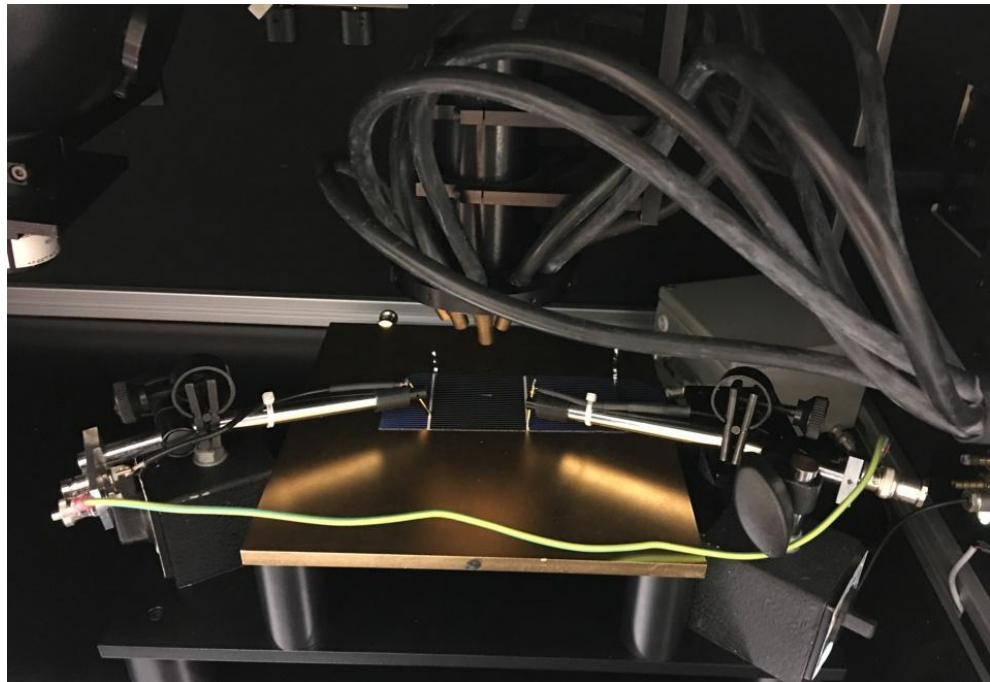


Figure 3.13. Experimental set-up of the EQE measurement.

Figure 3.13 shows the experimental set up where a cut cell is placed on a 200 mm × 200 mm vacuum mount which allows controlling the temperature in the range of 15 to 65 °C. The measurement is performed by shining a monochromatic probe beam onto the solar cell's effective surface and registering the photocurrent generated as a function of wavelength. The external quantum efficiency, η , can therefore be determined directly from the following equation [109]:

$$\eta = 100 \frac{I \times E_v}{P \times e} \quad (3.1)$$

where P is the power in the beam, I is the generated current, E_v and e represent the photon energy and the charge of the electron respectively. The probe is characterised by using a silicon detector with known responsivity (A/W) to determine the beam power. The system has been previously calibrated with the National Metrology Institutes (NMIs) traceable calibrated photodiodes [110].

3.4 Materials Fabrication Machines

In this section, the equipments used for the preparation of titanium dioxide (TiO₂)-based nanoaerogel materials are briefly introduced. These equipments include a high-pressure compact stirred reactor that allows for the fabrication of nanomaterials with high specific surface area and porous structures and a chamber box furnace that used for corresponding thermal annealing process.

3.4.1 High Pressure Compact Laboratory (HPCL) Reactor

Fabrication of nanostructured TiO₂-based aerogels materials was conducted using a Parr series 5500 autoclave high-pressure compact stirred reactor system (Parr Instrument Company, USA) in a laboratory fume hood. Figure 3.14 shows the exterior and interior of the reactor where the corresponding components are highlighted.

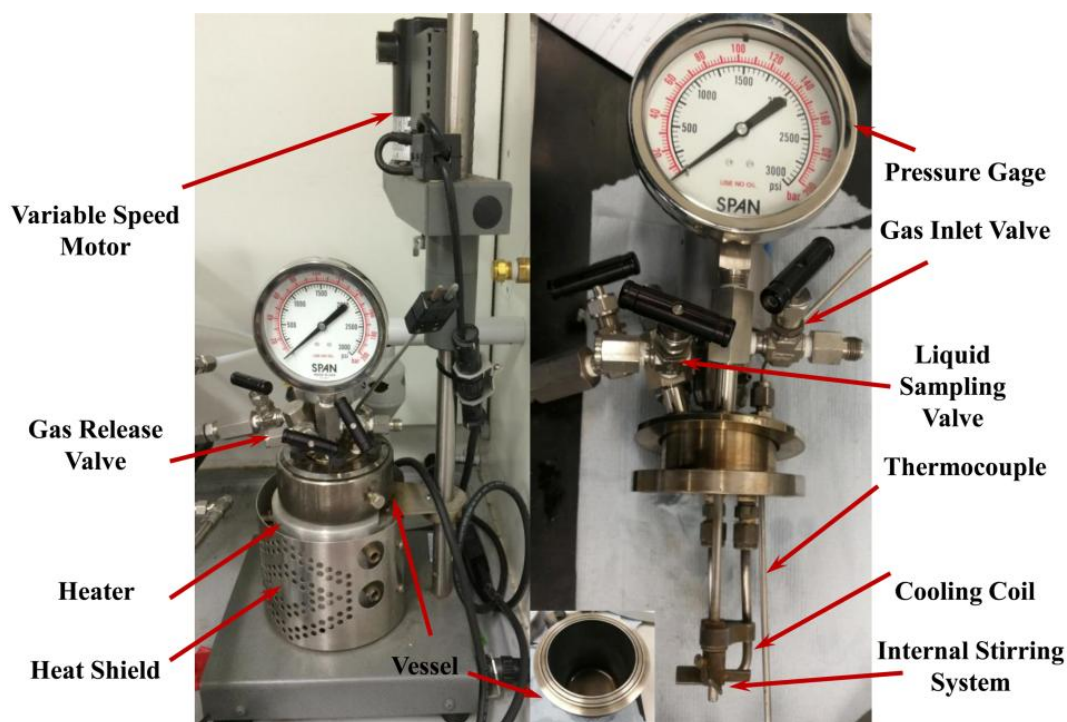


Figure 3.14. Digital graph of the high-pressure compact stirred reactor.

The reactor is made from the standard type 316 stainless steel, with a vessel volume of 300 ml. The heating unit consists of an aluminum heater that is connected with a Parr model 4836 temperature/stirring controller (Parr Instrument, USA), and a thermocouple encased in a metal sheath extends directly into the vessel. At the neck of the reactor, inlet and outlet valves are interconnected for charging gas into the vessel and releasing gas from the reactor severally, where behind the valves, a variable speed motor drive is magnetically coupled to an internal stirrer shaft with attached impeller which forms an internal stirring system. The stirring speeds can be adjusted in the range of 0 to 1400 rpm through the controller while the maximum allowable working pressures and temperatures, adhered to the American Society of Mechanical Engineers (ASME) design criteria, are restricted to 3000 psi (206.8 bar) and 225 °C respectively [111].

3.4.2 Chamber Box Furnaces

Thermal annealing and curing for resultant materials is performed by using a Linderberg/Blue M Moldatherm chamber box furnace (Thermo Fisher Scientific, USA), with a heating temperature range of 100 °C to 1100 °C. The furnace employs unique

insulation and heating element composites for minimising the temperature interference from the outer surface and thus maintaining uniform heat distribution within the chamber. Moreover, a PID (proportional-integral-derivative) control system is applied, which is capable of offering controlled heating-up rate so as to prevent the temperature overshoot, and thus to avoid thermal shock to the reactants. In addition, the air vent and inlet situated at the top and rear of the chamber could provide an insert-atmosphere exchange for particular annealing process. The experimental configuration in respect to the materials fabrication is shown in below Figure 3.15.



Figure 3.15. Photograph showing the experimental set-up for materials fabrication where the furnace (at left) and reactor system (at right) are placed inside the laboratory fume hood.

3.5 Instruments for optical characterisation

After the anti-reflection coatings (ARCs) and luminescent phosphor layers were grown on the solar cells' surface and then their properties were evaluated with different methods to characterise their optical behavior and functionality. This section introduces the equipments used for optical and ellipsometry measurements where the reflectance and absorption of mono-Si solar cells before and after coating, the transmittance, as well as the refractive index of the deposited films can be obtained for further analysis.

3.5.1 Ultra Violet (UV/Vis) spectrophotometer

An optical spectrophotometer is mostly used for indentifying the substances in solution and producing spectral line through the measurement of light intensity over a particular portion of the electromagnetic spectrum. Generally, a spectrophotometer system comprises of four basic components, a light source, a monochromator, a detector and a data acquisition unit which is controlled by a terminal computer through proceeding specific software. To obtain the complete spectra in the UV/Vis range (190 nm to 780 nm), double beam instruments are usually employed.

In this study, the reflectance, transmission, and absorption spectra with regard to various types of substrates such as solar cells, quartz and glass slides that are with or without coating, are recorded by using a Lambda 650S UV/Vis spectrophotometer (Perkin Elmer, USA), which is shown in Figure 3.16. The spectrometer is equipped with a dual-beam system which allows a synchronous measurement of both reference and sample beams. Additionally, double holographic grating monochromators were assembled with spectral slit width down to 0.17 nm, which could ensure a high optical density for measured samples. The light sources for the spectrometer include a tungsten halogen bulb which could cover the spectral range of 330 to 900 nm, and a deuterium bulb for the UV region from 190 to 350 nm [112].

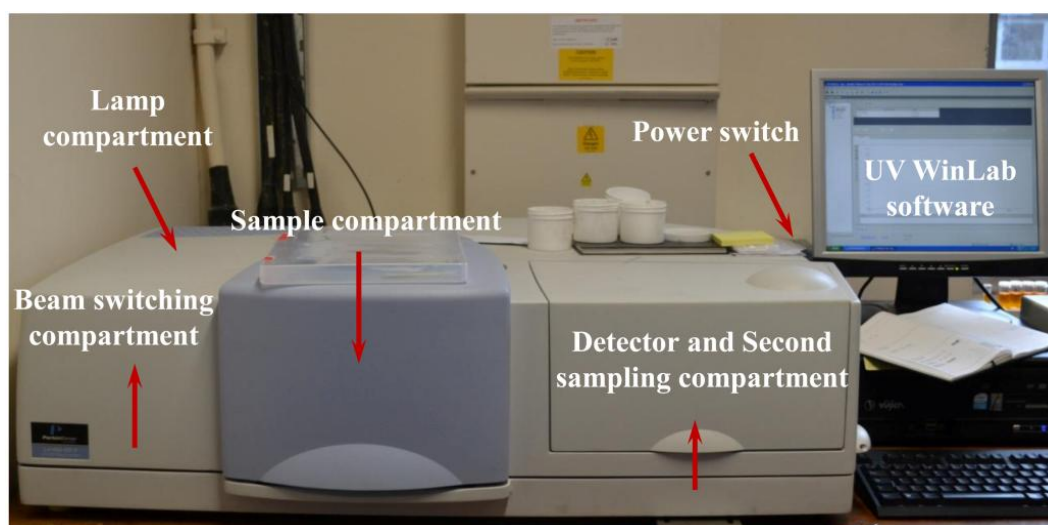


Figure 3.16. Photograph of PerkinElmer Lambda 650S UV/Vis Spectrophotometer system.

Figure 3.17 shows the optical arrangements in the dual-beam spectrophotometer system. In a particular measuring process, a source of incoming light passes through the slit and is firstly split into single wavelength by the etched diffraction grating. Next, the light beam is divided into two paths by the half-mirrors. The path of partial selected beam is directed to the measured sample while the rest part travels through the reference object, and both reference and sample would be affected equally. Then, the intensity of two transmitted beams of light is recorded and measured by a high-sensitivity UV/Vis photomultiplier tube (R955, Hamamatsu, Japan). Data interpretation is performed by using PerkinElmer's UV WinLab software which is controlled by a terminal PC computer. It is noteworthy that the obtained optical information is a relative value by dividing the light intensity to that of reference reflectance or transmittance spectra, and thus is presented in ratio while the absorbance is the difference in light intensity between the two transmitted light beams gathered previously.

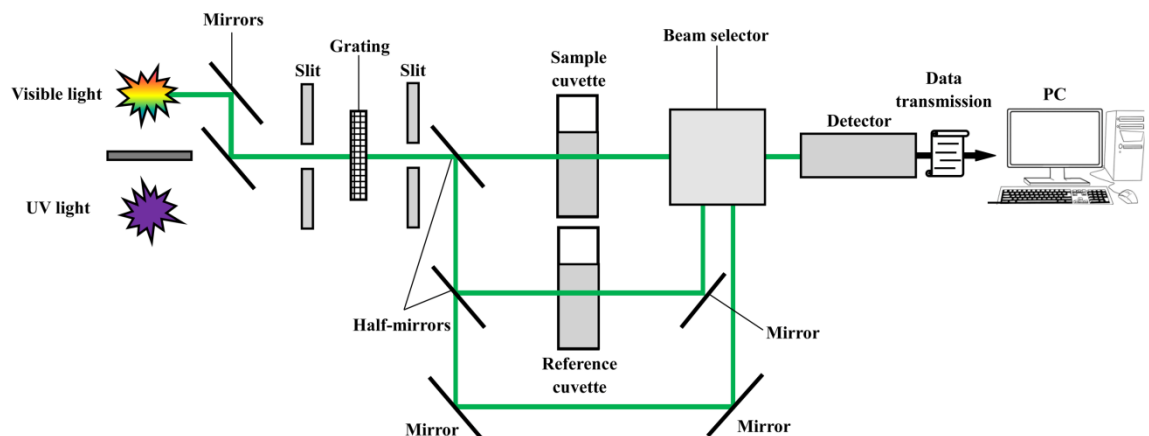


Figure 3.17. Optical layout of the dual-beam UV/Vis spectrophotometer. The optical path is highlighted in green lines [113].

Above technique follows the law of energy conversion and the energy balance for the incident light can be expressed as [114]:

$$I_0 = I_A + I_T + I_R + I_S \text{ or } 1 = I_A (\%) + I_T (\%) + I_R (\%) + I_S (\%) \quad (3.2)$$

This is because that the incident light with intensity of (I_0) may be partially reflected at the optical interfaces (I_R) of the measured specimen, or may be scattered into different directions (I_S) when it is incident on the heterogeneous media, and absorbed (I_A) in the

specimen, finally, the remaining part will transmit (I_T) through the sample.

3.5.2 Ellipsometry Measurements

Ellipsometry is an optical technique for the investigation of most thin films dielectric and optical characteristics based on the variations of polarization on reflection of incident light at a particular surface. The refractive index, n , and extinction coefficient, k , can be calculated from the measurement of the ellipsometric angles “ Ψ ” and “ Δ ”, where “ Ψ ” represents the relative variation of amplitude and “ Δ ” is the phase shift between the p- and s-directions of the complex Fresnel reflection coefficients, at a given wavelength and incident angle of beam [115].

In this work, the ellipsometry measurements were used to find out the refractive index “ n ” and the thickness “ d ” of the deposited thin films as these parameters affect directly the reflectance losses at the air/polymer interfaces, which in our case is crucial for optimising the optical path, and thus improving the light harvesting for the silicon solar cells. The instrument used is presented in Figure 3.18. Ellipsometry measurements were carried out by using a Rudolph Auto EL III null-seeking monochromatic ellipsometer (Rudolph Research, USA) equipped with a Helium-Neon red laser operating at wavelength of 632.8 nm and incident beam angle of $70^\circ \pm 0.02^\circ$ [116].

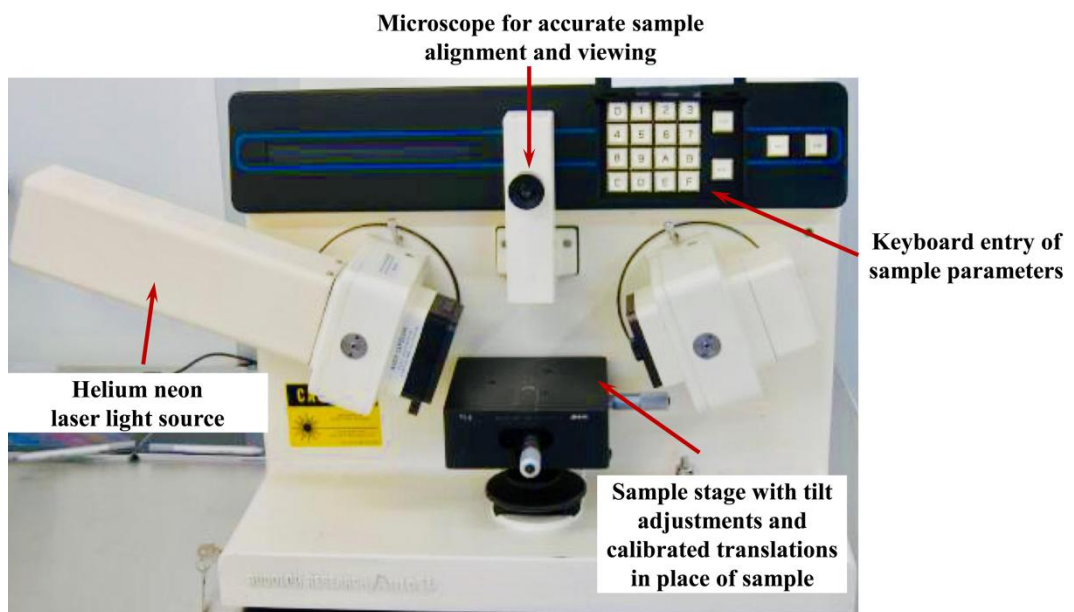


Figure 3.18. The Rudolph Auto EL III for ellipsometry measurements.

Figure 3.19 shows the configuration of the monochromatic ellipsometer. A null ellipsometer follows the principle, that it induces polarized light on a sample surface by rotating its polarizer, and then finds the intensity minimum by rotating the analyzer. After this, the azimuthal angles, the angle of incidence θ , as well as the ellipsometric parameters such as Δ and Ψ , can be obtained for the derivation of the wanted n and d . For a single film that placed on the substrate (substrate-film-ambient system), the film thickness d can be expressed by the Maxwell equation [115]:

$$d = \frac{\lambda}{2\sqrt{n_1^2 - (n_a \sin\theta)^2}} \quad (3.3)$$

where n_a and n_1 represent the refractive index of transparent ambient and thin film respectively, θ denotes the angle of incidence, λ is the wavelength of incidence wave. It is worth nothing that the deposited film thickness is determined by a periodic function of the real angle θ and thus it may be the given value plus the product of the periodic term [115].

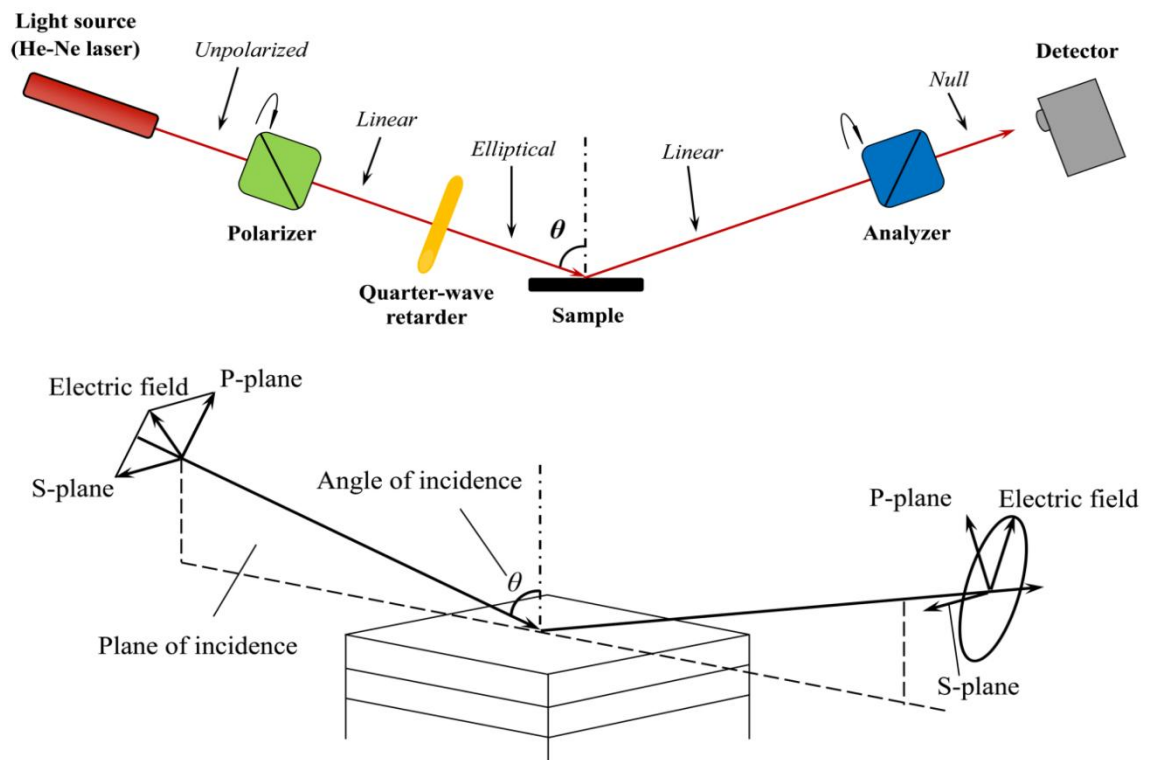


Figure 3.19. The configuration of the as-used null ellipsometer (top), and a schematic diagram showing its operating principle (bottom). The figure is reproduced from [115].

To perform the measurement, the substrate should be reflective at wavelength of 632.8 nm so that light beam would reflect back and induce the polarization ellipse in the electrical field. The substrates used were silicon wafers (Agar Scientific, UK) with an orientation of $\langle 101 \rangle$ and diameter of 3 inches (76.2 mm). These wafers were boron-doped (p-type) with resistivity in the range of 1 to 30 $\Omega\cdot\text{cm}$. They are 407.5 ± 25 μm in thickness with single-side polished and without a silicon oxide top coating. A photograph of the silicon wafer is shown in Figure 3.20. The deposited films were presumed isotropic and homogeneous for the ellipsometry measurement.



Figure 3.20. The p-type silicon wafer used for the ellipsometry measurement.

3.6 Materials characterisation instruments

In this section, the instruments and methods that used to characterise the as-prepared powder samples in regarding to the TiO_2 -based nanoaergels and the terbium-doped gadolinium oxysulfide phosphor material are introduced in detail, which cover scanning electron microscopy, transmission electron microscopy, X-ray powder diffraction, photoluminescence spectroscopy, and the technique of nitrogen (N_2) gas physisorption.

3.6.1 Scanning Electron Microscope

In characterising the morphologies of the powder samples and observing the

surface coverage and microstructures of the coated solar cells, an ultra high performance field emission scanning electron microscope (FE-SEM), model SUPRA 35VP, ZEISS, Germany was used, which is shown in Figure 3.21. Comparing with a regular SEM, the tungsten filament for a FE-SEM that used to create the beam is more of a sharp in shape and an electric field is set to drive the electrons to the tip's head, where they exit the tip through tunneling effect rather than a simple thermal process. Thus, in a FE-SEM, the electron beam is more powerful and it gives higher resolution and better quality of images [117].

In ZEISS SUPRA 35VP, the microscope offers high-vacuum and variable pressure operating capability. The built-in Gemini optical column in combination with a variable pressure operating system make it available for high resolution imaging and analysis of samples at both low and high beam current conditions without losing their natural state. The magnification range allows a large field of view at the lowest magnification of $\times 15$, whilst at higher magnifications, over $\times 200k$ for those specimens with nano-scale microstructures. In addition, the FE-SEM system is also incorporated with an integrated energy dispersive analysis X-ray spectroscopy (EDS) detector for analysing elemental composition and measuring coating quality.



Figure 3.21. ZEISS SUPRA 35VP field emission scanning electron microscope.

Powder samples for SEM analysis were prepared with special handling for sample mounting where the detailed procedure is described as follows: A piece of double-sided sticky carbon conductive tape was cut and stuck to the pin mount specimen holder where the other side of the tape was gently pressed down by using a SEM mount tweezer to flatten the tape surface. Next, a small amount of powder was dispersed in isopropyl alcohol (IPA) by gentle ultra-sonication. After removing the backing paper, spread a few drops of suspension on the surface of carbon tape using a transfer pipette and wait until it was dried for around 15 mins to give a cleaned and thin powder layer.

Preparation of solar cell samples for cross-section imaging is performed by cutting the coated silicon solar cell into small pieces (5 mm × 5 mm) using a low-speed saw with diamond wafering blade. The cut sample was then plasma cleaned for 5 mins using a Gatan Solarus plasma cleaner (Model 950, Gatan, UK), and then loaded into a SEM cross-section holder.

Before being placed in the vacuum chamber, the samples were coated with gold using a Polaron sputter coater, model SC7460, UK, as shown in Figure 3.22, so as to create electrical conduction for better observation in SEM as well as to reduce the charging effect on the obtained SEM images. The coater is equipped with a peltier cooler which could minimise thermal damage onto the sample surface. The coating procedure is described as follow:

- Ensure the leak valve is closed before placing the samples in the vacuum chamber, switch the argon gas regulator on and set the pressure at around 5-10 psi (0.7 bar).
- Shut the chamber lid and press the MANUAL button. Set the coating time and voltage to 30 seconds and 1.5 kV respectively before pressing the START SEQUENCE button to start the pump.
- Wait until the chamber pressure fall to around 1×10^{-2} mbar and then operate the timer START button to start the coating in which the plasma is discharged and it will strike and deposite gold target material on the sample stage through

the sputtering process.

- The coating process is completed when the END indicator lights up. Stop the vacuum pump by pressing and holding the VENT/STOP button, and the chamber will be vented to process argon gas.
- Wait until the chamber is depressurised and then remove the coated samples. Shut the chamber lid and turn off the argon gas.

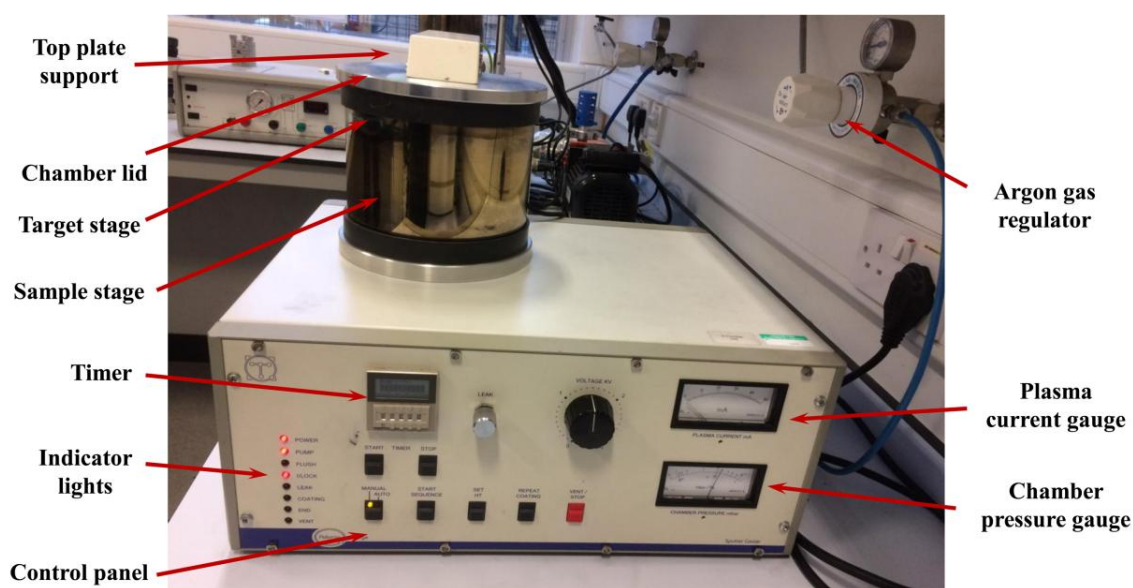


Figure 3.22. Photograph of the Polarab sputter coater.

3.6.2 Transmission Electron Microscope

The structural features and cathodoluminescence properties of the synthesised powder samples were examined using a JEOL model JEM-2100 field emission gun transmission electron microscope (TEM) (as shown in Figure 3.23) equipped with a Gatan Vulcan™ cathodoluminescence (CL) detector for imaging and spectroscopic purpose. This instrument used lanthanum hexaboride (LaB₆) filament as the electron gun and a Schmidt-Czeny-Turner imaging spectrometer with back illuminated couple-charged device (CCD) camera (SC600, Gatan, USA) for collection of CL emission spectra. The microscope is operated in scanning mode with a spot size of 1.5 nm. TEM images and analyses were acquired using its built-in Gatan Microscopy Suite Version 3 (GM3) software.

Preparation of TEM samples is described as follows: A tiny amount of powders were suspended in ethanol and gently ultra-sonicated to provide a single particulate dispersion. A droplet of the sample suspension was drop-cast onto carbon holey film support on copper 200-mesh grids (TAAB, UK). Excess fluid was wicked away using a small piece of filter paper, after which the samples were left to air dry in a laboratory fume hood. Once dried, the samples were plasma cleaned using a Gatan Solarus plasma cleaner (Model 950, Gatan, UK), and then loaded into a Vulcan-CL TEM holder.

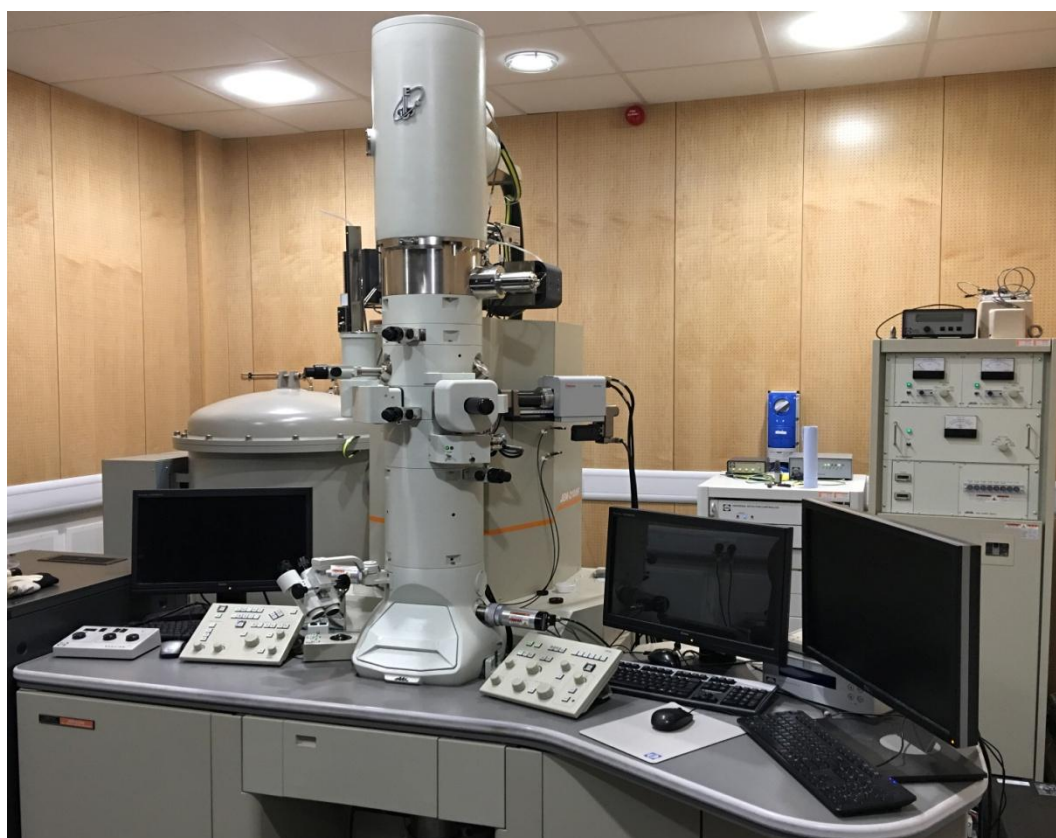


Figure 3.23. JEOL JEM-2000F scanning transmission electron microscope.

3.6.3 X-Ray Powder Diffraction

X-ray powder diffraction (XRPD) is used to identify the crystalline phases of the synthesised powder samples. In this study, the diffraction patterns of the TiO₂-based nanomaterials and phosphor materials were performed using a Bruker D8 Advance X-ray powder diffractometer, as shown in Figure 3.24, fitted with a copper source and LynxEye™ silicon strip detector. The diffractometer was previously calibrated using

an aluminium oxide line position standard from Bruker and LaB₆ National Institute of Standards and Technology Standard Reference Material (NIST SRM) 660a line profile standard. The emission of the nickel filtered copper source ($\text{CuK}\alpha = 0.154 \text{ nm}$) and therefore the instrumental line broadening was determined by fitting the NIST standard using the Bruker's Total Pattern Analysis Solution (TOPAS) version III rietveld refinement software. The estimated crystallite sizes, lattice parameters, and inter-planar spacing of the synthesised samples were calculated using the TOPAS 5 software package of Bruker.

Preparation of all the powder samples were carried out by filling and pressing the powder from the middle of the XRD sample holder until a flat surface is formed where the surface level is flush with the upper edge of the holder groove, which can be seen from the inserted images of Figure 3.24. All of samples were scanned over the Bragg angle (2θ) range from 10° to 100° for 35 minutes in step scan mode.

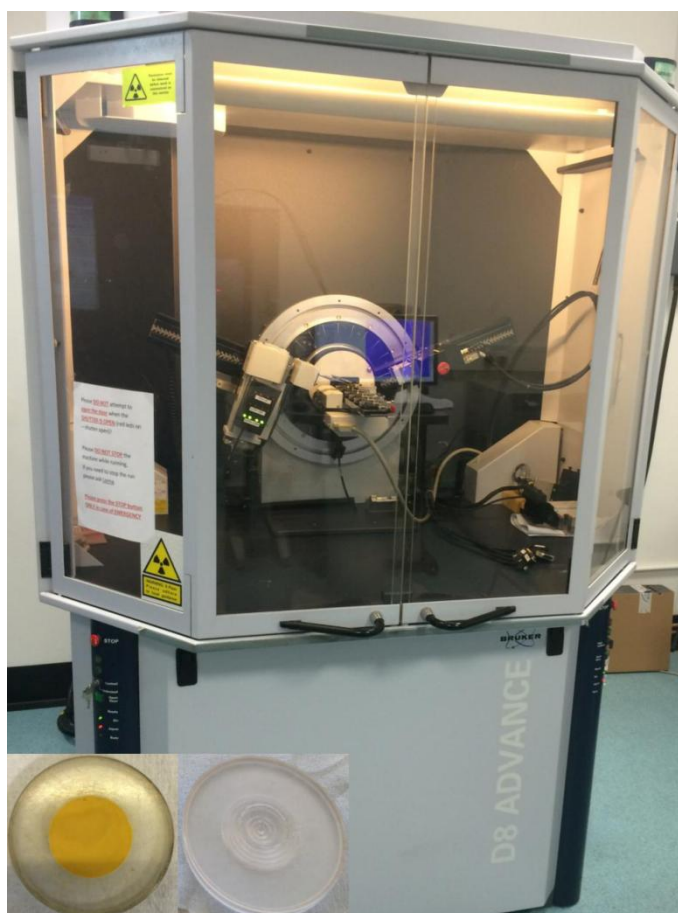


Figure 3.24. Bruker D8 Advance X-ray powder diffractometer. Inset photographs show the standard XRD sample holder with and without powder sample.

3.6.4 Photoluminescence spectroscopy

In present work, the photoluminescence (PL) spectroscopy is used to investigate the luminescence properties of the rare earth doped phosphor materials where the PL and photoluminescence excitation (PLE) spectra can be obtained for further analysis.

The measurements were carried out by using a Bentham Instruments dual-monochromator system (Bentham M300, UK) incorporated with BenWin+ software (see Figure 3.25). Emission spectra were recorded from 300 nm to 800 nm with step size of 1 nm using 254 nm UV light as exciting source, while the excitation spectra were recorded by monitoring the corresponding dominant emission peak.

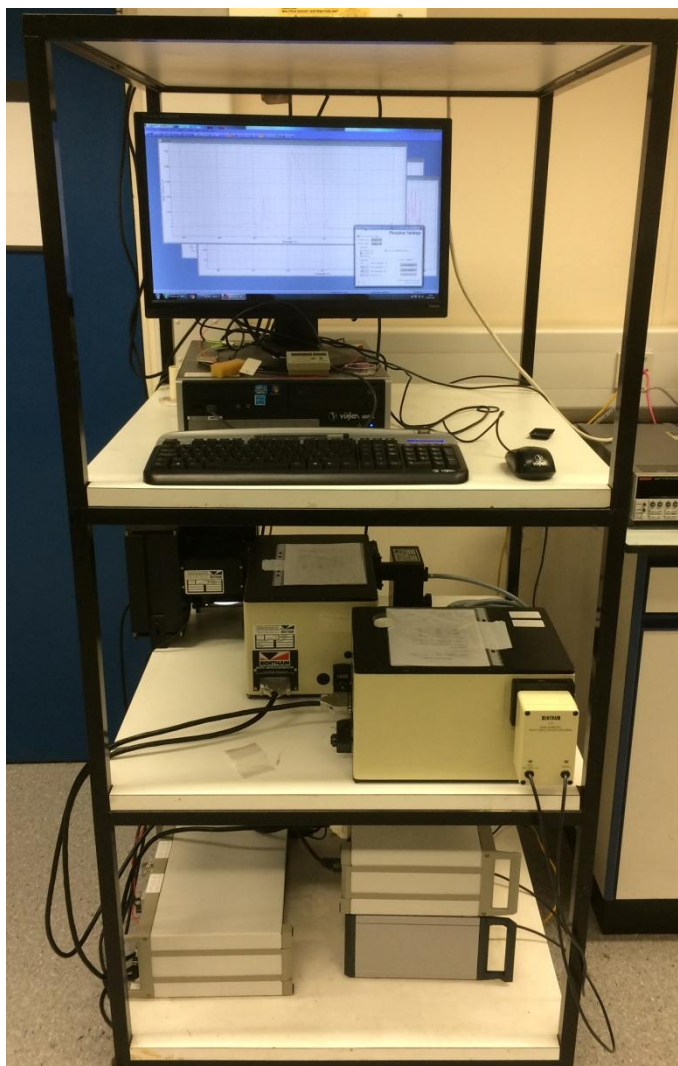


Figure 3.25. Bentham M300 monochromator detector system.

3.6.5 Nitrogen (N₂) gas physisorption

Physisorption can be described as the physical bonding of gas molecule to the surface of adsorbents that is driven by the Van der Waals forces in which an adsorbable gas (also referred to as “the adsorptive”) is brought in contact with the surface of a solid or liquid at low temperature conditions. It is widely used for the surface and textural characterisation of nanoporous materials.

In this work, the specific surface area and pore diameter of synthesised TiO₂-based aerogel nanomaterials were measured from the adsorption isotherm of nitrogen (N₂) gas physisorption by using a Novatouch model LX (Quantachrome Instrument, USA) surface area and pore size analyser (see Figure 3.26) incorporated with TouchWin™ software for data acquisition and reporting. Additionally, the sample cell employs filler rods with coolant level sensor which can minimise the cold zone volume by pushing liquid nitrogen up to warm zone where the coolant will evaporate soon, thus increasing the data accuracy. This nanometric instrument provides also low surface area capabilities with a lower limit of 0.01-m²/g, and a broad pore size measuring range of 0.35 to 500 nm [118].

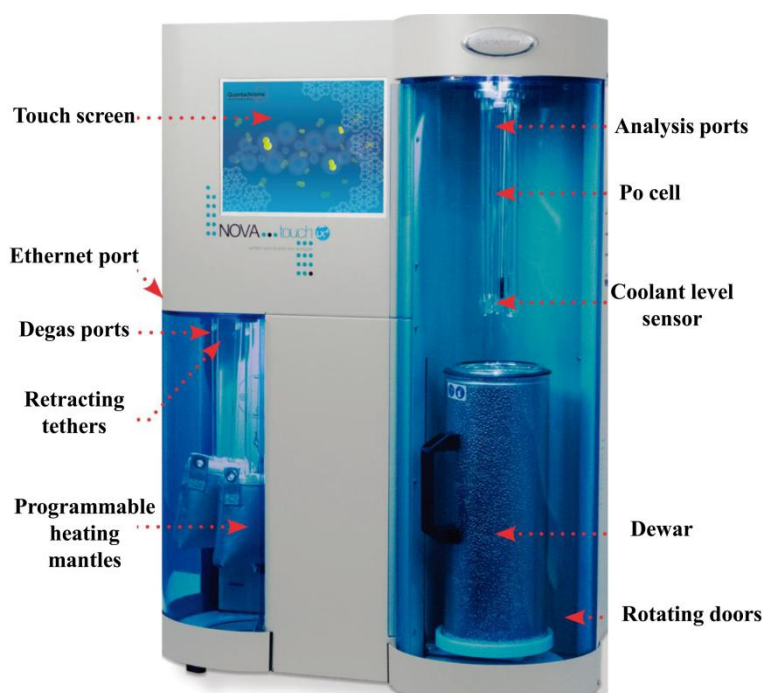


Figure 3.26. NOVA touch surface area and pore size analyser [118].

For N₂ physisorption measurements, the samples were firstly degassed at 80 °C under vacuum for 8 hours and a further 4 hours at 100 °C under vacuum immediately prior to analysis. The internal volume of the measurement zone (also referred to as the “free space”) was measured at the start of analysis with helium gas (99.9995% purity) and equilibration time was 5 seconds throughout. N₂ adsorption and desorption isotherm were analysed at 77.4K (-196.5 °C) such that a nominal 40 adsorption data points and 25 desorption data points were collected.

The BET surface area was obtained by using the Brunaur-Emmett-Teller equation to a relative pressure (P/P₀) range of 0.1 to 0.3 of the adsorption isotherm such that BET dimensionless constant (C) values were positive and the correlation coefficient exceeded 0.999. The pore diameter is determined from the adsorption branch of isotherm by applying a density functional theory (DFT) model. The pore volume was assessed by the amount of N₂ adsorbed at the highest relative pressure (P/P₀) of ~ 0.95.

3.7 Differential Scanning Calorimetry

Differential Scanning Calorimetry (DSC) is a thermo-analysis technique which aims at studying the variations or changing regularity of the difference in the heat flow rates of the sample in comparison to a reference sample as a function of temperature under linear heating or cooling conditions. By measuring the amount of heat that adsorbed or released during such thermodynamic transition process, both physical changes and chemical reaction within the sample can be investigated [119].

DSC measurement in this work was used in characterising the curing process of EVA that served as the binder and matrix material for the integration of composited layer onto the solar cells surface. The aim is to determine the curing temperature that enhances the optical properties and thermal stability of the EVA polymeric material that contributes to improving the energy performance of the photovoltaic cells. Similar attempt has been made by employing conventional Soxhlet extraction method with the use of organic solvent. However, this technique is considered to be fairly laborious and time-consuming, which is not suitable for a fast production process [120].

The type of instrument used in the measurements is a commercial single-furnace differential scanning calorimeter (PerkinElmer DSC 6000, USA) with a temperature operating range of -180 to 450 °C that is controlled by its Pyris™ software (as shown in Figure 3.27). The instrument is equipped with a built-in cooling accessory IntraCooler II refrigerator. Nitrogen (BOC, UK, 99.998% purity) was used as purge gas at a flow rate of 20-ml/min.

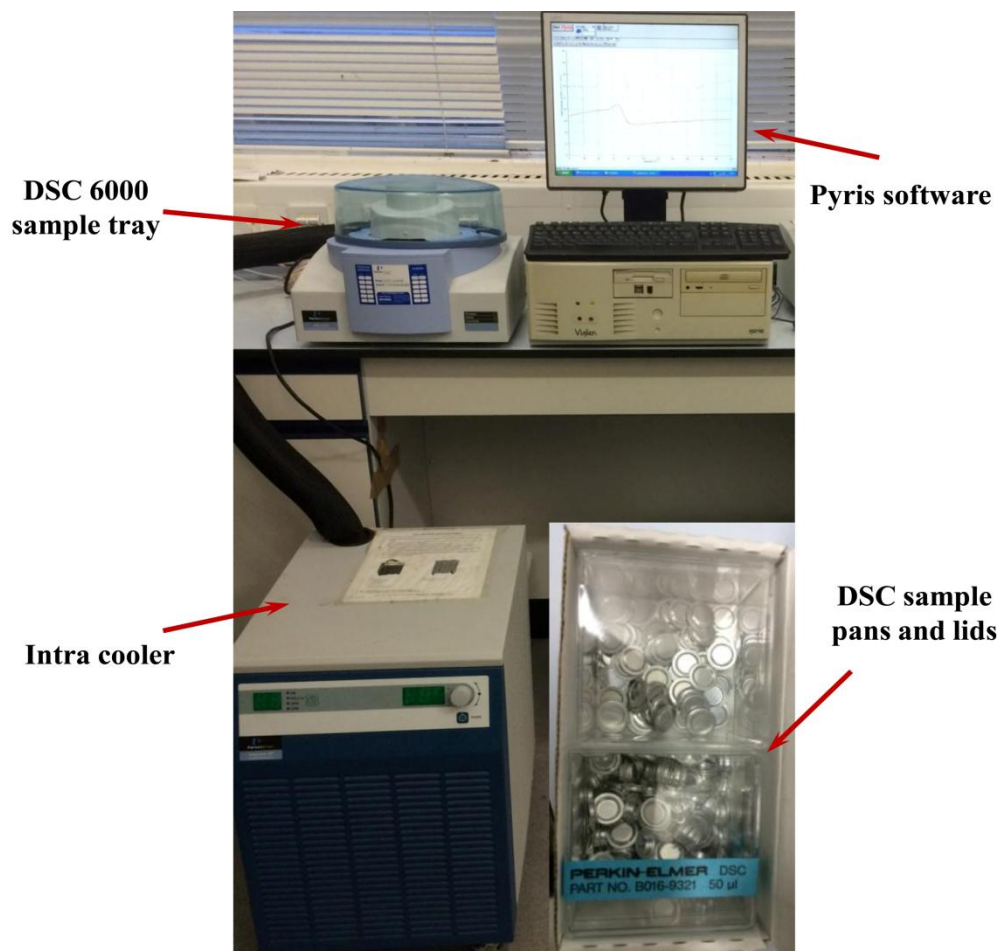


Figure 3.27. Differential scanning calorimetry system. Inset image shows the standard aluminum sample pans and covers used for enclosing the EVA sample.

Prior to the measurement, Ethylene Vinyl Acetate (EVA) sheet supplied from (Dupont, USA) with a thickness of ~45 μm , was cut into small shreds and weighted in around 12 mg before being enclosed in a standard 50- μl aluminium sample pan (see insert image in Figure 3.27), in order to avoid the direct contact with the furnace and temperature sensors. The preparation and operation procedure for DSC measurement are described as follow:

- Check the balance level and ensure that the air bubble is located at the centre of the circular area. Transfer the EVA shreds directly in the sample pan and weigh the sample being tested (12 mg).
- Place the lid on the pan, with its indentation facing down. Put the covered pan in the black holder for compression.
- Place the holder under the press and pull the handle down where the pan and lid are sealed. Repeat with an empty pan to be used as a reference.
- Place the sealed sample pan and reference pan in the sample tray and reference slot respectively. Turn on the nitrogen gas and the power to the cooler.
- Open the Pyris software, and set the purge gas flow at 20-ml/min. Enter the parameters for the operating procedure before starting the program, in our case, the sample is heated from -20 to 220 °C at 10 °C/min for 2 cycles while testing the heat flow.
- When the program ends, turn off the cooling system and switch off the nitrogen gas.

3.8 Summary

In this chapter, the equipment and instruments used for light-harvesting materials and solar cells characterisation are introduced. Detailed descriptions in regard to the operating principle of particular devices are also given. With the aim to more clearly demonstrate their uses, characteristics and working conditions, all the apparatus employed at corresponding experimental stage are indicated and listed below in Table 3.8.

In the next following two chapters, a variety of potential oxide materials for silicon solar cells performance enhancement will be investigated. Chapter 4 shows the light promotion in commercial single junction mono-Si solar cells through the application of high surface area of titanium oxide (TiO₂)-based nanoaerogels and the use of silicon

oxide (SiO₂) thin film anti-reflection coatings where in chapter 5, rare earth ion-doped gadolinium oxysulfide and alkaline aluminates phosphor materials are employed as effective UV spectral downconverters in order to resolve the spectral mismatch and Fresnel reflection of silicon solar cells. The relevant background regarding the as used light-harvesting candidates, the experimental results on improved mono-Si solar cells as well as the mechanisms underlying the enhanced cell efficiency are performed.

Table 3.8. Equipments and instruments for experimental tests.

<i>Name of apparatus/instruments</i>	<i>Measuring Objectives</i>	<i>Area of Measurement</i>
Laser cutting-engraving machine	Cutting for solar cell	Solar cell preparation
Digital soldering station	Soldering for solar cell	
Thermal couple and data logger	PV cell temperature measurement	Temperature acquisition
Flash solar simulator	I-V characteristics measurement	Electrical characterisation
Keithley source-meter	I-V characteristics measurement	
Solar cell response system	Solar cell EQE measurement	
High pressure compact reactor	TiO ₂ -based aerogels preparation	Materials fabrication
Chamber box furnace	Heat treatment for resultant materials	Materials annealing
UV/Vis spectrophotometer	Solar cell surface reflectance, transmission and absorption measurement	Optical characterisation
Ellipsometer	Deposited film refractive index and thickness measurement	
Scanning Electron Microscope	Powder samples morphologies observation, Surface microstructures observation of coated solar cells	Morphology, structure and crystalline phase characterisation
Transmission Electron Microscope	Powder samples structural features and catholuminescence properties analysis	
X-Ray powder diffractometer	Powder crystalline phases identification and crystallite size measurement	
Monochromator detector system	Phosphor luminescence properties investigation and quantum efficiency measurement	Photoluminescence characterisation
Surface area and pore size analyser	TiO ₂ -based nanoaerogels specific surface area and pore diameter measurement	Physisorption and textural characterisation
Differential Scanning Calorimetry	EVA curing temperature measurement	Thermodynamic characterisation

Chapter 4 Titanium Oxide-Based Nanoaerogels for Crystalline Silicon Solar Cells

4.1 Introduction

Titanium dioxide (TiO_2) and magnesium oxide (MgO) are environmentally friendly and economically low in cost, which have attracted a lot of academic attention due to their novel applications in the domain such as optoelectronic devices, catalysis, reflecting and antireflection coatings [138]. The light harvesting performance of TiO_2 can be further improved by doping with MgO on the basis of two mechanisms: surface modification and size optimisation. The surface modification of the mixed oxide system by introducing small amount of MgO might induce a variety of crystal defects on TiO_2 surface that acted as trapping centres, which could effectively inhibit the recombination of photogenerated charge carriers during the migration from inside of TiO_2 particles to the surface. This is expected to contribute to overall enhancements of photoactivity and light absorption in both UV and visible range [138, 139]. On the other hand, doping TiO_2 with porous MgO in controlled content could lead to the increase in the specific surface area and therefore more possibilities for light diffusion on the solar cell interface and multiple reflections inside the material, which are able to provide enhanced scattering behavior as well as to promote the photogenerated-electron transfer to the conduction band of TiO_2 lattice [140]. In addition, MgO exhibit high optical transparency and low refractive index, which will not overshadow the potential enhancement derived from the intrinsic antireflection properties of TiO_2 [141].

In this chapter, the experimental process executed in the laboratory focus primarily on investigating the potential application of TiO_2 and MgO -doped TiO_2 NPs to improve the conversion efficiency of commercial single junction mono-Si solar cells. In the present work, meso-porous TiO_2 and MgO -doped TiO_2 aerogels were prepared through an innovative approach by using a precipitation method in conjunction with a modified

sol-gel process [151]. In order to encapsulate the TiO₂ based NPs on the textured surface of the solar cells without loss of UV activity, ethylene vinyl acetate (EVA), with high optical transparency ($T = 93/100$ in the range of 400 to 850 nm), moderate index value ($n = 1.48$) and UV cut-off wavelength ($\lambda_c = 250$ nm), was used as the matrix and binder. In addition, this copolymer exhibits good colour stability that help resist yellowing after 5000 hours of damp heat testing and it shows strong adhesion to glass substrate [156]. Such a combination of element doping method with the use of nanoporous photocatalyst is expected to compensate for the low spectral response of silicon solar cells at the UV-blue wavelengths while improving light trapping. The experimental objectives are listed below:

- To obtain high specific surface area of TiO₂-based nanoaerogels for the promotion of light absorption of mono-Si solar cells at wavelength of UV-blue region, thus improving the power conversion efficiency.
- To demonstrate the formation of a novel anti-reflection layer comprising EVA/TiO₂ based nanocomposites on top surface of the mono-Si solar cells by using blade screen printing technique.
- To examine the effectiveness of the synthesised TiO₂-based nanoaerogels for the energy performance enhancement of mono-Si solar cells through the investigation of the microstructure of the nanocomposite layer, as well as the illustration of electrical, optical, and EQE response of solar cells before and after coating.

4.2 TiO₂ and its applications

In recent years, titanium dioxide (TiO₂) has received a growing academic interest and concern owing to its low-toxicity, chemical stability, high photocatalytic activity, as well as the excellent optical and dielectric properties. These outstanding features allow a wide range of applications such as sunscreen agents, humidity and oxygen sensor, photographic plates, and photocatalyst for environmental protection. TiO₂ exhibits good

reactivity under ultraviolet (UV) light and adapted refractive index ($n \approx 1.8-2.9$), which also make itself being served as a standard anti-reflection coating in the domain of solar PV industry [98, 121].

TiO₂ in nature can exist in three distinct crystalline types: rutile, anatase and brookite. Among all these polymorphs, only rutile is relatively abundant and thermodynamically stable with the highest formation enthalpy, while anatase and brookite are metastable that can be transmitted into rutile phase, but they are scarce in earth. Since brookite is difficult to fabricate, and hence is not comprehensively discussed in this chapter. Anatase phase shows good response to ultraviolet (UV) light and has a more superior photocatalytic performance compared to other two [122-124].

Comparing with the rutile TiO₂ (110) surface, the crystal defects on the surface of anatase TiO₂ (101) are relatively unstable and energetically prefer to occupy the subsurface sites. As a result, the greater amounts of oxygen vacancies (V_O) (or shallow traps) on the surface of anatase TiO₂ particles result in more Ti³⁺ sites, thus trapping electrons, which could more efficiently inhibit the recombination of charge carriers (photoexcited holes and electrons) [121, 124]. Secondly, the photogenerated charge carriers show the lowest recombination rate within the anatase TiO₂ due to the lightest polaron effective mass for anatase than for other phases, which gives the fastest migration of charge carriers from the interior to the particle surface [125, 126]. The lower electron-hole recombination rate in anatase is also believed to arise from the materials' typical smaller grain size which results in higher adsorption capacity [125]. In addition, anatase belongs to indirect band gap semiconductor category which has a longer charge carrier lifetime compared to that direct band gap of rutile and brookite, which allows for easier surface reactions [124, 126].

Anatase (I4₁/amd space group) and rutile (P4₂/mnm space group) belong to orthorhombic system and are both tetragonal crystallographic in structure, which comprise of the same TiO₆ octahedral ([TiO₆]⁸⁻) geometry, sharing four edges with surrounding octahedrons in anatase and two in rutile. The unit cell of anatase TiO₂ contains four Ti atoms and eight O atoms while two Ti atoms and four O atoms for

rutile phase [128, 129]. These structures are shown in Figure 4.1-4.3.

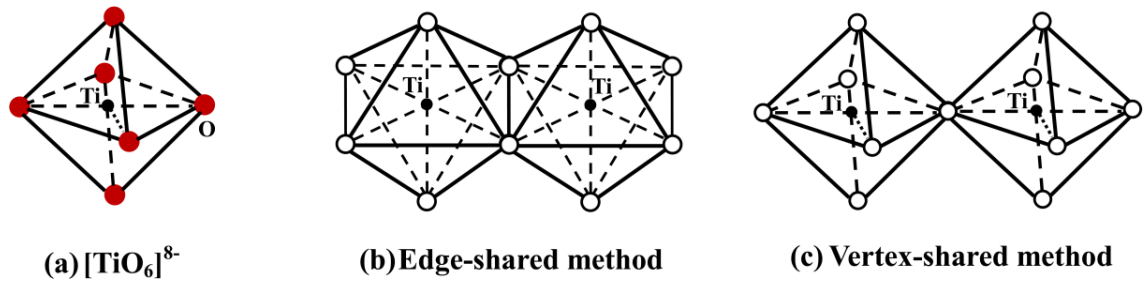


Figure 4.1. Sketch showing the titanium dioxide ($[\text{TiO}_6]^{8-}$) octahedral geometry and its connection methods.

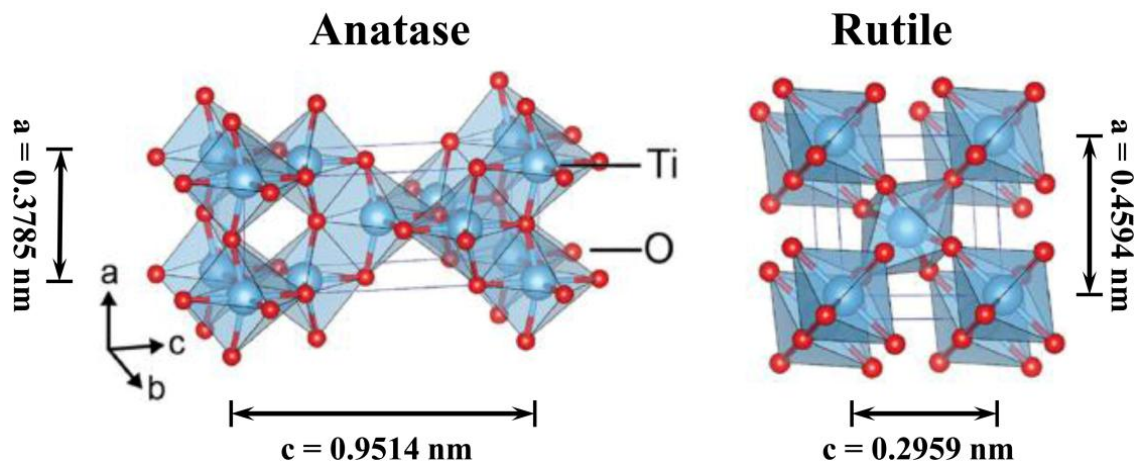


Figure 4.2. Crystal structures of TiO_2 anatase (tetragonal, $I4_1/amd$) and rutile (tetragonal, $P4_2/mnm$) polymorphs. Figure is adapted from [127].

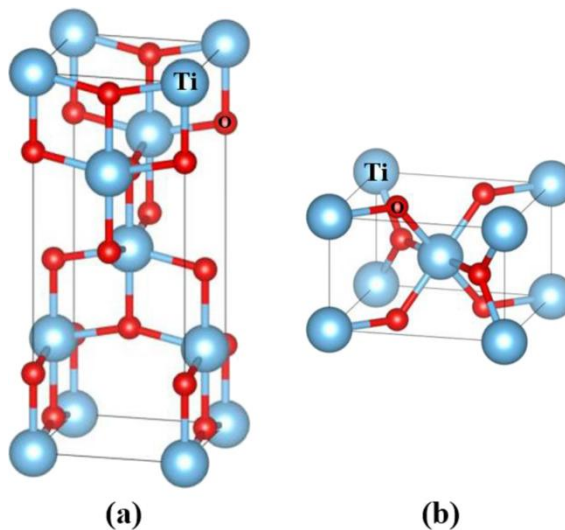


Figure 4.3. Geometrical structures of the unit cells in respect to: (a) anatase and (b) rutile TiO_2 . The blue and red spheres are Ti and O atoms, with corresponding coordination number of 6 and 3 respectively [129].

Table 4.1. Properties comparison between anatase and rutile TiO₂ [128].

<i>Property</i>	<i>Anatase</i>	<i>Rutile</i>
Crystal structure	Tetragonal	Tetragonal
Formulas per unit cell (Z)	4	2
Space group	I4 ₁ /amd	P4 ₂ /mnm
Lattice parameters (nm)	a = 0.3785 c = 0.9514	a = 0.4594 c = 0.2959
Unit cell volume (nm ³)	0.1363	0.0624
Density (kg/m ³)	3894	4250
Calculated indirect band gap		
(eV)	3.23-3.59	3.02-3.24
(nm)	345.4-383.9	382.7-410.1
Experimental (optical) band gap		
(eV)	~3.2	~3.0
(nm)	~387	~413
Refractive index	2.54, 2.49	2.79, 2.903
Solubility in HF	Soluble	Insoluble
Solubility in H ₂ O	Insoluble	Insoluble
Hardness (Mohs)	5.5-6	6-6.5
Bulk modulus (GPa)	183	206

Figure 4.4 shows the X-ray diffractograms of TiO₂ powders calcined at temperature range of 300-800 °C that are reported by Miszxxzak and Pietrzyk. In their work, anatase-rutile phase of TiO₂ powders were obtained through analogous sol-gel process by dissolving titanium (IV) butoxide (Ti([O(CH₂)₃CH₃)₄]) in anhydrous ethanol [122]. This is particularly relevant to the current research scope since sol-gel method has been considered to be one of the most effective techniques for preparation of metallic oxide materials in nano-scale [136, 151]. However, the use of such metal-organic starting material requires strict control of the synthesis condition because the butoxide is easily hydrolysed in ambient air. Furthermore, titanium butoxide is usually produced by treating titanium tetrachloride (TiCl₄) with addition of butanol, it may have higher production cost than direct use of TiCl₄ precursor that restricts the commercialisation of this method [137].

Typically, anatase is formed when calcined at temperature above 350 °C and rutile at temperature greater than 800 °C [124]. The transformation from anatase to rutile phase is an irreversibly reconstructive process in which the bonds breaking and

reforming occur, leading to a contraction of c-axis and reduction in unit cell volume. Therefore, rutile is more densely packed and exhibits a greater density in comparison with anatase. The temperature of this phase transition depends on various factors, such as the sample fabrication method, crystallite size, oxygen defects, the presence of impurities or dopants, and the annealing atmosphere [128]. The basic properties of rutile and anatase TiO₂ are outlined in Table 4.1.

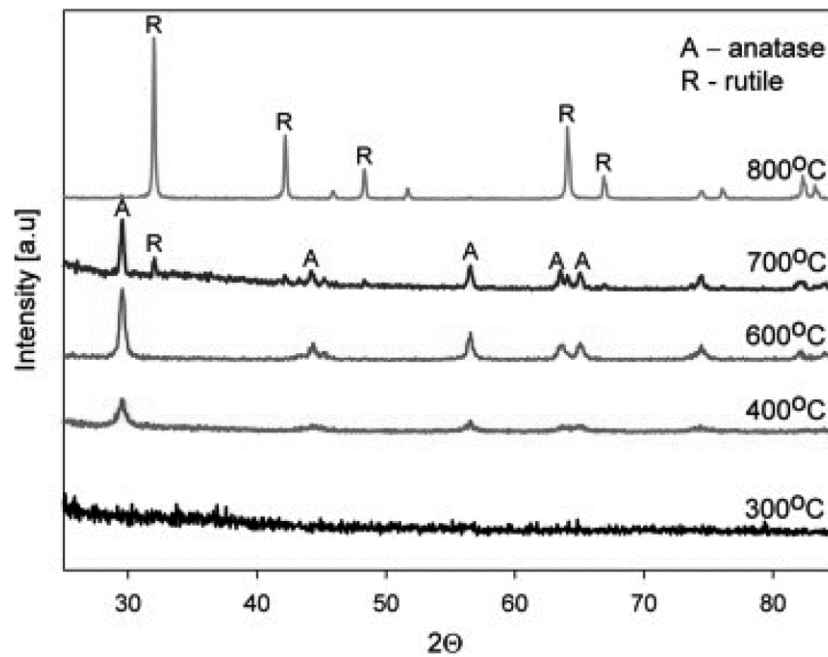


Figure 4.4. XRD patterns of TiO₂ powders calcined at 300-800 °C [122].

The structural features such as the phase, particle and crystallite size, as well as the specific surface area of crystal affect fundamentally the functional properties of both TiO₂ powders and thin films. Research on functional materials has now focused on nanomaterials with structure on the nanometer scale due to the unique features arising from their small size.

Nanomaterials with various sizes and morphologies have shown the great potential in improving the light trapping in solar cells in a wide range of wavelength. Furthermore, nanostructured TiO₂, such as nanotubes, nanosheets, nanospheres, nanowires and nanoparticles have been proven to provide superior photocatalytic performance due to their large surface area [130]. Jin et al reported successful synthesis of anatase TiO₂ nanowires which leads to 1.26 times increase in photodegradation rate of the organic

pollutant methylene blue under UV illumination compared to that of commercial Degussa P25 TiO₂ (80% anatase and 20% rutile), which is ascribed to the mesoporous structure and large specific surface area (267.56 m²/g) [131]. Al-Attafi et al demonstrated that the hierarchically structured anatase TiO₂ nanoparticles can be used as high surface area scattering layer for Dye-sensitized solar cell performance enhancement. These aggregated particles (average grain size = 8.5 nm) contributed to a high power conversion efficiency of 9.1% in comparison with 7.4% by using those of commonly used large particles scattering layer [146].

However, the wide semiconductor band gap of TiO₂ (3.2 eV for anatase and 3.0 eV for rutile) restricts the absorption to the UV region [132]. For this reason, a number of approaches have been devised, such as doping with metallic (e.g., Fe, Cr, Mg) [133, 134, 138] and nonmetallic elements (e.g., N, S) [142, 143] into the TiO₂ lattice. This is because that the substitution of Ti⁴⁺ cations or lattice oxygen with such doping ions that having a lower valence would induce crystal defects and the creation of oxygen vacancies on TiO₂ surfaces, which could effectively improve the photocatalytic activity of TiO₂ in both UV and visible regions.

An alternative strategy is to obtain high surface area of TiO₂ particles with micro- or meso-porous structures since the porous texture on the TiO₂ NPs opens up the possibility for light diffusion on the interface of semiconductor, promotes rapidly the photogenerated-electron transfer to the conduction band of TiO₂ NPs. Moreover, the high surface-to-volume ratios and porous structure allow multiple reflections of incident light and provide a good scattering effect, which enhances the light harvesting capability of TiO₂ across a wide wavelength [144-147]. In addition, a high surface area usually gives a small particle size and relatively lower surface energies, giving rise to a higher density of localised states and subsequent surface-adsorbed hydroxyl radicals, which can be served as trapping sites for effective separation of photo-generated electron-hole pairs as well as for inhibition of charge carrier recombination [128].

There are a number of methods for fabrication of porous TiO₂ nanomaterials, commonly used ones include hydrothermal process [147], vapour-liquid-solid

mechanism [148], electrospinning [149], and sol-gel synthesis route [150]. Among them, sol-gel processing is generally accepted as a simple and easy operation method in which the creation of nanostructures is solely based on the chemical reaction of either atom- or molecular-size precursors. It has been widely used for fabricating metal oxide materials with various shapes such as porous and hollow structures, dense powder, monoliths and thin films. Furthermore, this method is also an economical way to synthesise titania-based nanomaterials with relatively high purity and controllable chemical composition, which allows for easy scale-up and wide application. In addition, the chemical characteristics of resultant materials synthesised via sol-gel method exhibit high homogeneity in comparison with that of TiO_2 obtained from other routes [151].

Sol-gel synthesis method consists of two important chemical procedures: hydrolysis and condensation reactions of sol to form a stable gel that possessing high specific surface area and unique porous structure.

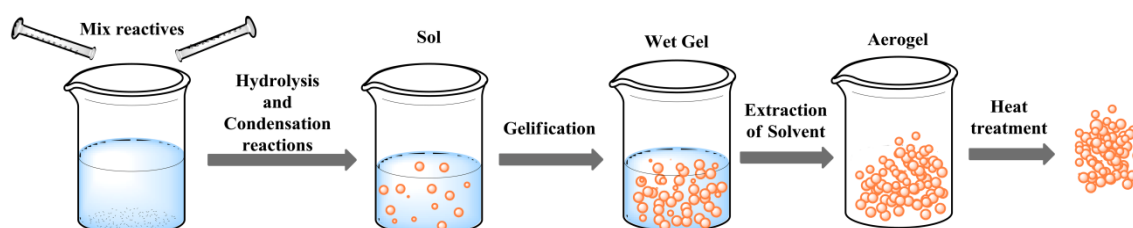


Figure 4.5. Schematic representation of the different stages of the sol-gel process.

Figure 4.5 shows the typical sol-gel protocol, in these chemical procedures, a colloidal solution is formed by mixing metal alkoxides or soluble inorganic metal species with alcohols which are usually served as the precursor of the target products and the solvent respectively. The metal compounds undergo hydrolysis and poly-condensation, resulting in a sol in which colloidal particles are dispersed without any precipitation. The fine aerosol particles in the colloidal solution were then solidified from sol into a wet gel-like diphasic system that contains both a liquid and solid phase. A drying process is followed to remove the remaining liquid solvents, and thus to yield a dry gel. In the last step, a post heat treatment process is pivotal in completing recrystallisation as well as improving the mechanical properties and structural stability

of the resultant materials [152]. It is deserved to mention that drying of the gel at room temperature results in the formation of less porous and more denser-materials, which is known as xerogels. This arises from the porous network collapse due to the interfacial tension accompanying with the formation of a liquid-vapour interface. One efficient method to eliminate the interface is by removing the solvent in a supercritical condition. Aerogels were thereby obtained through this approach and the resultant materials show low agglomeration, low density, and relatively high specific surface area as compared to the xerogels [151]. Nowadays, aerogels have been used in a wide range of applications such as luminescence [153], battery [154], and space [155].

4.3 Experimental Methods

4.3.1 Materials used for the fabrication of TiO₂-based aerogels

Fabrication method of titanium dioxide-based nanoaerogel materials was inspired by the research work done by Parayil et al, who had successfully synthesised high surface area of anatase TiO₂ aerogels in a compact nitrogen reactor via High temperature supercritical drying of sol-gel method [151]. By using a similar approach with some modification, titanium dioxide nanomaterials with porous structure and higher specific surface area can be obtained. The following chemicals were used in the laboratory for the fulfillment of this approach:

Methanol (Alfa Aesar, UK, 99%) was used as the solvent, titanium tetrachloride (TiCl₄) (Sigma Aldrich, UK, 99.9% trace metal basis) and magnesium nitrate hexhydrate (Mg(NO₃)₂ 6H₂O) (Sigma Aldrich, UK, 99.999 %) were used as the precursor of the target oxide and the doping agent respectively. All chemicals were used as received without further purification.

4.3.2 Synthesis of TiO₂ based aerogels

For preparation of nanostructured TiO₂ based nanoaerogels, titanium (IV) chloride (TiCl₄) and magnesium nitrate hexahydrate (Mg(NO₃)₂ 6H₂O) were used as the

precursor of TiO₂ and MgO dopant respectively. In a typical synthetic process, 1.4 ml of TiCl₄ was gently injected into a glass beaker (see Figure 4.6 left) containing 150 ml of methanol and 63.6 mg of Mg(NO₃)₂ · 6H₂O salt to obtain a 1/50 molar ratio of magnesium to titanium in the synthesised NPs. This molar ratio is suggested by a study in which different molar ratios of MgO-doped TiO₂ NPs were prepared by using an aerogel method and it was found that a solid solution of MgO-TiO₂ mixed oxides of 1:50 ratio exhibited the optimum UV-active photocatalysis performance [138].



Figure 4.6. Solution mixing process (left) and vessel (right) of the high-pressure compact stirred reactor.

The mixture of that solution was vigorously stirred for 15 minutes where TiCl₄ is fully dissolved in methanol at room temperature. The contents were then poured into a vessel (see Figure 4.6 right) of the autoclave (Parr Model 5500 high-pressure compact stirred reactor, see Figure 3.13) and hydrogen gas (H₂) (BOC, UK, 99.995% purity) was introduced into the autoclave at an initial pressure of 20 bar (2 MPa). The autoclave was then heated to a setting temperature of 200 °C and maintained for 2 hours. The internal pressure was finally observed at around 80 bar (8 MPa). The autoclave was cooled down to room temperature and the remaining H₂ gas was released. The autoclave was disassembled and the solution poured back into that beaker.

The solid aerogel obtained was washed two times with methanol and dried in a fume hood overnight at room temperature. The synthesised powder was finally calcined

in a chamber furnace (see Figure 3.14) at 400 °C for 10 hours under a static air environment. The synthetic process for undoped TiO₂ aerogel is similar with that of MgO-doped TiO₂ and the only difference between those two cases is the adding of Mg dopant. The final products of TiO₂ and MgO-doped TiO₂ aerogel materials before and after heat treatment are shown below in Figure 4.7.

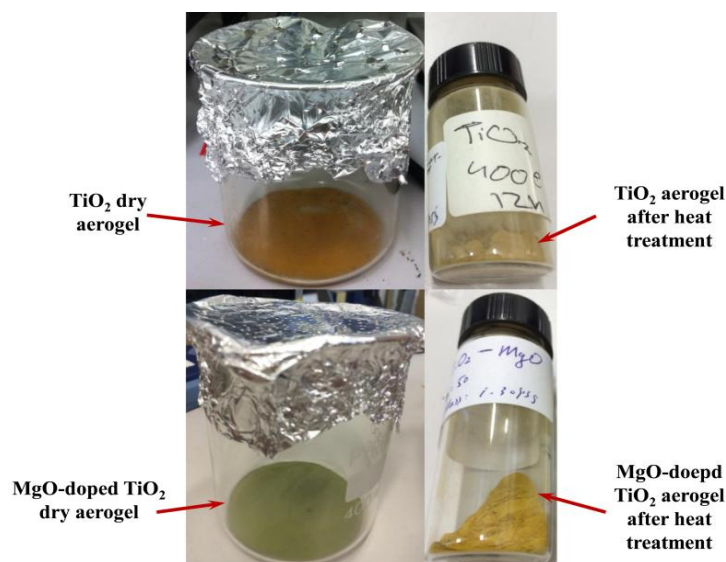


Figure 4.7. TiO₂ (top) and MgO-doped TiO₂ (bottom) aerogel nanomaterials before and after annealing at 400 °C for 10 hours.

It can be seen that the synthesised TiO₂ and MgO-doped TiO₂ aerogels show brown and greenish yellow colour respectively, which may be due to the presence of metallic dopants or impurities around the lower edge of conduction band of TiO₂. The colour of TiO₂ can vary from white to reddish which depends on the fabrication method and the level of purity. White TiO₂ is the purest form possessing a bandgap of 3.2 eV while it cannot absorb visible light. The impurities are most likely coming from the stainless steel autoclave that contains metallic elements such as Cr, Fe, V and Mn [175]. However, these transitional metals or metallic particles may help in improving the visible photoactivity of TiO₂ [133-135]. Detailed elemental composition analysis and their potential effects on the light absorption performance of the aerogels coatings will be discussed in the latter section (Section 4.4.1.1).

4.3.3 Formation of the deposited layer

Mono-crystalline silicon solar cells, model XS156B3-200R from Motech were used in the layer coating process. The mono-Si solar cells were cut into 3 equal sizes (156 mm × 52 mm) by using a CTR-TMX90 high power laser machine. TiO₂-based nanoparticles were encapsulated in ethylene vinyl acetate (EVA) copolymer resins, and the obtained composite solutions of EVA/TiO₂-based nanoaerogels were blade screen printed on top of random pyramid structure of SiN_x anti-reflection layer of the solar cells. Each cell has a coated area of 5 × 5 cm². In the following subsections, preparation of the solely EVA layer and EVA/TiO₂-based nanocomposited layer as well as their integration onto the surface of mono-Si solar cells are described in detail.

4.3.3.1 Binding Materials

In order to encapsulate the TiO₂-based nanomaterials on the textured surface of mono-Si solar cell, an appropriate binding agent is required. This binding material must possess relatively high transmittance or even provide anti-reflective functionalities that would not offset the potential enhancement brought by the TiO₂-based nanoaerogels.

The binder used in present experiments is Ethylene Vinyl Acetate (EVA) (Elvax 150, Dupont), also called poly ethylene vinyl acetate (PEVA) with chemical formula [(C₂H₄)_n(C₄H₆O₂)_m], which is a random copolymer of ethylene and vinyl acetate, with a long ethylene chain and pedant acetate groups. Figure 4.8 shows its chemical structure where the functional groups of ethylene (-CH₂-CH₂), vinyl (-CH₂-CH-), and acetate (CH₃-CO₂) are illustrated. This commercial transparent resin of EVA copolymer contains 32% weight ratios of vinyl acetate, with melt flow rate of 4.3 g/min and UV cut-off wavelength down to 250 nm. The detailed composition, physical and thermal properties of this material are given in Table 4.2.

Table 4.2. Elvax 150 EVA properties [159].

<i>Typical Characteristics</i>	
Composition	
Vinyl acetate	32 wt%
Butylated hydroxytoluene (BHT) antioxidant	0.2 wt%
Physical	
Thickness	0.45 mm
Density	0.957 g/cm ³
Melt flow index (190 °C/2.16 kg)	43 g/ 10 min
Electrical resistivity	1014 Ω cm
Refractive index	1.486
Thermal	
Melting point	63 °C
Softening point	36 °C
Degradation temperature	235 °C

Typically, EVAs incorporate 5 to 50% vinyl acetate. The feature of EVA varies with the change in vinyl acetate (VA) content. EVA with high VA content, around 20% to 40%, are less crystalline because of the relative bulkiness of the acetoxy side chain (see Figure 4.8), which increases the difficulty in close packing of polymer chains. This gives rise to higher transmittance, tackiness and flexibility while at very low proportion of VA content, it behaves like a tough thermoplastic. In addition, the increase of VA content usually results in the polarity of the copolymer, which contributes to improving adhesion and electrical insulation properties [157,158].

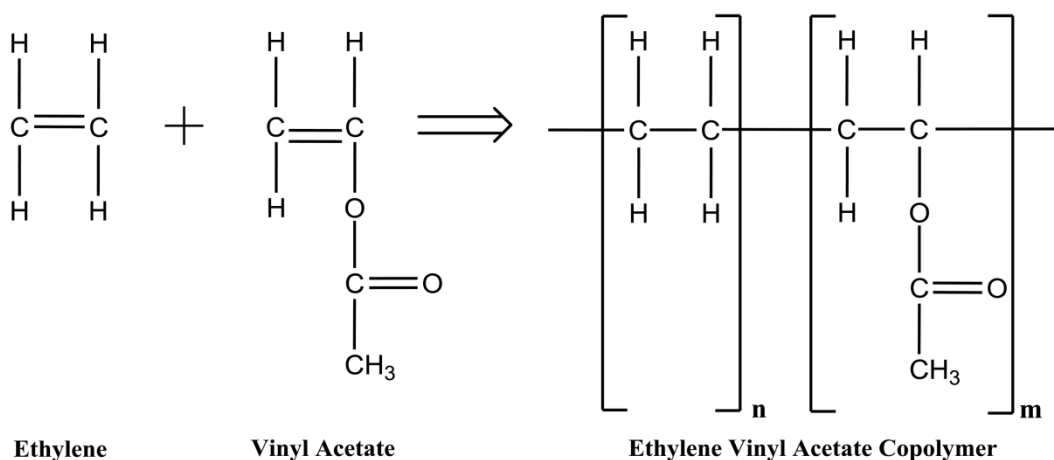


Figure 4.8. Chemical structures of ethylene and vinyl acetate comonomers, and poly ethylene vinyl acetate [160].

EVA is an elastomeric material, meaning that it develops irreversible cross-links when being cured. The level of cross linking highly influences the optical transmittance capabilities and dielectric properties, therefore proper curing is an essential part of EVA encapsulation. Typical curing method to control the cross-linking process of EVA includes thermal heat treatment that is usually monitored by the differential scanning calorimetry (DSC) in order to detect the physical variations during the cross-linking reactions and thus determine the curing temperature. Prior to that process, the EVA resin was formulated with other additives such as chemical curing agents, stabilisers, UV absorbers, photo- and thermo-antioxidants [119, 161, 162].

Cross-linked EVA exhibits excellent optical properties, good thermal stability, and strong adhesion to glass substrate, which has been widely used as PV modules encapsulant for over decades. Furthermore, its outstanding features such as low temperature flexibility, chemical resistance and easier handling, superior durability and higher performance-cost ratio, which give itself advantages over other polymers and different types of encapsulation materials [161]. In addition, it is reported that the EVA films used for the solar cell encapsulation also show good light absorption particular in the short wavelength of solar spectrum [163]. Therefore, this polymeric binder is expected to be a suitable matrix for the encapsulated TiO₂-based NPs that would contribute to a further enhancement in light absorption and thus conversion efficiency for the silicon solar cell.

4.3.3.2 Polymer Solvent

The formation of EVA or EVA/TiO₂-based nanocomposite layer requires proper solvents to dissolve the polymer and so as to apply the liquid mixture onto the surface of solar cell. Therefore, the selection of polymer solvent becomes vital in determining the morphology as well as the homogeneity of the deposited layer. Attempts have been made through screening testing among different types of solvents in order to find the suitable ones for dissolution of EVA copolymer. Generally, EVA copolymer is soluble in most of aromatic, aliphatic, alicyclic and chlorinated organic solvents at room

temperature where among them trichloroethylene has been proven to be the most effective one that is capable of dissolving cross-linked EVA at 80 °C [164,165]. However, due to the health, safety and environmental reasons, this candidate is not employed in current research. Alternative solvents with relatively lower toxicity such as cyclohexane and xylene are considered to be the most favourable candidates to dissolve EVA at relatively low temperature.

Various factors in terms of solvent properties that may have great impacts on the morphology of the deposited layer which include the vapour pressure, boiling point, surface tension and the viscosity of the solvent. In addition, the annealing temperature plays a critical role in varying the solubility of solid substances since it determines directly the kinetic energy of the solvent molecules that could potentially overcome or succumb to the attractive forces among solute particles [166].

Table 4.3. Physical properties of the solvents.

<i>Properties</i>	<i>Solvents</i>	P-xylene [167]	Cyclohexane [168]	Toluene [169]
Molecular Formula		C ₈ H ₁₀	C ₆ H ₁₂	C ₇ H ₈
Colour		Colourless	Colourless	Colourless
Density (g/cm ³ at 20 °C)		0.866	0.779	0.867
Vapour Pressure (mbar at 20 °C)		9	104	28
Boiling Point (°C)		138	78	111
Surface Tension (mN/m at 20 °C)		28.27	24.95	28.52
Viscosity (mPa.s at 20 °C)		0.648	0.940	0.590

The solvent liquid used in this project is p-xylene (Alfa Aesar, UK, 99%) where its physical properties along with other screened solvents are summarised in Table 4.3. This liquid has shown to be effective in dissolving polymer materials with relatively lower flammability and toxicity, making it appropriate for the current project.

4.3.3.3 EVA Layer Preparation

The EVA was used as encapsulant for TiO₂-based NPs to the solar cell. EVA copolymer resin was supplied from Dupont Company in rolls with a thickness of 0.45

mm. Prior to investigating various concentrations of the TiO₂-based nanomaterials for the solar cell performance enhancement, a study to determine the best weight percentage (wt%) of EVA was undertaken. The weight ratio refers to the percentage of EVA in the final solution by mass applied to the cell, which is expressed by the equation:

$$\text{Wt\% of EVA} = \frac{\text{Mass of EVA (g)}}{\text{Mass of EVA(g) + Mass of Solvents (g)}} \quad (4.1)$$

The solvent used in layer application process was p-xylene. This stage is important as the EVA serves as a binder for the TiO₂-based NPs. These layers tend to block light, decreasing the cell's efficiency. Due to this fact, it is pivotal to find a certain wt% of EVA that decreases efficiency by fairly small amount or even provides some minor enhancement.

In order to determine the best weight ratio (wt%) of EVA to TiO₂ based NPs that contributes to an optimum enhancement in power conversion efficiency (PCE) of the coated solar cells, various weight ratios of EVA/p-xylene liquid mixtures (9, 12, 15, 18 and 21 wt%) were prepared by dissolving 500 mg of EVA foils in a certain amount of p-xylene solvent. EVA sheet in respect to different wt% was previously cut into small pieces for better dissolving and added to a glass beaker that contains p-xylene solvent (see Figure 4.9).



Figure 4.9. EVA sheet (left) and the preparation of EVA/p-xylene solution (right) where the beaker is placed on top of the hotplate magnetic stirrer.

Considering the inevitable evaporation of solvent during stirring process, the amount

of p-xylene added at this stage is slightly higher than that of calculated ideal value. EVA/p-xylene mixture was then stirred at 30-35 °C for 10 minutes until a uniform solution is formed. Once the EVA foils has been fully dissolved and the desired wt% is reached, the solution is ready for layer application.

4.3.3.4 Composite Layer Preparation

The synthesised undoped TiO₂ and MgO-doped TiO₂ NPs were ready to be used in the process of layer application. Prior to that process, 1.5 mg of each powder was measured and then dispersed in p-xylene using an ultrasonic bath (see Figure 4.10). The solution with different concentrations of dispersed powder (0.2 mg/ml, 0.3 mg/ml, 0.4 mg/ml, 0.6 mg/ml and 0.8 mg/ml) are prepared and then separately mixed with certain amounts of EVA sheet in which the weight ratio of EVA in that of mixture is fixed at 15 wt%. This ratio has given rise to a homogeneous EVA layer applied onto solar cell as well as exhibiting superior optical transmission and reflection properties to other ratios of solely EVA coatings, which potentially contributes to the maximum enhancement in conversion efficiency. The mixture solution was then left above 30 °C under magnetic stirring until uniform colloidal solutions are observed. In order to ensure the accuracy and consistency on the amount of EVA/TiO₂-based NPs that applied on the solar cell, the volume of the mixed solution for each coating was fixed as 1.3 ml (one shot of the pipette) and the TiO₂/EVA weight ratio for different concentrations of prepared solution can thereby be determined by substituting the known conditions into equation 4.1:

$$\begin{aligned}
 15\text{-Wt\% of EVA} &= \frac{\text{Mass of EVA (g)}}{\text{Mass of EVA(g) + Mass of Solvents (g)}} \\
 &= \frac{\text{Mass of EVA (g)}}{\text{Mass of EVA(g) + 1.3ml} \times 0.866\text{g/ml}}
 \end{aligned}$$

Hence, the mass of EVA that applied on each coated solar cell is 0.198 gram and the TiO₂ or MgO-TiO₂/EVA ratio for all tested concentration solutions can be calculated. Typically, 0.13, 0.2, 0.26, 0.39 and 0.53 wt% is obtained at 0.2-mg/ml, 0.3-mg/ml, 0.4-mg/ml, 0.6-mg/ml and 0.8-mg/ml respectively. Note that since the synthesised

powders are expected at the nanoscale, all prepared solutions are controlled in a relatively low concentration range so as to avoid the potential shading effects on solar cell surface due to the serious particle aggregation.



Figure 4.10. Ultrasonic bath used for dispersing TiO_2 -based nanoaerogels in p-xylene solvent.

4.3.3.5 Layer Application

Integration of solely EVA coating and EVA/ TiO_2 -based nanocomposite coating onto the surface of mono-Si solar cells were accomplished by using blade screen printing technique. This coating method provides fast film deposition and allows for the formation of coating films with defined thickness. In addition, this method is particularly suitable when coating solution possesses relatively high viscosity [170].

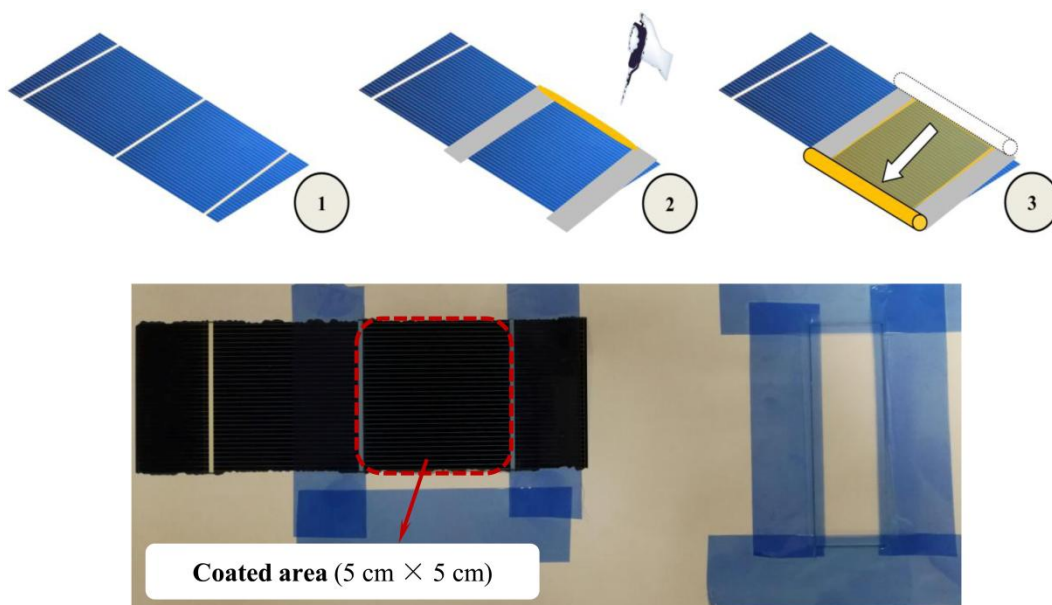


Figure 4.11. Blade screen printing process of mono-Si solar cell.

Figure 4.11 shows the layer coating process where the solar cell is fixed on the experimental table by using a low tack masking tape (Mercateo, UK) with thickness of ~ 0.1 mm. The tape is also served as the “Guides” to mark out the desired area for each coating. Next, the solution of EVA or EVA/TiO₂ (MgO-doped TiO₂) mixture is dropped through a pipette along the two Guides where near the bottom edge of the solar cell. After that, the solution is linearly moved by pulling the coating rod across the solar cell with constant pressure, leaving behind a wet thin film and eventually producing a coated area of 5 cm \times 5 cm on top surface of the cell. In order to demonstrate the accuracy of the coating effects on the energy performance enhancement of solar PV cells, three samples for each concentration of coated cell are prepared. In addition, the glass and quartz slides are also coated in the same route to investigate the optical properties of the deposited layers. The final thickness of the wet film is determined by various factors such as the surface energy of the cell, the surface tension and viscosity of the solution, as well as the thickness of the tape. Among them, the thickness of the Guides plays the most important role in varying and controlling the wet film thickness of the formulated layer [102].

Once the wet film was formed, the coated cells were dried in a fume hood and then cured in a furnace at 190 °C for 5 minutes at a heating rate of 10 °C/min. The curing temperature is suggested by the results obtained from Differential Scanning Calorimeter (DSC) measurements which will be discussed in detail in latter section. After the heat treatment, the applied mixture formed a glossy layer on the textured surface of the solar cell (see Figure 4.12). An illustration of the steps for preparation of TiO₂-based nanoaerogels and their integration on the surface of mono-Si solar cell is presented in Figure. 4.13.

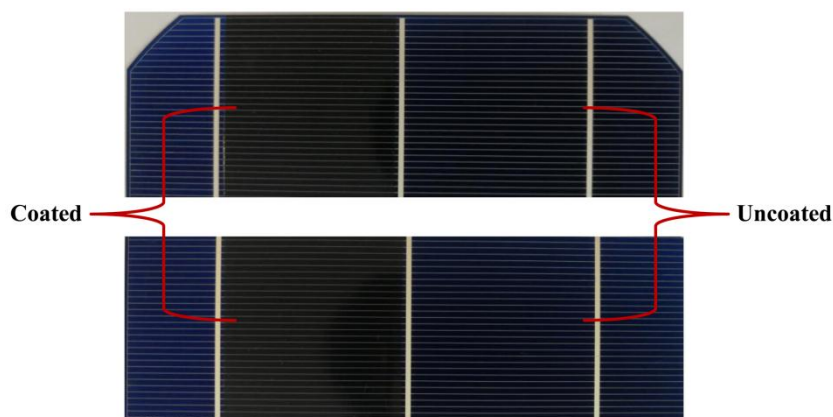


Figure 4.12. Coated solar cells after curing at 190 °C for 5 mins.

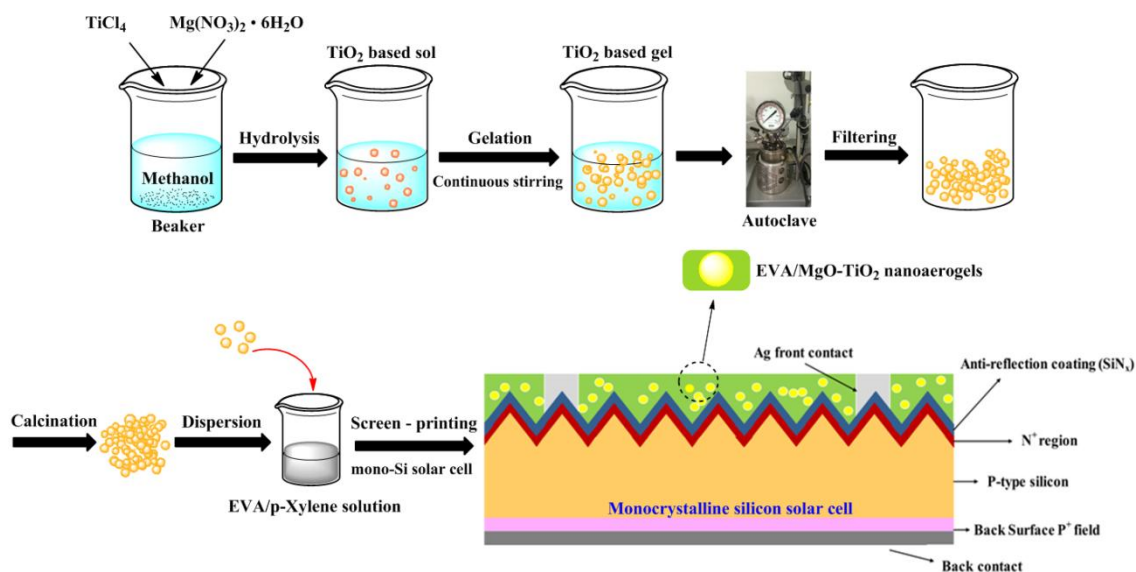


Figure 4.13. Flow diagram showing the fabrication process of TiO_2 based nanoaerogels and their integration onto the surface of mono-Si solar cell.

4.3.4 Equipments used in experiment

In order to perform the experiments and research outcomes of nanostructured TiO_2 -based aerogels materials for improving energy performance of commercial model XS156B3-200R mono-Si solar cells, various equipments and apparatus were used. Most of their operating principles and methods with respect to certain testing purposes have been described in the preceding chapter (Chapter 3). These equipments and instruments include solar simulator, J-V source meter, monochromator-solar cell response system, Differential Scanning Calorimeter, UV/Vis spectrometer, pore size analyser, field emission scanning/transmission electron microscope, and X-ray powder diffractometer.

4.4 Results and Discussion

4.4.1 Synthesised TiO₂-based nanoaerogels

In this section, the experimental results obtained from x-ray powder diffraction, field emission scanning electron microscopy, scanning transmission electron microscopy and nitrogen gas phsorption analyses on the morphological and structural features of as prepared TiO₂ and MgO-doped TiO₂ nanoaerogels are presented and compared.

4.4.1.1 Crystalline phases and Morphology analysis

Figure 4.14 depicts the X-ray diffraction patterns of the MgO-doped TiO₂ and undoped TiO₂ powders annealed at 400 °C. The first peak of each diffraction pattern indicates the most stable plane of TiO₂ ($2\theta = 25.30^\circ$, $d_{101} = 3.5174\text{\AA}$) and MgO-doped TiO₂ ($2\theta = 25.25^\circ$, $d_{101} = 3.5239\text{\AA}$) respectively, which are in good agreement with the standard tetragonal anatase TiO₂ phase (JCPDS 84-1286, $2\theta = 25.32^\circ$, $d_{101} = 3.5141\text{\AA}$) (indicated by the simple bars in Figure 4.14). However, the XRD patterns of MgO-TiO₂ (1:50M) did not show the presence of MgO as the quantity of added dopant is too low to form an independent crystalline phase of MgO and the Mg²⁺ ions could disperse into the TiO₂ lattice. Note that the diffraction peak of TiO₂ tended to broaden with the addition of small amount of MgO (2-mol%), which reveals an alleviation of the severe aggregation in the TiO₂ particles and thus a reduction in crystallinity. In addition, at the interface of the mixed oxide system, the substitution of Ti by Mg given rise to lattice distortions that affects the original crystalline behavior and these may explain the weaker peak that was observed for the MgO-doped TiO₂ in comparison with that of pure TiO₂ nanoparticles [171].

The line broadening of MgO-doped TiO₂ XRD patterns also indicates a slight structural change, suggesting a reduction in the crystallite size. The average crystallite size (τ XRD) of the TiO₂-based NPs was determined using Scherrer's equation [172]:

$$\tau = \frac{K\lambda}{\beta \cos\theta} \quad (4.2)$$

where λ is the wavelength of the incident X-rays (1.5406 Å), β is the full-width at half-maximum (FWHM) in radian, θ is the diffraction angle of the considered diffraction line, K is a dimensionless number of the order of unity, known as the Scherrer constant (defaults to 0.89), typically the K values are within the range of 0.7~1 which depends on the crystallite shape and the crystallite-size distribution [173]. Based on the technical reference of TOPAS functionality, the variation of Scherrer constant in terms of seven common crystal systems in determining the particles crystallite size is demonstrated in below Table 4.4.

Table 4.4. Variation of Scherrer constant K for crystallites of different shapes [174].

<i>System of crystallisation</i>	<i>Scherrer constant K</i>
Cubic	0.99
Hexagonal	0.95
Trigonal	0.95
Tetragonal	0.95
Orthorhombic	0.89
Monoclinic	0.85
Triclinic	0.72

In our case, the K value is set to 0.95 and the results show comparable crystallite sizes of ~9.8 nm and ~7.6 nm for TiO₂ and MgO-doped TiO₂ respectively. Other than that, the estimated tetragonal lattice parameters, and interplanar spacing (d_{hkl}) of the synthesised samples are summarised in Table 4.5

Table 4.5. The tetragonal lattice parameters of TiO₂ and MgO-doped TiO₂ nanoparticles from XRPD data.

<i>Sample</i>	<i>Crystallite Size (nm)</i>	<i>a (Å)</i>	<i>c (Å)</i>	<i>(hkl)</i>	<i>d_{hkl} (Å)</i>
TiO ₂	9.8	3.7824	9.5025	101	3.5174
MgO-TiO ₂	7.6	3.7806	9.5011	101	3.5239

a,c = Lattice Constant; h,k,l = Miller Indices; d_{hkl} = Lattice Spacing (or d-Spacing).

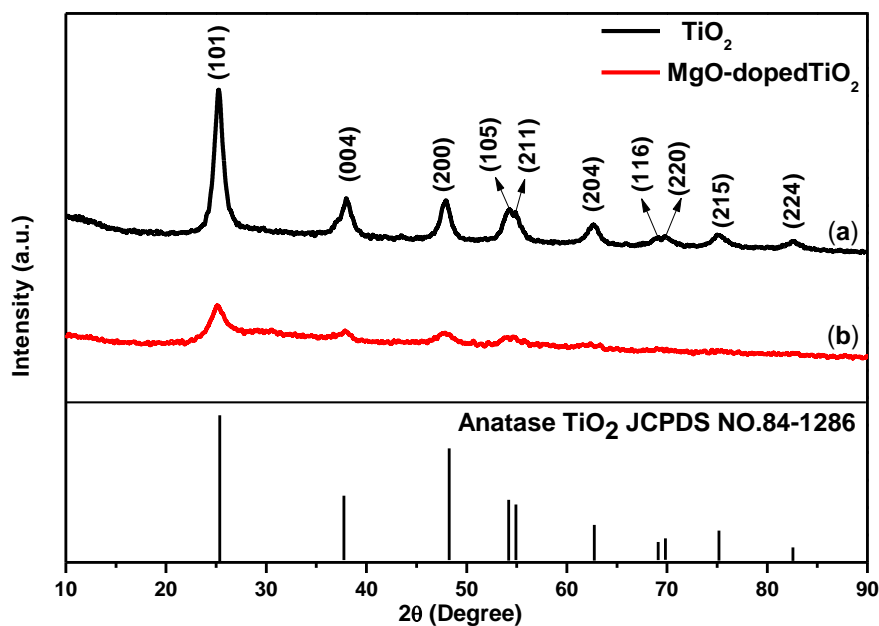


Figure 4.14. X-ray powder diffractometer patterns of (a) TiO_2 and (b) MgO-doped TiO_2 nanoparticles annealed at 400 °C for 10 hours.

The surface morphologies and elemental composition of the synthesised TiO_2 -based nanoaerogels were examined using a field emission scanning electron microscope (FE-SEM) in conjunction with energy dispersive X-ray spectroscopy. Figure 4.15 shows the high-resolution FE-SEM micrographs of TiO_2 and MgO-doped TiO_2 NPs annealed at 400 °C. The agglomeration of the particles with roughly spherical shape can be clearly observed. In addition, the agglomerated particles exhibit compact and uniform surface morphology with small grains homogeneous in size.

The corresponding energy dispersive X-ray spectroscopy (EDS) spectra from the random FE-SEM scanned area of TiO_2 and MgO-doped TiO_2 NPs are illustrated in Figure 4.16, which confirm the presence of titanium (Ti), oxygen (O), and magnesium (Mg) elements in the synthesised powder samples. The additional peaks in regard to carbon (C) and gold (Au) are from the background (carbon film and gold coating). The comparable intensity peaks of iron (Fe) and chrome (Cr) are most likely arisen from the contamination during the fabrication process when the reaction solution is being stirred in a high -temperature and -pressure environment enclosed in the stainless steel-made autoclave [175]. However, this may also bring extra benefits on improving the overall photoresponse of the synthesised TiO_2 -based NPs. Due to the high band gap energy

(3~3.2 eV), the photoreaction efficiency of TiO₂ is largely limited by its capability of absorbing only UV radiation. Unexpectedly, Fe and Cr are reported as two most popular transition metal dopants used for modification of the TiO₂ optical properties by extending the absorption edge from UV to visible light range because the oxidation products of Fe₂O₃ (2.2 eV) [176] and Cr₂O₃ (2.9 eV) [177] possess comparably narrow bandgap which could give rise to the alteration of electron-hole recombination in TiO₂ and more importantly, the radii of Ti⁴⁺ (average ionic radius = 0.058 nm), Fe³⁺ (average ionic radius = 0.060 nm) and Cr³⁺ (average ionic radius = 0.061 nm) are very similar that Fe³⁺ and Cr³⁺ ions can be easily incorporated into the TiO₂ lattice and acted as shallow traps, which contributes to enhancement of photoactivity [133,134]. Therefore, we could expect such co-doping system to achieve a more pronounced light harvesting for silicon solar cells particular in the visible range of solar spectrum.

The composition of the powder samples that were analysed using the integrated EDS is summarised in Table 4.5.

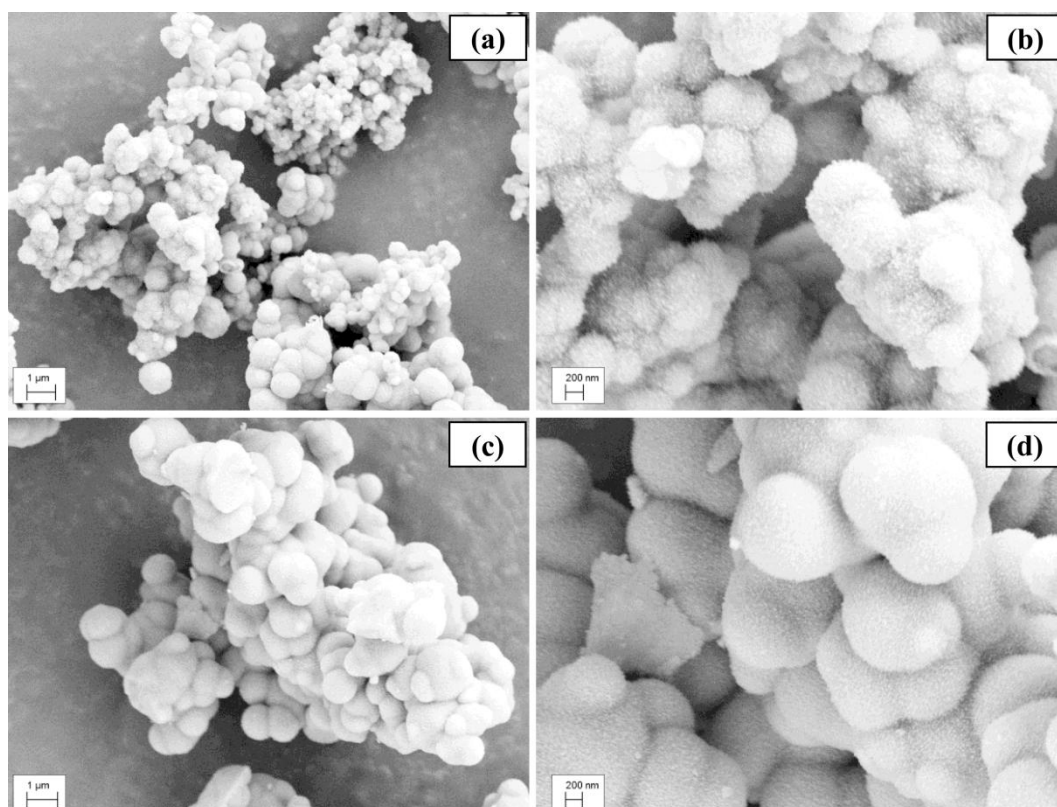


Figure 4.15. Field emission scanning electron microscope micrographs of (a), (b) TiO₂ and (c), (d) MgO-doped TiO₂ nanoaerogels annealed at 400 °C.

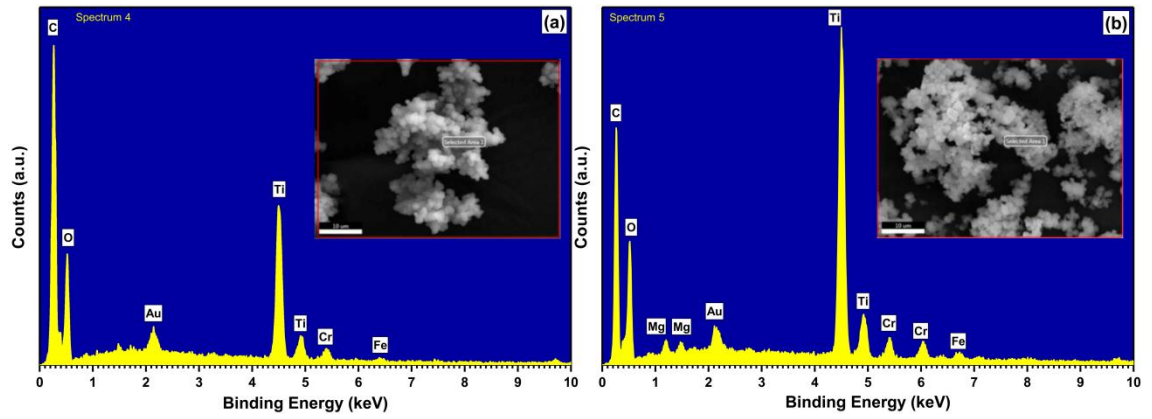


Figure 4.16. Energy-dispersive X-ray spectroscopy (EDS) of (a) TiO_2 and (b) MgO-doped TiO_2 nanoaerogels. Inset SEM micrographs refer to the corresponding selected area, and the scale bar for each case is 10 μm .

Table 4.6. Elemental composition of TiO_2 and MgO- TiO_2 powder samples from the EDS spectra.

<i>TiO₂</i>			
Sr. N	Elements	Atomic (%)	Weight (%)
1	O K	64.48	37.72
2	Ti K	35.03	61.34
3	Cr K	0.38	0.71
4	Fe K	0.11	0.23
Total		100	100
<i>MgO-TiO₂</i>			
Sr. N	Elements	Atomic (%)	Weight (%)
1	O K	65.13	38.77
2	Ti K	32.43	57.68
3	Mg K	1.16	1.03
4	Cr K	0.99	1.91
5	Fe K	0.29	0.61
Total		100	100

The background elements such as C and Ag have been removed from the composition analysis.

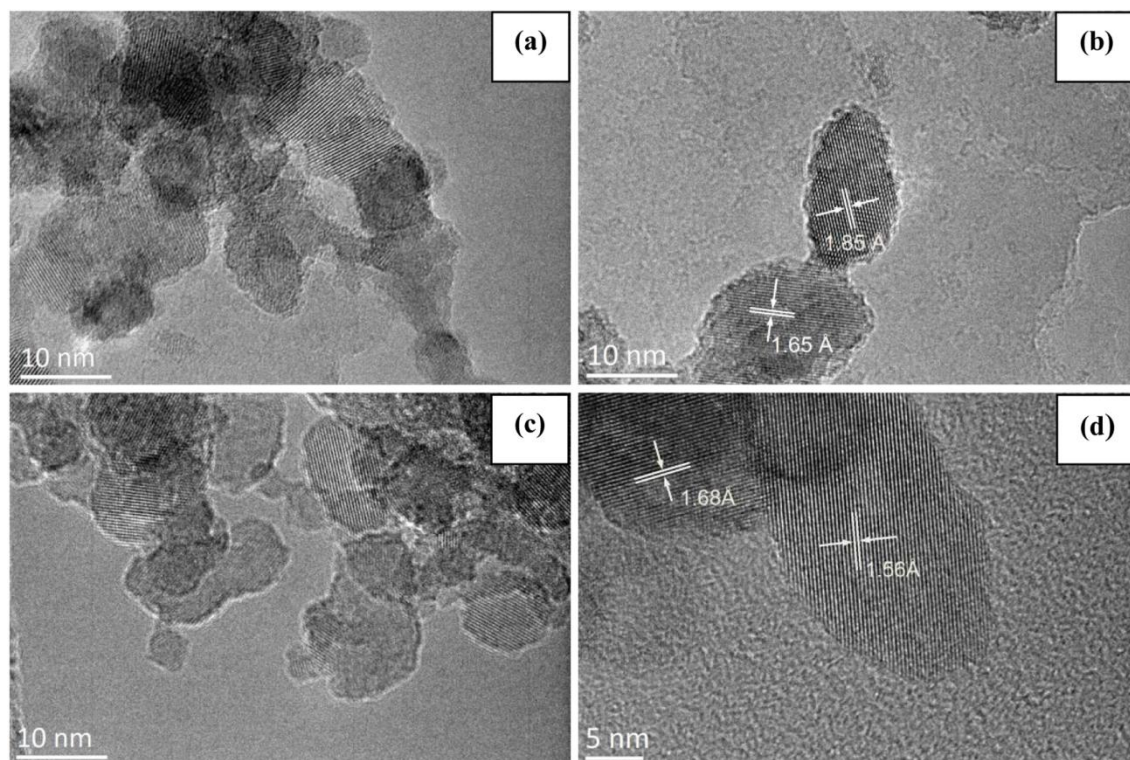


Figure 4.17. (a) to (c), Field emission transmission electron microscope microrgraphs of TiO₂. (d), MgO-doped TiO₂ nanoaerogel annealed at 400 °C.

The synthesised TiO₂-based nanoaerogels were also investigated by TEM analysis to obtain the morphology and structure characteristics. The high resolution FE-TEM images {see Figure 4.17(b) and (d)} of dispersed NPs indicate their crystalline nature with lamellar lattice morphology. However, the statistical analysis of the size distribution from TEM data was difficult to obtain due to the agglomeration of the NPs. The grain size ranges of 5-15 nm were measured from those discrete particles, which is consistent with the structural parameters that are obtained from the XRPD measurements.

4.4.1.2 Structural properties

Figure 4.18(a) and (b) shows the nitrogen-sorption isotherms of TiO₂ and MgO-doped TiO₂ aerogels prepared in current work. The isotherms show mono-layer at the low value of relative pressure (P/P_0), followed by the formation of multi-layer and capillary condensation. The TiO₂ aerogels show a specific surface area of $\sim 154.3 \text{ m}^2/\text{g}$, which is comparable to the aerogels ($82 \text{ m}^2/\text{g}$) prepared using high temperature

supercritical drying of sol-gel methods as reported by Parayil et al [151].

The density functional theory (DFT) pore size distribution (PSD) plot of undoped-TiO₂ aerogels {see Figure 4. 18(c)} indicates a typical mesopore range from 4 to 20 nm with pores centred at 6.8 nm. This isotherm exhibits a combination of Type IV and Type H2 (a) hysteresis {categorised by International Union of Pure and Applied Chemistry (IUPAC)} [178]. In case of MgO-doped TiO₂ aerogels, the PSD plot {see Figure 4.18(d)} exhibits a sharp peak and triangle-like shape, indicating comparatively smaller pores centred at 5.2 nm, a larger surface area of $\sim 231.4 \text{ m}^2/\text{g}$ was observed.

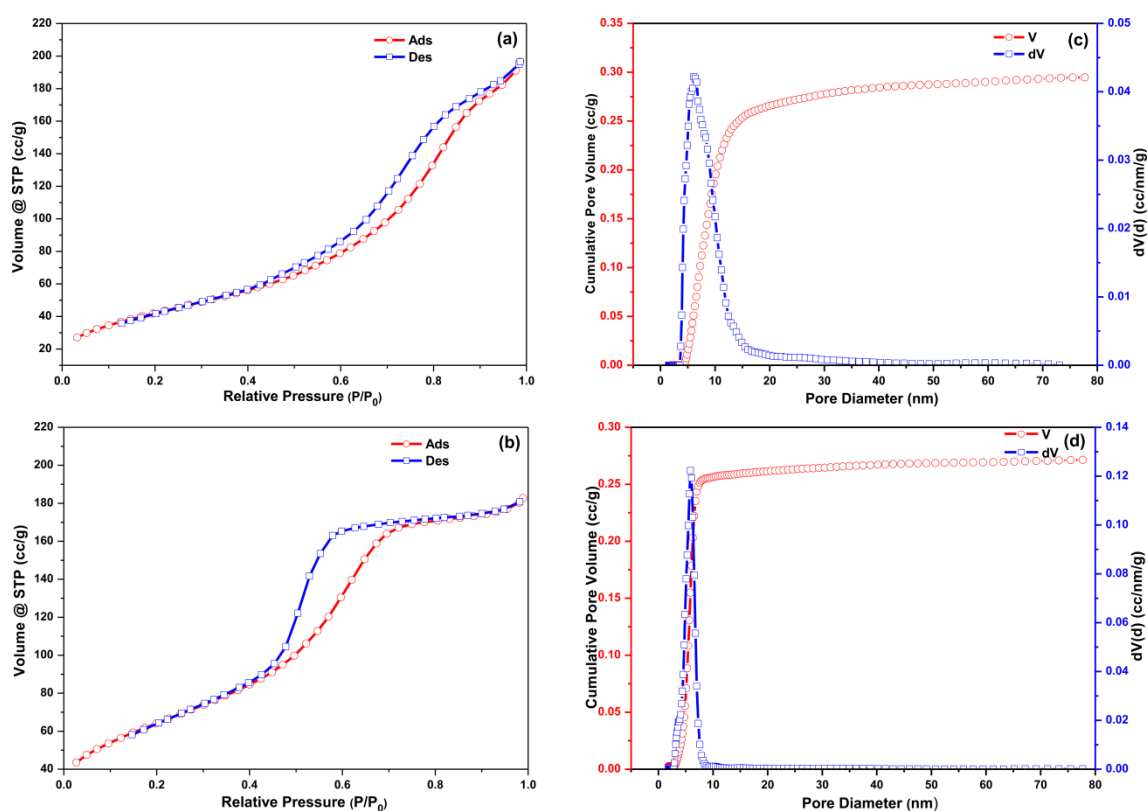


Figure 4.18. N₂-sorption isotherms of (a) representative TiO₂ aerogel and (b) MgO-doped TiO₂ aerogel; c and d, the corresponding pore size distribution plots are shown.

The remarkable increase of surface area in MgO-doped TiO₂ nanoaerogels is attributed to the slight reduction in grain size, which is mainly caused by the interface stress and lattice contraction resulting from the replacement of Ti (Ti⁴⁺ average ionic radius = 0.058 nm) by Mg (Mg²⁺ average ionic radius = 0.071 nm) [179]. The detailed structural properties of the aerogels are summarised in Table 4.6.

Table 4.7. Structural properties of TiO₂-based nanoaerogles.

Materials	S_{BET} (m ² /g)	Pore Volume (cm ³ /g)	Pore diameter (nm)	Crystallite size (nm)
TiO ₂ (this work)	154	0.29	6.8	10
MgO-doped TiO ₂ (this work)	231	0.27	5.2	8
TiO ₂ [127]	82	0.25	11	20

4.4.2 Solely EVA Layer

DSC thermodynamic measurement was used to determine the curing temperature that enhances the transparency of the EVA raw material. Figure 4.19 shows the heat flow diagram of raw EVA material obtained from the DSC measurements.

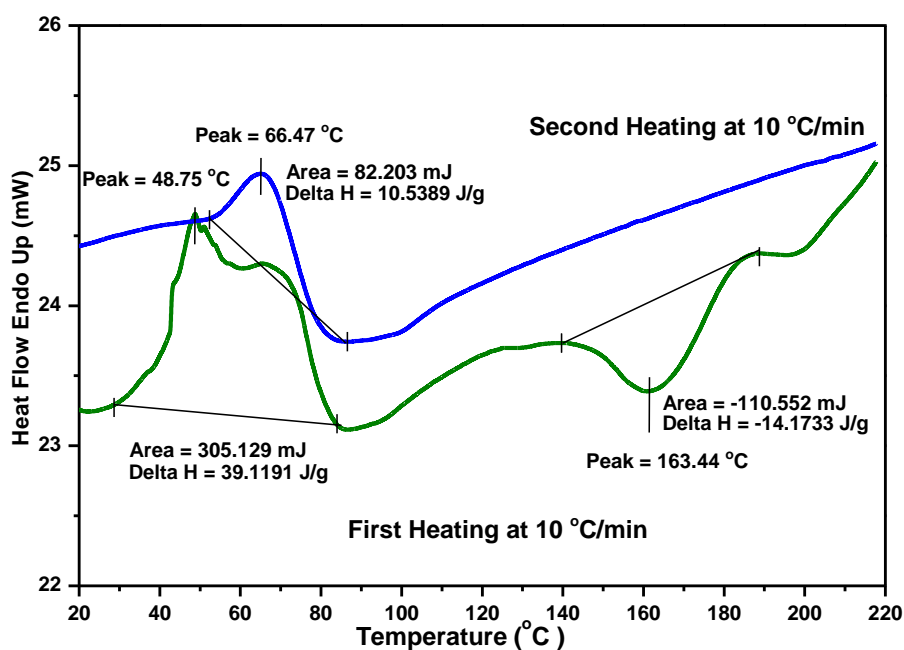


Figure 4.19. The differential scanning calorimetry heating curves of raw ethylene vinyl acetate material.

It can be seen from Figure 4.19 that the first heating curve shows an endothermic peak at 48.75 °C with an enthalpy of 39.12 J/g. The exothermic peak occurred at 163.44 °C with the curing enthalpy of 14.17 J/g. The second heating curve shows a lower melting peak of 10.54 J/g compared to the first scan (39.12 J/g), and no exothermic peak can be detected, implying full curing of EVA. The shift in the endothermic peak, the reduction of the melting enthalpy and the disappearance of the curing peak, suggest

a complete crosslinking in the EVA's crystal structure [120]. From the first heating curve, it was observed that the exothermic region is completed at 186 °C, which represents the optimum curing temperature for the coated solar cell.

Figure 4.20 shows the transmission spectra of glass substrates coated with solely EVA layers at different weight ratio (wt%) after the heating process. It can be seen that the coated layers with concentration of 9, 12, 15, 18 and 21wt% exhibit good light transparency with transmittance close to that of a glass substrate within the tested wavelength of 200 to 800 nm. Since the thickness of masking tape that determines the wet film thickness is fixed and the coating procedure for each coated layer is nearly consistent, the higher value of wt% means more EVA content in the dry layer that is obtained. This results in more additives contained in the deposited layer that slightly reducing the transmittance, as can be seen from the inset plot of Figure 4.20.

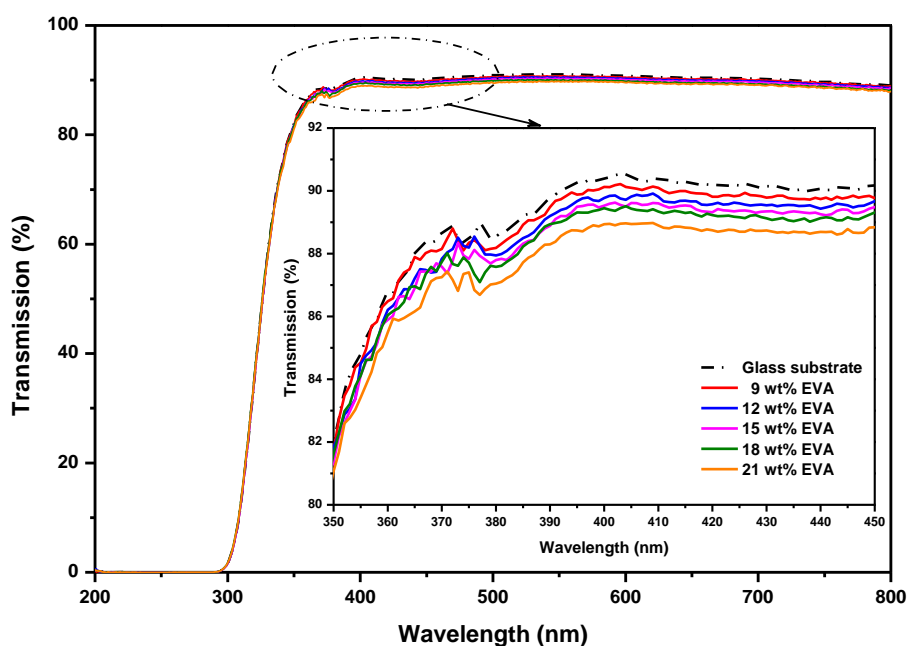


Figure 4.20. Transmission spectra of solely EVA layers with different weight ratio (wt%) deposited on the glass substrate.

Figure 4.21 shows the optical reflection and absorption spectra of the uncoated and coated cells with various wt% ratios of solely EVA layers. It could be seen that coated cells with EVA layers show overall less reflectance and higher absorbance compared with uncoated cells across the measured spectral wavelength range from 260 to 800 nm. A significant reduction in reflectance especially in the UV-region of 280 nm to 400 nm

was observed. This is due to the promotion of light trapping particular in the short wavelength of solar spectrum by adding the EVA layer on top surface of the mono-Si solar cells. These results basically coincide with the initial expectations because the average refractive index of EVA ($n \approx 1.48$) is between the SiN_x anti-reflection coating layer ($n \approx 1.9$) and air ($n \approx 1$) [156, 180]. As indicated the EVA serves as a binder for the TiO_2 based NPs, which also has the tendency to block the incoming light and thus decreasing the cells' efficiency, whereas in fact, the solely EVA coatings at different wt% possess good light-transparency with transmittance close to that of a glass substrate, which is confirmed by the transmittance measurement (see Figure 4.20).

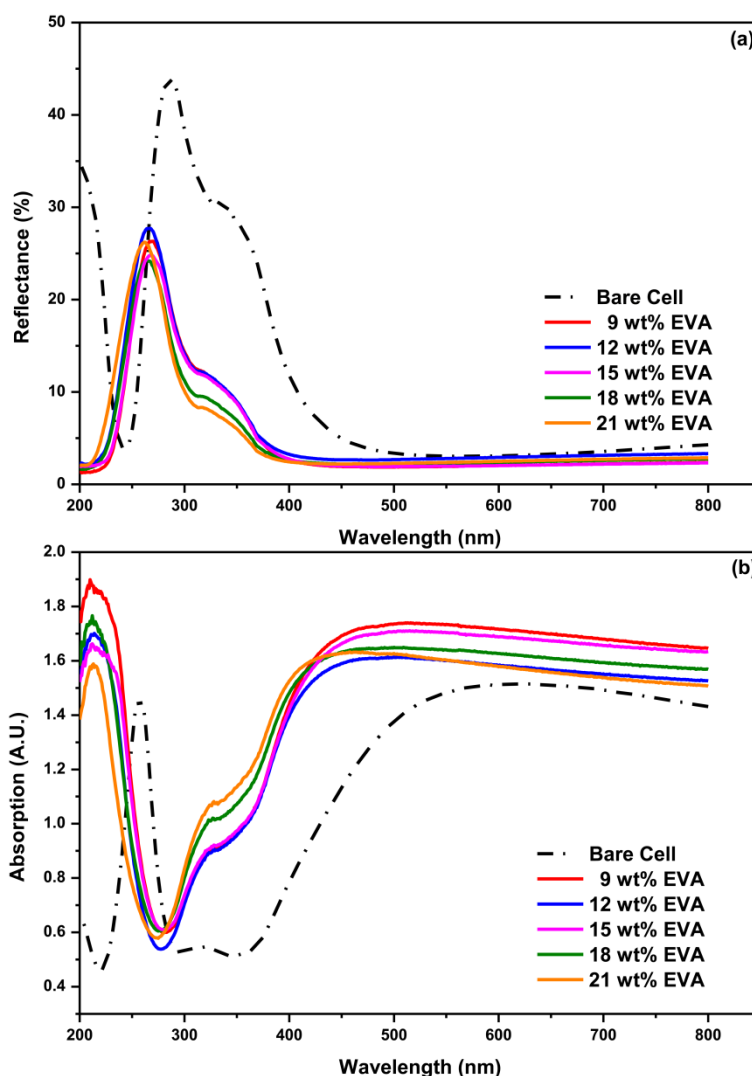


Figure 4.21. Reflection and absorption spectra of uncoated cell and cell coated with various weight ratios of EVA.

Table 4.8 summarises the influence of EVA coatings on the electrical characteristics

of the mono-Si solar cells in which the J - V curve for optimum coating condition is shown in Figure 4.22. It was found that the coated cell with EVA at 15-wt% has resulted in a minimum decrease in cells photovoltaic performance among other tested ratios of solely EVA coatings in which the J_{sc} and V_{oc} showed negligible reduction of 0.2 mA/cm² (from 36.59 mA/cm² to 36.39 mA/cm²) and 0.3 mV (from 599.1 mV to 598.8 mV) respectively, which leads to a marginal decrease of 0.11% (from 15.76% to 16.65%) in power conversion efficiency. Hence, this ratio is considered to be as the most suitable candidate for encapsulating TiO₂-based NPs to the solar cell that potentially contributed to maximising the PCE enhancement.

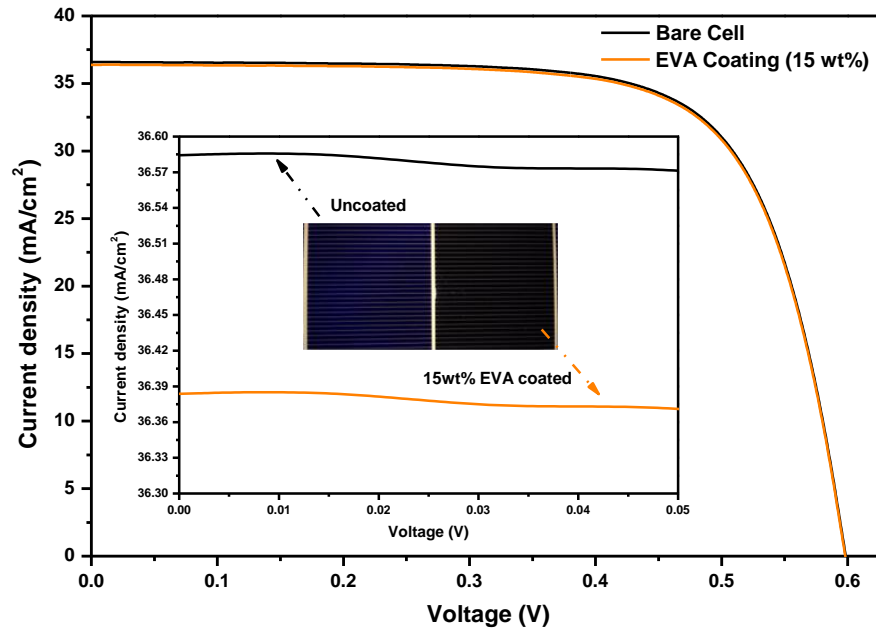


Figure 4.22. Photovoltaic J-V curves of mono-Si solar cell before and after coating with 15 wt% EVA examined at 1000 W/m² and 25 °C, with illuminated surface area of 8.553 cm².

Table 4.8. PCE change in mono-Si solar cell coated with different wt% ratios of EVA.

<i>Cell type</i>	<i>Concentration in wt%</i>	<i>Uncoated η (%)</i>	<i>Coated η (%)</i>	<i>Change in Absolute η (%)</i>
EVA	9	15.79	15.36	-0.43
EVA	12	15.67	15.41	-0.26
EVA	15	15.76	15.65	-0.11
EVA	18	15.76	15.61	-0.15
EVA	21	15.78	15.59	-0.19

Another factor that has to be considered is the fluidity of the coating solution. Although the solar cells with EVA coating at 18 wt% and 21 wt% ratios show also minor reduction in conversion efficiency, but their liquid solutions appear to have much higher viscosity than other ratios. This can be seen in Figure 4.23 in which the mixture solutions of EVA/p-xylene with 18 wt% and 21 wt% show dynamic viscosity of 260.8 Pa·s and 316.7 Pa·s respectively at 30 °C, more than twice that of the solution with 15 wt% ratio (111.5 Pa·s). An increase in viscosity of the coating solution gives rise to a decrease in fluidity and mobility [181], which inevitably brings technical difficulties during the coating procedure. This factor, however, is influential on the surface homogeneity and uniformity of the wet film coating as well as the optical properties of the dry layer. Therefore, it is of importance to maintain liquid viscosities at a certain level in order to effectively transfer the liquid materials onto the surface of solar cell.

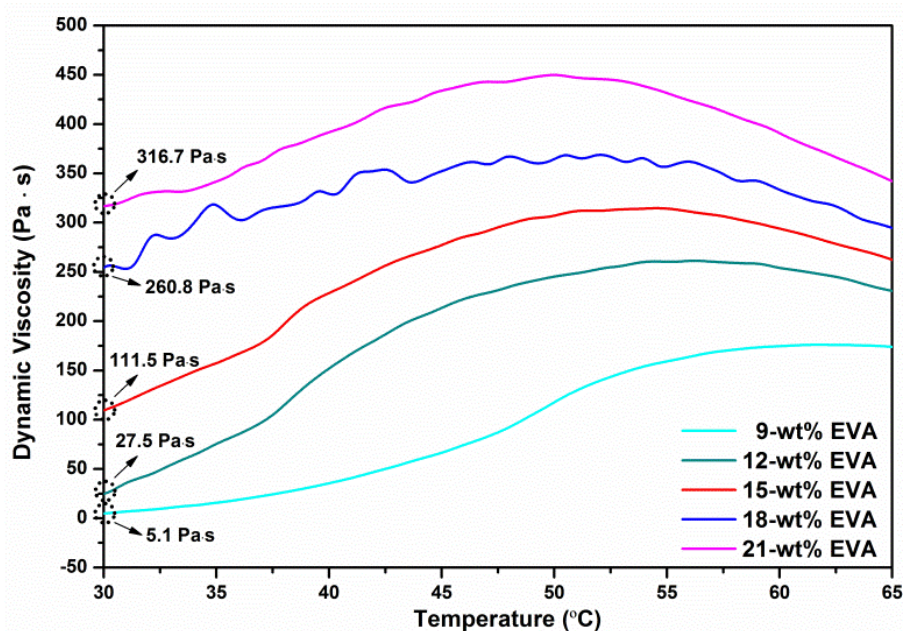


Figure 4.23. Viscosity as a function of temperature for different concentrations of EVA/p-xylene solutions.

4.4.3 EVA/TiO₂ and EVA/MgO-TiO₂ composite layer

4.4.3.1 Electrical characteristics of coated solar cell

The *J-V* characteristics of bare, solely EVA binder-coated, EVA/TiO₂, and

EVA/MgO-TiO₂-coated solar cells are shown in Figure 4.24. The bare mono-Si solar cell exhibited a *PCE* of 15.76%, a short-circuit current density (J_{sc}) of 36.59 mA/cm², and an open-circuit voltage (V_{oc}) of 599.1 mV. After coating with 15-wt% EVA on the textured surface, the *J-V* characteristics showed a slight change in J_{sc} (36.39 mA/cm²) and V_{oc} (598.8 mV). The formation of the EVA layer on top of the solar cells resulted in a marginal reduction of 0.11% (from 15.76% to 15.65%) in conversion efficiency. This coating provides the best electrical performance compared to other ratios of solely EVA coatings, which has been demonstrated in previous section (see Table 4.7).

In the case of the cell that was coated with EVA/TiO₂ nanocomposite at 0.3-mg/ml concentration, the *J-V* characteristics exhibited significant increase with $\Delta J_{sc} = 0.59$ mA/cm² and $\Delta V_{oc} = 4.5$ mV, corresponding to an overall enhancement of 3.4% (from 15.76% to 16.29%) in *PCE* relative to those for a bare cell. The highest increase of $\Delta J_{sc} = 1.14$ mA/cm², corresponding to a maximum enhancement of 6.0% (from 15.76% to 16.70%) was achieved by integrating EVA/MgO-doped TiO₂ nanocomposite (0.3-mg/ml) on the cell's textured surface.

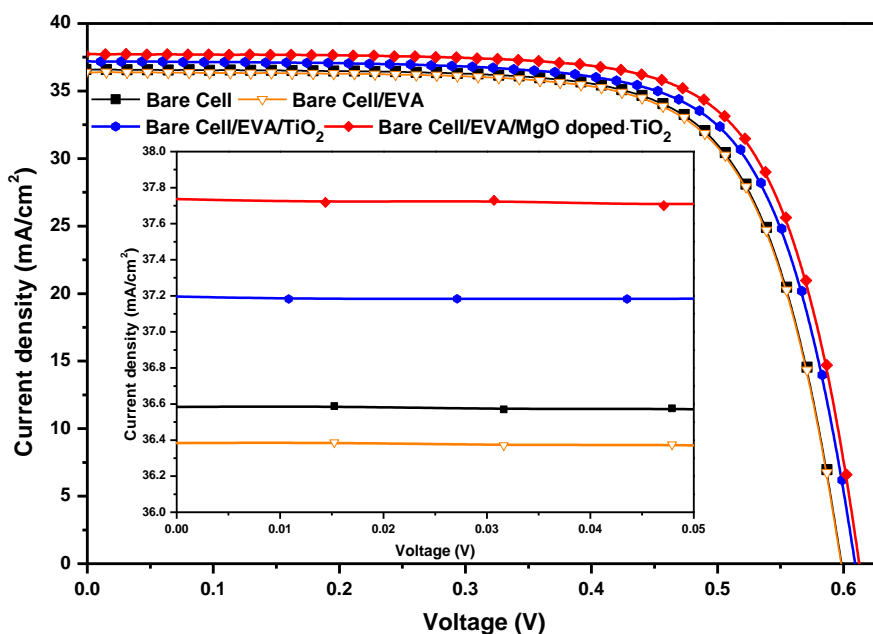


Figure 4.24. Photovoltaic *J-V* curves of mono-Si solar cells before and after coating with solely EVA, EVA/TiO₂, and EVA/MgO-doped TiO₂.

Also, the results demonstrated that the concentration of dispersed TiO₂ NPs encapsulated in EVA binder has a strong influence on the amount of light absorbed and

thus the PCE of the solar cells. Figure 4.25 shows the enhancement in PCE of the coated cells as a function of deposited TiO₂ based NPs with different particle concentrations. It can be seen that the cells coated with MgO-doped TiO₂ NPs increased the conversion efficiency at all tested concentrations. Typically, 0.46%, 0.94%, 0.64%, 0.39% and 0.04% is obtained at 0.2-mg/ml, 0.3-mg/ml, 0.4-mg/ml, 0.6-mg/ml and 0.8-mg/ml respectively. The only reduction in PCE occurs in the cell that coated with undoped TiO₂ NPs at 0.8-mg/ml (15.76% to 15.63%) due to the aggregation of particles that diminishes the light-trapping capability of the cell's intrinsic textured surface, which can cause excessive backward scattering [182]. The detailed characteristics of coated cells with TiO₂ based NPs at different concentrations are summarised in Table 4.9

Table 4.9. J-V characteristics of mono-Si solar cells before and after coating with solely EVA, EVA/TiO₂ and EVA/MgO doped-TiO₂.

<i>Cell Type</i>	<i>J_{sc}</i> (mA/cm ²)	<i>V_{oc}</i> (mV)	<i>P_{max}</i> (W)	<i>FF</i> (%)	<i>PCE</i> (%)
Uncoated	36.59	599.1	0.1348	71.91	15.76
Cell/EVA	36.39	598.8	0.1339	71.85	15.65
Cell/EVA/TiO ₂ (0.2 mg/ml)	36.77	602.6	0.1367	72.10	15.98
Cell/EVA/TiO ₂ (0.3 mg/ml)	37.18	603.9	0.1394	72.58	16.29
Cell/EVA/TiO ₂ (0.4 mg/ml)	36.97	602.9	0.1381	72.44	16.15
Cell/EVA/TiO ₂ (0.6 mg/ml)	36.66	601.4	0.1352	71.70	15.81
Cell/EVA/TiO ₂ (0.8 mg/ml)	36.47	597.2	0.1337	71.77	15.63
Cell/EVA/MgO-TiO ₂ (0.2 mg/ml)	36.97	606.4	0.1387	72.40	16.22
Cell/EVA/MgO-TiO ₂ (0.3 mg/ml)	37.73	608.1	0.1428	72.77	16.70
Cell/EVA/MgO-TiO ₂ (0.4 mg/ml)	37.47	607.2	0.1411	72.53	16.50
Cell/EVA/MgO-TiO ₂ (0.6 mg/ml)	37.06	606.3	0.1381	71.89	16.15
Cell/EVA/MgO-TiO ₂ (0.8 mg/ml)	36.61	601.7	0.1351	71.79	15.80

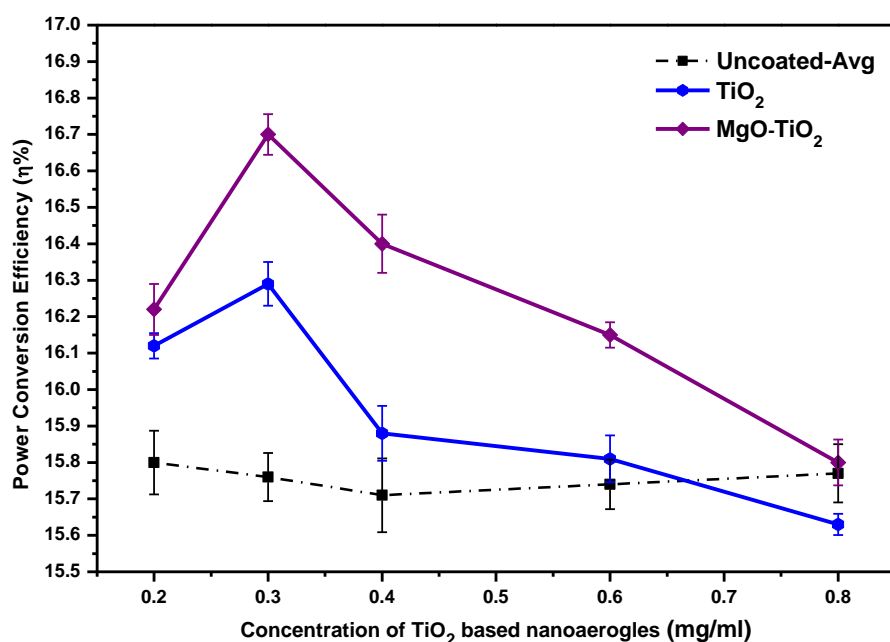


Figure 4.25. Enhancement in power conversion efficiency of mono-Si solar cells coated with EVA/TiO₂ and EVA/MgO-doped TiO₂.

By comparing the electrical performance of uncoated, solely EVA coated and EVA/TiO₂ based nanoparticle coated cells at different particle concentrations, it was found that the enhancement in power conversion efficiency is attributed to the effects of both EVA binder and TiO₂ nanocomposite. The EVA encapsulated MgO-TiO₂ with 1:50M coating provides a maximum enhancement of 0.94% absolute efficiency enhancement at concentration of 0.3-mg/ml. For the pure TiO₂ coating with 0.3-mg/ml, this increase is not as much as MgO doped TiO₂, which is 0.53%.

Figure 4.26 shows the temperature coefficient of open circuit voltage (V_{oc}) for the uncoated, EVA-coated, EVA/TiO₂ and EVA/MgO-doped TiO₂-coated solar cells. It can be seen that the V_{oc} for each case of tested cells shows varying degrees of drop with the increasing of cell temperature. In addition, the results demonstrate expressly that the solar cells with enhanced photovoltaic performance exhibit overall less voltage drop of ~ -2.7 mV/°C and ~ -2.3 mV/°C for EVA/TiO₂ and EVA/MgO-doped TiO₂-coated cells respectively, compared to that of uncoated cell (-3.1 mV/°C).

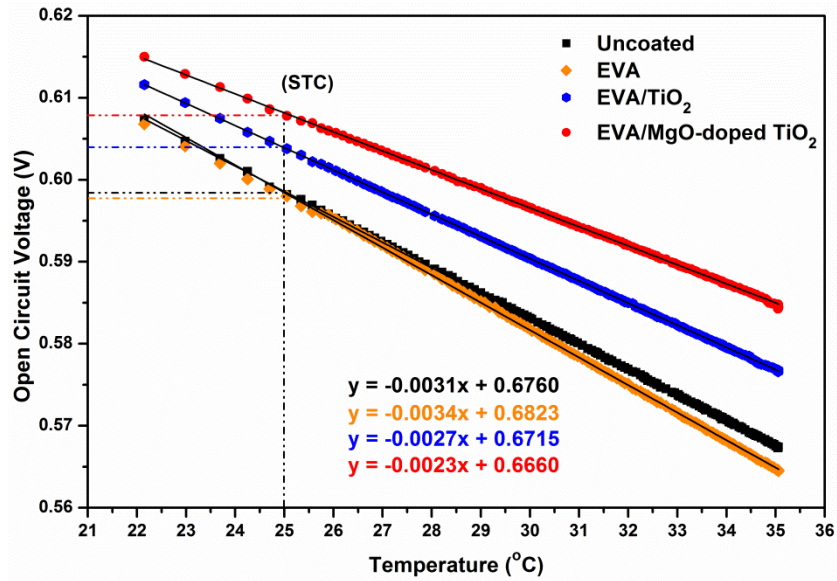


Figure 4.26. Fundamental temperature coefficient of open circuit voltage as a function of cell temperature. The inset fitting equations were derived for each case of tested solar cell.

J-V measurements were also carried out under UV illumination with light intensity of 45.9 W/m^2 at room temperature of $25 \text{ }^\circ\text{C}$. The current density-voltage (*J-V*) characteristics that were obtained from the uncoated, solely EVA-coated (15-wt% ratio), EVA/TiO₂-coated, and EVA/MgO-TiO₂-coated solar cells (0.3-mg/ml) are shown in Figure 4.27.

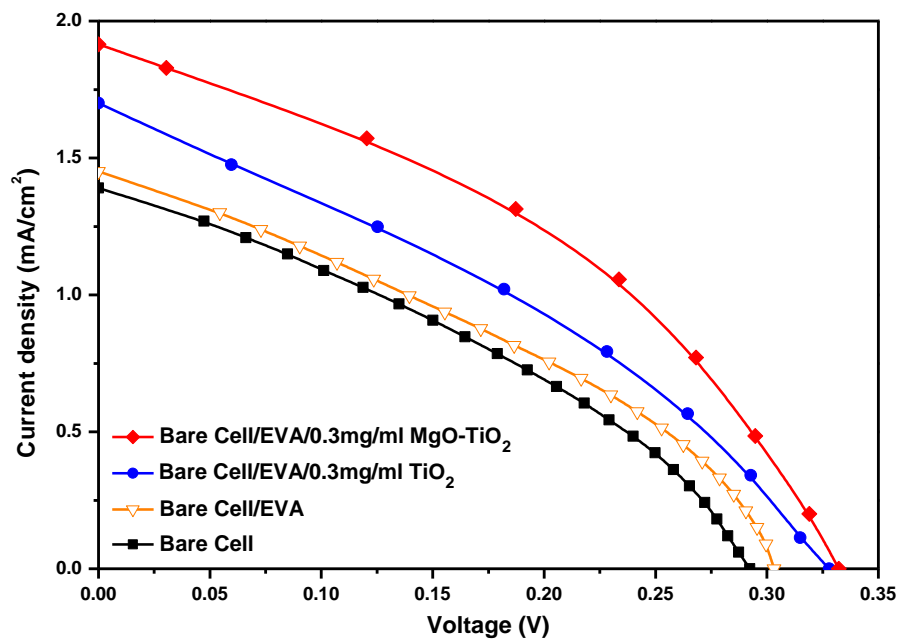


Figure 4.27. *J-V* characteristics of the uncoated cell and cells coated with solely EVA, EVA/TiO₂, and EVA/MgO-doped TiO₂ under UV illumination with light intensity of 45.9 W/m^2 .

The coated cells show overall higher J_{sc} and V_{oc} than that of bare cell, and thus contribute to enhancement in PCE. It was found that the best results were achieved when the cell coated with EVA/MgO-doped TiO_2 (0.3-mg/ml) in which the $J_{sc} = 1.92 \text{ mA/cm}^2$, $V_{oc} = 332 \text{ mV}$, compared to that of EVA/ TiO_2 (0.3-mg/ml) coated cell where $J_{sc} = 1.70 \text{ mA/cm}^2$, $V_{oc} = 323 \text{ mV}$, and uncoated cell with $J_{sc} = 1.39 \text{ mA/cm}^2$, $V_{oc} = 293 \text{ mV}$. Other parameters show varying degrees of enhancement. The cell with solely EVA coating at 15 wt% ratio also shows marginal increase in both J_{sc} and V_{oc} compared to the bare cell. Detailed electrical characteristics of the coated solar cells are summarised in Table 4.10.

Table 4.10. Electrical characteristics of the uncoated and coated solar cells under UV illumination with light intensity of 45.9 W/m^2 .

<i>Cell Type</i>	<i>J_{sc} (mA/cm²)</i>	<i>V_{oc} (mV)</i>	<i>P_{max} (mW)</i>	<i>FF</i>	<i>PCE (%)</i>
Uncoated	1.39	293	1.20	0.34	3.06
EVA	1.45	303	1.31	0.34	3.34
EVA/ TiO_2	1.70	323	1.59	0.33	4.05
EVA/MgO-doped TiO_2	1.92	332	2.11	0.38	5.37

4.4.3.2 Microstructure of coated solar cell

Figure 4.28 displays the cross-section FE-SEM images of the mono-Si solar cells coated with EVA/ TiO_2 and EVA/MgO-doped TiO_2 composite layers. The images show clearly the morphology of pyramidally textured silicon surface and the coated layers comprised of EVA/ TiO_2 and EVA/MgO- TiO_2 with an average thickness of $9.2 \text{ }\mu\text{m}$ and $9.0 \text{ }\mu\text{m}$ respectively. In addition, the coated layers show good uniformity, some of the particles are deposited onto the solar cell's surface through blade screen printing technique while most of them are well encapsulated by the EVA binder.

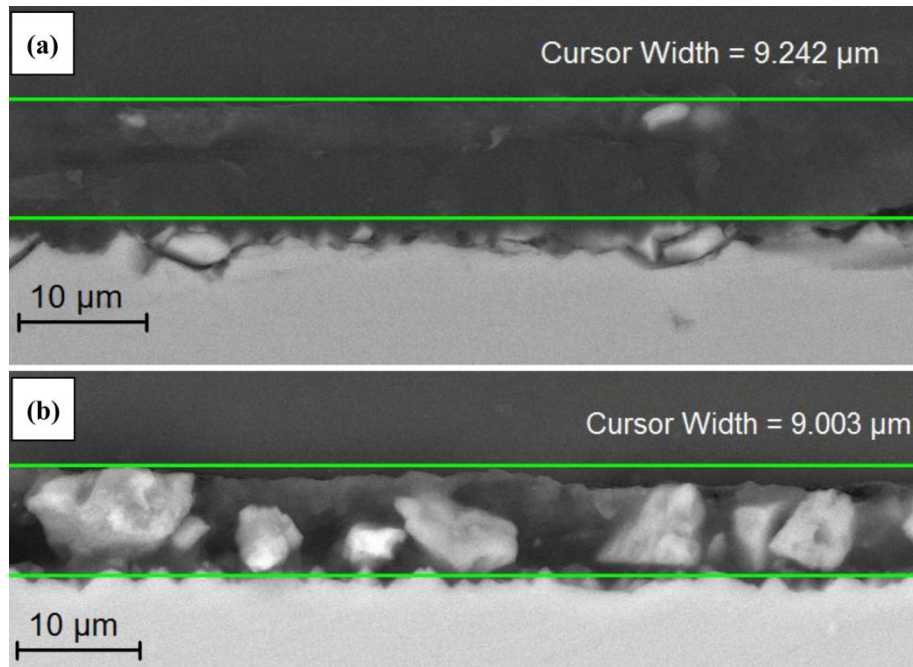


Figure 4.28. Cross section SEM images of the coated mono-Si solar cells with (a) EVA/TiO₂ and (b) EVA/MgO-doped TiO₂.

The corresponding EDS spectra from the entire FE-SEM scanned area of the coated cells are presented in Figure 4.29. It expressly confirms the presence of titanium (Ti), oxygen (O) and magnesium (Mg) elements in the deposited layers. The additional peaks corresponding to C are from the EVA binder. The insignificant intensity peaks of Fe and Cr observed in the spectra are due to the contamination during the fabrication process of powder samples as explained previously. No detectable chlorine peak was found, indicating that the TiCl₄ precursor has been decomposed prior to the deposition.

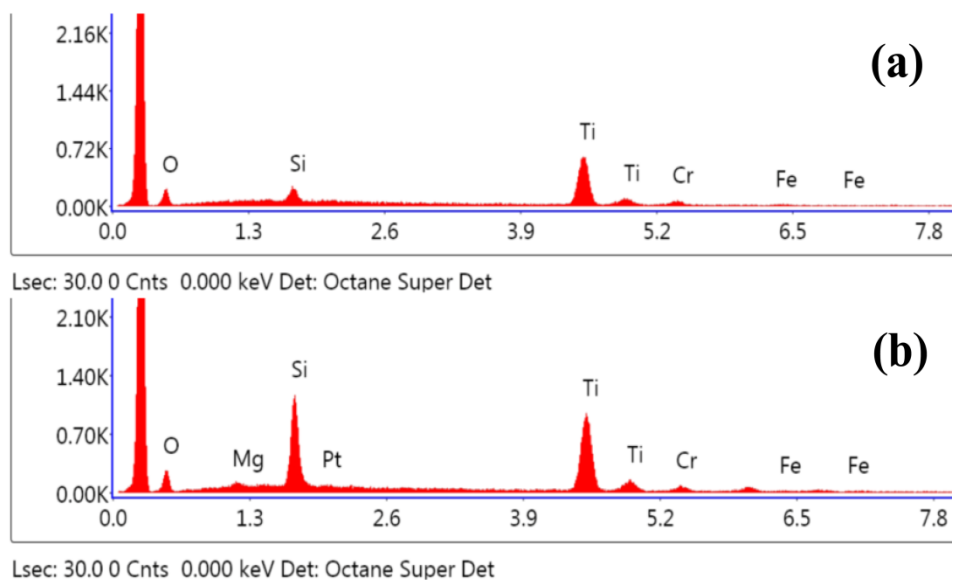


Figure 4.29. Energy-dispersive X-ray spectroscopy of mono-Si solar cells coated with (a) EVA/TiO₂ and (b) EVA/MgO-doped TiO₂.

4.4.3.3 Optical characteristics of coated solar cell

To further validate the obtained results regarding the efficiency enhancement brought by the TiO₂-based nanoaerogels, the reflectance measurements for these devices were performed. Figure 4.30 shows the optical reflectance and absorption spectra measured from uncoated, EVA/TiO₂ coated, and EVA/MgO-TiO₂ coated-solar cells with varying degrees of particle densities. Comparison between these cells indicates that TiO₂-based nanoaerogels coating on the surface of mono-Si solar cells could effectively reduce the reflection in the UV range. The coated cells with enhanced electrical characteristics exhibit overall less reflectance and higher absorbance compared with uncoated cells across the measured spectral wavelength range from 200 to 800 nm.

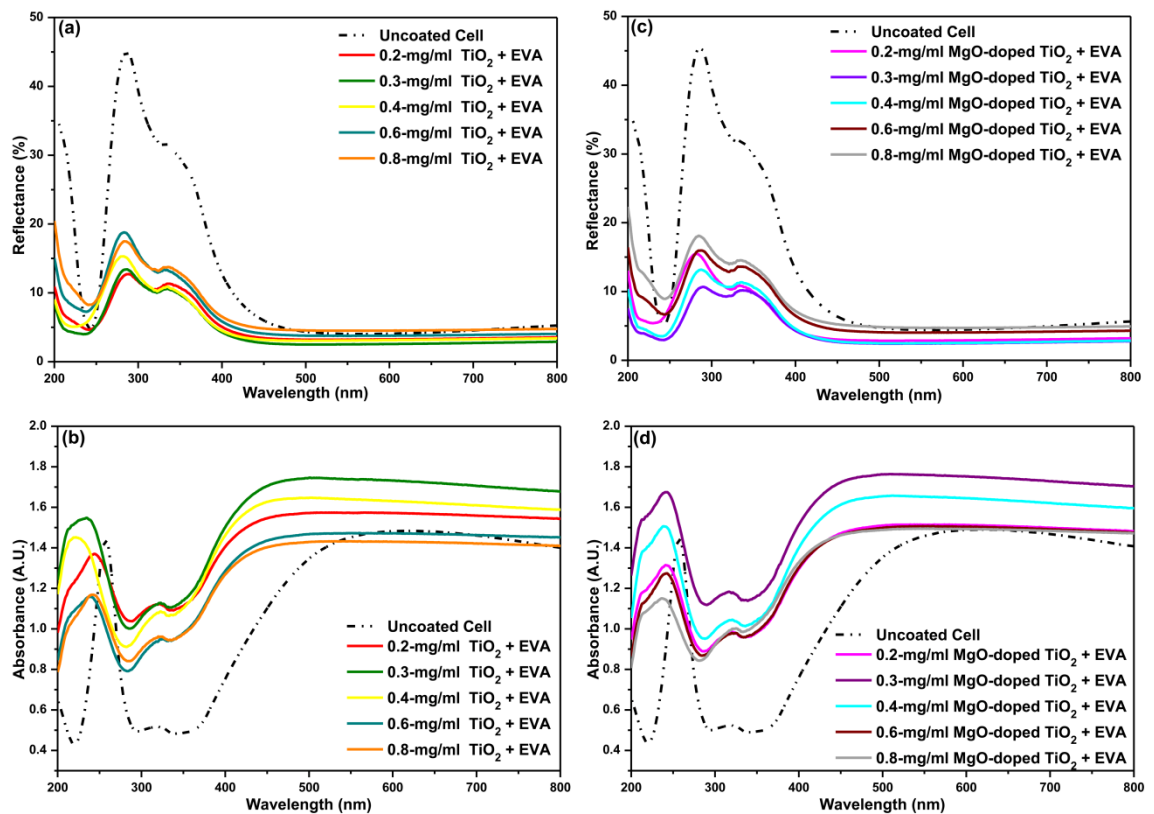


Figure 4.30. Comparison of optical reflectance and absorption spectra for uncoated and coated cells with the following configurations: (a), (b) EVA/TiO₂-coated and (c), (d) EVA/MgO-doped TiO₂-coated cells compared to those of bare cells.

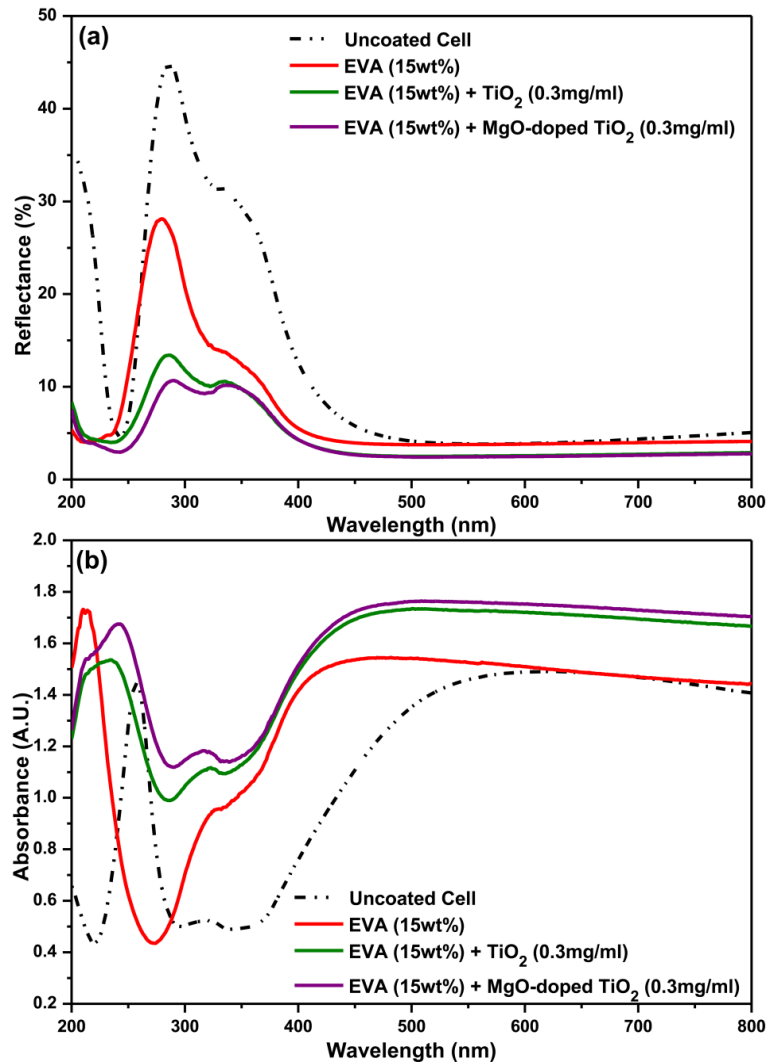


Figure 4.31. Optical (a) reflectance and (b) absorbance of uncoated and cells coated with solely EVA (15-wt%), EVA/TiO₂ (0.3-mg/ml) and EVA/MgO-doped TiO₂ (0.3-mg/ml).

Figure 4.31 compares the optical reflectance and absorption spectra for uncoated, solely EVA-coated (15-wt%), EVA/TiO₂-coated (0.3-mg/ml), and EVA/MgO-TiO₂-coated (0.3-mg/ml) solar cells that contribute to the maximum enhancement in power conversion efficiency. It can be seen clearly that the reflectance of coated cell with EVA/MgO-TiO₂ shows a more significant reduction at wavelengths of 280 to 400 nm. The reduced reflectance for the enhanced solar cells is achieved by the light scattering from the spherical TiO₂ based nanoaerogels, as a result of improving in overall light trapping at the interface of the textured ARC layer. Since the light scattering abilities rely largely upon the particle size, the larger particles may cause an increased cross-section for backward scattering, which shades the pyramid structures

[182]. In this work, the diameter of the TiO₂ based nanoaerogels (5-15 nm) was much less than the spacing between the pyramids. Hence, the particles didn't impair the light benefits on the original ARC layer, whereas, the incident light was forward scattered into the cell through the TiO₂ based NPs. Furthermore, the aerogels with meso-porous microstructure potentially allow more incident light to transmit through the pore and shine onto the ARC layer over a large angular range, increasing the optical path length of photons in the cell, thereby enhancing the light harvesting [144, 146]. The drastic reduction of reflectance in the range of 250-350 nm is due to the absorption of high-energy incident photons mainly in the short-middle wavelength UV-region. This can be confirmed by the UV-Vis absorption spectra as performed on the quartz substrates (see Figure 4.32) in which a more pronounced enhancement in absorption by MgO-TiO₂ mixed oxides (MgO:TiO₂ = 1:50) was observed at the shorter wavelength.

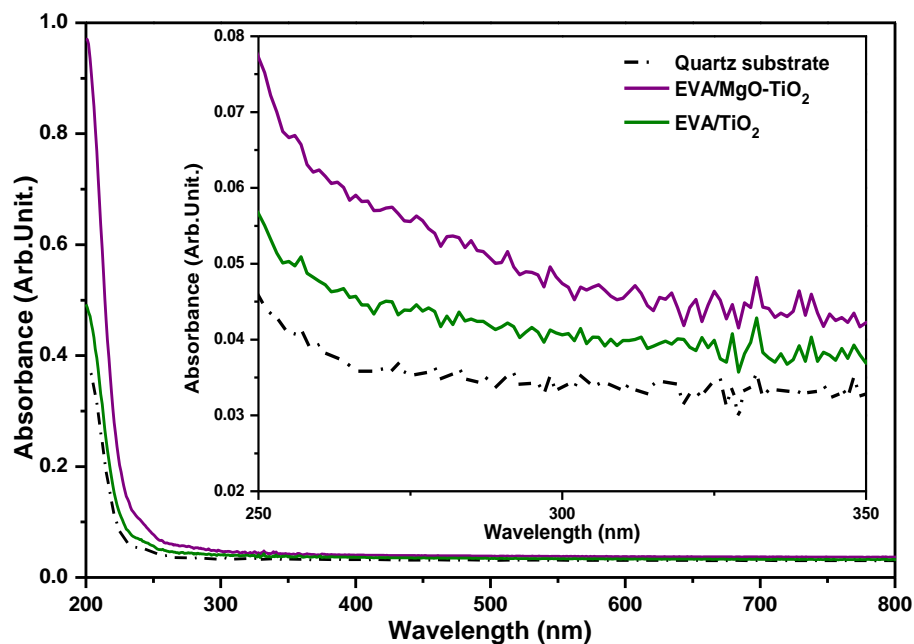


Figure 4.32. Ultra-visible absorption spectra of quartz substrate and the deposited nanocomposite films of EVA/TiO₂ and EVA/MgO-doped TiO₂.

The surface modification of the mixed oxide by adding small amounts of MgO into TiO₂ nanoaerogels is a more reasonable explanation for the additional reduced reflectance. When Mg²⁺ ions are doped into the TiO₂ nanoaerogels, various types of crystal defects and vacancies are created to compensate the charge neutrality in TiO₂ crystal, contributing to further enhancement in the UV photocatalytic reactivity [132,

156, 180]. In addition, the smaller NPs with higher surface-to-volume ratio may probably induce more photons to be absorbed at the short-middle wavelength UV region for photo-current conversion [138, 143].

The comparison from reflection spectra also indicates that the reflectance in the spectrum range of 300 to 450 nm can be reduced when the cell's surface is coated with 15-wt% EVA layer, which has been demonstrated in the previous section. This finding also confirms the outstanding light absorption properties of EVA in the short-wavelength of solar spectrum [152]. Since the EVA serves as a binder for the TiO₂ based NPs, it has to provide a relatively high transmittance so as not to block the incident light, and thus more savings of incoming energy. At the same time, it should also possess with adapted refractive index to minimise the Fresnel reflection loss during the light absorption at the interface of solar cell. Actually, the average refractive index of EVA ($n \approx 1.48$) is between the SiN_x anti-reflection coating layer ($n \approx 1.9$) and air ($n \approx 1$) [156, 180], which provides improved RI matching when sandwiched between the SiN_x layer and air. Additionally, from the transmission measurements of the coated layers, it was observed that the solely 15 wt% EVA coating possesses good light-transparency with transmittance close to that of a glass substrate, which is shown in Figure 4.33. This coating is featured by its high light transmittance over 86% in the visible spectrum range of 400 to 800 nm. Hence, EVA can serve as a good binder and matrix. Moreover, the coated substrate with EVA/MgO-doped TiO₂ shows slightly higher transmittance as compared to the EVA/undoped-TiO₂ and the transmission spectra of the coated glass substrates reveals a gradually decrease with increased concentration of the dispersed TiO₂-based nanopowder, which can be observed in Figure 3.33 and Figure 3.34. This also explains the slight reduction in the J_{sc} and thus lower conversion efficiency in the case of solar cell that coated with undoped TiO₂ NPs at 0.8-mg/ml. The reduction in PCE (15.76% to 15.63%) is most likely due to the aggregation of particles that results in shading effects on the cell's intrinsic textured surface.

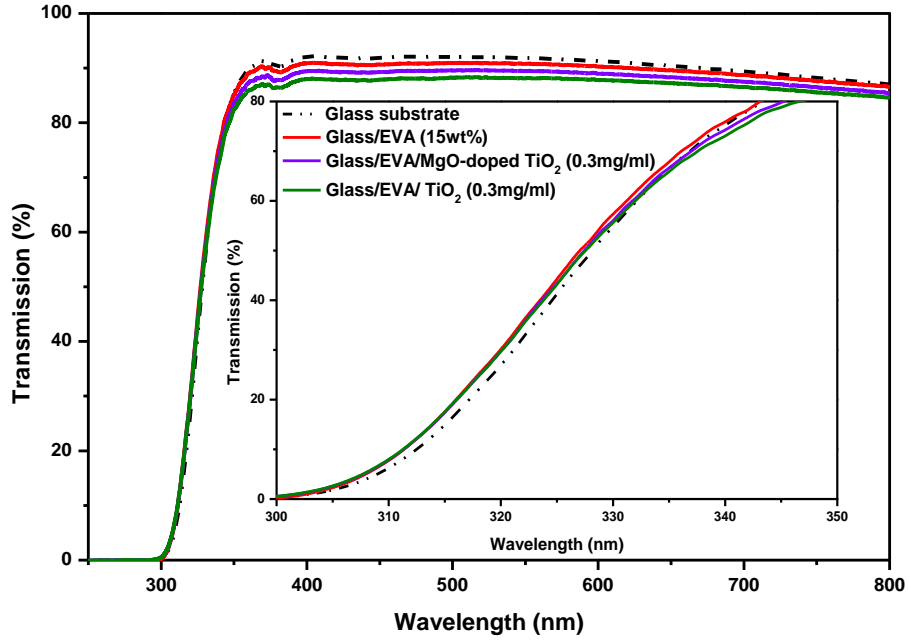


Figure 4.33. Transmission spectra for glass substrate and the deposited composite films with the following configuration: glass with solely EVA, glass with EVA/TiO₂, and glass with EVA/MgO-doped TiO₂.

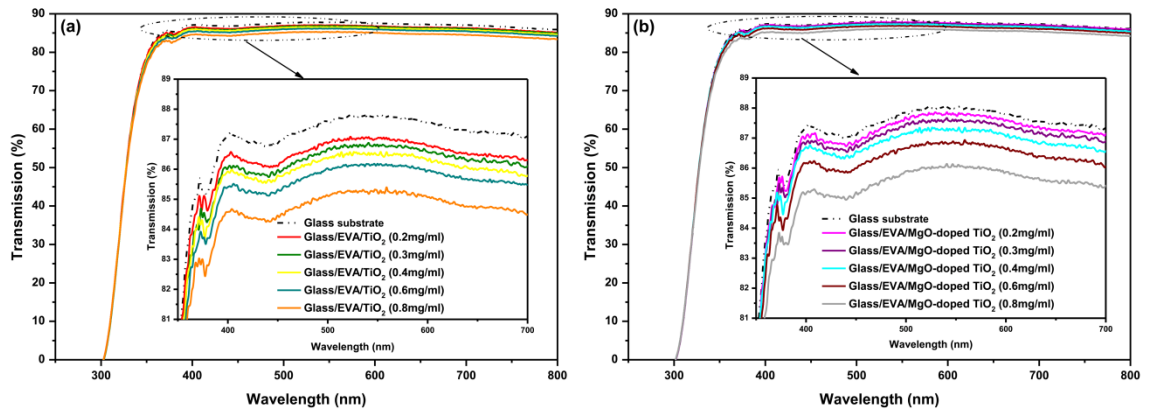


Figure 4.34. Transmission spectra for glass substrate and the deposited composite films with the following configuration: (a) EVA/TiO₂ and (b) EVA/MgO-TiO₂ at different particle densities.

The obtained transmittance spectra were also used to estimate the optical energy band gaps of the deposited composite films. In case of shorter wavelengths which close to the optical bandgap, the scattering losses are dominated by the fundamental absorption and the absorption coefficient α is given by the expression [185]:

$$\alpha = d^{-1} \ln(1/T) \quad (4.3)$$

where d is the thickness of the film and T is the optical transmittance. Considering that the indirect allowed transition dominates over the optical absorption, the optical energy

bandgap of the deposited TiO₂/EVA and MgO-TiO₂/EVA films can be correlated to the absorption coefficient, α , using the Tauc expression [186, 187]:

$$(\alpha h\nu)^{1/2} = B (h\nu - E_g) \quad (4.4)$$

where E_g is the optical band gap, $h\nu$ is the absorbed photon energy, B is the band tailing parameter. The Tauc plots of $(\alpha h\nu)^{1/2}$ as a function of the photon energy are presented in Figure 4.35 (black and red). Note that the E_g values of the deposited films are obtained by extrapolating the linear portion of the curves to the photon energy axis rather than simply drawing the tangent line along the random point on the curves [187]. Therefore, the uncertainties in deriving bandgap energies depend solely on the determination coefficient values R^2 of the linear fit in each plotted curve. Here, the plotted curves show good approximation of optical energy band gaps of 3.10 eV and 3.17 eV for the deposited EVA/TiO₂ and EVA/MgO-TiO₂ with R^2 values of 0.935 and 0.897 respectively.

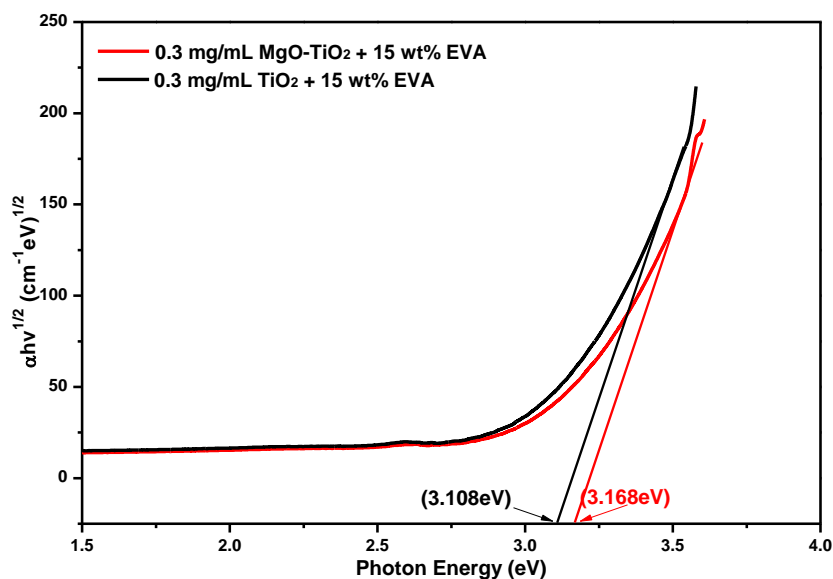


Figure 4.35. Optical energy bandgap of EVA/TiO₂ and EVA/MgO-TiO₂ composite films obtained by extrapolating the linear portion of the versus $h\nu$ value.

4.4.3.4 External quantum efficiency of coated solar cell

Figure 4.36(a) presents the EQE response for bare, solely EVA binder-coated, EVA/TiO₂ coated, and EVA/MgO-TiO₂ coated solar cells. The EQE value for binder-coated cells is fairly close to that of bare cells and is slightly higher at wavelengths of 300-330 nm, which achieves a close match with the reflectance measurements {see Figure 4.31(a)}. Furthermore, the solar cells coated with EVA/TiO₂ and EVA/MgO-TiO₂ composite layers provide enhanced photocurrent across the entire wavelength range from 300 to 1100 nm and more significant increase in EQE in the UV-region compared to the bare cell. This is due to the improved anti-reflective properties of EVA/TiO₂ and SiN_x, giving rise to an overall increase of photon harvesting on the cell's textured surface. Compared to the EVA/TiO₂ coated cell, the solar cell with EVA/MgO-TiO₂ layer achieves a more pronounced increase in EQE, particularly at wavelengths of 300-350 nm. These findings are also consistent with those observed variations in reflectance and J_{sc} . Figure 4.36(b) plots the enhancement factor of EQE for all cells evaluated in this work. The cells coated with EVA/MgO-TiO₂ obtained the maximal EQE enhancement factor (>1, 300-1100 nm) followed by the cells coated with EVA/TiO₂.

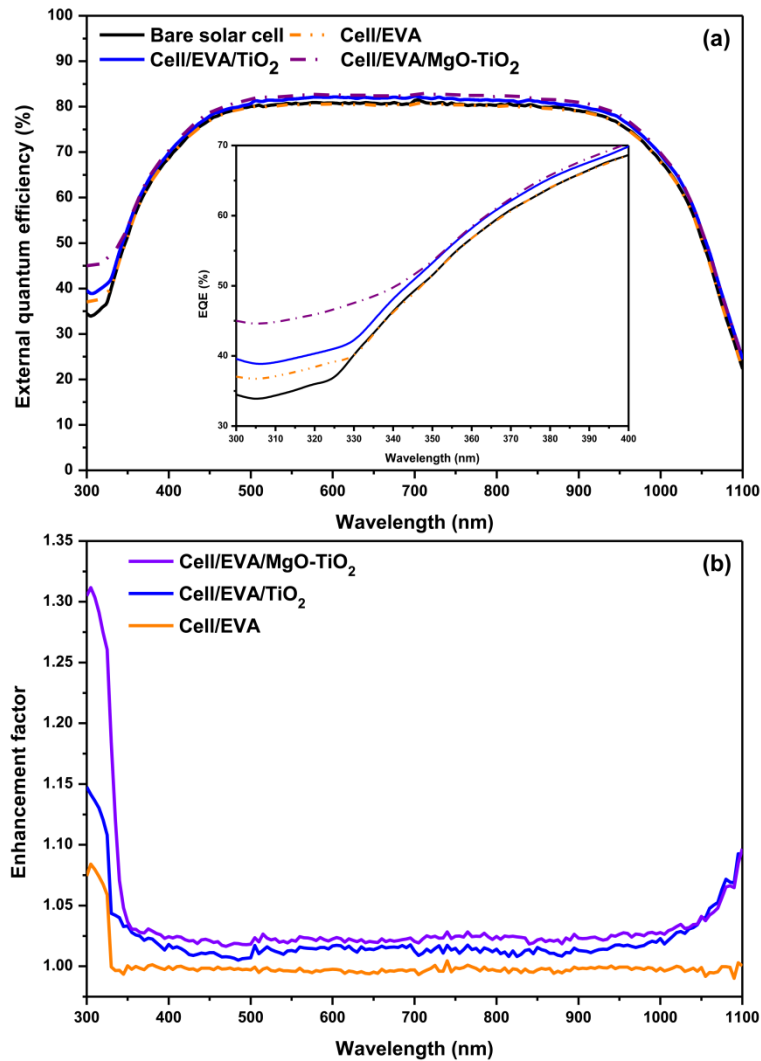


Figure 4.36. External quantum efficiency (EQE) curves and (b) enhancement factor of EQE for cell coated with Solely EVA, EVA/TiO₂, and EVA/MgO-TiO₂, compared that of bare cell.

4.5 Silicon Oxide for Crystalline Silicon Solar Cells

4.5.1 Introduction

Fabrication of silicon oxide (SiO₂) thin films was part of the experimental design in this chapter since SiO₂ is a standard antireflective material with a suitable refractive index value ($n \approx 1.4$ to 1.55) [224], which can effectively reduce the surface reflection and expand the spectral operating range toward the UV region of solar spectrum, and thus improve the energy performance of silicon solar cells. In addition to the antireflective properties, SiO₂ thin films can be also served as a passivation layer which could help to minimise the recombination of charge carriers at the solar cell surface

[12].

This section demonstrates an investigation into electrical and optical characteristics of commercial p-type single junction mono-crystalline silicon solar cells before and after coating with single and double anti-reflection layers of silicon oxide via low-temperature Plasma Enhanced Chemical Vapour Deposition (PECVD) method by using Tetramethylsilane (TMS) as a silicon precursor and oxidised in situ with potassium permanganate (KMnO_4) in a low cost economic manner.

4.5.2 Experiment method

In this work, Plasma Enhanced Chemical Vapour Deposition (13.6 MHz Radio Frequency (RF) powered) processing was used for its ability to produce and deposit single and double layers of SiO_2 thin films on the silicon solar cells' (T6S-3A, Motech Industries, Taiwan) surface at low temperature conditions. Such a cost-effective scheme is expected to obtain an energy performance enhancement in commercial single-junction silicon solar cells. A picture of the experimental configuration of this coating system is shown in Figure 4.37.

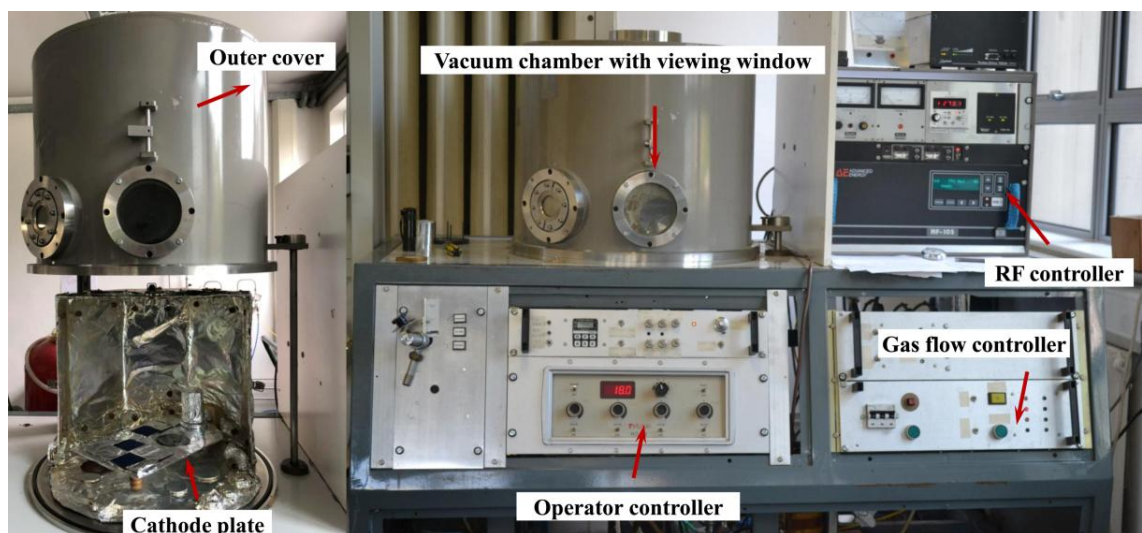


Figure 4.37. Photograph of PECVD coating system.

The vacuum chamber has a dimension of 50 cm in diameter and 50 cm in height, which consists of inner and outer covers. The inner cover is served to facilitate uniform distribution of vaporised gases during the coating process, meanwhile, the gas condition

inside the chamber can be observed through the viewing window at the outer cover. The solar cells were placed on the cathode plate, mounted within the grounded chamber alongside with the in-situ oxidising agent.

In a typical procedure, the plasma, comprised of ions, electrons and numerous neutral species is formed and sustained through the application of high RF to a low pressure gas. The applied electric field provides the electrons with sufficient energy to become highly reactive without significantly increasing the temperature. For deposition of SiO₂, the Tetramethylsilane (TMS) (C₄H₁₂Si) was used as the precursor material and potassium permanganate (KMnO₄) was served as an in situ oxidation agent. TMS gas was introduced into the chamber followed by an additional cleaning process using argon gas while the gases flow rate is controlled and monitored through the mass flow controllers. The growth and properties of such films are primarily determined by the substrate temperature and voltage bias. Table 4.11 summarises the coating parameters for solar cells with single and double antireflection layer of SiO₂ films. These depositing conditions are based on the experimental work done by Tahhan et al who obtained a maximum enhancement of 0.31% (11.05% to 11.36%) in electrical conversion efficiency of mono-Si solar cells by using those ARCs [228].

Table 4.11. Summary of the coating parameters and conditions for mono-Si solar cells with single and double antireflection layers of silicon oxide [228].

<i>Coating Conditions</i>	<i>Layer 1 (bottom)</i>	<i>Layer 2 (top)</i>
DC Bias (volts)	100	100
TMS Flow Rate(cm ³ /min)	25	25
Time (mins)	15	15
KMnO ₄ Mass (grams)	20	10
Temperature inside vacuum chamber (°C)	200	200

4.5.3 Result and discussion

Figure 4.38 shows the $J-V$ curves of coated cells with a single and double antireflection layer using above depositing parameters. The performance of uncoated cell was also presented for comparison. A visible increase in photocurrent and neglectable change in open-circuit voltage (V_{oc}) can be clearly observed due to a further exploitation of incident light by SiO_2 . Compared to the single antireflection layer, the solar cell coated with double layers of SiO_2 shows a more significant increase in J_{sc} (from 37.68 mA/cm^2 to 38.37 mA/cm^2), contributing to a maximum enhancement of 2.7% (16.45% to 16.89%) in conversion efficiency relative to those of a bare cell. Detailed electrical characteristics of evaluated solar cells are summarised in Table 4.12.

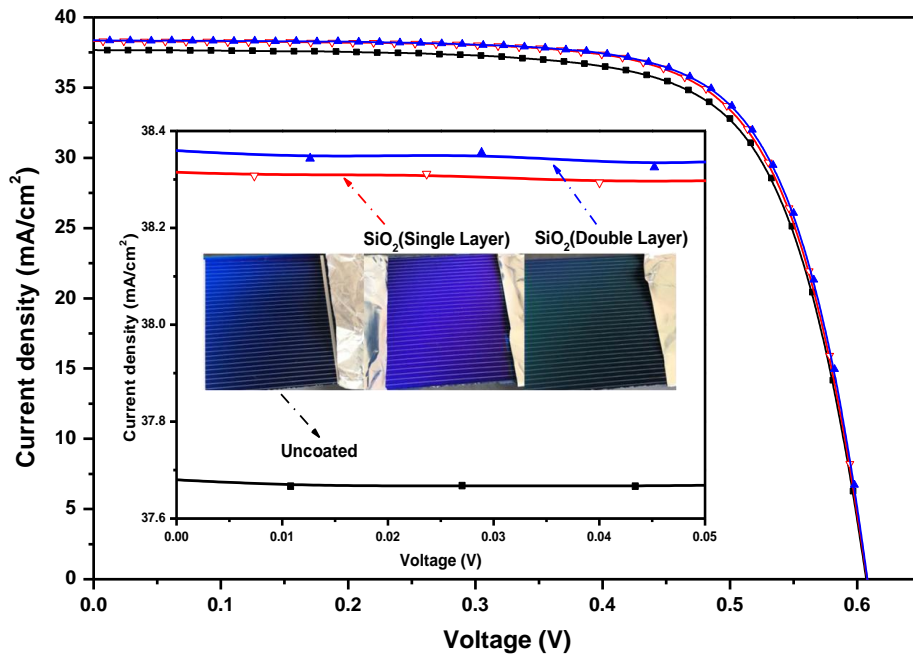


Figure 4.38. $J-V$ curves of the coated cells at the maximum performance enhancement acquired using AM 1.5 illumination. Inset shows a photograph of coated cells with different surface colour compared to the uncoated cell.

Table 4.12. Electrical characteristics of all evaluated solar cells in this work under AM1.5 illumination condition.

Type	J_{sc} (mA/cm^2)	V_{oc} (mV)	P_{max} (W)	FF (%)	PCE (%)	Absolute Enhancement	Relative Enhancement
Uncoated	37.68	607.3	0.1406	71.91	16.45	-	-
Cell/ SiO_2 (Single Layer)	38.31	608.2	0.1438	72.07	16.81	0.36%	2.2%
Cell/ SiO_2 (Double Layer)	38.37	609.8	0.1445	72.16	16.89	0.44%	2.7%

Figure 4.39 shows the optical reflectance and absorption spectra of coated solar cells at maximum performance. It can be seen that the solar cells with single and double layer of SiO₂ coating exhibit overall reduction in reflectance across the measured wavelength of 200 to 850 nm compared to the uncoated cell. A more remarkable change in reflectance was observed in the spectral region of 250 to 300 nm and 350 to 400 nm when the solar cell was coated with double antireflection layer. This is attributed to the absorption of UV photons by SiO₂ thin films due to its intrinsic anti-reflective properties.

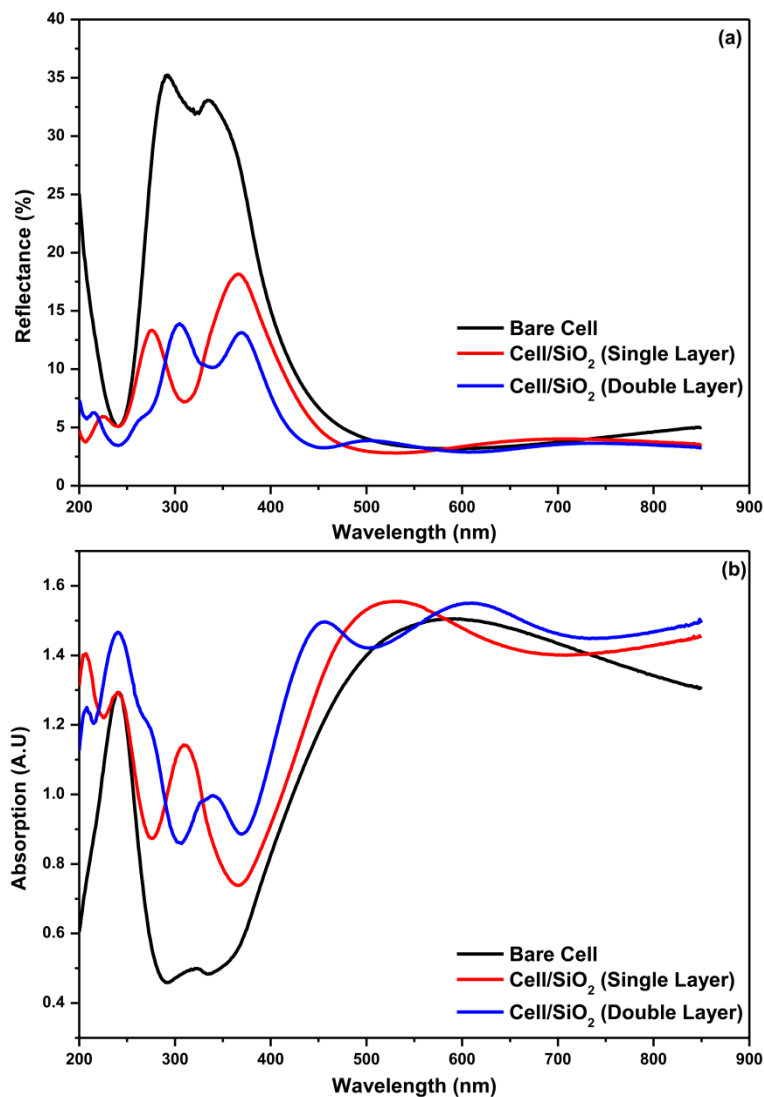


Figure 4.39. Optical reflectance (a) and absorption (b) spectra of coated cells with single and double layers of SiO₂ coating compared to those for a bare cell.

In addition, the double layer of SiO₂ thin film shows outstanding light transmission properties at visible region (see Figure 4.40, $T(\lambda)_{DLARC}$ versus $T(\lambda)_{quartz} = 91.9/92.7$ across the range from 400 to 850 nm), which could ensure an efficient photon harvesting in silicon solar cells.

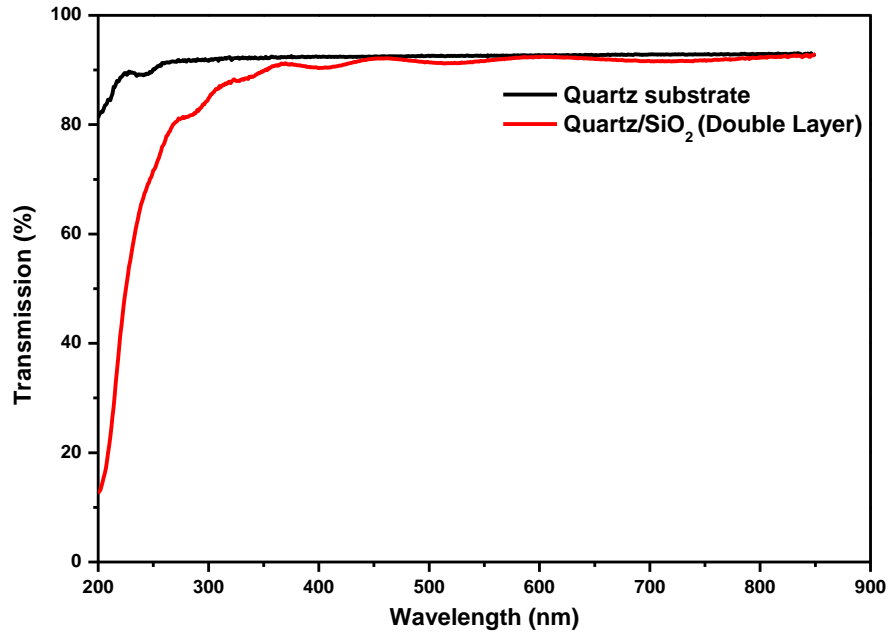


Figure 4.40. Transmission spectra for quartz substrate and double anti-reflection layers for solar cells with optimum enhancement obtained.

Given that the silicon solar cells exhibit weak response to short wavelength of light, an alternative ingenious approach to suppress the spectral mismatch is proposed in chapter 5 where the light promotion in silicon PV cells via modification of incident spectrum by using photoluminescent species is comprehensively studied.

4.6 Summary

This chapter separately demonstrated the potential application of high surface area TiO₂ based nanoaerogels and silicon oxide films in improving the energy performance of commercial monocrystalline silicon solar cells. A novel and simple anti-reflection coating (ARC) was developed by screen printing a solution of TiO₂ based NPs dispersed in a polymeric matrix onto the solar cell's textured surface. SiO₂ oxide films were produced by low-temperature PECVD for efficiency enhancement of solar cells at low fabrication costs.

The crystallite size of synthesised TiO₂ based nanomaterial shows a marginal decrease by adding small contents of MgO dopant. The N₂-sorption analysis revealed that the as prepared MgO-TiO₂ aerogels with low content of MgO (2 mol%) have a higher surface area (231 m²/g) compared to that of undoped TiO₂ aerogels (154 m²/g), and their application to the textured surface of solar cells through blade screen printing technique formed a uniform layer which contributed to significant improvements in J_{sc} and EQE. The enhancement was attributed to the conjunction effects of improved anti-reflective properties of TiO₂ based NPs and EVA binder.

Nanoporous TiO₂ could enhance the light scattering capability and increase the photon harvesting on the pyramidal structures. The EVA binder with 15-wt% ratio provides good optical and mechanical host conditions for the TiO₂ based NPs. Moreover, the results demonstrated that the concentration of dispersed TiO₂ based NPs play a critical role in altering the enhancement factor of coated solar cells. EVA encapsulated TiO₂ NPs enhance electrical performance but not as much as MgO-doped TiO₂ since doping nanostructured TiO₂ with MgO yields led to further promotion of light absorption and thus more pronounced enhancement in conversion efficiency. An optimum relative enhancement of 6.0% (from 15.76% to 16.70%) was observed in a cell with MgO-doped TiO₂ nanocomposite at particle density of 0.3 (mg/ml).

In case of silicon oxide thin film ARC, with optimised oxygen diffusion in the silicon films for solar cells coated with a single layer of silicon oxide can contribute to a competitive power conversion efficiency as compared to a double layer of silicon oxide coating where the solar cells showed a maximum increase of 2.7% in conversion efficiency in relative to that of a bare cell.

Chapter 5 Phosphor for Crystalline Silicon Solar Cells

5.1 Introduction

The aim of experimental works in this section is to develop a down-converting luminescent layer on textured surface of commercial mono-Si solar cell by using down-converting phosphor materials which could absorb and convert high-energy UV photons into visible range where silicon solar cells exhibits a robust spectral response and thus to improve the overall conversion efficiency. The main objectives through experiments are summarised as follow:

- Analyse and evaluate the potential application of down-converting Tb^{3+} doped Gd_2O_2S phosphor and Eu^{2+} doped $SrAl_2O_4$ phosphors in an attempt to improve the power conversion efficiency of silicon-based single-crystalline cells.
- To demonstrate a low-cost effective luminescent layer comprising EVA/Phosphor mixture on top surface of commercially available mono-Si solar cells through rotary screen printing technique.
- Compare and examine systematically the effectiveness of down-converting phosphor in terms of improved light absorption and scattering on the cells' PV performance through a comprehensive study on electrical, optical, and external quantum efficiency response of solar cell before and after coating, and moreover, the investigation on luminescent and morphological properties of the phosphor particles.

5.2 Spectrum Modification for Silicon Solar Cells

Currently, the crystalline silicon (c-Si)-based solar cells are still dominating the global solar PV market owing to their abundance, stability, and non-toxicity [12]. However, the conversion efficiency of PV cells is constrained by the spectral mismatch

losses, non-radiative recombination, and strong thermalisation of charge carriers. Generally, the c-Si solar cells are only able to absorb photons within a limited fraction of solar spectrum, with ultraviolet (UV)-blue and most of the infrared (IR) region of light untapped.

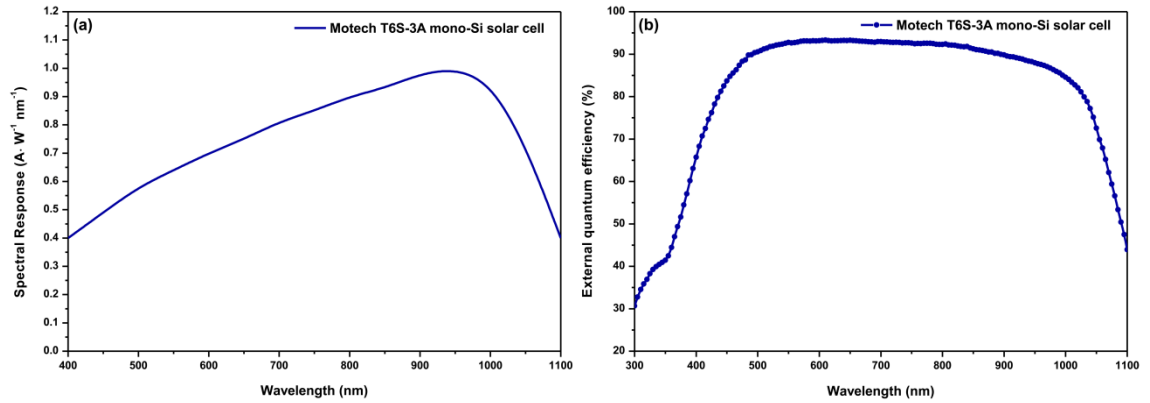


Figure 5.1. (a) Spectral response (SR) and (b) external quantum efficiency (EQE) as a function of wavelength for Motech T6S-3A mono-Si solar cell.

Figure 5.1(a) shows the spectral response (SR) curve of the currently used mono-Si solar cells as a function of wavelength, and Figure 5.1(b) presents the corresponding external quantum efficiency (EQE) spectrum in the range from 300 to 1100 nm. It can be seen that the spectral response exhibits an increasing trend longer than the wavelength of 400 nm (3.15 eV), with a peak centred at 980 nm and then gradually fall back to zero after reaching the band gap of silicon at wavelength around 1100 nm (1.12 eV). Here, since silicon belongs to an indirect band gap semiconductor and therefore there is no evident observation of sharp cut off in the SR curve.

The limitation of spectral response at longer wavelength as described in previous sections is due to the inability of silicon to absorb photons with energy below the band gap ($h_\nu < E_g$) while at short wavelength, photons with higher energy above the band gap ($h_\nu > E_g$) cannot be fully utilised, instead, it creates excess heat as a result of strong thermalisation losses, which accounts for almost 50% of energy conversion. Similar constraint encountered in corresponding EQE curves which can be seen in Figure 5.1(b).

Reducing these losses in c-Si solar cells may be achievable through the spectrum

modification by employing down-converting phosphors as these luminescent materials are able to absorb incident radiation with relatively high energy and emit light which usually fall into visible region [188-190]. In a down-conversion (DC) process, a high-energy incident photon is absorbed by the DC phosphors and re-emitted as two or more-lower energy photons at longer wavelengths where the silicon solar cells exhibit a strong spectral response [191, 192]. As a consequence, more photons could be exploited for the generation of charge carriers, which makes it available to reduce the energy loss of short wavelength photons and thus to increase the power conversion efficiency of silicon solar cells. It is anticipated that the potential of using a silicon solar cell ($E_g = 1.1$ eV) in conjunction with an ideal DC material can obtain a theoretically maximum conversion efficiency of 38.6% under non-concentrated sunlight compared to the limiting efficiency of 30.9% for the same cell without a luminescent DC layer overlaid [191].

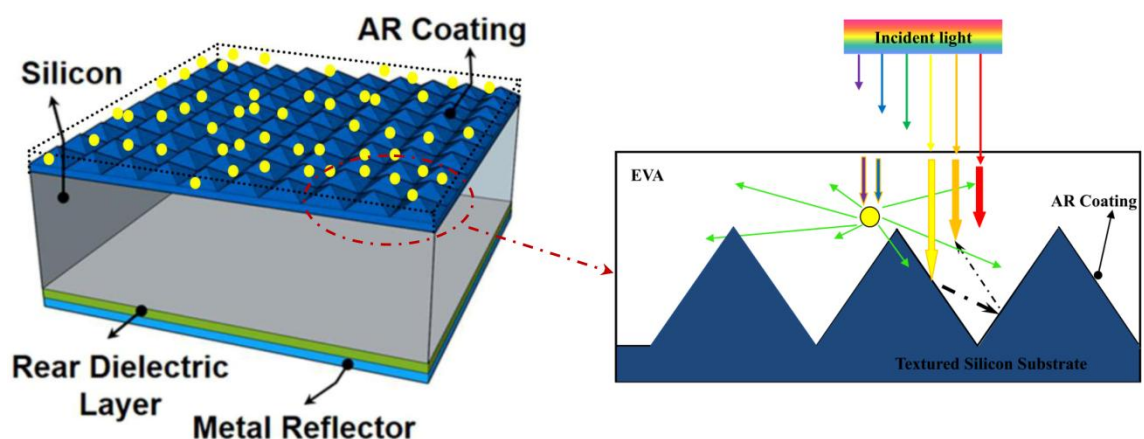


Figure 5.2. Sketch showing the working principle of the luminescent down-converting material. Figure is adapted from [161].

Spectral modification employed in the current study incorporates a composite-luminescent layer comprising down-converting phosphors encapsulated in a transparent matrix of ethylene vinyl acetate (EVA) on the front-textured surface of mono-Si solar cells, which is shown in Figure 5.2. A portion of incident UV light shining on the luminescent layer is absorbed by the phosphor particles and is then re-emitted into solar cells as green or blue light. The rest of incident photons that solar cell could harness are directly absorbed for photocurrent generation. In addition, a

pyramidally textured surface in combination with the non-stoichiometric silicon nitride (SiN_x) anti-reflection coating is to overcome the effect of Fresnel reflection [195].

However, despite the fact that DC process fundamentally increases the overall number of electron-hole pairs through each down-converted photon, the re-emitted photons still cannot be fully utilised by the underlying solar cell since the emission of phosphor is multi-directional and the photons are actually emitted in all directions. This can be seen from the enlarged image of the schematic design, as shown in Figure 5.2. Typically, a fraction of re-emitted photons escape to the front-side and edge of the cell due to the isotropic emission while other ones that strike on the front-side are being lost through either direct reflection or re-absorption [61,198, 199].

Therefore, the down-converting phosphor particles always serve as photon scatters. It is believed that more than half of the photons re-emitted by the down converter could contribute to the photocurrent generation when DC material is placed on top of the cell since the pyramidally textured SiN_x surface could help to compensate for some reflection losses and therefore enhance the PV effect. However, the particle size and surface coverage of DC materials that affect significantly the light scattering behavior are required to be maintained in a certain range for obtaining efficient light trapping in silicon solar cells. In terms of the Lorenz-Mie-Debye theory [200], smaller particles usually exhibit small scattering cross-section but more equivalent distribution of the scattering angles while large particles possess dominant scattering intensity that focused primarily on very limited scattering angles. This indicates that larger particles may be more suitable for attaining efficient trapping of light in the solar cells due to their large cross-section and forward scattering tendency. There exists an optimal particle size to achieve maximum light trapping. In general, the amount of scattered light is maximal at particle of approximately 100 nm. For particles (such as atoms and molecules) that having smaller size below 100 nm, Rayleigh scattering occurs due to the induction of dipole oscillations [195,200]. However, in case for the phosphor materials, the smaller particles (<100 nm) have larger specific surface area (or surface-to-volume ratio) which may induce more non-radiative recombination sites of surface defects, giving rise to a

reduction in luminescent quantum efficiency [196]. Particles greater than or equal to 1.0 μm are larger than the wavelengths of visible light and hence will reflect most of incident illumination, and more seriously, it may result in backward scattering, which reduces the original transmittance towards the cell surface in both UV and visible ranges [195]. In addition, most importantly, the optical properties of the binding layer need to be optimised prior to the phosphor integration process, in order to maximise the photon harvesting, and thus the enhancement in conversion efficiency.

The majority of phosphors comprise two fundamental components: a host lattice and an activator where in both sides are mainly constituted by the rare earth elements. These elements exhibit uniform emission properties when they are doped and function as the luminescent centre in the host crystal. This is owing to their unique electronic configuration where the electron transition usually occurring within the incompletely filled 4f shell, or alternatively, between the 4f and 5d shells, consequently leads to luminescence and distinct optical, electrical as well as magnetic properties. Luminescent materials in terms of lanthanide phosphors have made great progress in driving the lighting and display industry [201].

Rare-earth ions doped-oxysulfides, such as $\text{Gd}_2\text{O}_2\text{S:Tb}^{3+}$, $\text{Y}_2\text{O}_2\text{S:Tb}^{3+}$, and $\text{Gd}_2\text{O}_2\text{S:Pr}^{3+}$, have been extensively investigated and studied due to their efficient performance as luminescent materials. Moreover, their high conversion efficiency from x-ray wavelengths to visible light, low toxicity, non-deliqescence, high radiation and chemical stability, and easy preparation, which has seen their use in a wide range of applications such as emissive display devices [201], optical temperature sensors [202], oxygen storage [203], x-ray detector systems and scintillators [204]. $\text{Ln}_2\text{O}_2\text{S}$ ($\text{Ln} = \text{Gd}, \text{Y}$) has a trigonal structure with P-3m1 space group where its crystal structure is schematically shown in Figure 5.3. Each Ln atom is bonded to three sulphur (S) and four oxygen (O) atoms, which formed a seven-coordinate geometry complex.

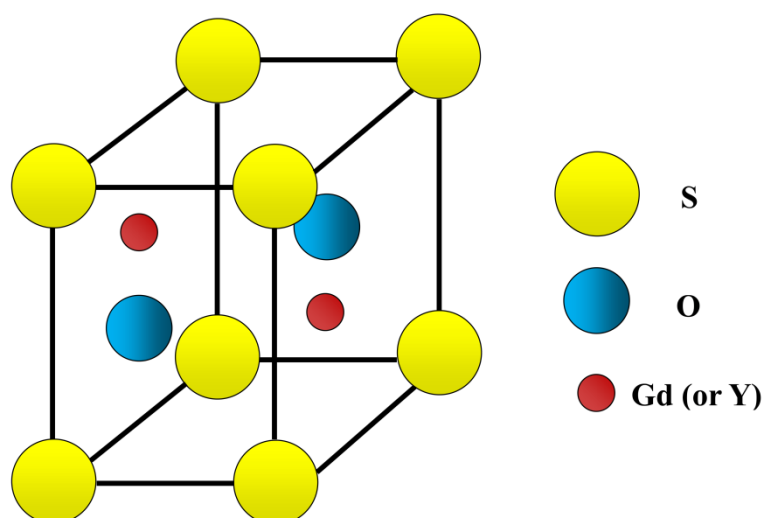


Figure 5.3. Schematic crystal structure of $\text{Ln}_2\text{O}_2\text{S}$ (Ln = Gd, Y).

Most recently, lanthanide oxysulfide phosphors have also found contributions in the domain of photovoltaic device, the intense green emission ($\lambda_{\text{em}} = 545 \text{ nm}$) of the $\text{Gd}_2\text{O}_2\text{S}:\text{Tb}^{3+}$ phosphor under UV excitation ($\lambda_{\text{ex}} = 292 \text{ nm}$), which implies its great potential of being used as an efficient spectral converter, in an attempt to reduce the spectral mismatch losses while improving the overall light absorption in silicon solar cell [212,213].

The reason that a submicron $\text{Gd}_2\text{O}_2\text{S}:\text{Tb}^{3+}$ phosphor was chosen in place of a commercially available sample was twofold. Firstly, due to the surface texture of the mono-Si solar cell, commercial $\text{Gd}_2\text{O}_2\text{S}:\text{Tb}^{3+}$ phosphor particles with large grain size (average size around 3.5 micrometres) would not form a close packed thin phosphor layer, instead, they would reflect some of the incident light and shade the cell because they are larger than the width and depth profile of the textured structures. Secondly, according to the reported research work with soft x-ray detectors by using submicron $\text{Gd}_2\text{O}_2\text{S}:\text{Pr}^{3+}$ phosphor particles to form a thin phosphor layer, it was found that they gave higher detection efficiency than a much larger commercial $\text{Gd}_2\text{O}_2\text{S}:\text{Pr}^{3+}$ sample. The higher detection efficiency of the smaller $\text{Gd}_2\text{O}_2\text{S}:\text{Pr}^{3+}$ particles was due to their ability to form a thin close packed layer with very few ‘pinholes’, thereby capturing more x-rays [213].

There are many chemical approaches to fabricate nanometer sized phosphor

particles. In the present work, the Tb^{3+} -doped $\text{Gd}_2\text{O}_2\text{S}$ phosphor powder was prepared by the homogeneous precipitation method with a subsequent sintering process. This synthesis method is on the basis of slow hydrolysis reaction of solute cations, for instance, Gd^{3+} for the preparation of gadolinium hydroxycarbonate precursor ($\text{Gd}(\text{OH})\text{CO}_3:\text{Tb}^{3+}$), which can be simply described as the release of CO_2 and NH_3 with the promotion of urea decomposition, followed by the sequential addition of the OH^- and CO_3^{2-} to the Gd^{3+} as soon as the concentration of reactants reaches critical supersaturation, and meanwhile, the precipitation takes place.

5.2.1 Performance Enhancement through Luminescent Materials

The integration of a down-converting luminescent layer onto the top surface of a silicon solar cell has the opportunities to generate multiple low-energy photons with band gap greater than the silicon for each incident high-energy photon, which has also attracted a number of researchers to dedicate on the study of spectrum modification so as to enhance the energy performance of silicon devices.

Given the potential of this spectrum enhancement method, many experimental works have been conducted. Huang et al. reported an improved light harvesting of silicon solar cell by depositing luminescent down-shifting $\text{YVO}_4:\text{Bi}^{3+}$, Eu^{3+} nanophosphors directly onto the textured surface of crystalline silicon (c-Si) solar cell via spin coating technique. An absolute enhancement of 0.7% in power conversion efficiency was obtained for the optimised devices [193]. Also, Chen et al have showed an absolute enhancement of 0.64% in the power conversion efficiency of a pc-Si solar cell by using down-converting $\text{KGaGd}(\text{PO}_4)_2:\text{Eu}^{2+}$ phosphor dispersed in a polymethyl methacrylate (PMMA) matrix [188]. In addition, Hung and Chen demonstrated an increase of 6.74 mA/cm^2 in short-circuit current density corresponding to an enhancement around 2.8% in conversion efficiency by spin coating a mixture solution of submicron $\text{Gd}_2\text{O}_2\text{S}:\text{Eu}^{3+}$ phosphor impregnated in a poly-vinyl-pyrrolidone (PVP) host material on the front side of commercial polycrystalline silicon (pc-Si) solar cells [195].

Tahhan et al. achieved 0.54% absolute increase in conversion efficiency of commercial p-type monocrystalline silicon (mono-Si) solar cell by applying a luminescent composite layer of $\text{Gd}_2\text{O}_3\text{S}(\text{Er}_{0.2}, \text{Tb})_{0.01}$ phosphor encapsulated in an ethylene vinyl acetate (EVA) co-polymer binder on solar cells' textured surface [214]. This work is particularly relevant to the current study, as extensive experimental tests are carried out using commercially available silicon PV cells, phosphor particles are embedded in an EVA matrix and the mixture of EVA/phosphor are screen-printed on the front surface of mono-Si solar cell.

Down-conversion of a high energy ultraviolet photon to a less energetic red emitting photon using luminescent down-shifting technique has also been reported by Liu et al, who successfully developed a simple coating of polyvinyl acetate film doped with Eu^{3+} complexes onto the surface of c-Si PV module, which achieves an overall enhancement of 0.32% in PV module efficiency [215].

5.2.2 Encapsulation of Luminescent Materials

There are several ways to incorporate the DC materials into a PV device or module:

- Embedding luminescent materials in commercial encapsulants, most commonly used encapsulation binders include ethylene vinyl acetate (EVA), polyvinylpyrrolidone (PVP), poly vinyl acetate (PVA), and poly methyl methacrylate (PMMA). Such polymeric binding agents possess adapted optical properties and good thermal stability as to not offset the potential enhancement derived from the phosphor materials. Researchers have shown the feasibility of mixing various DC materials with these of binders and subsequently coated onto the solar cell surface [188, 195].
- Doping the luminescent materials on top of glass float PV module [215].
- Depositing the phosphor directly onto the surface of silicon solar cell [193].

5.3 Experimental Methods

In this section, methodologies used to prepare submicrometer-sized terbium-doped gadolinium oxysulfide phosphor powder and its integration on the textured surface of mono-Si solar cells are described in more details.

The Tb³⁺-activated Gd₂O₂S phosphor particles were synthesised through a typical two-step process:

The first step was the preparation of Tb³⁺-doped gadolinium hydroxycarbonate precursor (Gd(OH)CO₃:Tb³⁺) via a urea-based hydrothermal homogeneous precipitation method with minor modifications [216-218]. Since the precipitate is amorphous, the morphology of the obtained precursor particle assumes a spherical shape so as to ensure a reduction of its free energy.

The second step was the sulfuration of the Gd(OH)CO₃:Tb³⁺, followed by appropriate sintering process to produce oxysulfide phosphors. In order to obtain the highest luminance in the Gd₂O₂S:Tb³⁺ phosphor samples, the ratio of Tb³⁺ ions was suggested to set to 2 mol% in respect to that of Gd³⁺ molar concentration [212].

In this way, the Tb³⁺ ions were doped into Gd₂O₂S phosphor host lattices and their luminescent properties were then characterised.

Finally, during the layer application process, the as-prepared phosphor powder was encapsulated in ethylene vinyl acetate (EVA) co-polymer resin and applied on the front-textured surface of solar cell using rotary screen printing technique.

5.3.1 Preparation of Gd₂O₂S:Tb³⁺ phosphor particles

The following chemicals were used as the starting materials in preparation of Gd(OH)CO₃:Tb³⁺ precursor powders: gadolinium oxide (Gd₂O₃) (Ampere Industries, France, 99.99%), terbium oxide (Tb₄O₇) (Neo materials, UK, 99.99%), urea (NH₂)₂CO (Sigma Aldrich, UK, ≥98%), and nitric acid (HNO₃) (Fisher Scientific, UK, >68%).

Gadolinium nitrate ($\text{Gd}(\text{NO}_3)_3$) (0.25 M) and terbium nitrate ($\text{Tb}(\text{NO}_3)_3$) (0.25 M) stock solutions were prepared by respectively dissolving Gd_2O_3 and Tb_4O_7 in dilute nitric acid until the solution reached pH between 1 to 3.

$\text{Gd}(\text{NO}_3)_3$ (0.25 M, 50 ml) and $\text{Tb}(\text{NO}_3)_3$ (0.25 M, 1 ml) solutions were mixed with deionised (DI) water (900 ml in a beaker). The solution was then heated until boiling, followed by the addition of urea (30 g). Figure 5.4 shows the mixed solution being heated on a hot plate under vigorous stirring. The solution was boiled until turbidity (see Figure 5.4 left) was observed at which point the solution was aged for 1 hour at the same temperature. After that, the solution turned from turbidity to milky white, as shown in Figure 5.4 (right), which suggests the decomposition of urea and the formation of precipitation.

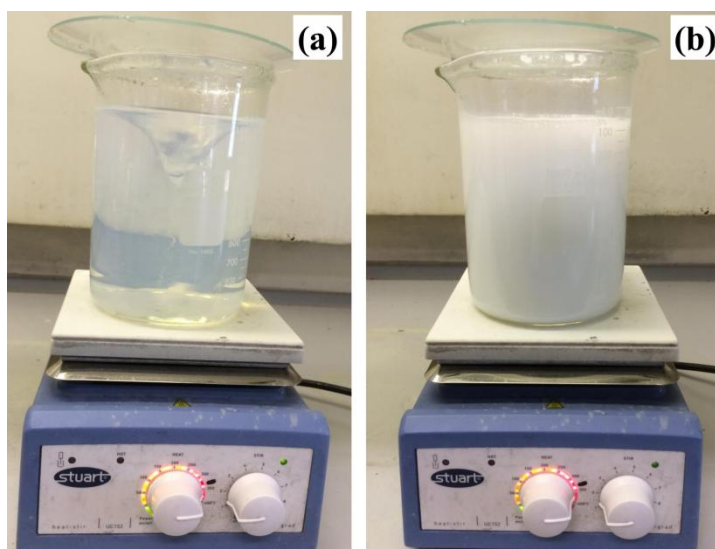


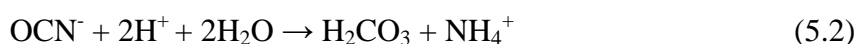
Figure 5.4. Reaction solution was heated at 85 °C with continuous stirring.

The precipitates (see Figure 5.5) were then filtered at the pump while still hot, followed by washing twice with DI water (100 ml) and then dried in an oven at 100 °C overnight to yield soft precursor powders. The chemical reactions during the fabrication process of phosphor precursors are described by the follow equations [210]:

Hydrothermal decomposition of urea (rate 4% per hour at ~ 100 °C) supplying reactants in a controlled manner,



With increasing pH (<pH3) the cyanate ion rapidly reacts,



The rare earth element ions are weakly hydrolysed in water and the subsequent release of hydronium ions promotes urea decomposition, the resulting release of carbonate ions causes precipitation, once the concentration of reactants reaches critical supersaturation,

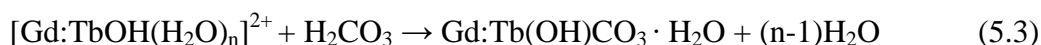
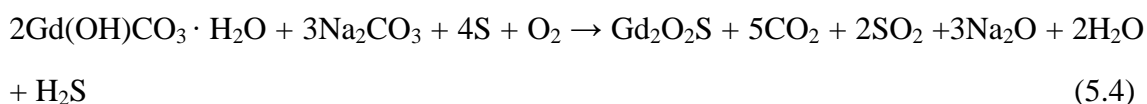


Figure 5.5. The resulting precipitates filtered by a Buchner funnel. Inset image shows the soft precursor powders dried at 100 °C for 24 hours.

Figure 5.6 shows the sulfuration process of the precursor powders, the as-prepared $\text{Gd}(\text{OH})\text{CO}_3:\text{Tb}^{3+}$ dry powder was thoroughly mixed with sodium carbonate (Na_2CO_3) (Sigma Aldrich, UK, 99.9%) and sulfur (S) (Sigma Aldrich, UK, 99.9%), compacted into an alumina crucible, and then covered with a mixed top layer comprised of Gd_2O_3 , Na_2CO_3 and S in which the molar ratio of the precursor/ Gd_2O_3 / Na_2CO_3 /S is 1/1/1.5/2. A lid was then placed on the crucible and annealed at 900 °C for 1 hour. The chemical reaction of the $\text{Gd}_2\text{O}_2\text{S}:\text{Tb}^{3+}$ during the sintering process is given as:

The resulting ($\text{Gd}(\text{OH})\text{CO}_3:\text{Tb}^{3+}$) precursor powders were converted to the $\text{Gd}_2\text{O}_2\text{S}:\text{Tb}^{3+}$ phosphor by heating at 900 °C in a sulfur atmosphere,



After sintering the top layer was discarded, the bottom layer was then washed in boiled DI water (50 ml) for 15 mins before filtration. The obtained precipitates were dried again at 100 °C to yield white soft powders. For comparison, the undoped-Gd₂O₂S particles were also prepared in the same route without adding of Tb dopant.

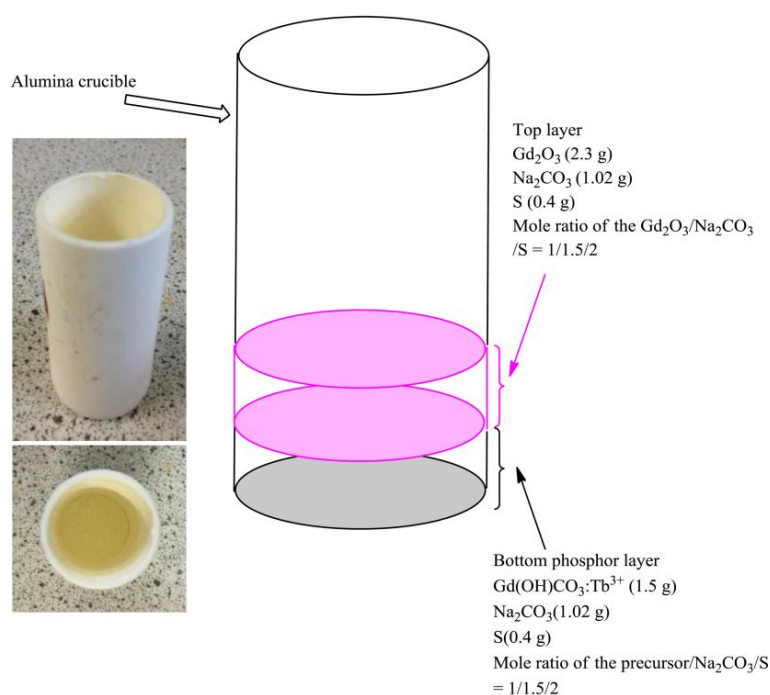


Figure 5.6. Schematic diagram of sulfuration method of as prepared Gd(OH)CO₃:Tb³⁺ precursor powder. Inset photographs show the front and top view of the alumina crucible with the mixed powder filled in.

5.3.2 Formation of the luminescent layer

The solar cells used in the layer coating process were commercial p-type mono-Si solar cell (T6S-3A, Motech Industries, Taiwan) pre-structured with dark silicon nitride (SiN_x) anti-reflection coatings (ARCs) on the front-textured surface. The SiN_x layers were deposited by low pressure plasma-enhanced chemical vapour deposition method

(PECVD) with an average thickness of ~ 80 nm. For experimental purposes, the cell was previously cut into three equal pieces (15.6 cm × 5.2 cm) using a high-power laser (TMX90, CTR, UK). Phosphor particles were encapsulated in ethylene vinyl acetate (EVA) resins and then screen-printed on the textured surface of the solar cells using a commercial rotary roller (K Lox Proofer, RK PrintCoat Instruments, UK). The coated cells with wet films (coated surface area = 5 cm × 5 cm) were dried in a fume hood and then cured in a furnace at 190 °C for 5 mins in order to obtain a glossy and thermal stable layer. In this section, preparation of the EVA/phosphor composited layer and their integrations onto the surface of mono-Si solar cells are introduced.

5.3.2.1 EVA and EVA/Phosphor layer preparation

Preparation of EVA layer was same as described in the previous chapter in which the EVA (Elvax 150, DuPont, USA) foils were dissolved p-xylene solvent in different ratios of 9, 12, 15, 18 and 21 wt% respectively. In such way, the best weight ratio (wt%) of EVA to phosphor particles that potentially contributes to an optimum enhancement in solar cells' electrical performance can be determined and then selected for mixing with the luminescent phosphor materials. The EVA sheet was previously cut into small shreds in convenience for facilitating the dissolving process. Next, EVA and p-xylene were mixed in a glass beaker and heated on a hot plate with continuous stirring for 10 minutes.

Phosphor powder $\text{Gd}_2\text{O}_2\text{S:Tb}^{3+}$ fabricated at Centre for Phosphor and Display Materials at Brunel University was used in the experiment. In a typical procedure, a stoichiometric amount of phosphor powder was weighed and dispersed in p-xylene using an ultrasonic bath. A series of solutions containing the $\text{Gd}_2\text{O}_2\text{S:Tb}^{3+}$ /p-xylene with 1.0, 1.5, 2.0, 2.5, and 3.0-mg/ml particle densities was prepared and then separately mixed with various amounts of EVA shreds to fix an EVA ratio at 15-wt% in each of photo-luminescent solution, since this ratio has given rise to a homogeneous EVA layer applied onto solar cell as well as exhibiting superior optical transmission and reflection properties to other ratios of solely EVA coatings, which potentially contributes to the

maximum enhancement in conversion efficiency. When the solution became colloidal (see Figure 5.7) it was left at 30-35 °C under continuous stirring until uniform solutions were formed. The solution of undoped-Gd₂O₃/p-xylene was prepared in the same route for comparison.

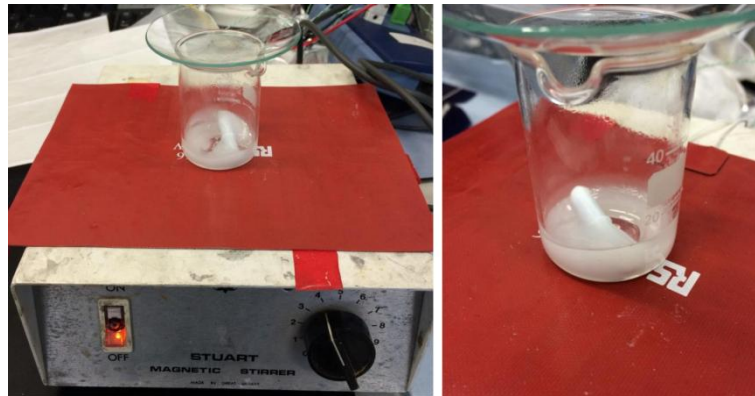


Figure 5.7. Preparation of EVA/p-xylene/Gd₂O₃:Tb³⁺ solution where the glass beaker is placed on top of the hotplate magnetic stirrer.

5.3.2.2 Layer application

In the current study, the integration of EVA and EVA/Phosphor layer on top of mono-Si solar cells are performed through the application of rotary screen printing technique by using a commercial rotary roller. This printing method is actually a reformative roll-to-roll (R2R) process based on the screen printing where the screen is of a cylinder shape and the substrates (the silicon solar cells) are usually placed at the bottom of the rotary screen as they are fragile.

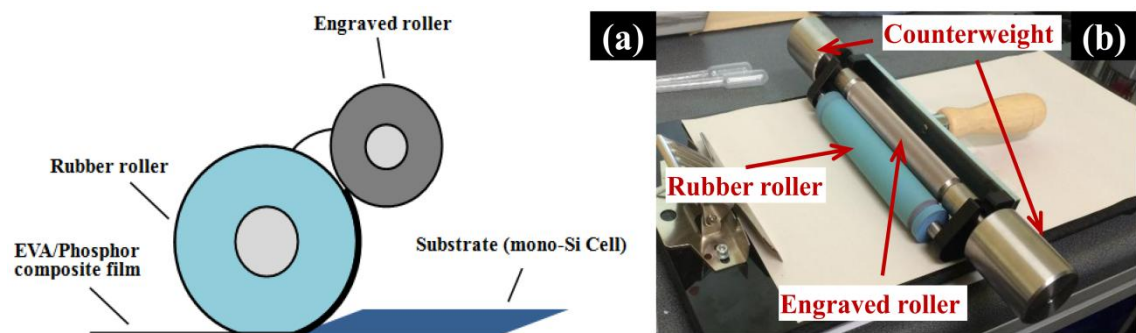


Figure 5.8. Rotary screen printing process in current work (left), and a photograph of the K Lox Hand Proofer (right).

Figure 5.8(a) schematically illustrates the layer coating process where the solar cell was fixed at the laboratory table by using a low tack masking tape (Mercateo, UK). The coater used in current study {see Figure 5.8(b)} (K Lox Proofer, RK PrintCoat Instruments, UK) consists of an engraved roller and a rubber roller assembled in a support holder that connected with a wood handle. During the coating process, the solution of EVA or EVA/Phosphor mixture is placed between the engraved- and rubber-roller as shown in Figure 5.8(a). Next, by slowly pushing the handle, the rubber roller is smoothly drawn over the solar cell, meanwhile bringing the solution in contact with the cell's surface, and eventually formed a uniform coating with a coated area of 5 cm \times 5 cm and an average wet-film thickness of \sim 2 μ m. It is worth noting that the two metal counterweights mounted outside the engraved roller on both sides, are used to ensure constant pressure between the rollers, and thus consistent prints for each coated substrate. In addition, the quartz slides and silicon wafer are also coated in the same manner to obtain the optical features of the deposited thin layers.

Again, once the wet film was formed, the coated cells were dried in a fume hood and then cured in a furnace at 190 $^{\circ}$ C for 5 minutes at a heating rate of 10 $^{\circ}$ C/min. Figure 5.9 shows a sample of solar cell coated with EVA/Gd₂O₂S:Tb³⁺ composite layer under UV light illumination where on top surface, the coated area shows a highly uniform green emission, which indicates that the luminescent material was successfully deposited on the cell surface. The fabrication process of the EVA/Gd₂O₂S:Tb³⁺ modified mono-Si solar cell is illustrated in Figure 5.10.

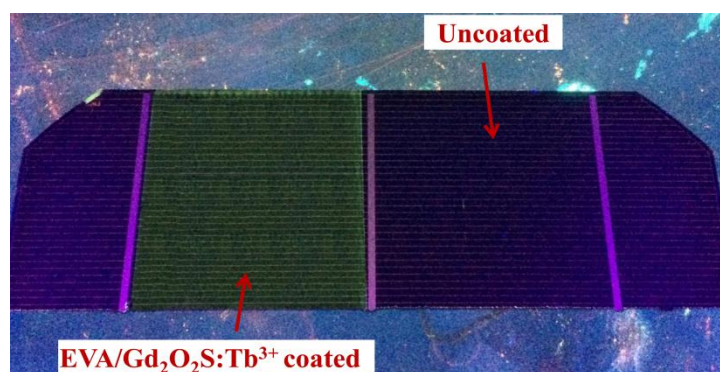


Figure 5.9. A photograph of solar cell coated with EVA/Gd₂O₂S:Tb³⁺ composite layer irradiated by UV light.

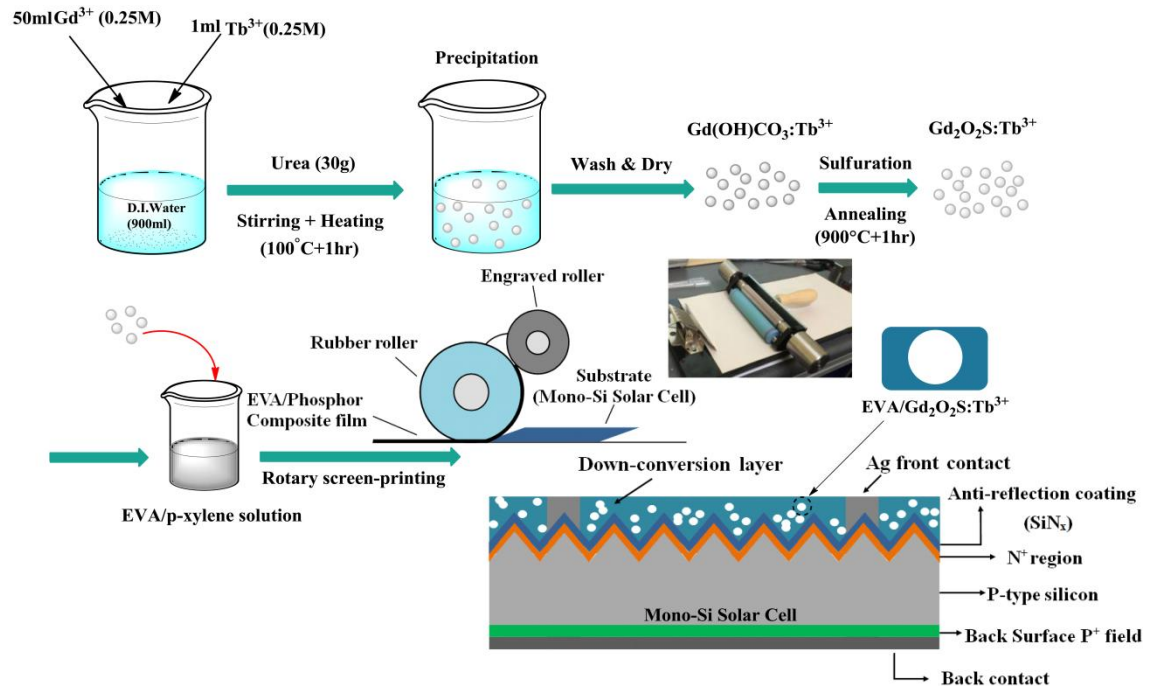


Figure 5.10. Flow diagram showing the fabrication process of $Gd_2O_2S:Tb^{3+}$ and the integration of composite material ($EVA/Gd_2O_2S:Tb^{3+}$) on textured surface of mono-Si solar cell.

5.3.3 Instruments used for experiment

The instruments used in this chapter for demonstrating the experimental results of improved photovoltaic performance of commercial model T6S-3A mono-Si solar cells via down-converting phosphor materials are similar to those that have been used for evaluating the solar cells performance through the application of TiO_2 -based nanoaerogels coatings (as described in Chapter 4), and there are few categories of equipments updated, such as the monochromatic ellipsometer and dual-monochromator system with the purpose of characterising the optical and luminescent properties of the synthesised phosphor powders. The detailed functions of corresponding apparatus in performing the experiments are described in the previous Chapter 3.

5.4 Results and Discussion

5.4.1 Phosphor characterisation

In this section, comparative results from x-ray powder diffraction, field emission scanning electron microscopy, scanning transmission electron microscopy and photoluminescence spectroscopy studies on the microstructure and luminescent properties of the synthesised $\text{Gd}_2\text{O}_2\text{S}:\text{Tb}^{3+}$ and undoped $\text{Gd}_2\text{O}_2\text{S}$ are reported.

5.4.1.1 X-Ray Powder Diffraction (XRPD)

X-ray powder diffraction (XRPD) is used to determine the crystal phase of the resulting phosphors. Figure 5.11 presents the XRPD patterns of the as-synthesised $\text{Gd}_2\text{O}_2\text{S}:\text{Tb}^{3+}$ and undoped- $\text{Gd}_2\text{O}_2\text{S}$ samples calcined at 900 °C.

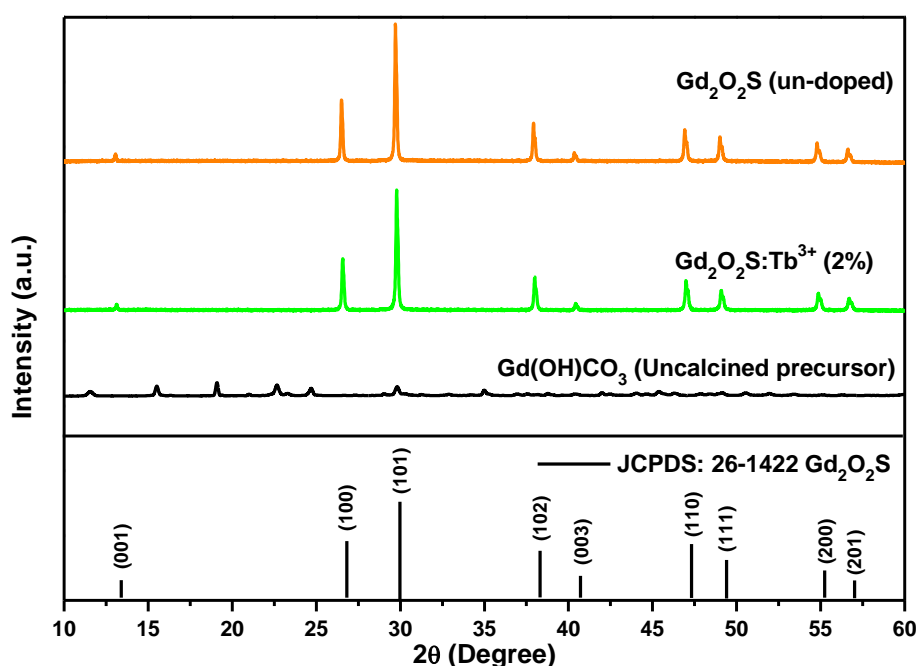


Figure 5.11. XRPD patterns of $\text{Gd}_2\text{O}_2\text{S}:\text{Tb}^{3+}$ and undoped- $\text{Gd}_2\text{O}_2\text{S}$ samples annealed at 900 °C for 1h in air atmosphere, compared to that of uncalcined precursor powder.

The obtained result indicates that the fired particles show the characteristic XRPD pattern of hexagonal $\text{Gd}_2\text{O}_2\text{S}$ crystal, the representative diffraction peaks at 13.29° (13.27°), 26.72° (26.69°), 29.95° (29.89°), 38.16° (38.12°), and 40.59° (40.56°) for

Gd₂O₂S:Tb³⁺ and undoped-Gd₂O₂S can be indexed to the (001), (100), (101), (102), and (003) plane of the hexagonal Gd₂O₂S phase respectively, which are in good accordance with the standard JCPDS data file (No. 26-1422), and no other detectable XRPD patterns were found, indicating that the resultant products are highly purified, and that the doping ion (Tb³⁺) induces little variation in the Gd₂O₂S host crystal structure. The estimated crystallite sizes, hexagonal lattice parameters, and interplanar spacing of the synthesised Gd₂O₂S samples are summarised in Table 5.1.

Table 5.1. The crystallite size and hexagonal lattice parameters of Gd₂O₂S:Tb³⁺ phosphor and Gd₂O₂S host particles from XRPD data.

<i>Sample</i>	<i>Crystallite Size (nm)</i>	<i>a (Å)</i>	<i>c (Å)</i>	<i>(hkl)</i>	<i>d_{hkl} (Å)</i>
Gd ₂ O ₂ S:Tb ³⁺	157.4	3.854	6.667	100	3.334
Undoped Gd ₂ O ₂ S	158.2	3.852	6.666	100	3.337

5.4.1.2 Photoluminescence properties of Gd₂O₂S:Tb³⁺ phosphor

Figure 5.12 shows the PL and photoluminescence excitation (PLE) spectra of Gd₂O₂S:Tb³⁺ measured at room temperature. The excitation spectrum shows a wide absorption band from 250 nm to 334 nm with a peak maximum at 292 nm. When the calcined Gd₂O₂S:Tb³⁺ phosphors were excited by 292 nm UV light, the emission bands at 488 nm, 543 nm, 585 nm, and 622 nm were observed respectively in the PL spectrum.

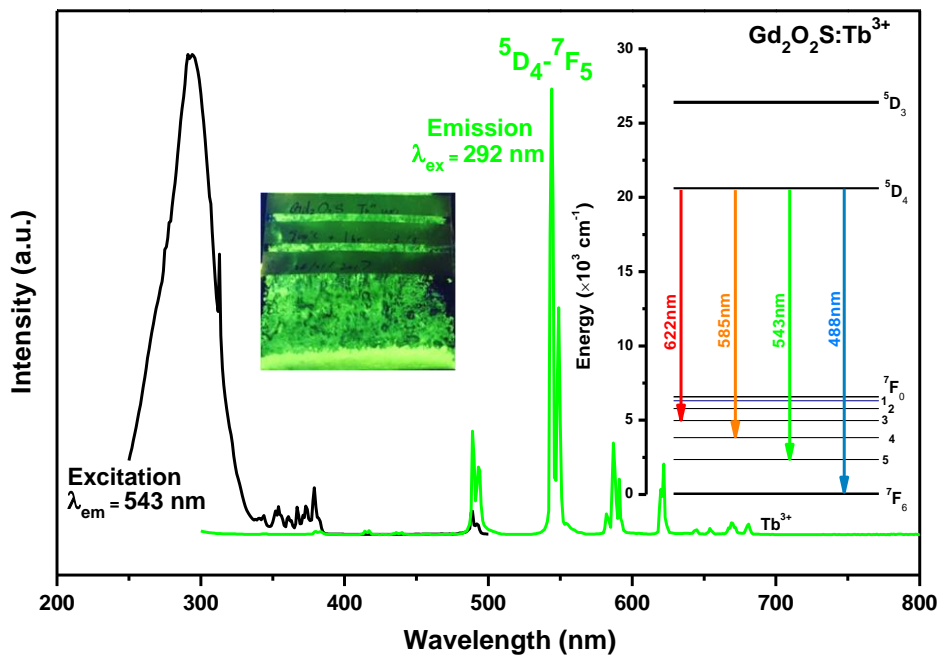


Figure 5.12. Excitation ($\lambda_{em} = 543$ nm) and emission ($\lambda_{ex} = 292$ nm) spectra of $Gd_2O_2S:Tb^{3+}$ particles calcined at 900 °C for 1 h. The inset shows the schematic energy level diagram of a free Tb^{3+} cation with proposed excitation and emission process, and a photograph of as-prepared phosphor sample showing bright green emission under irradiation with a 365 nm quartz tube lamp.

Among them, the green emission at 543 nm is the most intense band, with PL intensity reaching 39.1% in comparison with that of values for the sub-emission bands centred at 488 nm (9.2%), 585 nm (3.7%), and 622 nm (6.2%) respectively. This is assigned to the $^5D_4 \rightarrow ^7F_5$ energy level transitions of Tb^{3+} cations, as is revealed in the inset plot of Figure 5.12. This transition also proved for the intense green luminescence that can be seen by the naked eye under the irradiation of an UV lamp (see inset photograph in Figure 5.12).

The colour coordinate for the Tb^{3+} doped sample is $x = 0.339$ and $y = 0.586$, which is located in the green region of the CIE 1931 chromaticity diagram, as shown in Figure 5.13. The result suggests that this phosphor can be a candidate as an adapted green phosphor for UV-blue lights.

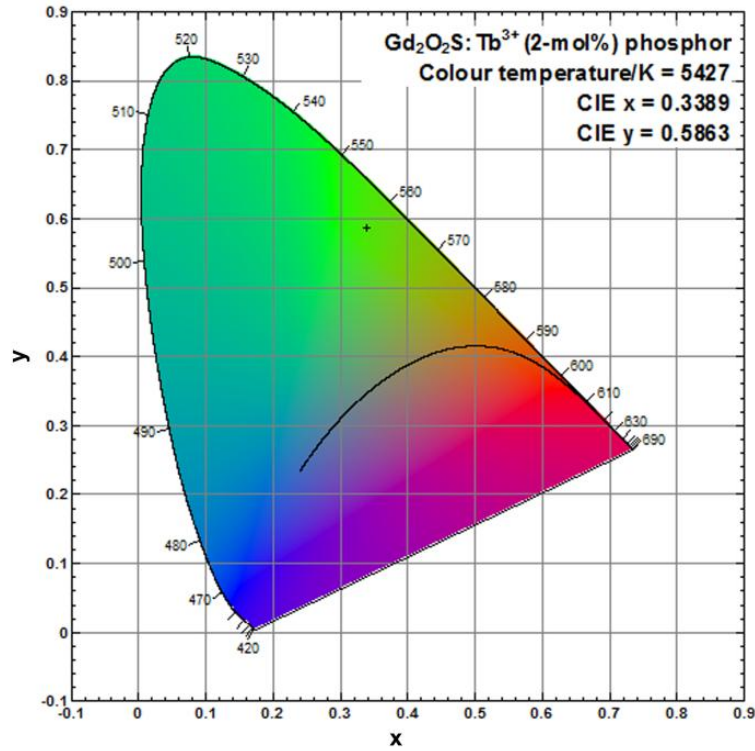


Figure 5.13. CIE chromatic diagram showing the x and y coordinates of Gd₂O₂S:Tb³⁺ sample excited by 254 nm UV light.

To evaluate the performance and the emission efficiency of Tb-doped phosphor for solar cell applications, the PL quantum yield (QY) measurements are performed. Table 5.2 summarises the QY (η) and energy absorption efficiency (ϕ) of the synthesised Gd₂O₂S:Tb³⁺ at excitation wavelength of 254 and 292 nm respectively. In present work, the QY (η) and (ϕ) were measured within an integrating sphere by using the absolute optical method presented by De Mello *et al* [219]. Results indicate that under excitation wavelength at 292 nm, the measured QY (η) and (ϕ) of the Gd₂O₂S:Tb³⁺ submicron-hexagons show the highest values of 47.3% and 57.2% respectively, which conforms to the required luminescent down-converter QY value of 40% to improve the energy performance of solar cell devices [220].

Table 5.2. PL quantum yield and energy absorption efficiency of the Gd₂O₂S:Tb³⁺ phosphor sample.

Sample ID	QY (η)	ϕ
Gd ₂ O ₂ S:Tb ³⁺ (2 mol%)	(%)	(%)
Ex 254 nm	40.9	50.3
Ex 292 nm	47.3	57.2

These obtained results also suggest that the as-prepared $\text{Gd}_2\text{O}_2\text{S}:\text{Tb}^{3+}$ phosphor possesses the down-converting properties by absorbing and converting high-energy UV photons into to the visible spectrum which could potentially contribute to enhanced photocurrent production, thus raising the conversion efficiency of mono-Si solar cells.

5.4.1.3 Crystal structures and morphological analysis

Figure 5.14(a) and (b) show the typical FE-SEM micrographs of synthesised $\text{Gd}_2\text{O}_2\text{S}:\text{Tb}^{3+}$ and undoped- $\text{Gd}_2\text{O}_2\text{S}$ particles fired at 900 °C. It can be seen that all the samples exhibit smooth and well-formed crystals although there is some agglomeration. Most of the particles have truncated spherical-like shape and they are smaller than 200 nm, which is more than 15 times smaller in diameter than that of commercial $\text{Gd}_2\text{O}_2\text{S}$ phosphors. The corresponding average particle size obtained from Lorentzian fitting of FE-SEM observations is 160.3 nm for $\text{Gd}_2\text{O}_2\text{S}:\text{Tb}^{3+}$ and 161.1 nm for undoped- $\text{Gd}_2\text{O}_2\text{S}$ (with determination coefficient R^2 values of 0.911 and 0.971 respectively), as demonstrated in the histograms presented in Figure 5.15. These results are consistent with the calculated data from the XRPD measurements (see Table 5.1).

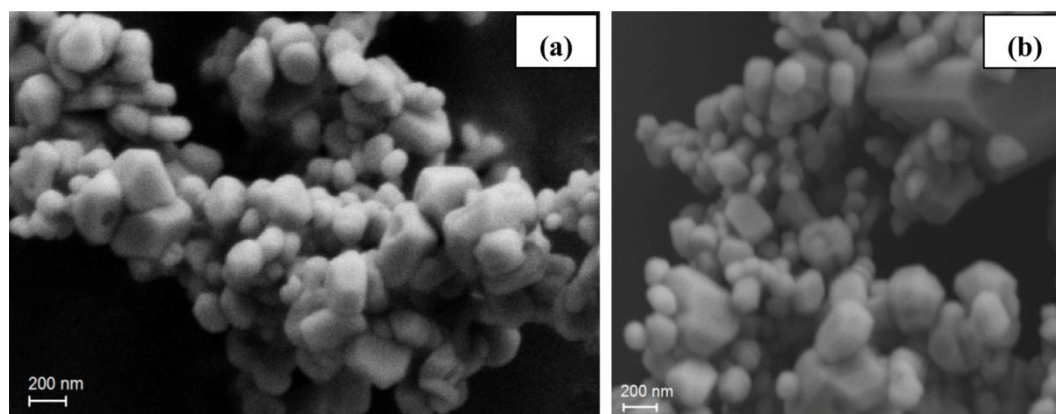


Figure 5.14. FE-SEM images of (a) representative $\text{Gd}_2\text{O}_2\text{S}:\text{Tb}^{3+}$ and (b) undoped- $\text{Gd}_2\text{O}_2\text{S}$ particles fired at 900 °C.

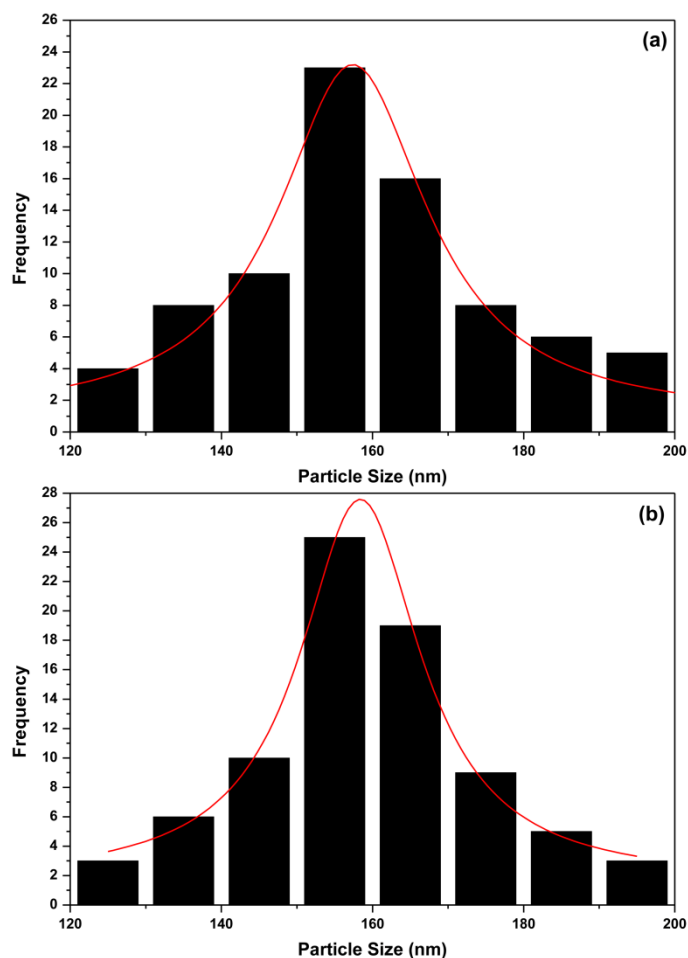


Figure 5.15. Histogram of (a) Gd₂O₂S:Tb³⁺ and (b) undoped Gd₂O₂S submicron phosphor samples showing Lorentzian curve fit in red.

Figure 5.16 shows the energy dispersive X-ray spectroscopy (EDS) spectra of the prepared phosphor powder sample from the FE-SEM observations. The presence of Tb in the prepared phosphor could be clearly seen from the corresponding EDS spectra. Furthermore, the results confirmed the existence of gadolinium (Gd), sulfur (S), and oxygen (O) elements in both synthesised powder samples. The additional peaks in the spectra with respect to carbon (C) is ascribed to the background (conductive carbon film), and there appeared to be less intense emissions regarding sodium (Na). This is caused by the insufficient separation between the bottom phosphor layer and the discarded top layer resulting from the sampling process (see Figure 5.6) where at their interface, small amounts of Na₂CO₃ may be blended with the phosphor layer after the sintering. However, for the moment, no data regarding the effects of Na element on either the luminescence intensity or the luminous efficacies of the Gd₂O₂S phosphors has been observed in the available bibliography.

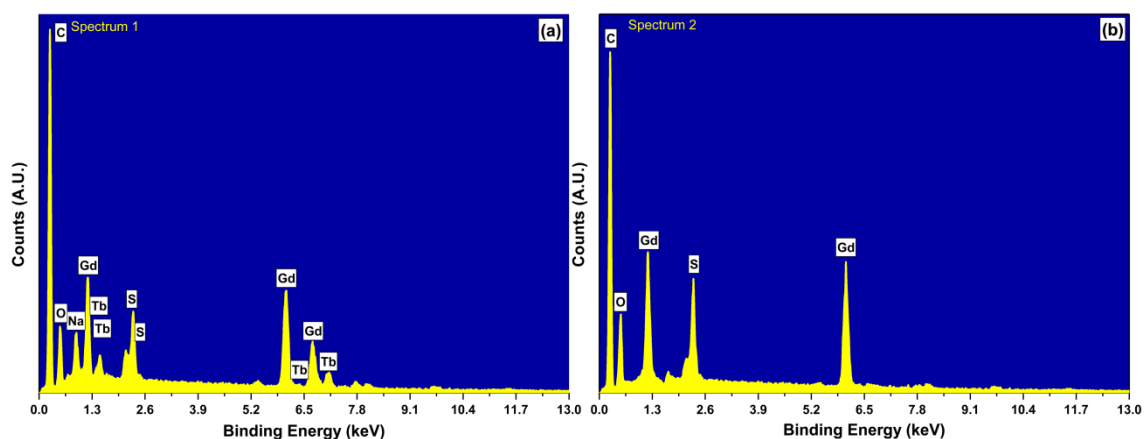


Figure 5.16. EDS spectra of (a) $Gd_2O_2S:Tb^{3+}$ phosphor and (b) undoped- Gd_2O_2S host materials.

Table 5.3. Elemental composition of $Gd_2O_2S:Tb^{3+}$ and undoped- Gd_2O_2S powder samples from the EDS spectra.

Gd_2O_2S			
Sr. N	Elements	Atomic (%)	Weight (%)
1	O K	41.85	9.63
2	S K	22.89	10.56
3	Gd L	35.26	79.81
Total		100	100
$Gd_2O_2S:Tb^{3+}$			
Sr. N	Elements	Atomic (%)	Weight (%)
1	O K	42.13	9.16
2	S K	19.32	8.43
3	Gd L	37.68	80.53
4	Tb L	0.87	1.88
Total		100	100

The background element such as C has been removed from the composition analysis.

Figure 5.17 shows the high angle annular dark field (HAADF) STEM images of the $Gd_2O_2S:Tb^{3+}$ particles fabricated in this work. In Figure 5.17(a), the discrete particles of roughly hexagonal shape with apparently a smooth surface can be clearly observed. In Figure 5.17(b), the light distribution image of a small cluster is seen, and the distribution of light appearing from part of the crystals is fairly uniform where some areas are brighter. The overlay image {see Figure 5.17(c)} shows the high uniformity of visible light (green) emission from the submicron sized phosphor particles.

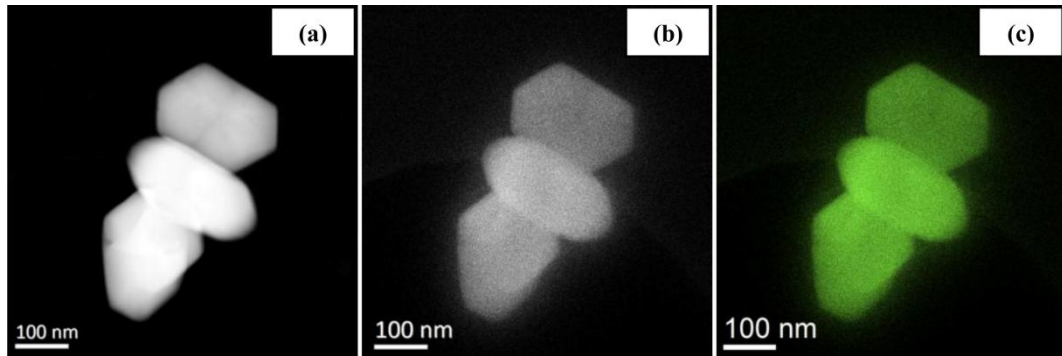


Figure 5.17. STEM micrographs of (a) single crystals of $\text{Gd}_2\text{O}_2\text{S:Tb}^{3+}$; (b) total visible light (CL) image using the VULCAN detector; (c) overlay of images of (a) and (b).

5.4.2 EVA Layer

Figure 5.18 shows the transmission spectra of quartz substrates coated with solely EVA layers after the annealing process. Results indicate that EVA layers that were dissolved in p-xylene solvent at different weight ratios of 9, 12, 15, 18 and 21-wt% show outstanding transmission properties especially in the visible region of wavelength from 400 to 850 nm in comparison with that of a quartz substrate and the decrease of transmission value is accompanied by the increased EVA ratio, which can be clearly observed from the inset plot in Figure 5.18.

Since in the current study, the thickness of wet film for each case of coated cell that obtained by rotary screen printing is determined by the distance between the rubber and engraved roller, as well as the volume of coating solution, which are fixed during the coating process. In this case, a higher wt% usually gives a thicker dry-film thickness and thus more EVA content in the prepared layer. Hence, it contains more additives such as chemical curing agents, stabilisers, and antioxidants which in turn results in a slight reduction of transmittance.

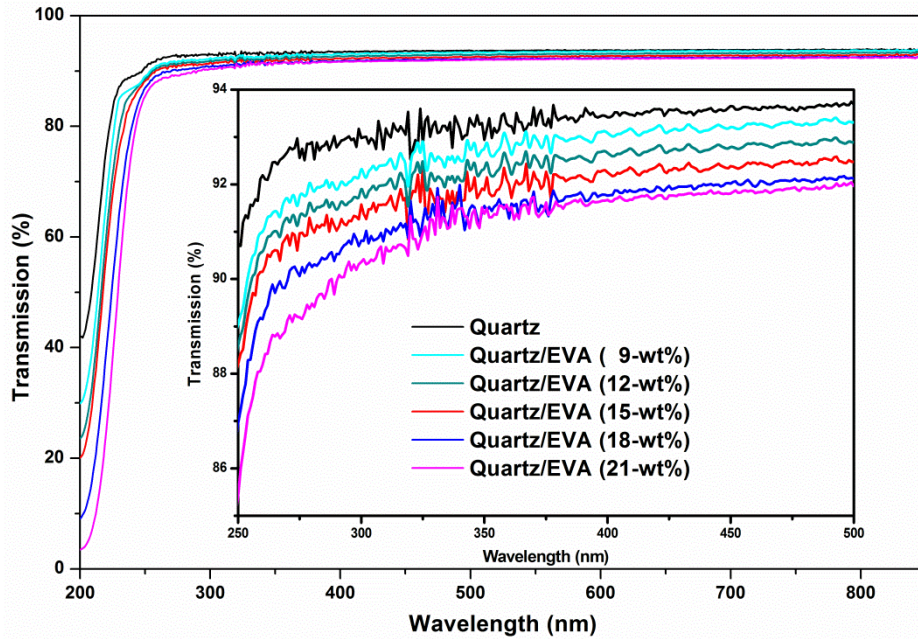


Figure 5.18. Transmission spectra of solely EVA layers with different weight ratio (wt%) deposited on the quartz substrates.

Figure 5.19 shows the reflection spectra of the uncoated cell and solar cells coated with solely EVA layers. Solar cells coated with EVA layers at tested wt% ratios show overall less reflectance in comparison with that of the uncoated solar cell over the measured wavelength range of 250 to 850 nm. In addition, the significant reduction in reflectance at wavelength of 250 to 400 nm can be clearly observed. This is attributed to the promotion of light trapping within the UV region resulting from the intrinsic anti-reflective properties of EVA raw materials. The obtained results also achieves good agreement with the relevant results in respect to the EVA's optical properties as reported in literature where the EVA films used for the encapsulation of silicon solar cell possess significant light absorption mainly in the short-wavelength of UV-region [163].

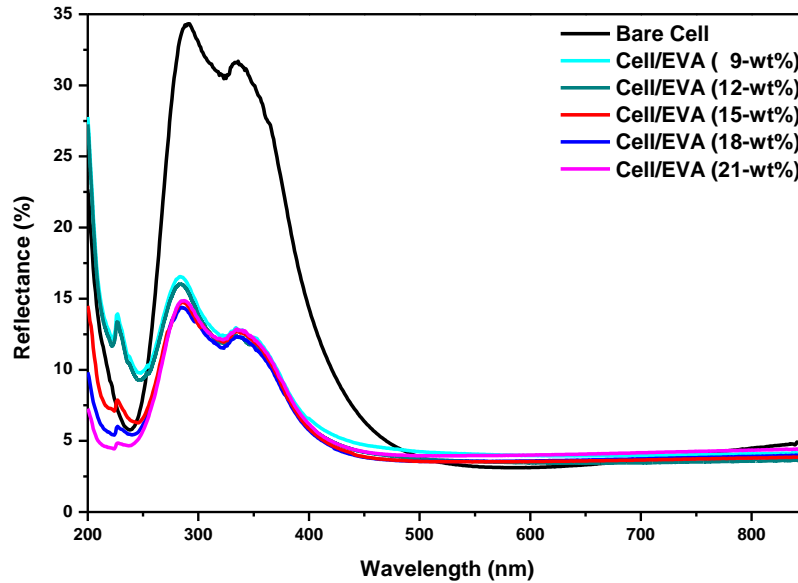


Figure 5.19. Reflection spectra of uncoated cell and solar cells coated with different ratios of EVA.

Table 5.4 summarises the effects of EVA coatings at tested weight ratios on the electrical characteristics of the mono-Si solar cells where the $J-V$ curve for the optimum coating condition is shown in Figure 5.20. It was found that coated cell with solely EVA at 15-wt% ratio provides the best electrical performance compared to other ratios of solely EVA coatings, with conversion efficiency reduced by 0.07% (from 16.43% to 16.36%), which potentially contributed to maximising the PCE enhancement. As indicated the EVA serves as binder for the phosphor particles and these layers tend to slightly reduce the solar cell's efficiency. In this case, it is pivotal to find a certain wt% of EVA that decreases efficiency by the smallest amount. Furthermore, since EVA coated cell with 15, 18, and 21-wt% exhibit similar reflectance performance in both UV and visible region (see Figure 5.19), the lower wt% may contribute to an increase in overall transmission of the resultant luminescent layer. Therefore, the ratio of 15-wt% was selected for mixing with the phosphor materials.

Table 5.4. PCE change in mono-Si solar cell coated with different wt% ratios of EVA.

<i>Cell Type</i>	<i>Ratio-in wt%</i>	<i>Uncoated η (%)</i>	<i>Coated η (%)</i>	<i>Variation in η (%)</i>
EVA	9	16.45	16.24	-0.21
EVA	12	16.38	16.25	-0.13
EVA	15	16.43	16.36	-0.07
EVA	18	16.40	16.30	-0.10
EVA	21	16.44	16.28	-0.16

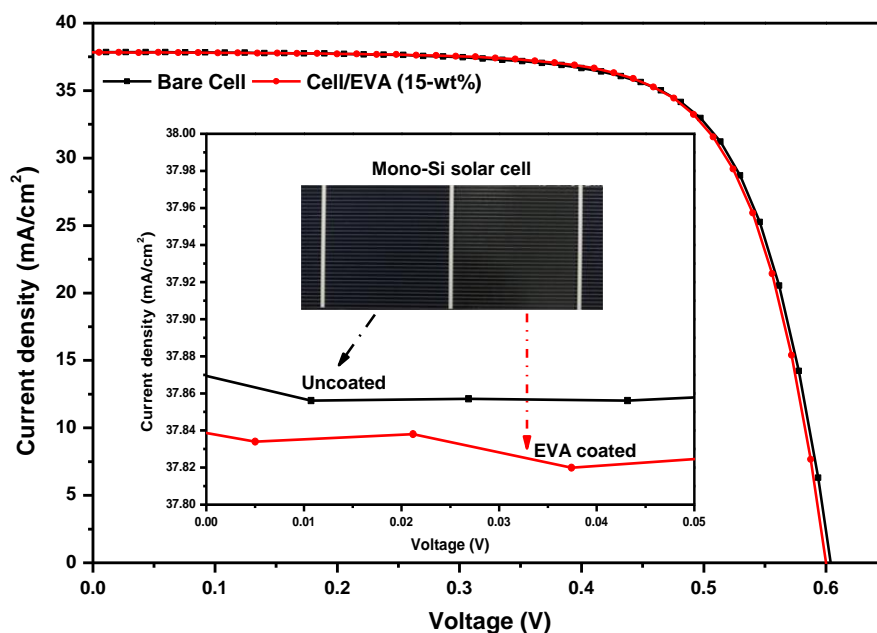


Figure 5.20. Photovoltaic J-V curves of mono-Si solar cell before and after coating with 15 wt% EVA examined at 1000 W/m^2 and $25 \text{ }^\circ\text{C}$, with illuminated surface area of 8.553 cm^2 . Inset shows a photograph of mono-Si solar cell with and without an EVA layer.

5.4.3 EVA/Gd₂O₂S:Tb³⁺ and EVA/Gd₂O₂S layer

5.4.3.1 Electrical characteristics

Figure 5.21 presents and compares the J - V curves of bare, solely EVA (15-wt%) binder-coated, EVA/Gd₂O₂S:Tb³⁺-coated, and EVA/undoped-Gd₂O₂S-coated solar cells at their maximum enhanced conversion efficiency. The corresponding electrical characteristics that were obtained are summarised in Table 5.5. The bare mono-Si solar cell exhibited a power conversion efficiency (PCE) of 16.43%, a short-circuit current density (J_{sc}) of 37.85 mA/cm^2 , and an open-circuit voltage (V_{oc}) of 604.6 mV. After coating with 15-wt% EVA on the textured surface, the J - V characteristics showed negligible variations in V_{oc} (603.5 mV) and J_{sc} (37.82 mA/cm^2), giving rise to a marginal decrease of 0.07% (from 16.43% to 16.36%) in PCE.

The highest increase in J_{sc} and V_{oc} , corresponding to a maximum enhancement of 3.6% (from 16.43% to 17.02%) in PCE compared with that of bare cell, was achieved by applying EVA/Gd₂O₂S:Tb³⁺ (2.0-mg/ml particle density) on the cell's textured

surface. This coating led to a relative increase of 2.5% in J_{sc} (from 37.85 to 38.81 mA/cm²), which is most likely the factor that contributed to the enhancement in PCE. Other electrical parameters such as maximum power (P_{max}) and fill factor ($F.F.$) also exhibit varying degrees of increase. In comparison, the enhancement brought by the EVA/undoped Gd₂O₂S coating at same particle density is less obvious, with J_{sc} increased by 1.5% (from 37.85 to 38.40 mA/cm²), corresponding to an overall increase of 2.3% (from 16.43% to 16.80%) in conversion efficiency. This phenomenon is due to the absence of doping agent (Tb³⁺) and thus the lack of certain UV photons for subsequent down conversion process, in such case, the improved light absorption is solely expected to benefit from the light scattering of the host particles.

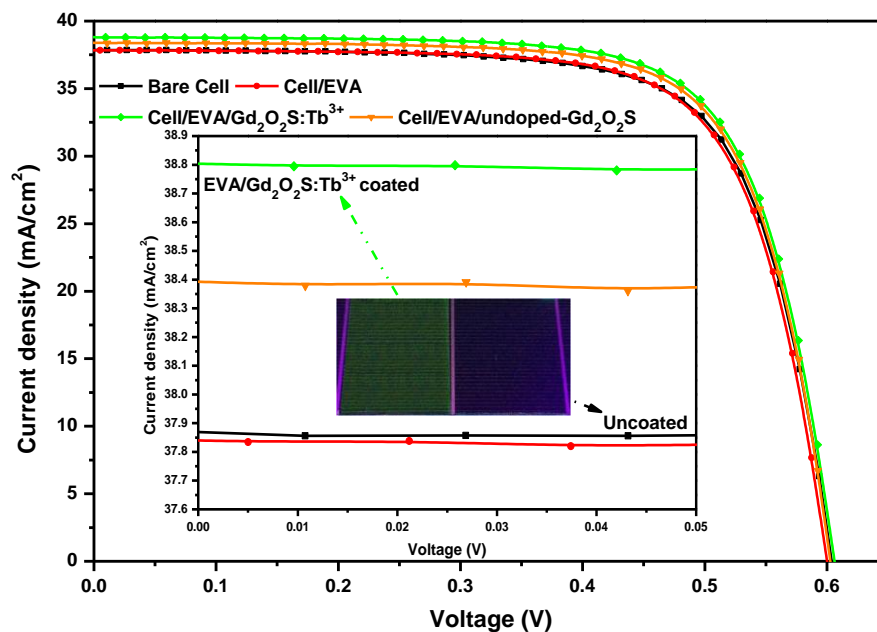


Figure 5.21. J-V curves of mono-Si solar cells with the following configurations: a bare cell, a cell coated with solely EVA (15-wt%) binder, a cell coated with EVA/undoped-Gd₂O₂S (2.0-mg/ml), and a cell coated with EVA/Gd₂O₂S:Tb³⁺ (2.0-mg/ml). Inset shows a digital photograph of solar cell coated with EVA/Gd₂O₂S:Tb³⁺ (2.0-mg/ml) composite layer irradiated by UV light.

In addition, the results demonstrate that the enhancement contributed from both dispersed phosphor and host particles at different concentrations in EVA binder can be achieved (see Table 5.5 and Figure 5.22). As illustrated in Figure 5.22, in both cases, the enhancement coefficient started to drop when the particle density exceeded 2.0-mg/ml, and eventually, the conversion efficiency began to deteriorate when the particle concentrations were higher than around 2.7-mg/ml. The reduction in PCE at 3.0-mg/ml

particle density may have been caused by the significant backward scattering arising from the serious particle aggregation.

Table 5.5. J-V characteristics of all evaluated solar cells.

Type	J_{sc} (mA/cm^2)	V_{oc} (mV)	P_{max} (W)	FF (%)	PCE (%)
Uncoated	37.85	604.6	0.1405	71.81	16.43
Cell/EVA	37.82	603.5	0.1399	71.71	16.36
Cell/EVA/Gd ₂ O ₂ S:Tb ³⁺ (1.0 mg/ml)	38.04	605.3	0.1415	71.88	16.54
Cell/EVA/Gd ₂ O ₂ S:Tb ³⁺ (1.5 mg/ml)	38.40	606.9	0.1440	72.19	16.83
Cell/EVA/Gd ₂ O ₂ S:Tb ³⁺ (2.0 mg/ml)	38.81	608.0	0.1456	72.15	17.02
Cell/EVA/Gd ₂ O ₂ S:Tb ³⁺ (2.5 mg/ml)	38.42	605.8	0.1430	71.90	16.72
Cell/EVA/Gd ₂ O ₂ S:Tb ³⁺ (3.0 mg/ml)	37.56	598.5	0.1377	71.60	16.10
Cell/EVA/Gd ₂ O ₂ S (1.0 mg/ml)	37.90	604.6	0.1407	71.83	16.45
Cell/EVA/Gd ₂ O ₂ S (1.5 mg/ml)	38.19	605.6	0.1421	71.86	16.61
Cell/EVA/Gd ₂ O ₂ S (2.0 mg/ml)	38.40	606.4	0.1437	72.12	16.80
Cell/EVA/Gd ₂ O ₂ S (2.5 mg/ml)	38.12	604.9	0.1417	71.83	16.57
Cell/EVA/Gd ₂ O ₂ S (3.0 mg/ml)	37.50	598.7	0.1374	71.63	16.06

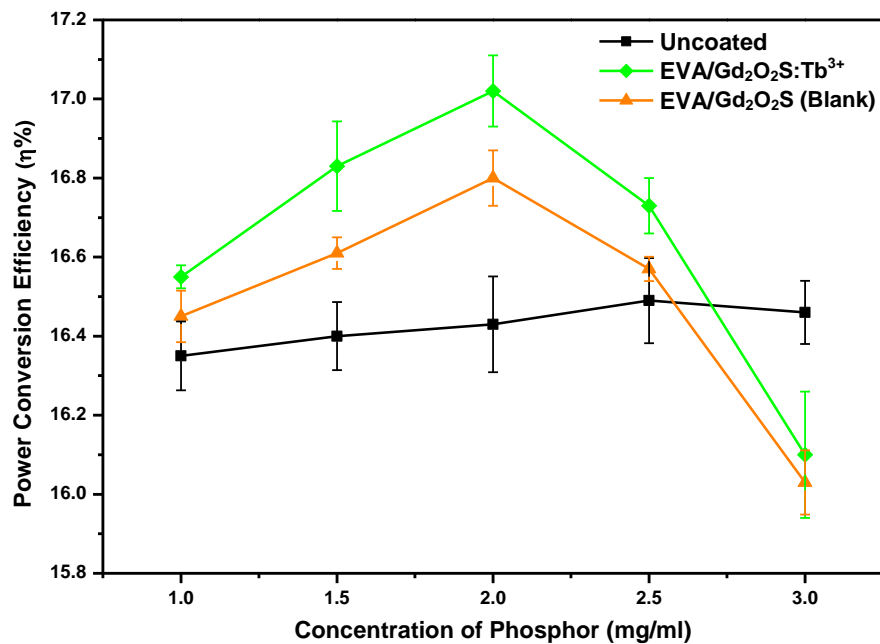


Figure 5.22. Enhancement in PCE of mono-Si solar cells coated with different concentrations of Gd₂O₂S:Tb³⁺ and Gd₂O₂S (blank) materials.

5.4.3.2 Optical Properties

In order to clarify the underlying mechanism for the observed efficiency enhancement, the reflectance measurements were performed. Figure 5.23 presents the reflectance and absorption spectra of uncoated solar cell and EVA/Gd₂O₂S:Tb³⁺

phosphor-coated cells at tested concentration. Comparing with the bare solar cell, the coated cell with EVA/Gd₂O₂S:Tb³⁺ at concentration of 1~2.5-mg/ml exhibit overall reduction in reflectance and higher absorbance over the measured spectral wavelength range of 200 to 850 nm.

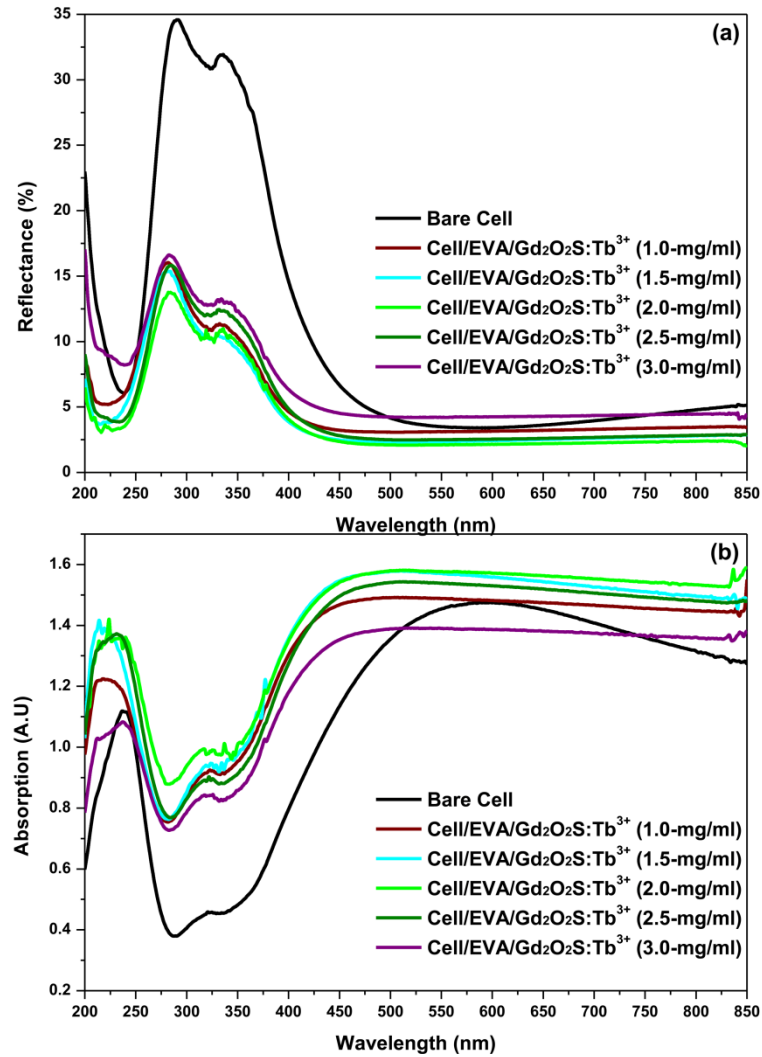


Figure 5.23. Comparison of reflectance and absorption spectra for uncoated and coated cells with EVA/Gd₂O₂S:Tb³⁺ at different phosphor concentrations.

Among them, the coated cell with EVA/Gd₂O₂S:Tb³⁺ at 2.0-mg/ml particle density shows a more significant reduction in the reflectance around the spectral region of 300 nm. This can be better explained by comparing the reflectance spectra with its corresponding EVA/undoped-Gd₂O₂S-coated cell, as shown in Figure 5.24. As can be seen from Figure 5.24(a), in the range of wavelength below 400 nm, the reflectance dropped because of the absorption of UV photons by Gd₂O₂S:Tb³⁺ phosphor particles.

The drastic reduction particularly in the UV-region of 290 to 380 nm by absorbing high-energy incident photons eventually achieved an overall reduction by almost 20% compared to that of a bare cell.

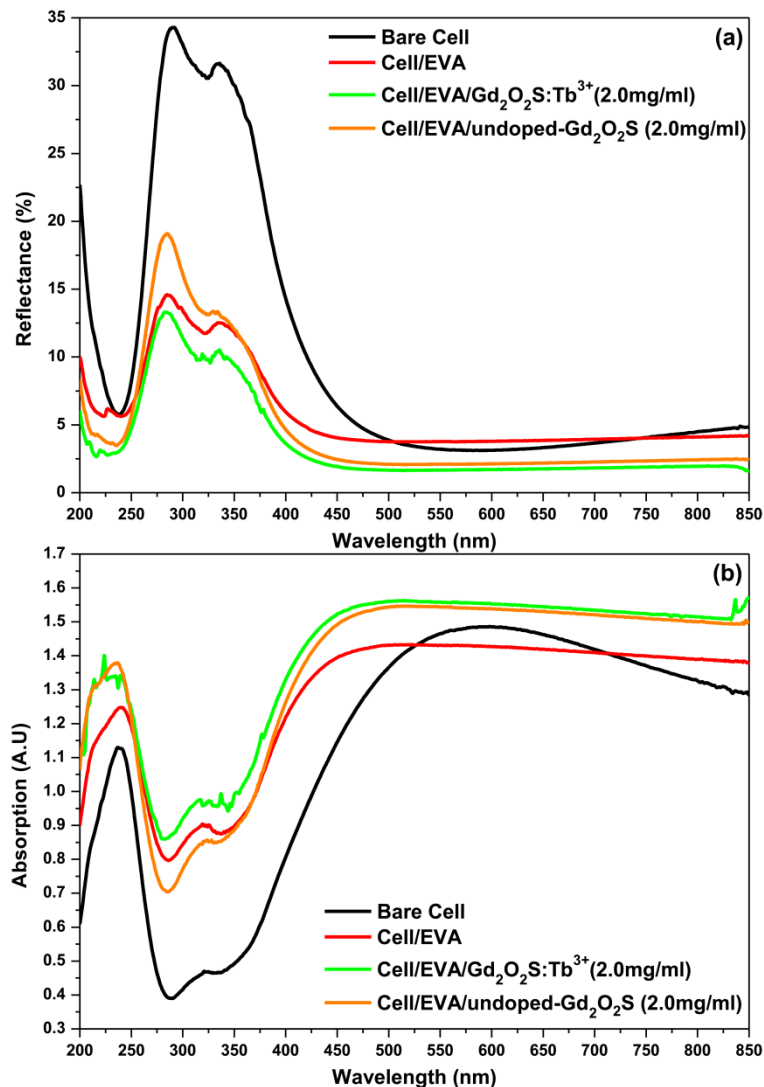


Figure 5.24. Comparison of reflectance and absorption spectra for uncoated and coated cells with solely EVA, EVA/Gd₂O₂S:Tb³⁺ (2.0-mg/ml), and EVA/undoped-Gd₂O₂S (2.0-mg/ml).

On the other hand, as shown in Figure 5.24(b) where in the range of wavelength above 400 nm, the absorption spectrum shows obvious increase in light absorption in the spectral range from 500 nm to 850 nm, since there is no PLE signal presented in the excitation spectrum (see Figure 5.12), therefore, the improved light absorption is associated with the light scattering from the phosphor particles. Similarly, in the case of EVA/undoped-Gd₂O₂S coated cell, analogous levels of light absorption in the visible region can be also observed. This is most likely because of the light scattering provided

from the hexagonal $\text{Gd}_2\text{O}_2\text{S}$ particles, which is believed to be essential for partially trapping and coupling of normally incident photons into the solar cells' active layers [161]. By contrast, the higher value of reflectance at UV-blue wavelengths compared to that of $\text{EVA}/\text{Gd}_2\text{O}_2\text{S}:\text{Tb}^{3+}$ coated device is ascribed to lacking functional features of UV absorbing ability without the presence of Tb doping agent in the host crystal.

However, as can be seen from Figure 5.23 where the reflectance spectrum of solar cell that coated with $\text{EVA}/\text{Gd}_2\text{O}_2\text{S}:\text{Tb}^{3+}$ at 3.0-mg/ml particle density shows slight higher reflectance value in the visible range of 500 to 750 nm than that of uncoated cell, and comparably higher reflectance to those of solar cells with lower concentration of phosphor coatings, which is largely due to the serious particle aggregation. At higher concentration, the substantial absorption in the UV region by $\text{Gd}_2\text{O}_2\text{S}:\text{Tb}^{3+}$ phosphors that may induce thicker phosphor films on the solar cell surfaces which undermines the original light-trapping capability from the solar cell's intrinsic textured surface and this will become more apparent with the increasing of areal particle density whether they are doped or undoped. As a result, it creates shading on the pyramid textured surface that affected significantly the original transmittance towards the cell in both UV and visible region, which in turn overshadowed the DC effects. This may also explain the reduction in corresponding electrical performance.

To further validate the obtained results regarding the efficiency enhancement, ellipsometry measurements on the deposited thin layers are carried out by coating a silicon wafer substrate using the same approach as preparing for the solar cells. The aims were to find out the optical refractive index "n" as well as the thickness "d" of the fabricated EVA/Phosphor composited films.

Due to the wavelength dependency, the refractive index is measured with monochromatic light at operating wavelength of 632.8 nm at 25 °C. Table 5.6 summarised the measured RI value and thickness for solely EVA coated, $\text{EVA}/\text{Gd}_2\text{O}_2\text{S}:\text{Tb}^{3+}$ and $\text{EVA}/\text{undoped-Gd}_2\text{O}_2\text{S}$ -coated thin films at different positions on their corresponding silicon wafer substrates as indicated in Figure 5.25. The measured results presume that there is no depolarization occurs on reflection from the tested

samples.

Table 5.6. Index of refraction (n) and film thickness (d) at 638.2 nm.

<i>Position</i>	<i>Refractive Index</i>	<i>Thickness (nm)</i>
(a) 1	1.644	1324.4
(a) 2	1.593	1494.3
(a) 3	1.543	1606.1
(a) 4	null	null
	Average: 1.593	Average: 1474.9
(b) 1	1.572	1509.2
(b) 2	1.563	1536.3
(b) 3	null	null
(b) 4	1.553	1482.9
(b) 5	1.556	1439.1
	Average: 1.561	Average: 1491.9
(c) 1	1.472	1332.8
(c) 2	1.482	1368.8
(c) 3	1.480	1315.9
(c) 4	1.495	1303.6
	Average: 1.482	Average: 1332

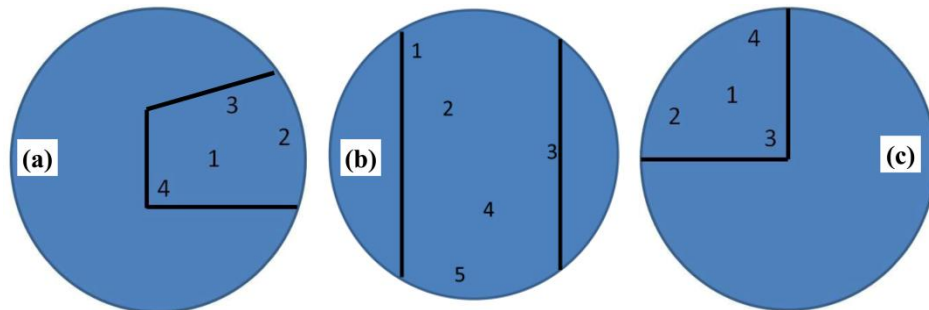


Figure 5.25. Pie charts showing the recorded beam positions of coated films on top of silicon wafer; (a) EVA/Gd₂O₂S:Tb³⁺ (2.0-mg/ml), (b) EVA/undoped-Gd₂O₂S (2.0-mg/ml), (c) solely EVA (15-wt%).

It is noteworthy that a matrix with a proper RI value is conductive, thus minimising the Fresnel reflection loss during the light absorption at the interface. As described in the previous chapter, to obtain the minimum reflection in a single-layer of anti-reflection coating (ARC), the refractive index of a typical antireflective material is expected to be approximate to the square root of refractive indices of the materials that bounding the coating [97]. As in our case, the deposited composite layer of EVA/Gd₂O₂S:Tb³⁺, EVA/undoped-Gd₂O₂S, and solely EVA film show average RI of $n = 1.593$, $n = 1.561$,

and $n = 1.482$ respectively, in each case, the coated layer is able to provide improved RI matching when sandwiched between the SiN_x layer and air, which can be potentially served as an alternative anti-reflection coating [193].

5.4.3.3 External quantum efficiency characterisation

External quantum efficiency measurements were performed to clarify the underlying mechanisms for the enhanced solar cell efficiency. The recorded EQE spectra are shown in Figure 5.26.

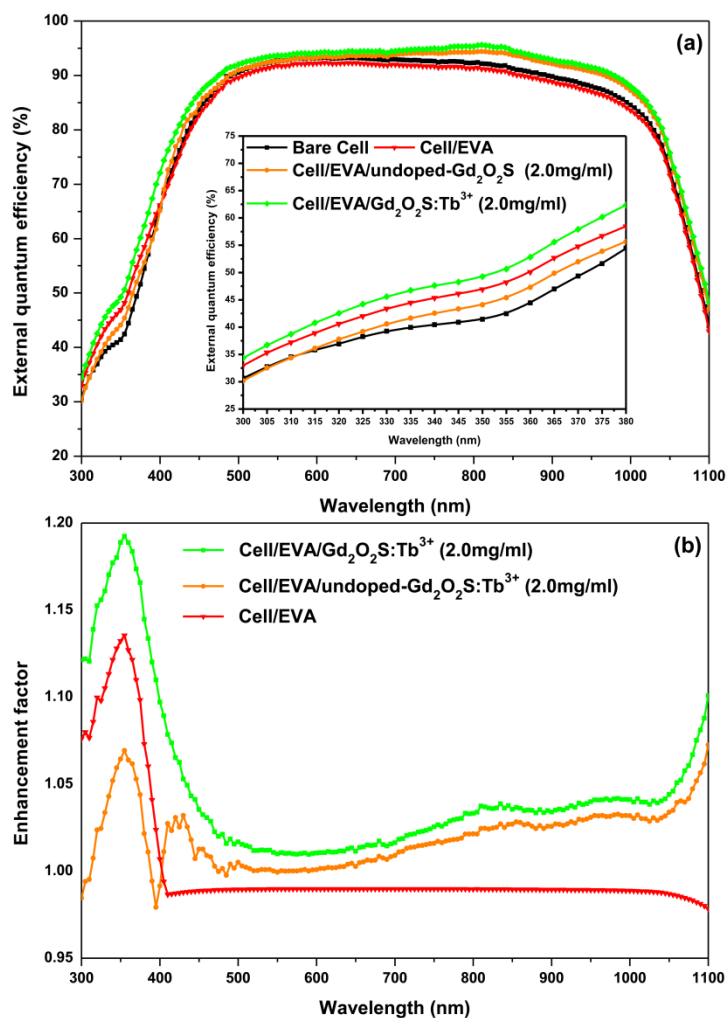


Figure 5.26. (a) EQE curves at maximum enhancement for solar cells integrated with $\text{Gd}_2\text{O}_2\text{S}$ submicron phosphors; (b) enhancement factor of EQE for solar cells coated with solely EVA, EVA/ $\text{Gd}_2\text{O}_2\text{S}:\text{Tb}^{3+}$, and EVA/undoped- $\text{Gd}_2\text{O}_2\text{S}$, compared to that of bare cell.

The EQE value for binder-coated cells is fairly close to that of bare cells and is slightly higher at wavelengths of 300-380 nm, which coincides with the obtained

reflectance results (see Figure 5.24). Moreover, the solar cell coated with EVA/Gd₂O₂S:Tb³⁺ composite layer shows overall higher EQE value than the bare cell throughout the entire wavelengths range of 300 to 1100 nm, and a maximum relative enhancement over 19% in the UV regions was observed, indicating explicitly that the increase in photocurrent is mostly arisen from the enhanced absorption of UV photons by the Gd₂O₂S:Tb³⁺ phosphors.

Since a large proportion of electron-hole pairs derived from absorbing high energy photons usually situated near the solar cell surface, the photo-generated carriers subsequently consume and disappear easily through their recombination due to the surface defects, which may in turn give rise to inferior carrier collection possibilities [195]. Nevertheless, since the phosphor particles are deposited onto the front surface of mono-Si solar cell, a greater number of photons can be absorbed closer to the solar cell's depletion region for photo-current generation as soon as the UV photons are down converted to the visible region of solar spectrum. With the effect of internal electric field (E-field), the photo-generated electron-hole pairs will be instantaneously separated, and thus the enhancement in PV effect.

As for the enhanced EQE response above 400 nm, the observed increase of EQE for both undoped-Gd₂O₂S and Gd₂O₂S:Tb³⁺ cases are in consistent with the variation of corresponding reflectance spectra, as illustrated in Figure 5.26. This enhanced behavior was mainly attributed to the improved light trapping on the basis of scattering by the submicrometer Gd₂O₂S hexagons. However, the reduced EQE value for EVA/undoped-Gd₂O₂S in comparison with that of EVA/Gd₂O₂S:Tb³⁺ particularly near the UV region (300 to 420 nm) proves that the doping ions (Tb³⁺) is solely responsible for the absorption of UV photons and later on the DC process for further photocurrent generation of mono-Si solar cells. These results also demonstrate that the integration of Gd₂O₂S:Tb³⁺ phosphor particles on the textured surface of mono-Si solar cells are able to increase the EQE within UV-region via DC effects and at longer wavelength through light scattering.

In addition, most importantly, the EVA binder used to encapsulate the phosphor

particles to the solar cell exhibits excellent visible light transmittance and also good light absorption particularly at short-wavelengths of UV-region {see Figure 5.18 and Figure 5.24(b)}, which did not disrupt the original DC functionality and uniform light scattering effect of the phosphor particles.

Figure 5.26(b) plots the enhancement factor for coated cells with maximum enhancement in EQE relative to those for a bare cell. The cells coated with EVA/Gd₂O₂S:Tb³⁺ (2.0-mg/ml) achieved the maximal EQE enhancement factor (>1.15, at 300-400 nm and >1.03 at 400-1100 nm), followed by the cells coated with EVA/undoped-Gd₂O₂S (2.0-mg/ml) (>1, at 410-1100 nm), and then by solar cell coated with solely EVA (15-wt%) binder (>1, at 300-400 nm).

5.4.3.4 Microstructure of the EVA/phosphor-coated cell

Figure 5.27 displays the cross-section image of a mono-Si cell after coating with EVA/Gd₂O₂S:Tb³⁺ (2.0-mg/ml particle density) using rotary screen printing technique. It shows clearly the morphology of pyramidally textured silicon surface and the coated luminescent layer composed of EVA/Gd₂O₂S:Tb³⁺ with an average thickness of 1.56 μm, which is close to the result of 1.47 μm that acquired from ellipsometry measurements. In addition, it can be seen that some of the Gd₂O₂S:Tb³⁺ particles are deposited onto the cell's surface through rotary screen printing, and most of the particles are well encapsulated by the EVA binder.

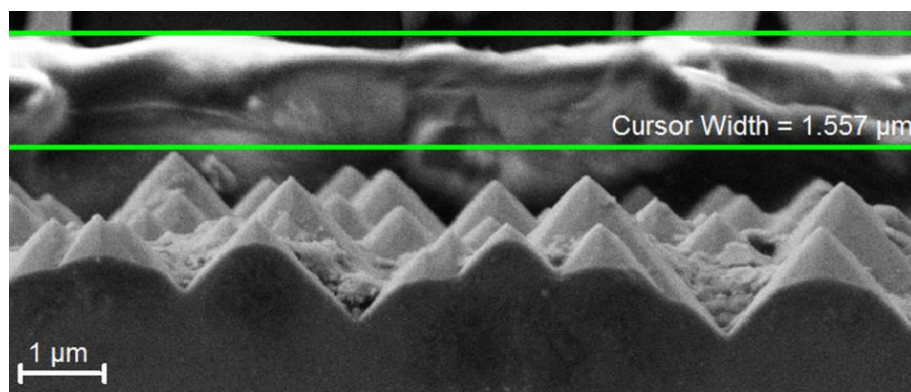


Figure 5.27. FE-SEM cross-section image of the mono-Si solar cell after coating with EVA/Gd₂O₂S:Tb³⁺.

The EDS results (see Figure 5.28) from the frontal-scanning area of coated cells confirmed that the deposited layers contain gadolinium (Gd), oxygen (O), sulphur (S) and terbium (Tb) elements. The additional intense peak in regarding to carbon (C) is from the EVA binder and silicon (Si) due to the textured silicon surface of the solar cell.

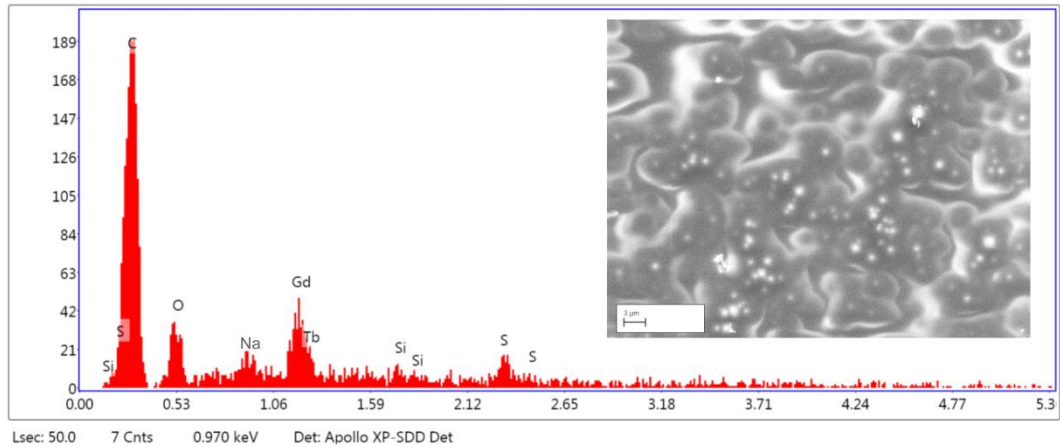


Figure 5.28. EDS spectrum and top-view SEM image of solar cell coated with EVA/Gd₂O₂S:Tb³⁺ at a concentration of 2.0-mg/ml; the scale bar is 3 μm.

5.5 Energy Performance Enhancement of Crystalline Silicon Solar cells Using Broadband Luminescent Down-converting Phosphor

5.5.1 Introduction

This section presents the experimental attempts of using broadband ultraviolet-spectral DC material for enhancing the spectral response and photovoltaic performance of mono-Si solar cells. The down-converting material employed in the experiment is Eu^{2+} -doped strontium aluminate ($\text{SrAl}_2\text{O}_4:\text{Eu}^{2+}$) where the phosphor material was encapsulated in Ethylene Vinyl Acetate (EVA) co-polymer resin and applied on the textured surface of solar cell using rotary-screen printing technique. Results from x-ray powder diffraction (XRPD), field emission scanning electron microscopy (FE-SEM) and photoluminescence spectroscopy studies on the microstructure and luminescent properties of the materials are reported.

5.5.2 Experiment method

The $\text{SrAl}_2\text{O}_4:\text{Eu}^{2+}$ phosphor was prepared by the high temperature solid state reaction method. This technique usually requires a heating of solid compounds at elevated temperature, which is recognised as the most suitable way to fabricate oxide luminescent materials with high emission intensity and crystallinity. The formation process of host and dopant through that of solid compounds is affected by many factors, such as the purity of the starting chemicals, the reaction temperature and ambient conditions [231]. The precursor materials used were strontium carbonate (SrCO_3 (99.9%)), aluminum oxide (Al_2O_3 (99.9%)), and europium oxide (Eu_2O_3 (99.9%)). All reagents were used without further purification.

In a particular experiment, stoichiometric amounts of raw materials were mixed and grinded through ball milling. The ratio of Eu element in Eu_2O_3 was set to 3 mol% with regard to that of SrAl_2O_4 molar concentration. Then grinded hybrids were placed in an alumina crucible and fired in a reduced atmosphere at 1350 °C for 3 hours. The reducing

atmosphere are generated with the help of 95% nitrogen (N₂) and 5% hydrogen (H₂) in order to convert Eu³⁺ to Eu²⁺ ions. At last step, after a natural cooling process, the sintered products were re-milled again and sieved to obtain fine powder.

The as-prepared SrAl₂O₄:Eu²⁺ phosphor powder was firstly dispersed in p-xylene to obtain a 2.0, 2.5, 3.0, 3.5, and 4.0-mg/ml solution and then separately mixed with a certain amount of EVA sheets. The mixture solution was then screen-printed on the textured surface of the solar cells (T6S-3A, Motech Industries, Taiwan) using the rotary roller. The coated cells were finally cured in a furnace at 190 °C for 5 mins.

5.5.3 Results and Discussion

Figure 5.29 shows the x-ray powder diffraction (XRPD) pattern for as-prepared SrAl₂O₄:Eu²⁺ DC phosphor. After the precursor is sintered at 1350 °C, two types of diffraction peaks have appeared in the XRD pattern. The intense peaks at $2\theta = 19.96^\circ$, 28.46° , 29.29° , 29.94° and 35.12° are ascribed to the diffraction of (011), (-211), (220), (211), and (031) plane of monoclinic SrAl₂O₄ crystal phase, matching well with the standard card (JCPDS 34-0379).

The excitation and emission spectra of as-prepared SrAl₂O₄:Eu²⁺ phosphor is shown in Figure 5.29(b). From the excitation spectrum, a broad excitation band from 250 nm to 500 nm can be observed, with a full width at half maximum (FWHM) reaching almost 100 nm. The most intense peak is centred at 358 nm. Furthermore, the PL spectrum shows a broad emission band from 450 nm to 650 nm under 358 nm excitation, with a emission peak centred at 520 nm, which is assigned to the $4f^65d^1$ to $4f^7$ ($^8S_{7/2}$) transition. The Stokes shift of the Eu-doped phosphor was estimated to be around 162 nm.

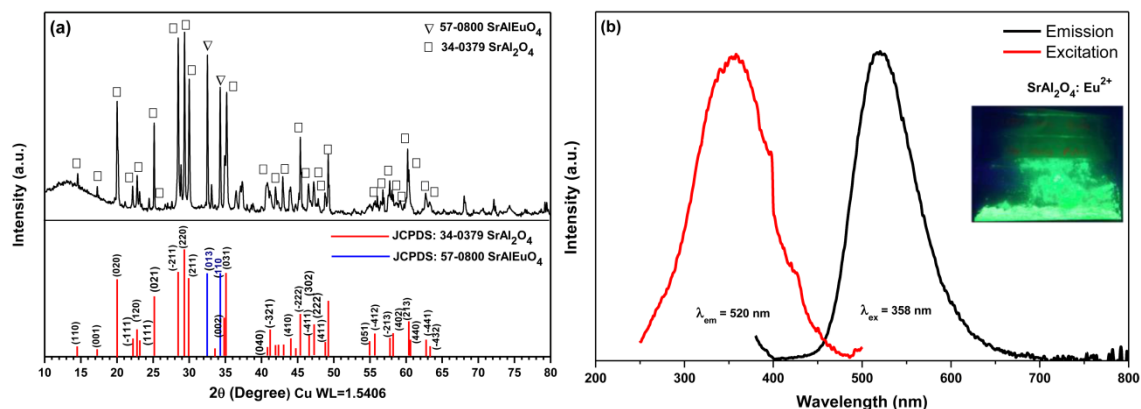


Figure 5.29. (a) XRPD pattern of $\text{SrAl}_2\text{O}_4:\text{Eu}^{2+}$ annealed at 1350 °C for 3h. (b) PLE and PL spectra of $\text{SrAl}_2\text{O}_4:\text{Eu}^{2+}$ at room temperature. Inset shows the digital photograph of as-prepared phosphor under 365 nm illumination.

Figure 5.30(a) and (b) show the typical FE-SEM micrographs of synthesised $\text{SrAl}_2\text{O}_4:\text{Eu}^{2+}$ phosphor. The micrograph {Figure 5.30(a)} shows a non-uniform distribution of particles and generally they are of irregular shape with smooth surface and well-formed crystalline forms. Unfortunately, the statistical analysis of the size distribution from SEM data was difficult to obtain due to the serious particle aggregation. The size ranges of 800 nm to 3.5 μm were measured from those well-discrete particles. The EDS spectra {see Figure 5.30(c)} obtained from the top-view of coated cell confirms that the deposited layers contain the chemical elements such as strontium (Sr), aluminium (Al), oxygen (O), and europium (Eu). The additional peaks corresponding to carbon (C) is from the EVA binder.

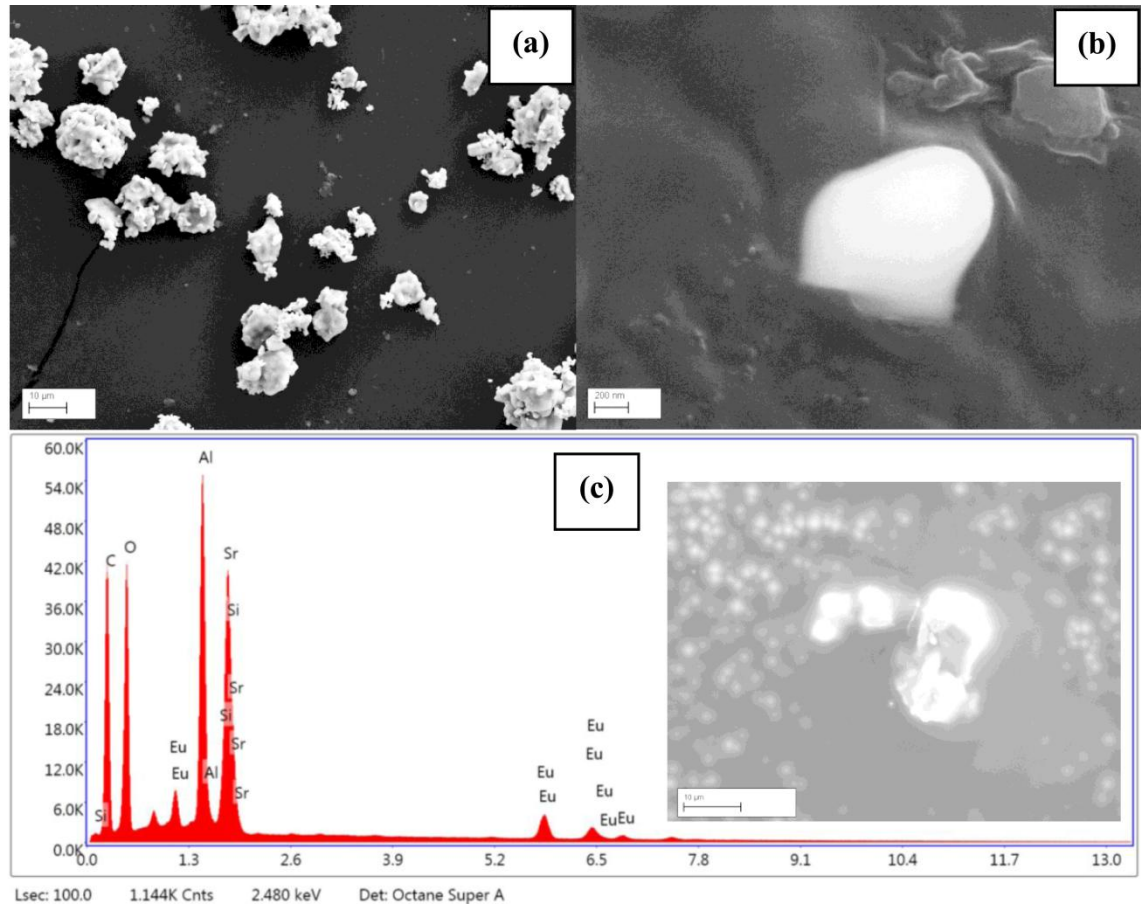


Figure 5.30. (a), (b) FE-SEM micrographs of SrAl₂O₄:Eu²⁺ annealed at 1350 °C. (c) EDS spectra of EVA/SrAl₂O₄:Eu²⁺ composite film deposited on mono-Si solar cell. Inset SEM micrograph shows the top-view of coated cell.

Figure 5.31(a) shows and compares the J-V curves of uncoated-, solely EVA-coated, and EVA/SrAl₂O₄:Eu²⁺-coated solar cells (3.0-mg/ml). Detailed electrical characteristics of all evaluated cells are summarised in Table 5.7. The power conversion efficiency (PCE), short circuit current density (J_{sc}), open circuit voltage (V_{oc}), and fill factor (FF) for bare cell were 16.43%, 37.87 mA/cm², 604.3 mV, and 71.85% respectively. These parameters are almost unaffected with the integration of EVA coating. The highest increase in J_{sc} (~0.5 mA/cm²), corresponding to a maximum efficiency enhancement of 0.28% was achieved when solar cell surface was coated with EVA/SrAl₂O₄:Eu²⁺ at particle density of 3.0-mg/ml. The efficiency deteriorated when the particle densities exceed 3.8-mg/ml {PCE lower than uncoated cell, see Figure 5.31(b)} since the serious particle aggregation resulted in a significant loss in transmittance towards the solar cell throughout the whole spectral range.

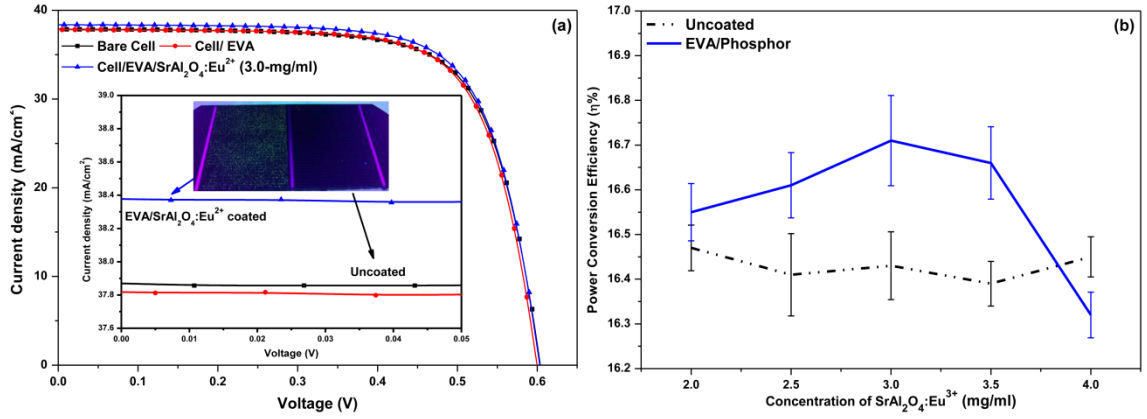


Figure 5.31. (a) J-V curves of mono-Si solar cells before and after coating with EVA, EVA/ $\text{SrAl}_2\text{O}_4:\text{Eu}^{2+}$ (3.0-mg/ml). Inset image shows the coated cell with EVA/ $\text{SrAl}_2\text{O}_4:\text{Eu}^{2+}$ composite layer under UV illumination. (b) Enhancement in PCE of coated cells at different.

Table 5.7. J-V characteristics of all evaluated solar cells.

Type	J_{sc} (mA/cm^2)	V_{oc} (mV)	P_{max} (W)	FF (%)	PCE (%)
Uncoated	37.87	604.3	0.1405	71.85	16.43
Cell/EVA	37.82	603.1	0.1399	71.73	16.36
Cell/EVA/ $\text{SrAl}_2\text{O}_4:\text{Eu}^{2+}$ (2.0 mg/ml)	38.10	604.6	0.1416	71.89	16.55
Cell/EVA/ $\text{SrAl}_2\text{O}_4:\text{Eu}^{2+}$ (2.5 mg/ml)	38.19	604.6	0.1420	71.94	16.61
Cell/EVA/ $\text{SrAl}_2\text{O}_4:\text{Eu}^{2+}$ (3.0 mg/ml)	38.37	605.3	0.1429	71.94	16.71
Cell/EVA/ $\text{SrAl}_2\text{O}_4:\text{Eu}^{2+}$ (3.5 mg/ml)	38.31	605.0	0.1425	71.89	16.66
Cell/EVA/ $\text{SrAl}_2\text{O}_4:\text{Eu}^{2+}$ (4.0 mg/ml)	37.58	604.3	0.1395	71.85	16.32

Figure 5.32 shows the variations in the reflectance of the mono-Si solar cells coated with $\text{EVA}/\text{SrAl}_2\text{O}_4:\text{Eu}^{2+}$ at different particle concentrations. For comparison, the reflectance spectra of bare cell and solely EVA coated cell are also presented. The results show that the coated cells with enhanced performance exhibited overall reduction in reflection at tested wavelength range of 200 to 850 nm. However, even at the optimal particle density of 3.0-mg/ml, the enhancement in reflectance within both UV and visible region is insignificant. This is most likely caused by the strong back scattering of the phosphor particles with grain size larger than the width profile of the pyramidal textured structures as they reflect a considerable fraction of incident light and decline the original transmittance towards the cell. As a result, the benefits in light harvesting obtained from down-conversion were largely offset by the shading effect.

However, this is inevitable since solid state method usually requires high reaction

temperature (1300-1900 °C) which eventually generated large- and highly-agglomerated particles. Further reduction in particle size through mechanical milling may induce additional structural and surface defects that increase the frequency of non-radiative recombination and relaxation process, which in turn impair the luminescent materials' optical properties and quantum efficiency [233,234].

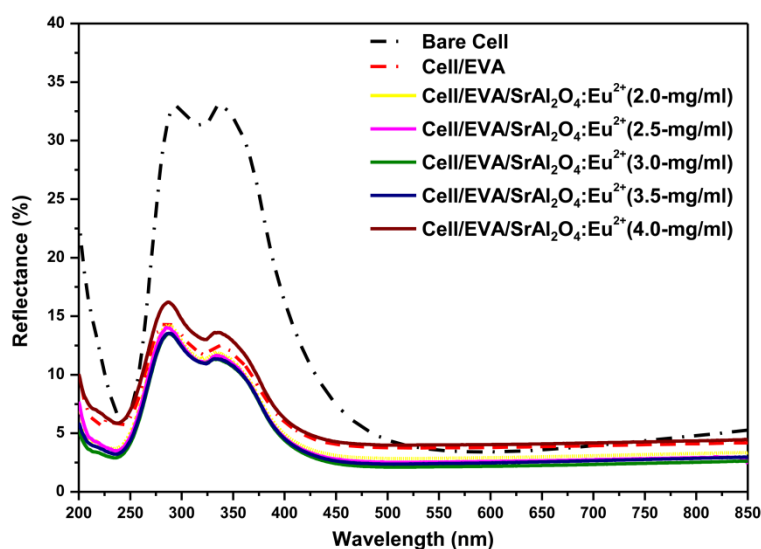


Figure 5.32. Reflectance spectra of all evaluated solar cells.

5.5.4 Conclusion

This work demonstrated the possibility of using broadband luminescent down-converting phosphor material for improving the electrical characteristics of commercial monocrystalline silicon solar cells. The $\text{SrAl}_2\text{O}_4:\text{Eu}^{2+}$ phosphor, prepared by solid state method shows high luminescent intensity and broad absorption band in the spectral region of 280 to 450 nm. This phosphor can be potentially used as a UV-spectral down converter and applied onto the mono-Si solar cell through rotary screen printing technique. Although the optimum design by integrating EVA/ $\text{SrAl}_2\text{O}_4:\text{Eu}^{2+}$ onto the cell surface showed only a marginal increase in PCE under AM 1.5G illumination, but it opens new possible approaches of utilising more Eu^{2+} -doped broadband DC phosphors to suppress the Fresnel reflection loss and to improve the spectral response of commercial mono-Si solar cells at short-wavelength of UV-region. Further efficiency gains can be expected by reducing the particle size and increasing the quantum efficiency of $\text{SrAl}_2\text{O}_4:\text{Eu}^{2+}$.

5.6 Summary

This chapter developed a simple and cost-effective luminescent layer applied onto the textured surface of mono-Si solar cells and demonstrated that the down-converting $\text{Gd}_2\text{O}_2\text{S:Tb}^{3+}$ phosphor could effectively improve the solar cell's conversion efficiency.

The empirical results showed an optimum enhancement of 3.6% (from 16.43% to 17.02%) in PCE relative to those for a pristine cell. This enhancement was attributed to the improved light absorption brought by the conjunction effects of EVA binder and $\text{Gd}_2\text{O}_2\text{S:Tb}^{3+}$ phosphor. The integration of Tb-doped phosphor particles on a front-textured solar cell can enhance the EQE within the UV-region through DC effects and within the visible-region through forward light scattering.

$\text{Gd}_2\text{O}_2\text{S:Tb}^{3+}$ submicron phosphor, as the down-converting material with a high photoluminescence quantum yield and good thermal stability, is a suitable alternative to obtain an enhanced solar cell performance at a relatively low cost and is environmentally friendly. EVA matrix provides promising host conditions for the phosphor particles and finally, the rotary screen-printing formed a relatively uniform layer and it is believed to be applied to various types of photovoltaic devices and other phosphor powders.

In this chapter, efforts and attempts on obtaining a further breakthrough in improving device performance through expanding of the luminescence bandwidth were also made by applying a broadband luminescent down-converting europium (Eu)-doped strontium aluminate (SrAl_2O_4) phosphor/EVA composite layer onto the silicon solar cell surface via rotary screen printing. Although the optimal design showed only a marginal increase of 0.28% in PCE, but it opens new possible schemes to resolve the reflection loss in silicon solar cell. Unprecedented device performance and further efficiency gains can be expected by reducing the particle size down to submicron-scale.

Chapter 6 Summary and Future Work

This chapter gives the summary and conclusion for this thesis. Expectations of future research are briefly discussed.

6.1 Summary and Conclusion

Overview and Motivation

The main target of this work aims at exploring an efficient and suitable approach to improve the photovoltaic performance of single crystalline silicon solar cells through the application of novel light-harvesting materials. Candidate materials investigated include porous titanium dioxide (TiO_2) and magnesium oxide doped-titanium dioxide nanoaerogels (MgO-TiO_2), as well as the europium-doped strontium aluminates ($\text{SrAl}_2\text{O}_4:\text{Eu}^{2+}$) and the submicron-sized terbium-doped gadolinium oxysulfide ($\text{Gd}_2\text{O}_2\text{S}:\text{Tb}^{3+}$) phosphors.

A simple and cost-effective laboratory method for producing dual-function ARC on mono-Si solar cells was developed by screen-printing a mixture solution of those candidates dispersed in an EVA co-polymeric matrix onto the solar cells' textured surface. In this thesis, integrations of ARCs on the surface of silicon solar cells were successfully demonstrated using two different coating techniques. Blade screen printing method is used for the deposition of titanium dioxide-based nanocomposite layer while the EVA/phosphor luminescent-composite layer was obtained by using the rotary screen printing technique.

EVA/TiO₂ Antireflection Coating

In chapter 4, anatase phase TiO_2 and MgO-TiO_2 mixed oxide nanoparticles were investigated and used as the precursor materials of ARC for silicon solar cells owing to their outstanding UV-photocatalytic performance and excellent optical properties. Mesoporous TiO_2 -based nanoaerogels with high specific surface area have been

successfully prepared by colloidal homogeneous precipitation sol-gel method and their application on commercial p-type single-junction mono-Si solar cells have showed great capability in promoting the light absorption as well as in improving the electrical characteristics. Significant reduction in optical reflectance particularly at short-middle wavelength of UV-region can be clearly observed when these nanoaerogel coatings are deposited on the cell's surface due to the absorption of high-energy photons by TiO₂-based nanoparticles. On the other hand, in the visible region, more incident photons are able to penetrate through the porous nanoaerogels and subsequently reach at the interface of the textured layer, giving rise to an overall enhancement in light-harvesting and the photoelectric conversion efficiency of silicon solar cells.

In this chapter, the effects of MgO dopant on boosting the light scattering capacity of TiO₂ NPs are investigated. Doping small amount of MgO into TiO₂ crystals resulted in a remarkable increase in specific surface area and enhancement in photon absorption performance as the substitution of Ti⁴⁺ by Mg²⁺ could induce crystal defects and vacancies at the surface of mixed oxide system, which may potentially helps in suppressing the recombination of charge carriers near the device surface and increasing the photon transition and conversion because the light is more easier to transmit through the pore and strike on the SiN_x layer. This is responsible for the further promotion in light absorption as well as the more pronounced increase in power conversion efficiency. Furthermore, the concentration of dispersed TiO₂-based nanoaerogels is closely linked to the enhanced electrical performance of coated cells. The optimum design for boosting the light-harvesting efficiency was achieved by integrating EVA/MgO-doped TiO₂ nanocomposite on solar cells' textured surface where a relative enhancement of 6.0% in power conversion efficiency has been demonstrated at particle density of 0.3-mg/ml.

In this study, fabrication of TiO₂-based aerogel nanomaterials is simple and environmental friendly without any toxic product. The nanometer sized TiO₂ spheres are more stable and economical than other metallic nanoparticles due to their intrinsic feature of oxides, which may allow this design feasible for solar cells at production scale. Blade screen printing method formed a homogeneous nanocomposite layer which

served as an efficient ARC to compensate for the low spectral response of silicon solar cells at UV-blue region. Moreover, film thickness and size produced through this approach is controllable with the use of different coating guides which could be applied in other types of photovoltaic devices.

EVA/Phosphor Down-conversion Coating

An alternative scheme to overcome the poor spectral response of silicon solar cells at short wavelength has been proposed in chapter 5 where the green-emission terbium-doped gadolinium oxysulfide phosphor material was employed as a spectral down-converter. In this work, the submicrometer-sized (~ 160 nm) $\text{Gd}_2\text{O}_2\text{S:Tb}^{3+}$ hexagons, with a high quantum yield ($\sim 47\%$) and relatively broad UV absorption band, are qualified to improve the solar cell's performance. Compared to most metallic nanoparticles and quantum dots, they are more stable and efficient in attaining enhancement on conversion efficiency of solar cells in a low cost manner.

Fabrication of the luminescent-composite layer by encapsulating the phosphor particles in an EVA matrix could produce a dual-function coating on mono-Si solar cells' textured surface because this coating not only serves as a down-converting layer at short-wavelength of solar spectrum but also acts as an antireflective layer in the longer wavelength region. Under an AM 1.5 illumination condition, the best design by applying EVA/ $\text{Gd}_2\text{O}_2\text{S:Tb}^{3+}$ on the textured surface of mono-Si solar cell achieved a highest increase of 2.5% in J_{sc} , corresponding to a maximum enhancement of 3.6% in power conversion efficiency. The potential mechanism behind the observed enhancement can be attributed to the luminescent down conversion, as well as to the improved visible light trapping and optical index matching, benefiting from the combined effects of EVA binder and phosphor particles. Comparative analysis on enhanced solar cells revealed that the presence of submicron $\text{Gd}_2\text{O}_2\text{S:Tb}^{3+}$ phosphor gives rise to a noticeable increase in EQE and drastic reduction in reflectance in the UV range, which also explains the more pronounced increase in photocurrent and conversion efficiency whereas these are not observed when solar cells are coated with undoped- $\text{Gd}_2\text{O}_2\text{S}$ bulk materials. Meanwhile in the visible region, the enhancement in

EQE is mostly likely due to the outstanding scattering behavior provided by the hexagonal Gd_2O_3 particles because no PLE signal is detected in this region. A further enhancement in conversion efficiency can be expected with the increase of luminescent quantum yield as long as the particle concentration is adjusted to its optimal value. In addition, most notably, the EVA used in this work plays a pivotal role in contributing to obtaining the maximum performance enhancement in silicon solar cells since it not only serves as a binding material for encapsulating phosphor particles to the solar cell but also provides antireflective properties with an adapted refractive index which did not impair the DC effect and inherent light-scattering behavior of the phosphor particles. Finally, the rotary screen printing technique offers an easier alternative way of establishing a homogeneous dual-function ARC comprising an inorganic phosphor and polymeric matrix to overcome the spectral mismatch in silicon solar cells which can be applied to a variety of types of photovoltaic devices and other related phosphors.

6.2 Outlook and Future Direction

The application of TiO_2 -based nanoaerogels will continue to gather more research interest, with the obtained results, the expectation for future work is to explore for new candidate dopants in order to modify the optical properties of TiO_2 since its light absorption capacity is still confined to UV-region due to the wide bandgap (3.2 eV). Thus, for obtaining efficient light-harvesting performance, it is essential to extend its photon response range from UV to visible region of solar spectrum. Doping nanostructured TiO_2 with moderate level of transition metallic elements (e.g., Fe, Cr) that having lower band gap energy may contribute to a red shift of the absorption edge and in consequence the improved visible light photoactivity. In addition, it is expected that an optimum incorporation of metal ions in TiO_2 host matrix could help suppress the recombination of photogenerated electron-hole pair and prolong the lifetime of minority carriers in silicon solar cells.

As for the research of phosphor application on PV cell's performance enhancement conducted in this study, a possible avenue of future suggestion is to develop new

candidate materials for DC or luminescent down-shifting (LDS) layer by expanding the spectral operating range (absorption band) across the whole UV-region while retaining the photoluminescence quantum yield and particle size. This is of crucial importance since it could ensure a more efficient utilisation of solar spectrum for spectral conversion while maintaining the light scattering behavior across a large spectral region and thus further enhancement of light trapping in silicon solar cells. In addition, Tb, as an efficient rare earth element, which exhibited significantly high emission intensity and luminous efficacies, however, to some extent, it is also an expensive lanthanide in comparison with others and that replacement of Tb by other lanthanides (such as Eu, Yb and Pr) to reduce the production cost might be one of executable subjects in the future research work. Note that the phosphor in current work serves as UV-spectral converter and it is believed that such a luminescent-composite layer could help alleviate the degradation of EVA caused by the photothermal decomposition, which may find new applications in PV module encapsulation materials. Furthermore, an extra benefit from incident spectrum may be accomplished by applying luminescent species on the back surface of silicon cells as an up-converter without disrupting the absorption of high-energy photons by DC materials on the top surface, and therefore a further harvest of photocurrent.

References

1. Sen, S., Ganguly, S., Opportunities, barriers and issues with renewable energy development – A discussion. *Renewable and Sustainable Energy Reviews*, 2017. **69**: p. 1170-1181.
2. International Energy Agency (IEA)., *Global Energy & CO₂ Status Report*, Paris, France, 2018. [Online]. Available at: <http://www.iea.org/publications/freepublications/publication/GECO2017.pdf>. [Accessed: 1 August 2018].
3. British Petroleum public limited company (BP plc). *BP Statistical Review of World Energy (67th edition)*, London, United Kingdom, 2018.
4. Weisz, P.B., Basic Choices and Constraints on Long-Term Energy Supplies. *Physics Today*, 2004. **57**(7): p. 47-51.
5. Sims, R.E.H., Schock, R.N., Adegbululgbé, A., Fenhann, J., Konstantinaviciute, I., Moomaw, H.B., Schlamadinger, B., Torres-Martínez, J., Tuner, C., Uchiyama, Y., Vuori, S.J.V., Wamukonya, N., Zhang, X., 2007: Energy Supply. In *Climate Change 2007: Mitigation. Contribution of Working Group III to the Fourth Assessment Report of the Intergovernmental Panel on Climate Change* [Metz, B., Davidson, O.R., Bosch, P.R., Dave, R., Meyer, L.A., (eds)], Cambridge University Press, Cambridge, United Kingdom and New York, NY, USA.
6. European Council., *Conclusions EUCO 169/14.*, October. 2014. [Online]. Available at: <http://data.consilium.europa.eu/doc/document/ST-169-2014-INIT/en/pdf>. [Accessed: 2 August 2018].
7. Renewable Energy Policy Network for the 21st Century (REN21)., *Renewable 2018 Global Status Report*, Paris, France, 2018. [Online]. Available at: http://www.ren21.net/wp-content/uploads/2018/06/17-8652_GSR2018_FullReport_web_final.pdf. [Accessed: 3 August 2018].
8. International Energy Agency (IEA). *Technology Roadmaps: Solar photovoltaic energy*, 2017. [Online]. Available: https://www.iea.org/publications/freepublications/publication/pv_roadmap.pdf. [Accessed: 2 August 2018].
9. Parida, B., Iniyani, S., Goic R., A review of solar photovoltaic technologies. *Renewable and Sustainable Energy Reviews*, 2011. **15**(3): p. 1625-1636.
10. Obeidat, F., A comprehensive review of future photovoltaic systems. *Solar Energy*, 2018. **163**: p. 545-551.
11. Lincot., D., The new paradigm of photovoltaic: From powering satellites to powering humanity. *Comptes Rendus Physique*, 2017. **18**: p. 381-390.
12. Battaglia, C., Cuevas, A., Wolf S.D., High-efficiency crystalline silicon solar cell: status and perspectives. *Energy & Environmental Science*. 2016. **9**(5): p. 1552-1576.
13. Green, M.A., *Third Generation Photovoltaic: Advance Solar Energy Conversion*. Springer, Berlin & Heidelberg, Germany, 2003.
14. Taube, W.R., Kumar, A., Saravanan, R., Agarwal, P.B., Kothari, P., Joshi, B.C., Kumar, D., Efficiency enhancement of silicon solar cell with silicon nanocrystals embedded in PECVD silicon nitride matrix. *Solar Energy Materials & Solar Cells*, 2012. **101**: p. 32-35.
15. Kang, M.H., Ryu, K., Upadhyaya, A., Rohatgi, A., Optimization of SiN AR coating for Si solar cells and modules through quantitative assessment of optical and efficiency loss mechanism. *Progress in Photovoltaics: Research and Applications*. 2011. **19**(8): p. 983-990.
16. Kim, J., Inns, D., Fogel, K., Sadana, D.K., Surface texturing of single crystalline

- silicon solar cells using low density SiO₂ films as an anisotropic etch mask. *Solar Energy Materials & Solar Cells*. 2010. **94**(12): p. 2091-2093.
17. Strümpel, C., McCann, M., Beaucarne, G., Arkhipov, V., Slaoui, A., Švrček, V., Cañizo del. C., Tobias, I., Modifying the solar spectrum to enhance silicon solar cell efficiency—An overview of available materials. *Solar Energy Materials & Solar Cells*. 2007. **91**(4): p. 238-249.
 18. Yu, R., Lin, Q.F., Leung, S.F., Fan, Z.Y., Nanomaterials and nanostructures for efficient light absorption and photovoltaics. *Nano Energy*. 2012. **1**(1): p. 57-72.
 19. Richter, A., Benick, J., Feldmann, F., Fell, A., Hermle, M., Glunz, S.W., n-Type Si solar cells with passivating electron contact: Identifying sources for efficiency limitations by wafer thickness and resistivity variation. 2017. **173**: p. 96-105.
 20. Green, M.A., Hishikawa, Y., Dunlop, E.D., Levi, D.H., Hohl-Ebinger, J., Ho-Baillie, A.W.Y., Solar cell efficiency tables (version 51). *Progress in Photovoltaics: Research and Applications*. 2018. **26**(1): p. 3-12.
 21. Griffiths, D.J., Introduction to quantum mechanics, 2nd Edition, Pearson Prentice Hall, Upper Saddle River, New Jersey, 2005. ISBN: 0131118927.
 22. Smestad, G.P., Optoelectronics of Solar Cells. The International Society for Optical Engineering (SPIE) press, 2002. ISBN: 9780819444400.
 23. Johnson, F.S., The solar constant. *Journal of meteorology*. 1954. **11**(6): p. 431-439.
 24. Duffie, J.A., Beckman, W.A., Solar Engineering of Thermal Processes, 4th Edition. John Wiley & Sons, Inc., Hoboken, New Jersey, 2013. ISBN: 9781118671603.
 25. Green, M.A., Solar Cells: Operating Principles, Technology, and System Applications. Prentice-Hall, Inc. Englewood Cliffs, New Jersey, 1982. ISBN: 0138222703.
 26. Newport Corporation. Tutorial: Introduction to Solar Radiation., [Online] Available at: <https://www.newport.com/t/introduction-to-solar-radiation>. [Accessed 10 August 2018].
 27. ASTM G173-03(2012). Standard Tables for Reference Solar Spectral Irradiance: Direct Normal and Hemispherical on 37 °Tilted Surface, ASTM International, West Conshohocken, PA, 2012.
 28. Planck, M., The theory of heat radiation. Masius, M. (transl) (2nd edition). P. Blakiston's Son & Co. Philadelphia. 1914. [Online] Available at: <https://www.gutenberg.org/files/40030/40030-pdf.pdf>. [Accessed: 11 August].
 29. Honsberg, C., Bowden, S., [Online] Available at: <https://www.pveducation.org/> [Accessed: 6 August 2018].
 30. Cheng, C.L., Chan, C.Y., Chen, C.L., An empirical approach to estimating monthly radiation on south-facing tilted planes for building application. *Energy*. 2006. **31**(14): p. 2940-2957.
 31. Allan, J., The Development and Characterization of Enhanced Hybrid Solar Photovoltaic Thermal Systems. PhD thesis, Department of Mechanical, Aerogelspace and Civil Engineering, College of Engineering, Design and Physical Sciences, Brunel University London, 2016.
 32. EnergyPlus. Weather Data., [Online] Available at: <https://energyplus.net/weather>. [Accessed: 9 August 2018].
 33. Becquerel, E., On Electron Effects under the Influence of Solar Radiation. *Comptes Rendus de "I" Academie Sciences Paris*. 1839. **9**: p. 561.
 34. Shukla, K.A., Sudhakar, K., Baredar, P., A comprehensive review on design of building integrated photovoltaic system. *Energy and Buildings*. 2016. **128**: p. 99-110.
 35. Ranabhat, K., Patrikeev, L., Antal'evna Revina, A., Andrianov, K., Lapshinky, V.,

- Sofronova, E., An introduction to solar cell technology. *Journal of Applied Engineering Science*. 2016. **14**(405): p. 481-491.
36. Conibeer, G., Third-generation photovoltaics. *Materialstoday*. 2007. **10**(11): p. 42-50.
 37. Green, M.A., Third Generation Photovoltaics: Ultra-high Conversion Efficiency at Low Cost. *Progress in Progress in Photovoltaics: Research and Applications*. 2001. **9**: p. 123-135.
 38. Lewis, N.S., Toward Cost-Effective Solar Energy Use. *Science*. 2007. **315**(5813): p. 798-801.
 39. National Renewable Energy Laboratory (NREL)., Research Cell Record Efficiency Chart. [Online] Available at: <https://www.nrel.gov/pv/assets/images/efficiency-chart-20180716.jpg>. [Accessed: 10 August 2018].
 40. Chapin, D.M., Fuller, C.S., Pearson, G.L., A New Silicon p-n Junction Photocell for Converting Solar Radiation into Electrical Power. 1954. **25**(676): p. 676-677.
 41. Yoshikawa, K., Kawasaki, H., Yoshida, W., Irie, T., Konishi, K., Nakano, K., Uto, T., Adachi, D., Kanematsu, M., Uzu, H., Yamamoto, K., Silicon heterojunction solar cell with interdigitated back contacts for a photoconversion efficiency over 26%. *Nature Energy*. 2017. **2**(17032): p. 1-8.
 42. International Technology Roadmap for Photovoltaic (ITRPV)., International Technology Roadmap for Photovoltaic, 2017 Results (9th Edition). 2018. [Online] Available at: <http://www.itrpv.net/Reports/Downloads/>. [Accessed: 11 August 2018].
 43. Powell, D.M., Winkler, M.T., Choi, H.J., Simmons, C.B., Needleman, D.B., Buonassisi, T., Crystalline silicon photovoltaics: a cost analysis framework for determining technology pathway to reach busload electricity costs. *Energy & Environmental Science*. 2012. **5**(3): p. 5874-5883.
 44. Goetzberger, A., Hoffmann, V.U., Photovoltaic Solar Energy Generation. Germany: Springer, Berlin & Heidelberg; 2005.
 45. Callister, W.D., Jr., Rethwisch, D.G., *Materials Science and Engineering: An Introduction*, 7th Edition. John Wiley & Sons, Inc., New York, 2006. ISBN: 0-471-736961.
 46. Saga, T., Advances in crystalline silicon solar cell technology for industrial mass production. *NPG Asia Materials*. 2010. **2**(3): p. 96-102.
 47. Shockley, W., The Theory of p-n Junction in Semiconductors and p-n Junction Transistors. *Bell System Technical Journal*. 1949. **28**(3): p. 435-489.
 48. Sharma, B., Gupta, A., Viridi, A., Effect of Single and Double Layer Antireflection Coating to Enhance Photovoltaic Efficiency of Silicon Solar. *Journal of Nano- and Electronic Physics*. **9**(2): p. (02001-1)-(02001-4).
 49. Nelson, J., *The Physics of Solar Cells*. World Scientific Publishing Company. Singapore, 2003. ISBN-13: 978-1-86094-340-9.
 50. Singh, P., Ravindra., Temperature dependence of solar cell performance-analysis. *Solar Energy Materials & Solar Cells*. 2012. **101**: p. 36-45.
 51. Luque, A., Hegedus, S., *Handbook of Photovoltaic Science and Engineering*, Second Edition. John Wiley & Sons, Inc, 2011. ISBN: 9780470974704.
 52. Wolf, M., Rauschenbach, H., Series Resistance Effects on solar cell measurements. *Advanced Energy Conversion*. 1963. **3**: p. 455-479.
 53. Dhass, A.D., Natarajan, E., Lakshmi, P., Influence of Shunt Resistance on the Performance of Solar Photovoltaic Cell. *International Conference on Emerging Trends in Electrical Engineering and Energy Management (ICETEEEM)*

- Proceedings, pages 382-386, 2012.
54. Chander, S., Purohit, A., Nehra, A., Nehra, S.P., Dhaka, M.S., A Study on Spectral Response and External Quantum Efficiency of Mono-Crystalline Silicon Solar Cell. *International Journal of Renewable Energy Research*. 2015. **5**(1): p. 41-44.
 55. Sopian, K., Cheow, S.L., Zaidi, S.H., An overview of crystalline silicon solar cell technology: Past, present, and future. *AIP Conference Proceedings* 1877, 020004, 2017.
 56. Yang, W.J., Ma, Z.Q., Tang, X., Feng, C.B., Zhao, W.G., Shi, P.P., Internal quantum efficiency for solar cells. *Solar Energy*. 2008. **82**(2): p. 106-110.
 57. Beard, M.C., Knutsen, K.P., Yu, P.R., Luther, J.M., Song, Q., Metzger, W.K., Ellingson, R.J., Nozik, A.J., Multiple Exciton Generation in Colloidal Silicon Nanocrystals. *Nano Letters*. 2007. **7**(8): p. 2506-2512.
 58. Yao, J.Z., Kirchartz, T., Vezie, M.S., Faist, M.A., Gong, W., He, Z.C., Wu, H.B., Troughton, J., Watson, T., Bryant, D., Nelson, J., Quantifying Losses in Open-Circuit Voltage in Solution-Processable Solar Cells. *Physical Review Applied*. 2015. **4**(1): p. (014020-1)-(014020-10).
 59. Polman, A., Knight, M., Garnett, E.C., Ehrler, B., Sinke, W.C., Photovoltaic materials: Present efficiencies and future challenges. *Science*. **352**(6283).
 60. Heche, E., Optics, 4th edition. Addison-Wesley. 2001. ISBN-10: 0805385665.
 61. Richards, B.S., Enhancing the performance of silicon solar cells via the application of passive luminescence conversion layers. *Solar Energy Materials & Solar Cells*. 2006a. **90**(15): p. 2329-2337.
 62. Shockley, W., Queisser, H.J., Detailed Balance Limit of Efficiency of p-n Junction Solar Cells. *Journal of Applied Physics*. 1961. **32**(3): p. 510-519.
 63. Jäger, K., Isabella, O., Smet, A.H.M., Swaauj, R.A.C.C.M.V., Zeman Miro., *Solar Energy: Fundamentals, Technology, and Systems*. Delft University of Technology, 2014.
 64. Kothari, D.P., Singal, K.C., Ranjan, R., *Renewable Energy Sources and Emerging Technologies*, Institute of Technology and Management, Prentice-Hall of India Private., New Delhi, India, 2008. ISBN: 9788120333574.
 65. Timmerman, D., Izeddin, I., Stallinga, P., Yassievich, I.N., Gregorkiewicz, T., Space-separated quantum cutting with silicon nanocrystals for photovoltaic applications. *Nature Photonics*. 2008. **2**: p. 105-109.
 66. Klampaftis, E., Ross, D., McIntosh, K.R., Richards, B.S., Enhancing the performance of solar cells via luminescent down-shifting of the incident spectrum: A review. *Solar Energy Materials & Solar Cells*. 2009. **93**(8): 1182-1194.
 67. Bünzli, J.C.G., Piguet, C., Taking advantage of luminescent lanthanide ions. *Chemical Society Review*. 2005. **34**(12): p. 1048.
 68. Urquhart, P., Review of rare earth doped fibre lasers and amplifiers. *IEE Proceedings J. Optoelectronics*. 1988. **135**: p. 385.
 69. Kenyon, A.J., Recent development in rare-earth doped materials for optoelectronics. *Progress in Quantum Electronics*. 2002. **26**(4-5): p. 225-284.
 70. Dieke, G.H., Crosswhite, H.M., The spectra of the doubly and triply ionized rare earth. *Applied Optics*. 1963. **2**(7): p. 675-686.
 71. Carnall, W.T., Goodman, G.L., Rajnak, K., Rana, R.S., A systematic analysis of the spectra of the lanthanides doped into single crystal LaF₃. *Journal of Chemical Physics*. 1980. **90**(7): p. 3443-3457.
 72. Yan, X., *Phosphors for Lighting Applications*, PhD thesis, Department of Wolfson Centre for Materials Processing, College of Engineering, Design and Physical Sciences, Brunel University London, 2012.

73. Fthenakis, V., Third Generation Photovoltaics, InTech. Rijeka, Croatia, 2012. ISBN: 9789535103042.
74. Krämer, K.W., Biner, D., Frei, G., Güdel, H.U., Hehlen, M.P., Lüthi, S.R., Hexagonal Sodium Yttrium Fluoride Based Green and Blue Emitting Upconversion Phosphors. *Chemistry of Materials*. 2004. **16**(7): p. 1244-1251.
75. Donne, A.L., Dilda, M., Crippa, M., Acciarri, M., Binetti, S., Rare earth organic complexes as down-shifters to improve Si-based solar cell efficiency. *Optical Materials*. 2011. **33**(7): p. 1012-1014.
76. Yen, W.M., Shionoya, S., Yamamoto, H., Phosphor Handbook, 2nd Edition, CRC Press. New York, 2006. ISBN: 0849335647.
77. Wang, F., Liu, X., Recent advances in the chemistry of lanthanide doped upconversion nanocrystals. *Chemical Society Reviews*. 2009. **38**(4): p. 976-989.
78. Kulish, M.R., Kostilyov, V.P., Sachenko, A.V., Sokolovskiy, I.O., Khomenko, D.V., Shkrebtiy, A.I., Luminescent converter of solar light into electrical energy. *Review. Semiconductor Physics, Quantum Electronics & Optoelectronic*, 2016. **19**(3): p. 229-247.
79. Barnham, K., Marques, J.L., Hassard, J., O'Brien, P., Quantum-dot concentrator and thermodynamic model for the global redshift. *Applied Physics Letters*. 2000. **76**: p. 1197
80. Chatten, A.J., Barnham, K.W.J., Blieske, U., Ekins-Daukes, N.J., Malik, M.A., Marques, J.L., Williams, M.L., Characterising quantum dot concentrators. *Proceedings of 28th IEEE Photovoltaic Specialists Conference*. pages 865-868, 2000.
81. Jestin, Y., Pucker, G., Ghulinyan, M., Ferrario, L., Bellutti, P., Picciotto, A., Collini, A., Marconi, A., Anopchenko, A., Yuan, Z., Pavesi, L., Silicon solar cells with nanocrystalline silicon down shifter: experiment and modeling. *Proceeding of SPIE-The International Society for Optical Engineering*. Vol.77720B, 2010.
82. Han, H.V., Lin, C.C., Tsai, Y.L., Chen, H.C., Chen, K.J., Yeh, Y.L., Lin, W.Y., Kuo, H.C., Yu, P., A Highly Efficient Hybrid GaAs Solar Cell Based on Colloidal-Quantum-Dot-Sensitization. *Scientific Reports*. 2014. **4**: p. 1-9.
83. Chen, H.C., Lin, C.C., Han, H.V., Chen, K.J., Tsai, Y.L., Chang, Y.A., Shih, M.H., Kuo, H.C., Yu, P., Enhancement of power conversion efficiency in GaAs solar cells with dual-layer quantum dots using flexible PDMS film. *Solar Energy Materials & Solar Cells*. 2012. **104**: p. 92-96.
84. Hovel, H.J., Hodgson, R.T., Woodall, J.M., The effect of fluorescent wavelength shifting on solar cell spectral response. *Solar Energy Materials*. 1979. **2**(1): 19-29.
85. Earp, A.A., Smith, G.B., Franklin, J., Swifit, P., Optimisation of a three-colour luminescent solar concentrator daylighting system. *Solar Energy Materials & Solar Cells*. 2004. **84**(1-4): p. 411-426.
86. BASF. [Online] Available at: <https://www.basf.com/ca/en.html>. [Accessed: 2 September 2019].
87. Maruyama, T., Enomoto, A., Shirasawa, K., Solar cell module colored with fluorescent plate. *Solar Energy Materials & Solar Cells*. 2000. **64**(3): p. 269-278.
88. Meyer, T.J.J., Photon Transport in Fluorescent Solar Collectors, PhD thesis, Faculty of Engineering, Science and Mathematics, School of Engineering Sciences, University of Southampton, 2010.
89. Liang, Z.Q., Sun, J., Jiang, Y.Y., Jiang, L., Chen, X.D., Plasmonic Enhanced Optoelectronic Devices. *Plasmonics*. 2014. **9**(4): p. 859-866.
90. Pillai, S., Beck, F.J., Catchpole, K.R., Ouyang, Z., Green, M.A., The effect of dielectric spacer thickness on surface Plasmon enhanced solar cells for front and

- rear side depositions. *Journal of Applied Physics*. **109**, 073105 (2011).
91. Holman, Z.C., Wolf, S.D., Ballif, C., Improving metal reflectors by suppressing surface plasmon polaritons: *a priori* calculation of the internal reflectance of a solar cell. *Light: Science & Applications*. 2013. **2**(10), e106.
 92. Macdonald, D.H., Cuevas, A., Kerr, M.J., Samundsett, C., Ruby, D., Winderbaum, S., Leo, A., Texturing industrial multicrystalline silicon solar cells. *Solar Energy*. 2004. **76**(1-3): p. 277-283.
 93. Nakaya, H., Nishida, M., Takeda, Y., Moriuchi, S., Tonegawa, T., Machida, T., Nunoi, T., Polycrystalline silicon solar cells with V-grooved surface. *Solar Energy Materials & Solar Cells*. 1994. **34**(1-4): p. 219-225.
 94. Dobrzań, L.A., Drygala, A., Laser texturization in technology of multicrystalline silicon solar cells. *Journal of Achievements in Materials and Manufacturing Engineering*. 2008. **29**(1): p. 7-14.
 95. Panek, P., Lipiński, M., Dutkiewicz, J., Texturization of multicrystalline silicon by wet chemical etching for silicon solar cells. *Journal of Materials Science*. 2005. **40**(6): p. 1459-1463.
 96. Winderbaum, S., Reinhold, O., Yun, F., Reactive ion etching (RIE) as a method for texturing polycrystalline silicon solar cells. *Solar Energy Materials & Solar Cells*. 1997. **46**(3): p. 239-248.
 97. Macleod, H.A., *Thin-Film Optical Filters*, Adam Hilger Ltd, Bristol, 1986.
 98. Richard, B.S., Single-material TiO₂ double-layer antireflection coatings. *Solar Energy Materials & Solar Cells*. 2003. **79**(3): p. 369-390.
 99. Lien, S.Y., Wu, D.S., Yeh, W.C., Liu, J.C., Tri-layer antireflection coatings (SiO₂/SiO₂-TiO₂/TiO₂) for silicon solar cells using a sol-gel technique. *Solar Energy Materials & Solar Cells*. 2006. **90**(16): p. 2710-2719.
 100. Yao, L., He, J.H., Recent progress in antireflection and self-cleaning technology – From surface engineering to functional surfaces. 2014. **61**: 94-143.
 101. Fraunhofer ISE., New world record for solar cell efficiency at 46%., [Online] Available at: <https://www.ise.fraunhofer.de/en/press-media/press-releases/2014/new-world-record-for-solar-cell-efficiency-at-46-percent.html>. [Accessed 23 September 2018].
 102. Tahhan, A., Energy Performance Enhancement of Crystalline Silicon Photovoltaic Solar Cells. PhD thesis, Department of Mechanical, Aerospace and Civil Engineering, College of Engineering, Design and Physical Sciences, Brunel University London, 2016.
 103. Zarmai, M.T., Ekere, N.N., Oduoza, C.F., Amalu, E.H., A review of interconnection technologies for improved crystalline silicon solar cell photovoltaic module assembly. *Applied Energy*. 2015. **154**: p. 173-182.
 104. Ulbrich Solar Technology, Inc. Solar tabbing data sheet., [Online] Available at: <https://www.pvribbon.com/technology/solar-tabling-data-sheet/>. [Accessed 27 September 2018].
 105. IEC 60904-9 Ed. 2, Photovoltaic devices – Part 9: Solar simulator performance requirements. 2007.
 106. ASTM Committee E20 on Temperature Measurement., *Manual on the use of thermocouples in temperature measurement*, Fourth Edition, ASTM International, 2003. ISBN: 0-8031-1466-4.
 107. ASTM E230 / E230M-17., *Standard Specification for Temperature-Electromotive Force (emf) Tables for Standardized Thermocouples*, ASTM International, West Conshohocken, PA, 2017.
 108. OMEGA Engineering, Inc., *User's Guide: CL3512A Digital Thermometer &*

- Calibrator. [Online] Available at: <https://cn.omega.com/pptst/CL3512A.html>. [Accessed 3 October 2018].
109. Bentham, Spectral Characterisation of Photovoltaic Devices Technical Note. [Online] Available at: https://www.bentham.co.uk/fileadmin/uploads/bentham/Systems/PVE300/PVE300_Technical_Note.pdf. [Accessed 21 October 2018].
 110. Goebel, R., Stock, M., Report on the key comparison of spectral responsivity measurements in the wavelength range of 300 nm to 1000 nm. International Bureau of Weights and Measures (BIPM)-CCPR-K2.b report, 2004.
 111. ASME., Boiler and Pressure Vessel Code, An International Code, 2017 Edition., American Society of Mechanical Engineers, 2017.
 112. PerkinElmer. Lambda 650, 800, and 950, Spectrophotometers brochure., [Online] Available at: http://www.perkinelmer.co.uk/lab-solutions/resources/docs/BRO_Lambda950850650Americas.pdf. [Accessed 6 October 2018].
 113. Andreas, H., 2010. Spectroscopic Techniques: I Spectrophotometric Techniques. In: K. Wilson, J. Walker, 7th edition. 2010. Principles and Techniques of Biochemistry and Molecular Biology. Cambridge: Cambridge University Press. Ch.12.
 114. Gauglitz., G., Vo-Dinh, T., Handbook of Spectroscopy. WILEY-VCH Verlag GmbH & Co. KGaA, Weinheim, Germany, 2003.
 115. Tompkins, H.G., Irene, E.A., Handbook of Ellipsometry. William Andrew, Inc., 2005.
 116. Rudolph Research, Rudolph EL-III Specifications. [Online] Available at: http://www.sitekprocess.com/objects/catalog/product/extras/3255_Rudolph%20Auto%20EL-%20III%20Detailed%20specifications.pdf [Accessed 9 October 2018].
 117. Brodusch, N., Demers, H., Gauvin, R., Field Emission Scanning Electron Microscopy: New Perspective for Materials Characterization. Springer, 2017.
 118. Quantachrome Instruments., Brochure: NOVAtouch surface area & pore size analyzer. [Online] Available at: http://www.quantachrome.com/pdf_brochures/novatouch_rev1.pdf. [Accessed 17 October 2018].
 119. Hohne, G.W.H., Hemminger, W.F., Flammersheim, H.J., Differential Scanning Calorimetry, 2nd revised and enlarged edition. Spring-Verlag Berlin Heideberg, 2003.
 120. Stark, W., Jaunich, M., Bohmeyer, W., Lange, K., Investigation of the crosslinking behavior of ethylene vinyl acetate (EVA) for solar cell encapsulation by rheology and ultrasound. Polymer Testing. 2012. **31**(7): p. 904-908.
 121. Nakata, K., Fujishima, A., TiO₂ photocatalysis: Design and application. Journal of Photochemistry and Photobiology C: Photochemistry Reviews. 2012. **13**(3):p. 169-189.
 122. Miszczak, S., Pietrzyk, B., Anatase-rutile transformation of TiO₂ sol-gel coatings deposited on different substrates. Ceramics International. 2015. **41**(6): p. 7461-7465.
 123. Luttrell, T., Halpegamage, S., Tao, J., Kramer, A., Sutter, E., Batzill, M., Why is anatase a better photocatalyst than rutile? – Model studies on epitaxial TiO₂ films. Scientific Reports. 2014. **4**: 4043.
 124. Richards, B.S., Novel Uses of Titanium Dioxide For Silicon Solar Cells. PhD thesis, Centre for Photovoltaic Engineering and The School of Electrical Engineering, University of New South Wales Sydney, 2002.
 125. Zhang, J.F., Zhou, P., Liu, J.J., Yu, J.G., New understanding of the difference of

- photocatalytic activity among anatase, rutile and brookite TiO₂. *Physical Chemistry Chemical Physics*. 2014. **16**(38): p. 20382-20386.
126. Kakuma, Y., Nosaka, A.Y., Nosaka, Y., Difference in TiO₂ photocatalytic mechanism between rutile and anatase studied by detections of active oxygen and surface species in water. *Physical Chemistry Chemical Physics*. 2015. **17**(28): p. 18691-18698.
 127. Haggerty, J.E.S., Schelhas, L.T., Kitchaev, D.A., Mangun, J.S., Garten, L.M., Sun, W.H., Stone, K.H., Perkins, J.D., Toney, M.F., Ceder, G., Ginley, D.S., Gorman, B.P., Tate, J., High-fraction brookite films from amorphous precursors. *Scientific Reports*. 2017. **7**: 15232.
 128. Hanaor, D.A.H., Sorrell, C.C., Review of the anatase to rutile phase transformation. *Journal of Materials Science*. 2011. **46**(4): p. 855-874.
 129. Jia, J.J., Yamamoto, H., Okajima, T., Shigesato, Y., On the Crystal Structural Control of Sputtered TiO₂ Thin Films. *Nanoscale Research Letters*. 2016. **11**:324.
 130. Sajjan, C.P., Wageh, S., Al-Ghamdi, A.A., Yu, J.G., Cao, S.W., TiO₂ nanosheets with exposed {001} facets for photocatalytic applications. *Nano Research*. 2016. **9**(1): p. 3-27.
 131. Jin, Z., Meng, F.L., Jia, Y., Luo, T., Liu, J.Y., Sun, B., Wang, J., Liu, J.H., Huang, X.J., Porous TiO₂ nanowires derived from nanotubes: Synthesis, characterization and their enhanced photocatalytic properties. *Microporous and Mesoporous Materials*. 2013. **181**:p.146-153.
 132. Cheng, J., Wang, Y.T., Xing, Y., Shahid, M., Pan, W., A stable and highly efficient visible-light photocatalyst of TiO₂ and heterogeneous carbon core-shell nanofibers. *RSC Advance*. 2017. **7**(25): p. 15330-15336.
 133. Moradi, H., Eshaghi, A., Hosseini, S.R., Ghani, K., Fabrication of Fe-doped TiO₂ nanoparticles and investigation of photocatalytic decolorization of reactive red 198 under visible light irradiation. *Ultrasonics Sonochemistry*. 2016. **32**: p. 314-319.
 134. Hajjaji, A., Trabelsi, K., Atyaoui, A., Gaidi, M., Bousselmi, L., Bessais, B., Khakani, M.A.E., Photocatalytic activity of Cr-doped TiO₂ nanoparticles deposited on porous multicrystalline silicon films. *Nanoscale Research Letters*. 2014. **9**:543.
 135. Shon, H.K., Phuntsho, S., Okour, Y., Cho, D.L., Kim, J.B., Na, S., Kim, J.H., Visible Light Responsive Titanium Dioxide (TiO₂) - a review. *Journal of the Korean Industrial and Engineering Chemistry*. 2008. **19**(1): 1-16.
 136. Karkare, M.M., Choice of precursor not affecting the size of anatase TiO₂ nanoparticles but affecting morphology under broader view. 2014. **4**:111.
 137. Lee, D.S., Liu, T.K., Preparation of TiO₂ Sol Using TiCl₄ as a Precursor. *Journal of Sol-Gel Science and Technology*. 2002. **25**: p. 121-136.
 138. Shrestha, K.M., Sorensen, C.M., Klabunde, K.J., MgO-TiO₂ mixed oxide nanoparticles: Comparison of flame synthesis versus aerogel method; characterization, and photocatalytic activities. *Journal of Materials Research*. 2013. **28**(3): p. 431-439.
 139. Avasarala, B.K., Tirukkovalluri, S.R., Bojja, S., Magnesium Doped Titania for Photocatalytic Degradation of Dyes in Visible Light. *Journal of Environemnt & Analytical Toxicology*. 2016. **6**(2): p. 358.
 140. Jung, H.S., Lee, J.K., Nastasi, M., Lee, S.W., Kim, J.Y., Park, J.S., Hong, K.S., Shin, H., Preparation of Nanoporous MgO-Coated TiO₂ Nanoparticles and Their Application to Electrode of Dye-Sensitized Solar Cells. *Langmuir*. 2005. **21**: p. 10332-10335.
 141. Ye, C., Pan, S.S., Teng, X.M., Li, G.H., Optical properties of MgO-TiO₂ amorphous composite films. *Journal of Applied Physics*. 2007. **102**: p.013520.

142. Cheng, X.W., Yu, X.J., Xing, Z.P., Yang, L.S., Synthesis and characterization of N-doped TiO₂ and its enhanced visible-light photovoltaic activity. *Arabian Journal of Chemistry*. 2016. **9**: p. S1706-S1711.
143. Zhu, M.S., Zhai, C.Y., Qiu, L.Q., Lu, C., Paton, A.S., Du, Y.K., Goh, M.C., New Method to Synthesize S-Doped TiO₂ with Stable and High Efficient Photocatalytic Performance under Indoor Sunlight Irradiation. *ACS Sustainable Chemistry & Engineering*. 2015. **3**(12): p. 3123-3129.
144. Singh, N., Salam, Z., Subasri, A., Sivasankar, N., Subramania, A., Development of porous TiO₂ nanofibers by solvosonication process for high performance quantum dot sensitized solar cell. *Solar Energy Materials and Solar Cells*. 2018. **179**: p. 417-426.
145. Ming, H., Ma, Z., Huang, H., Lian, S.Y., Li, H.T., He, X.D., Yu, H., P, K.M., Liu, Y., Kang, Z.H., Nanoporous TiO₂ spheres with narrow pore size distribution and improved visible light photocatalytic abilities. *Chemical Communications*. 2011. **47**(28): p. 8025-8027.
146. Al-Attafi, K., Nattestad, A., Yamauchi, Y., Dou, S.X., Kim, J.H., Aggregated mesoporous nanoparticles for high surface area light scattering layer TiO₂ photoanodes in Dye-sensitized Solar Cells. *Scientific Report*. 2017. **7**:10341.
147. Yin, H.B., Wada, Y.J., Kitamura, T., Kambe, S., Murasawa, S., Mori, H., Sakata, T., Yanagida, S., Hydrothermal synthesis of nanosized anatase and rutile TiO₂ using amorphous phase TiO₂. *Journal of Materials Chemistry*. 2001. **11**(6): p. 1694-1703.
148. Zhuge, F.W., Yanagida, T., Nagashima, K., Yoshida, H., Kanai, M., Xu, B., Klamchuen, A., Meng, G., He, Y., Rahong, S., Li, X.M., Suzuki, M., Kai, S., Takeda, S., Kawai, T., Fundamental Strategy for Creating VLS Grown TiO₂ Single Crystalline Nano-wires. *The journal of Physical Chemistry C*. 2012. **116**(45): p. 24367-24372.
149. Li, D., Xia, Y.N., Fabrication of Titania Nanofibers by Electrospinning. *Nano Letters*. 2003. **3**(4): p. 555-560.
150. Keshimiri, M., Mohseni, M., Troczynski, T., Development of novel TiO₂ sol-gel-derived composite and its photocatalytic activities for trichloroethylene oxidation. *Applied Catalysis B: Environmental*. 2004. **53**(4): p. 209-219.
151. Parayil, S.K., Psota, R.J., Koodali, R.T., Modulating the textural properties and photocatalytic hydrogen production activity of TiO₂ by high temperature supercritical drying. *International Journal of Hydrogen Energy*. 2013. **38**(25): p. 10215-10225.
152. Nagai, H., Sato, M., Heat Treatment in Molecular Precursor Method for Fabricating Metal Oxide Thin Films. In: F. Czerwinski. 2012. HEAT TREATMENT-CONVENTIONAL AND NOVEL APPLICATIONS. Croatia: InTech. Ch.5.
153. Mo, C.M., Li, Y.H., Liu, Y.S., Zhang, Y., Zhang, L.D., Enhancement effect of photoluminescence in assemblies of nano-ZnO particles/silica aerogels. *Journal of Applied Physics*. 1998. **83**: p. 4389-4391.
154. Husing, N., Schubert U., Aerogels-airy materials: chemistry, structure, and properties. *Angewandte Chemie International Edition*. 1998. **37**: p. 22-45.
155. Tsou, P., Silica aerogel captures cosmic dust intact. *Journal of Non-Crystalline Solids*. 1995. **186**: p. 415-427.
156. French, R.H., Rodríguez-Parada, J.M., Yang, M.K., Derryberry, R.A., Pfeifferberger, N.T., Optical properties of polymeric materials for concentrator photovoltaic systems. *Solar Energy Materials & Solar Cells*. 2011. **95**(8): p. 2077-2086.

157. Crawford, R.J., Throne, J.L., Rotational Molding Technology. Plastic Design Library/William Andrew Publishing. Norwich, New York. 2001.
158. Fink, J.K., Handbook of Engineering and Specialty Thermoplastics: Volume 1: Polyofins and Styrenics. John Wiley & Sons, Inc and Scrivener Publishing LLC. Canada. 2010.
159. DuPont Company, USA, DuPont™ Elvax® 150 resins Product Data Sheet, 2017.
160. Chen, Y.M, Lin, P., He, Y., He, J.Q., Zhang, J., Li, X.L., Fast quantifying collision strength index of ethylene-vinyl acetate copolymer coverings on the fields based on near infrared hyperspectral imaging techniques. Scientific Reports. 2016. **6**: 20843.
161. Yuwawech, K., Wootthikanokkhan, J., Tanpichai, S., Enhancement of thermal, mechanical and barrier properties of EVA solar cell encapsulating films by reinforcing with esterified cellulose nanofibres. Polymer Testing. 2015. **48**: p. 12-22.
162. Klemchuk, P., Ezrin, M., Lavigne, G., Holley, W., Galica, J., Agro, S., Investigation of the degradation and stabilization of EVA-based encapsulant in field-aged solar energy modules. Polymer Degradation and Stability. 1997. **55**(3): p. 347-365.
163. Nagel, H., Aberle, A.G., Hezel, R., Optimised Antireflection Coatings for Planar Silicon Solar Cells using Remote PECVD Silicon Nitride and Porous Silicon Dioxide. Progress in Photovoltaics: Research and Applications. 1999. **7**: p. 245-260.
164. Doi, T., Tsuda, I., Unagida, H., Murata, A., Sakuta, K., Kurokawa, K., Experimental study on PV module recycling with organic solvent method. Solar Energy Materials & Solar Cells. **67**: p. 397-403.
165. Camacho, J., D éz, E., Ovejero, G., D a, I., Thermodynamic Interactions of EVA Copolymer-Solvent Systems by Inver Gas Chromatography Measurements. Journal of Applied Polymer Science. **128**(1): p. 481-486.
166. Jasper, J.J., The Surface Tension of Pure Liquid Compounds. Journal of Physical and Chemical Reference Data. **1**(4): p. 841-1010.
167. Alfa Aesar. P-xylene, Products SDS, CAS No 106-42-3, Alfa Aesar, Heysham Lancashire, UK, 2015. [Online] Available at: <https://www.alfa.com/en/content/msds/british/A10534.pdf>. [Accessed 6 November 2018].
168. Alfa Aesar. Cyclohexane, Products SDS, CAS No 110-82-7, Alfa Aesar, Heysham Lancashire, UK, 2015. [Online] Available at: <https://www.alfa.com/en/content/msds/british/A16070.pdf>. [Accessed 6 November 2018].
169. Alfa Aesar. Cyclohexane, Products SDS, CAS No 108-88-3, Alfa Aesar, Heysham Lancashire, UK, 2015. [Online] Available at: <https://www.alfa.com/en/content/msds/british/L10967.pdf>. [Accessed 6 November 2018].
170. Krieb, F.C., Fabrication and processing of polymer solar cells: A review of printing and coating techniques. Solar Energy Materials & Solar Cells. 2009. **93**(4): p. 394-412.
171. Wang, F., Zhou, Y., Li, P., Kuai, L.B., Zou, Z.G., Synthesis of bionic-macro/microporous MgO-modified TiO₂ for enhanced CO₂ photoreduction into hydrocarbon fuels. Chinese Journal of Catalysis. 2016. **37**: p. 863-868.
172. Cullity, B.D., Elements of X-Ray Diffraction. Reading, Massachusetts: Addison-Wesley Publishing Company, Inc; 1956, p. 262.
173. Langford, J.I., Wilson, A.J.C., Scherrer after Sixty Years: A Survey and Some New

- Results in the Determination of Crystallite Size. *Journal of Applied Crystallography*. 1978. **11**: p. 102-113.
174. Bruker. DIFFRAC.SUITE User Manual, TOPAS 5 Technical Reference., [Online] Available at: <https://www.bruker.com/products/x-ray-diffraction-and-elemental-analysis/x-ray-diffraction/xrd-software/topas.html>. [Accessed 22 August 2019].
 175. British Stainless Steel Association (BSSA). Chemical compositions of AISI (ASTM/ASME) and UNS austenitic stainless steel grades., [Online] Available at: <https://www.bssa.org.uk/topics.php?article=183>. [Accessed 9 November 2018].
 176. Misho, R.H., Murad, W.A., Band gap measurements in thin films of hematite Fe₂O₃, pyrite FeS₂ and troilite FeS prepared by chemical spray pyrolysis. *Solar Energy Materials and Solar Cells*. 1992. **27**(4): p. 335-345
 177. Cheng, C.S., Gomi, H., Sakata, H., Electrical and Optical Properties of Cr₂O₃ Films Prepared by Chemical Vapour Deposition. *Physica Status Solid A-Applications and Materials Science*. 1996. **155**: p. 417-425.
 178. Thommes, M., Kaneko, K., Neimark, A.V., Oliver, J.P., Rodriguez-Reinoso, F., Rouquerol, J., Sing, K.S.W., Physisorption of gases, with special reference to the evaluation of surface area and pore size distribution (IUPAC Technical Report). *Pure and Applied Chemistry*. 2015. **87**(9-10): p. 1051-1069.
 179. Qin, W., Nagase, T., Umakoshi, Y., Szpunar, J.A., Lattice distortion and its effects on physical properties of nanostructured materials. *Journal of Physics: Condensed Matter*. 2007. **19**(23): p. 1-8.
 180. Wei, M.C., Chang, S.J., Tsia, C.Y., Liu, C.H., Chen, S.C., SiN_x deposited by in-line PECVD for multi-crystalline silicon solar cells. *Solar Energy*. 2006. **80**(2): p. 215-219.
 181. Bloomfield, V.A., Dewan, R.K., Viscosity of Liquid Mixtures, *The Journal of Physical Chemistry*. 1971. **75**(20): p. 3113-3119.
 182. Tishkovets, V.P., Petrova, E.V., Jockers, K., Optical properties of aggregate particles comparable in size to the wavelength. *Journal of Quantitative Spectroscopy & Radiative Transfer*. 2004. **86**(3): p. 241-265.
 183. Anpo, M., Yamada, Y., Kubokawa, Y., Photoluminescence and photocatalytic activity of MgO powders with co-ordinatively unsaturated surface ions. *Journal of the Chemical Society. Chemical Communications*. 1986. **0**(9): p. 714-716.
 184. Pacchioni, G., Ferrari, A.M., Surface reactivity of MgO oxygen vacancies., *Catalysis Today*. 1999. **50**: p. 533-540.
 185. Mardare, D., Tasca, M., Delibas, M., Rusu, G.I., On the structural properties and optical transmittance of TiO₂ r.f. sputtered thin films. *Applied surface science*. 1999. **156**: p. 200-206.
 186. Rukade, D.A., Bhattacharyya, V., Single-phase TiO₂ formation by plasma oxidation of titanium thin films. *Surface and Interface Analysis*. 2015. **47**: p. 828-831.
 187. Wei, C.H., Chang, C.M., Polycrystalline TiO₂ Thin Films with Different Thickness Deposited on Unheated Substrates Using RF Magnetron Sputtering. *Materials Transactions*. 2011. **52**(3): p. 554-559.
 188. Chen, Y.C., Huang, W.Y., Chen, T.M., Enhancing the performance of photovoltaic cells by using down-converting KCaGd(PO₄)₂:Eu²⁺ phosphors. *Journal of Rare Earths*. 2011. **29**(9): p. 907-910.
 189. Shehata, N., Clavel, M., Meehan, K., Samir, E., Gaballah, S., Salah, M., Enhanced Erbium-Doped Ceria Nanostructure Coating to Improve Solar Cell Performance. *Materials*. 2015. **8**(11): p. 7663-7672.
 190. Wu, X.J., Meng, F.Z., Zhang, Z.Z., Yu, Y.N., Liu, X.J., Meng, J., Broadband

- down-conversion for silicon solar cell by ZnSe/phosphor heterostructure. *Optics Express*. 2014. **22**(S3): p.A735-A741.
191. Richards, B.S., Luminescent layers for enhanced silicon solar cell performance: Down-conversion. *Solar Energy Materials & Solar Cells*. 2006. **90**(9):1189-1207.
 192. Trupke, T., Green, M.A., Würfel, P., Improving solar cell efficiencies by down-conversion of high-energy photons. *Journal of Applied Physics*. 2002. **92**(3): 1668-1674.
 193. Huang, C.K., Chen, Y.C., Hung, W.B., Chen, T.M., Sun, K.W., Chang, W.L., Enhanced light harvesting of Si solar cells via luminescent down-shifting using $\text{YVO}_4:\text{Bi}^{3+}$, Eu^{3+} nanophosphors. *Progress in Photovoltaics: Research and Applications*. 2013. **21**: p. 1507-1513.
 194. Hung, W.B., Chen, J.Y., Sung, K.W., Chen, T.M., Enhanced conversion efficiency of crystalline Si solar cells via luminescent down-shifting using $\text{Ba}_2\text{SO}_4:\text{Eu}^{2+}$ phosphor. *Ceramic Processing Research*. 2014. **15**(3): p. 157-161.
 195. Hung, W.B., Chen, T.M., Efficiency enhancement of silicon solar cells through a downshifting and antireflective oxysulfide phosphor layer. *Solar Energy Materials & Solar Cells*. 2015. **133**: p. 39-47.
 196. Huignard, A., Gacoin, T., Boilot, J.P., Synthesis and luminescence properties of colloidal YVO_4 : Eu phosphors. *Chemistry of Materials*. 2000. **12**(4): p. 1090-1094.
 197. Wild, J.d., Rath, J.K., Meijerink, A., van Sark, W.G.J.H.M., Schropp, R.E.I., Enhanced near-infrared response of a-Si:H solar cells with $\beta\text{-NaYF}_4:\text{Yb}^{3+}$ (18%), Er^{3+} (2%) upconversion phosphors. *Solar Energy Materials & Solar Cells*. 2010. **94**(12): p. 2395-2398.
 198. Rothemund, R., Optical modeling of the external quantum efficiency of solar cells with luminescent down-shifting layers. *Solar Energy Materials & Solar Cells*. 2014. **120**: p. 616-621.
 199. Abrams, Z.R., Niv, A., Zhang, X., Solar energy enhancement using down-converting particles: A rigorous approach. *Journal of Applied Physics*. 2011. **109**(11): p. 114905(1-9).
 200. Mie, G., Beiträge zur Optik trüber Medien, speziell kolloidaler Metallösungen. *Annalen der Physik*. 1908. **330**: p. 377-445.
 201. Jiang, Y., Wu, Y., Xie, Y., Qian, Y.T., Synthesis and Characterization of Nanocrystalline Lanthanide Oxysulfide via a $\text{La}(\text{OH})_3$ Gel Solvothermal Route. *Journal of the American Ceramic Society*. 2004. **83**(10): p. 2628-2630.
 202. Jiang, G.C., Wei, X.T., Zhou, S.S., Chen, Y.H., Duan, C.K., Yin, M., Neodymium doped lanthanum oxysulfide as optical temperature sensors. *Journal of Luminescence*. 2014. **152**: p. 156-159.
 203. Zhao, F., Yuan, M., Zhang, W., Gao, S., Monodisperse Lanthanide Oxysulfide Nanocrystals. *Journal of the American Ceramic Society*. 2006. **128**(36): p. 11758-11759.
 204. Yoshida, M., Nakagawa, M., Fujii, H., Kawaguchi, F., Yamada, H., Ito, Y., Takeuchi, H., Hayakawa, T., Tsukuda, Y., Application of $\text{Gd}_2\text{O}_2\text{S}$ Ceramic Scintillator for X-Ray Solid State Detector in X-Ray CT. *Japanese Journal of Applied Physics*. 1988. **27**(8): p. L1572-L1575.
 205. Anan'eva, G.V., Gorokhova, E.I., Demidenko, V.A., Parfinskiĭ, V.A., Khristich, O.A., Optical properties of $\text{Gd}_2\text{O}_2\text{S}$ -based ceramic. *Journal of Optical Technology*. 2005. **72**(1): p. 58-61.
 206. Wang, X.J., Wang, X.J., Wang, Z.H., Zhu, Q., Zhu, G., Wang, C., Xin, S.Y., Li, J.G., Photo/cathodoluminescence and stability of $\text{Gd}_2\text{O}_2\text{S}:\text{Tb},\text{Pr}$ green phosphor hexagons calcined from layered hydroxide sulfate. *Journal of American Ceramic*

- Society. 2018. **101**: p. 5477-5486.
207. Raukas, M., Mishra, K.C., Peters, C., Schmidt, P.C., Johnson, K.H., Choi, J., Happek, U., Electronic structures and associated properties of $\text{Gd}_2\text{O}_2\text{S:Tb}^{3+}$. *Journal of Luminescence*. 2000. **87-89**: p. 980-982.
 208. Yasuda, R., Katagiri, M., Matsubay, M., Influence of powder particle size and scintillator layer thickness on the performance of $\text{Gd}_2\text{O}_2\text{S:Tb}$ scintillators for neutron imaging. *Nuclear Instruments and Methods in Physics Research Section A: Accelerators, Spectrometers, Detectors and Associated Equipment*. 2012. **680**: 139-144.
 209. Silva, A.A., Cebim, M.A., Davolos, M.R., Excitation mechanism and effects of dopant concentration in $\text{Gd}_2\text{O}_2\text{S:Tb}^{3+}$ phosphor. *Journal of Luminescence*. 2008. **128(7)**: p. 1165-1168
 210. Brüninghoff, R., Engelsen, D.D., Fern, G.R., Ireland, T.G., Dhillon, R., Silver, J., Nanosized $(\text{Y}_{1-x}\text{Gd}_x)_2\text{O}_2\text{S:Tb}^{3+}$ particles: synthesis, photoluminescence, cathodeluminescence studies and a model for energy transfer in establishing the roles of Tb^{3+} and Gd^{3+} . *RSC Advances*. 2016. **6(48)**: p. 42561-42571.
 211. Mckenna, B., Evans, R.C., Towards Efficient Spectral Converters through Materials Design for Luminescent Solar Devices. *Advance Materials*. 2017. **29(28)**: p. 1606491.
 212. Yan, X., Fern, G.R., Withnall, R., Silver, J., Effects of the host lattice and doping concentration on the colour Tb^{3+} cation emission in $\text{Y}_2\text{O}_2\text{S:Tb}^{3+}$ and $\text{Gd}_2\text{O}_2\text{S:Tb}^{3+}$ nanometer sized phosphor particles. *Nanoscale*. 2013. **5(18)**: p. 8640-8646.
 213. Fern, G.R., Ireland, T.G., Silver, J., Withnall, R., Michette, A., McFaul, C., Pfauntsch, S., Characterisation of $\text{Gd}_2\text{O}_2\text{S:Pr}$ phosphor screens for water window X-ray detection. *Nuclear Instruments and Methods in Physics Research Section A*. 2009. **600(2)**: p. 434-439.
 214. Tahhan, A., Dehouche, Z., Fern, G.R., Haverkamp, E., Photovoltaic cells energy performance enhancement with down-converting photoluminescence phosphors. *Internal Journal of Energy Research*. 2015. **39(12)**: p. 1616-1622.
 215. Liu, J., Wang, K., Zheng, W., Huang, W., Li, C.H., You, X.Z., Improving spectral response of monocrystalline silicon photovoltaic modules using high efficient luminescent down-shifting Eu^{3+} complexes. *Progress in Photovoltaics: Research and Applications*. 2013. **21(4)**: p. 668-675.
 216. Jing, X., Ireland, T.G., Gibbons, C., Barber, D.J., Silver, J., Vecht, A., Fern, G.R., Trowga, P., Morton, D.C., Control of $\text{Y}_2\text{O}_3\text{:Eu}$ spherical particle phosphor size, assembly properties, and performance for FED and HDTV. *Journal of the Electrochemical Society*. 1999. **146(12)**: p. 4654-4658.
 217. Silver, J., Withnall, R., Marsh, P.J., Lipman, A., Ireland, T.G., Fern, G.R., P-80: A New Oxide/Oxysulfide Based Phosphor Triad and High-Efficiency Green-Emitting $(\text{Y,Gd})_2\text{O}_2\text{S:Tb}$ Phosphor for FED Applications. *SID International Symposium Digest Technical Papers*. 2005. **36(1)**: p. 594-597.
 218. Yan, X., Fern, G.R., Withnall, R., Silver, J., Contrasting behaviour of the co-activators in the luminescence spectra of $\text{Y}_2\text{O}_2\text{S:Tb}^{3+}$, Er^{3+} nanometer sized particles under UV and red light excitation. *Nanoscale*. 2013. **5(3)**: p. 1091-1096.
 219. De Mello, J.C., Wittmann, H.F., Friend, R.H., An Improved Experimental Determination of External Photoluminescence Quantum Efficiency. *Advanced Materials*. 1997. **9(3)**: p. 230-232.
 220. Pi, X.D., Li, Q., Li, D.S., Yang, D., Spin-coating silicon-quantum-dot ink to improve solar cell efficiency. *Solar Energy Materials & Solar Cells*. 2011. **95(10)**: p. 2941-2945.

221. Malitson, I.H., Interspecimen Comparison of the Refractive Index of Fused Silica. *Journal of the Optical Society of America*. 1965. **55**(10): p. 1205-1209.
222. Kim, J., Park, J., Hong, J.H., Choi, S.J., Kang, G.H., Yu, G.J., Kim, N.S., Song, H., Double antireflection coating layer with silicon nitride and silicon oxide for crystalline silicon solar cell. *Journal of Electroceramics*. 2013. **30**(1-2): p. 41-45.
223. Lee, Y., Gong, D., Balaji, N., Lee, Y.J., Yi, J., Stability of SiNx/SiNx double stack antireflection coating for single crystalline silicon solar cells. *Nanoscale research letters*. 2012. **7**(1): p. 1-6.
224. Carrillo-López, J., Luna-López, J.A., Vivaldo-De la Cruz, I., Aceves-Mijares, M., Morales-Sanchez, A., García-Salgado, G., UV enhancement of silicon solar cells using thin SRO films. *Solar Energy Materials & Solar Cells*. 2012. **100**: p. 39-42.
225. Neralla, S., *Chemical Vapor Deposition: Recent Advances and Application in Optical, Solar Cells and Solid State Devices*. InTechopen, Rijeka, Croatia, 2016. ISBN: 9789535125730.
226. Santana, G., Morales-Acevedo, A., Optimization of PECVD SiN:H films for silicon solar cells. *Solar Energy Materials & Solar cells*. 2000. **60**(2): p. 135-142.
227. Cojocar, Q., Larrieu, S.G., Massines, L.T., Use of liquid precursor TMS for Deposition of Antireflective and Passivating a-SiC(N):H Thin Films with Low Pressure/Low Frequency PECVD. *Proceedings in 24th European Photovoltaic Solar Energy Conference*. Pages 1617-1622, 2009.
228. Tahhan, A., Dehouche, Z., Anson, T., Fern, G.R., Titanium dioxide nanoparticles for enhanced crystalline solar cell. In 40th IEEE Photovoltaic Specialist Conference (PVSC). P. 1299-1304.
229. Xue, Z.P., Deng, S.Q., Liu, Y.L., Lei, B.F., Xiao, Y., Zheng, M.T., Synthesis and luminescence properties of $\text{SrAl}_2\text{O}_4:\text{Eu}^{2+}$, Dy^{3+} hollow microspheres via a solvothermal co-precipitation method. *Journal of Rare Earth*. 2013. **31**(3): p.241-246.
230. Zhan, T.Z., Xu, C.N., Yamada, H., Terasawa, Y., Zhang, L., Iwase, H., Kawai, M., Enhancement of afterglow in $\text{SrAl}_2\text{O}_4:\text{Eu}^{2+}$ long-lasting phosphor with swift heavy ion irradiation. *RSC Advances*. 2012. **2**: p.328-332.
231. Sahu, I.P., Bisen, D.P., Brahme, N., Tamrakar, R.K., Luminescence behavior of europium activated strontium aluminate phosphors by solid state reaction method. *Journal of Materials Science: Materials in Electronics*. 2016. **27**: p. 3443-3455.
232. Yoshida, H., Fujino, S., Kajiwara, K., Afterglow luminance property of phosphorescent phosphor $\text{SrAl}_2\text{O}_4:\text{Eu}^{2+}$, Dy^{3+} -glass composites. *Journal of the Ceramic Society of Japan*. 2010. **118**(9): p. 784-787.
233. Rojas-Hernandez, Rubio-Macros, F., Enríquez, M.A., Rubia, D.L., Fernandez, J.F., A low-energy milling approach to reduce particle size maintains the luminescence of strontium aluminates. *RSC Advances*. 2015. **5**: p. 42559-42567.
234. Paterson, A.S., Raja, B., Garvey, G., Kolhatkar, A., Hagström, A.E.V., Kourentzi, K., Lee, T.R., Willson, R.C., Persistent Luminescence Strontium Aluminate Nanoparticles as Reporters in Lateral Flow Assays. *Analytical Chemistry*. 2014. **86**: p. 9481-9488.
235. McKeen, L.W., *Film Properties of Plastics and Elastomers*, 3rd Edition, William Andrew, Waltham, USA, 2012. ISBN: 9781455725519.

Appendix A Supplementary Information

A.1 Supplementary information: Comparison of solely EVA-coated solar cells by using two different screen-printing techniques

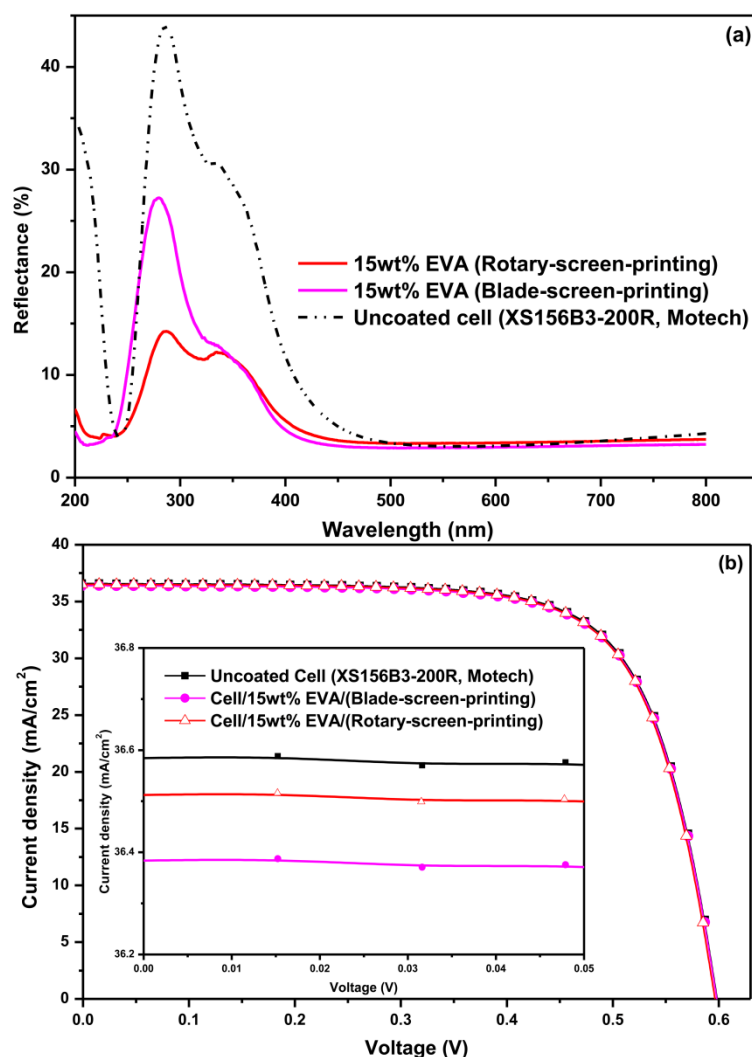


Figure A-1. Reflectance spectra (a) and J-V curves (b) of 15wt% solely EVA coated cells using two different screen-printing techniques.

Table A-1. Comparison of electrical characteristics of solely EVA coated cells using different screen-printing techniques.

Type	J_{sc} (mA/cm^2)	V_{oc} (mV)	P_{max} (W)	FF (%)	PCE (%)
Uncoated	36.58	599.3	0.1346	71.83	15.74
Cell/EVA (Blade-screen-printing)	36.39	598.9	0.1338	71.76	15.64
Cell/EVA (Rotary-screen-printing)	36.51	599.0	0.1341	71.71	15.68

A.2 Supplementary information: Electrical characteristics of EVA/Gd₂O₂S:Tb³⁺ coated cells under natural sunlight

In order to further prove the enhanced electrical performance brought by the Gd₂O₂S:Tb³⁺ phosphor, the optimised solar cells that obtained were also characterised under real sunlight. The solar irradiance was measured by a pyranometer (SP-110-SS, Apogee Instruments, USA) and a UV light meter (UV-340A, Luton Electronic, USA).

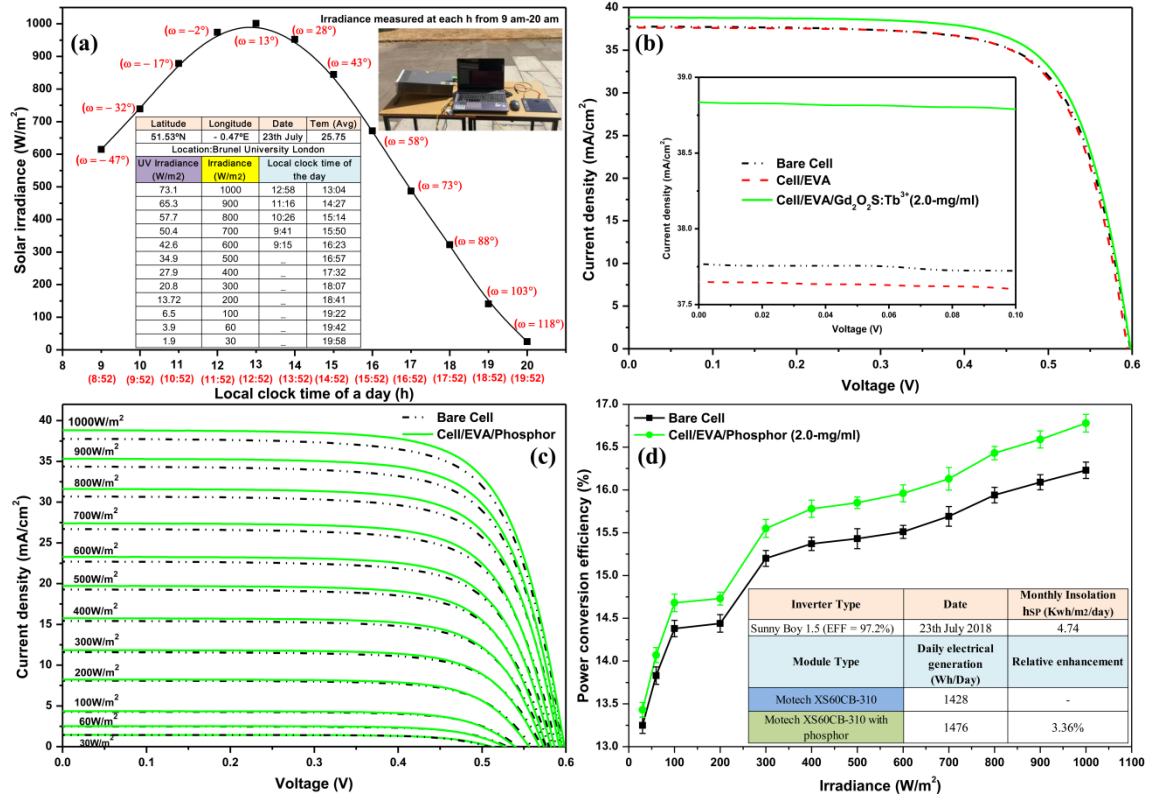


Figure A-2. (a) Distribution of solar irradiance per time of a particular day in July (the solar time for each recorded local clock time is labeled underneath, and the solar hour angle “ ω ” with regard to the corresponding solar time is highlighted). Inset image and table show separately the experimental set-up and the timely irradiance intensity as well as the geographic information. (b) J-V curves of solar cells before and after coating with solely EVA and EVA/Gd₂O₂S:Tb³⁺ (2.0-mg/ml) under natural sunlight illumination (1000 W/m²). (c) J-V curves of optimised solar cells at different irradiance levels. (d) Comparison of PCE between uncoated and coated cell with EVA/Phosphor as a function of irradiance variations. Inset table demonstrates an example of the phosphor application on a commercial Motech mono-Si PV module where the daily electric generations for XS60CB310 module with and without phosphor coating (2.0-mg/ml) are compared. The mass of Gd₂O₂S:Tb³⁺ phosphor for covering the effective area for a module is estimated to be at 506.7 mg.

Table A-2. J-V characteristics of mono-Si solar cells coated with EVA and EVA/Gd₂O₂S:Tb³⁺ (2.0-mg/ml) under natural sunlight illumination (light intensity =1000 W/m²).

Type	Jsc (mA/cm ²)	Voc (mV)	Pmax (W)	FF (%)	PCE (%)	Absolute Enhanc ement	Relative Enhanc ement
Uncoated	37.76	599	0.1388	71.71	16.23	-	-
Cell/EVA	37.64	595	0.1381	71.82	16.14	-0.09%	-0.55%
Cell/EVA/Gd ₂ O ₂ S:Tb ³⁺	38.85	600	0.1435	72.04	16.78	0.55%	3.4%

A.3 Supplementary information: Discussion of experimental attempts with regard to Ethyl Cellulose for PV cell encapsulation

In this thesis, in addition to EVA, Ethyl Cellulose (EC) (ETHOCEL™, Dow chemical EU) polymer was also attempted to be used as a potential alternative binder for encapsulating PV cell due to its unique organo-solubility as well as moderate refractive index value ($n = 1.47\sim 1.48$) and electrical properties [235].

However, the reason that an EVA was finally chosen in place of EC sample was twofold. Firstly, commercial EC with appearance of white powder and large particle size (average size around 15 micrometers) would not form a transparent binding layer at room temperature although it can be easily dissolved in p-xylene solution, instead, the precipitate would deposit and eventually form a cloudy-white film onto the cell surface as soon as the coated solution reached its saturation condition, which resulted in a significant shading effect that reduced the original transmittance towards the cell. Secondly, in terms of PV cell reliability, the encapsulant properties are critical in respond to UV irradiation, it was observed that EC film degraded easily under UV or natural sunlight illumination, however, this may largely inhibit the absorption capabilities of light harvesting materials (such as TiO_2 and phosphor) that having spectral operating or functionality particular in the UV-blue range. Therefore, the EC polymer may not be a suitable encapsulating candidate for the scenario in current research that both light transmittance and matching performance need to be taken into account.

Appendix B Poster Presentations

This appendix contains the posters presented in the conference events.

Nanostructured MgO-doped TiO₂ Aerogels for Enhanced Monocrystalline Silicon Solar Cells

Fanchao Meng*, Aorrapum Nutasarin, Dr Zahir Dehouche, Dr George Fern

* Corresponding author: Fanchao.Meng@brunel.ac.uk



Introduction:

The development of high-efficiency and low-cost silicon solar cells is important for the generation of electric power to satisfy the continuous worldwide energy demand in the future. Nanostructured materials have showed the great contribution to improve the light capturing capability of silicon PV devices [1].



Figure 1. Photovoltaic systems

TiO₂ has a large band gap range of 2.96-3.02eV. As a UV-absorbing dielectric material, it has relatively high refractive index and brilliant transparency in the wide wavelength rang from visible to infrared light [2]. It is indicated that MgO doped TiO₂ has the potential to reduce crystalline size of TiO₂. TiO₂ using MgO as dopant could result in a small red shift of both absorption and emission peak [3].

Objectives:

Since the thermalization usually occurs when the energy of illuminating photons is higher than the substrate (silicon solar cell), the excess energy of the active photons will convert into heat as result of insufficient response of light in short wavelength range. The objective of this research is to:

- To analyze and evaluate the effects of TiO₂ nanoparticles coating on silicon mono-crystalline PV cells.
- To compare quantitatively the two different level of effects on solar cells when coating with pure TiO₂ film and MgO doped TiO₂.
- To illustrate the electrical, optical and morphological characteristics of mono-crystalline solar cells for efficiency improvement.

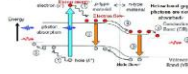


Figure 2. Losses in a silicon solar cell (1) Thermalization loss (2) Transparency/transmittance loss (3) Recombination loss

Methodology:

Nanostructured TiO₂ based aerogels were synthesized using a compact PARR high pressure reactor. The nanopowders were then oxidized in a furnace at 400°C for 10 hours.

Commercial single junction mono-crystalline solar cells were coated with pure TiO₂ and MgO doped TiO₂ nanoparticles. Both materials are encapsulated in Ethylene Vinyl Acetate (EVA) binder and applied to the active surface of the cells using the blank screen printing technique [4]. An average film thickness of 9µm was observed by Scanning Electron Microscopy (SEM).

Figure 3. High pressure reactor for the nanocomposite synthesis

Electrical characteristics:

The mono-crystalline solar cells were tested at 25°C under visible light with solar irradiance level around 1000W/m² and the illuminated area of solar cell is 8.04cm². The electrical performance of solar cells before and after coating with TiO₂ based nanoparticles are shown in the current versus voltage (I-V) and power versus voltage (P-V) diagrams.

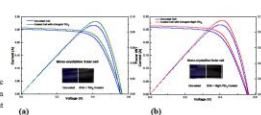


Figure 4. I-V and P-V curves of uncoated and coated cell with (A) EVA+TiO₂ and (B) EVA+ MgO doped TiO₂ under 25°C and solar irradiance of 1000W/m²

	Isc	Voc	Imp	Vmp	Pmp	FF	η	η _{rel}
Uncoated	0.035	0.570	0.007	0.450	0.003	0.58	5.20	
EVA+TiO ₂	0.035	0.570	0.007	0.450	0.003	0.58	5.20	
EVA+MgO-TiO ₂	0.035	0.570	0.007	0.450	0.003	0.58	5.20	
MgO-TiO ₂	0.035	0.570	0.007	0.450	0.003	0.69	6.17	

Table 1. Electrical results on Visible light for sample coated with TiO₂ and MgO-TiO₂

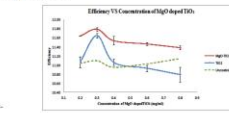


Figure 5. Efficiency enhancement of coated solar cells

The results demonstrated that the concentration of dispersed TiO₂ nanoparticles encapsulated in EVA binder has a strong influence on the amount of light absorbed and thus the conversion efficiency of the cells.

Optical properties:

The optical measurements were performed using a Perkin-Elmer Lambda 650S UV-Vis spectrometers with wavelength range from 200nm to 800nm.

The results show that coated cells with enhanced electrical characteristics exhibit less overall reflectance when compared with uncoated one in the wavelength range of middle and long ultraviolet, visible and near infrared regions, suggesting more photons are absorbed, which also confirm the antireflective properties of TiO₂.

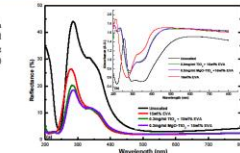


Figure 6. Comparison of (a) reflectance spectra and (b) absorption spectra for uncoated and coated cells

Structural Analysis:

Figure 7(a) shows a cross-section SEM image of the solar cell coated with TiO₂ based nanomaterial. The image indicates a good dispersion of segregated nanoparticles.

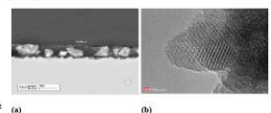


Figure 7. (a). Cross section SEM image of the coated cell with EVA+MgO doped TiO₂ (b). TEM image of nanostructure MgO-TiO₂ composite. The image shows also the pyramidal texture of the raw cell surface, and the coated layer of MgO doped-TiO₂ plus EVA with an average thickness of 9µm. The high resolution TEM images (Figure 8(b)) of a single nanoparticle show ordered nanoscale patterns with hexagonal lattice morphology.

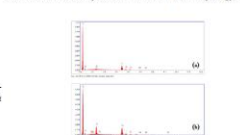


Figure 8. EDX spectra of coated mono-crystalline solar cells: (a). Cell coated with EVA+TiO₂ (b). Cell coated with EVA+MgO doped-TiO₂. Figure 8 shows the energy dispersive X-ray analysis spectrometers from the entire SEM scanned area of coated cells with enhanced electrical characteristics. The EDX spectra confirm the presence of expected chemical elements such as carbon, oxygen, titanium and magnesium in the deposited layers.

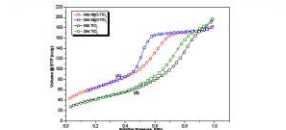


Figure 9. N₂ sorption isotherm of (A) representative MgO doped-TiO₂ aerogel and (B) TiO₂ aerogel

Materials	S _{sp} (m ² /g)	Crystallite size (nm)
TiO ₂ aerogel (the wide)	154.261	7.4
MgO-TiO ₂ aerogel (the wide)	231.364	5.0
TiO ₂ (1)	82	20

Table 2. Structural properties of TiO₂ based aerogel

It can be seen from the table 2 that TiO₂ aerogels synthesized in this work show a specific surface area of 154.261m²/g in comparison with 82m²/g prepared by studied method [5]. In case of MgO-doped TiO₂ aerogels, a larger specific surface area of 231.364 was observed.

Conclusion:

The electrical and optical characteristics results demonstrate that doping nanostructured TiO₂ with MgO yields increased electrical efficiency and substantial increase of overall photons absorption. EVA encapsulated TiO₂ nanoparticles enhance electrical performance, but not as much as MgO doped-TiO₂. Moreover, the results demonstrated that the concentration of dispersed TiO₂ based nanoparticles has a strong influence on the electrical efficiency of the coated cells. An optimum relative increase in power conversion efficiency of 6.2% in visible light has been obtained with MgO doped-TiO₂ nanocomposite at 0.3 (mg/ml) concentration. This enhancement can be further improved by optimizing the coating procedure.

Acknowledgement

We are thankful to Dr. Ashley Hawkins of ETC for SEM and TEM analysis.

References:

- Lee, Y.Y., Ho, W.J., Chen, Y.T. (2014). Performance of plasmonic silicon solar cells using indium nanoparticles deposited on a patterned TiO₂ matrix. *Thin Solid Films*, 570(2), pp. 174-180.
- Tatikainen, L. (2008). Nanostructures for photovoltaics. *Materials Science and Engineering: Reports*, 63(3), pp. 175-180.
- Karimova, K., Ponomarev, D., Kenedy, J., Mankadkar, E. (2014). SYNTHESIS OF Mg DOPED TiO₂ NANOCRYSTALS PREPARED BY WET CHEMICAL METHOD: OPTICAL AND MICROSCOPIC STUDIES. *International Journal of Biomedicine*, 32(4), pp. 1100-1114.
- Chen, P., Conte, P., Naranjo, M.K., Liska, P., Peck, P. (2007). et al. Fabrication of complementary p-n junctions from TiO₂ systems for dye-sensitized solar cells. *Progress in Photovoltaics: Research and Applications*, 15(7), pp. 495-512.
- Parisi, S.K., Pava, R.J., Kozicki, R.T. (2013). Modulating the structural properties and photo-catalytic hydrogen production activity of TiO₂ by high temperature supercritical drying. *International Journal of Hydrogen Energy*, 38(25), pp. 3015-3023.

This poster was presented in the 32nd European PV Solar Energy Conference and Exhibition (EU PVSEC), 2016. The poster titled “Nanostructured MgO-doped TiO₂ Aerogels for Enhanced Monocrystalline Silicon Solar cells”. Author of this work were Mr Fanchao Meng, Dr Zahir Dehouche, Miss Nutasarin Aorrapum, and Dr George Fern.

Photoluminescence of green-emitting Gd₂O₂S:Tb³⁺ phosphor for enhanced monocrystalline silicon solar cells

Fanchao Meng^{*1}, Zahir Dehouche¹, Terry G. Ireland² and George R. Fern²

Introduction:

The current photovoltaic (PV) market is still dominated by crystalline silicon (c-Si) solar cells owing to their abundance, stability and non-toxicity [1][2]. However, these devices suffer from different types of energy losses caused by spectral mismatch and the strong thermalization of charge carriers [3].

Reducing these losses in silicon solar cell could be achieved through the spectrum modification by employing down-converting phosphors [4]. In a down-conversion process (DC) (see Fig. 1), the phosphors absorb high-energy photons within ultraviolet (UV) region and re-emit at longer wavelength where the silicon solar cells exhibit a robust spectral response [5].

Objectives:

- The objective of this work is:
 - To investigate the potential applications of down-converting Tb³⁺-doped Gd₂O₂S phosphor in an attempt to improve the power conversion efficiency (PCE) of single-junction monocrystalline silicon (mono-Si) solar cells.
 - To develop a cost-effective luminescent layer on the textured surface of mono-Si solar cell.
 - To illustrate the electrical and optical characteristics of solar cells for efficiency improvement.

Methodology:

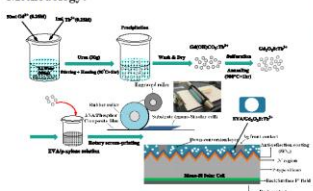


Fig. 2 Flow diagram showing the preparation and integration of Gd₂O₂S:Tb³⁺ phosphor on the surface of mono-Si solar cell.

Submicron-sized Gd₂O₂S:Tb³⁺ phosphor particles were prepared by a simple urea homogeneous precipitation method and subsequent annealing process. The luminescent layer was formed by screen printing the EVA-phosphor mixture on the textured surface of mono-Si solar cell using a rotary roller.

Structural and Morphological Analysis:

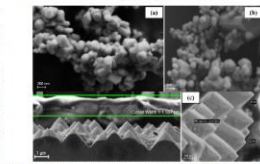


Fig. 3 FESM micrographs of (a) representative Gd₂O₂S:Tb³⁺ and (b) undoped-Gd₂O₂S particles annealed at 900 °C; (c) cross-section image of solar cell showing the morphology of pyramidal textured silicon surface and the coated layer composed of EVA/Gd₂O₂S:Tb³⁺ with an average thickness of 1.56 μm, and a 90°-oblique view for clear vision of the integration of phosphor particles on the cell's textured surface.

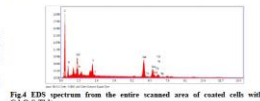


Fig. 4 EDS spectrum from the entire scanned area of coated cells with EVA/Gd₂O₂S:Tb³⁺.

Fig. 3 (a) and (b) shows the typical SEM micrographs of the synthesized Tb³⁺-doped Gd₂O₂S and undoped-Gd₂O₂S particles. The micrographs show well formed crystals of discrete particles and they are roughly truncated-spherical shape with apparently smooth surfaces. The EDS spectrum [Fig. 4] confirms the presence of the expected chemical elements such as gadolinium, oxygen, sulfur and terbium in the deposited layers.

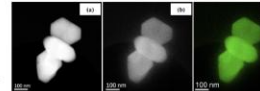


Fig. 5 STEM micrographs of (a) single crystals of Gd₂O₂S:Tb³⁺; (b) Total visible light image using the VCLCN detector; (c) overlay of images of (a) and (b).

Fig. 5 shows the composite STEM and Cathodoluminescence (CL) image taken in TEM that exhibits the high uniformity of visible light (green) emission from the synthesized phosphor. The size range of 190 to 240 nm were measured from those well discrete particles. The XRD analysis [Fig. 6] indicates that the particles show the characteristic XRPD pattern of hexagonal Gd₂O₂S crystal matching the standard JCPDS data file (No. 26-1422).

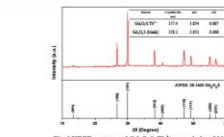


Fig. 6 XRPD pattern of Gd₂O₂S:Tb³⁺ annealed at 900 °C

Fig. 7 shows the photoluminescence excitation (PLE) and PL spectra of as-prepared Gd₂O₂S:Tb³⁺. The synthesized phosphor sample can be excited with 292 nm UV light and produces a strongest green emission band centered at 543 nm, which is assigned to the ⁵D₂ → ⁷F₃ transitions of Tb³⁺ cations.

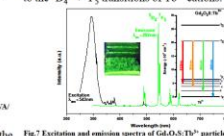


Fig. 7 Excitation and emission spectra of Gd₂O₂S:Tb³⁺ particles measured at room temperature.

Electrical characteristics:

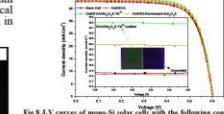


Fig. 8 J-V curves of mono-Si solar cells with the following configurations: 2 bare cells, a cell coated with solely EVA binder, a cell coated with EVA/Gd₂O₂S:Tb³⁺, and a cell coated with EVA/undoped Gd₂O₂S.

The enhancement brought by dispersed phosphor at different concentrations in EVA binder can be also achieved (see table 1 and Fig. 9).

Table 1. J-V characteristics of different phosphor cells.

Configuration	V _{oc} (V)	J _{sc} (mA/cm ²)	FF (%)	PCE (%)
2 bare cells	0.55	35.5	75	16.43
cell coated with EVA binder	0.55	35.5	75	16.43
cell coated with EVA/Gd ₂ O ₂ S:Tb _{0.01}	0.55	35.5	75	17.02
cell coated with EVA/Gd ₂ O ₂ S:Tb _{0.02}	0.55	35.5	75	17.02
cell coated with EVA/Gd ₂ O ₂ S:Tb _{0.03}	0.55	35.5	75	17.02
cell coated with EVA/Gd ₂ O ₂ S:Tb _{0.04}	0.55	35.5	75	17.02
cell coated with EVA/Gd ₂ O ₂ S:Tb _{0.05}	0.55	35.5	75	17.02
cell coated with EVA/undoped Gd ₂ O ₂ S	0.55	35.5	75	16.43

Optical characteristics:

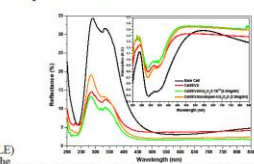


Fig. 9 Reflectance and absorption (near) spectra of mono-Si solar cells before and after coating with solely EVA, EVA/Gd₂O₂S:Tb³⁺, and EVA/undoped Gd₂O₂S.

Fig. 10 shows the reflectance and absorption spectra for all cells evaluated in this study. The results demonstrate that the EVA/Gd₂O₂S:Tb³⁺ exhibits higher reflectance across the wavelength range of 200 to 800 nm. A reduction in reflectance in the UV-region was observed. The corresponding EQE response of coated cells are presented in Fig. 11.

Fig. 10 External quantum efficiency (EQE) response of all cells compared in this work.

Conclusions:

We developed a cost-effective luminescent layer on the textured surface of mono-Si solar cell and demonstrated that the down-converting Gd₂O₂S:Tb³⁺ phosphor could effectively improve the conversion efficiency of the cell. Experimental results showed an optimum enhancement of 3.6% (from 16.43% to 17.02%) in PCE relative to those for a pristine cell. This enhancement is attributed to the conjunction effects of the EVA binder and the Gd₂O₂S:Tb³⁺ phosphor. More works to further improve the conversion efficiency by optimizing the appropriate phosphors properties is currently in progress.

References:

- [1] Battaglia C, Cuevas A, Wolf SD. High-efficiency crystalline silicon solar cells: status and perspectives. *Energy Environ Sci*. 2016;9(3):1537-1576.
- [2] Green MA, Hoekawa Y, Dunlop ED, Levy DH, Hohlhauser J, He, Huhner AWY. Solar cell efficiency tables (version-5). *Prog Photovolt Res Appl*. 2018;26(1):1-12.
- [3] Shockley W, Queisser HT. Detailed Balance Limit of Efficiency of a Junction Solar Cell. *J Appl Phys*. 1951;32(1):73-103.
- [4] Dupke T, Green MA, Welfel P. Improving solar cell efficiencies by down-conversion of high-energy photons. *J Appl Phys*. 2002;92(5):4111-4122.
- [5] Richards BS. Luminescent Layers for Enhanced Silicon Solar Cell Performance: Down Conversion. *Sol Energy Mater Sol Cells*. 2006;90:1189-1207.

Correspondence: Fanchao Meng, College of Engineering, Design and Physical Sciences, Brunel University London, Uxbridge, UB8 3PH, UK. E-mail: Fanchao.Meng@brunel.ac.uk

This poster was presented in the 2nd International Conference in Advanced Energy Materials (AEM), 2017. The poster titled “Photoluminescence of green-emitting Gd₂O₂S:Tb³⁺ phosphor for enhanced monocrystalline silicon solar cells”. Author of this work were Mr Fanchao Meng, Dr Zahir Dehouche, Dr Terry Ireland, and Dr George Fern.